PNC TN831 80-01

POWER REACTOR & NUCLEAR FUEL
DEVELOPMENT CORPORATION
JAPAN

TOKAI WORKS
ANNUAL PROGRESS REPORT

January 1979 ~ March 1980

September 1980

TOKAI WORKS
ANNUAL PROGRESS REPORT

January 1979～March 1980

TOKAI WORKS
POWER REACTOR & NUCLEAR FUEL DEVELOPMENT CORPORATION
TOKAI, IBARAKI, JAPAN

September 1980

動力炉・核燃料開発事業団 (Power Reactor and Nuclear Fuel Development Corporation)

PREFACE

The Power Reactor and Nuclear Fuel Development Corporation (PNC) is a semi-governmental organization responsible for the development of advanced power reactors and nuclear fuels in Japan.

The Tokai Works, the largest branch of the PNC has made numerous accomplishments on research and development of nuclear fuels since its foundation in 1958.

The main activities of the Tokai Works at present are the development and fabrication of plutonium-bearing fuels, the research and development of centrifugal uranium enrichment technology, the test operation of the Tokai Reprocessing Plant, and the related research and development work.

This progress report contains accomplishments in the activities of the Tokai Works during the period from Jan. 1979 to Mar. 1980.

We hope this report will offer an opportunity for mutual cooperation in the field of nuclear energy.

Yasuji NAKAMURA
Director of the Tokai Works,
Power Reactor and Nuclear Fuel
Development Corporation,
Tokai-Mura, Ibaraki-Ken, Japan

CONTENTS

Health and Safety Division

Reprocessing Plant

Uranium Enrichment Development Division

Plutonium Fuel Division

Activity of Plutonium Fuel Division (Jan. 1979—Mar. 1980)

Twenty-four fuel assemblies for the reactor FUGEN were fabricated and then shipped to the reactor site on March 6th, 1980 to be loaded in both 1st and 2nd reloadings. The work was initiated to fabricate the 3rd reloaded fuel. In the R & D of ATR fuel, measurements of high-temperature strength of MOX pellet and friction coefficient between pellet and zircalloy cladding were made, whose data are to be used for the evaluation of PCMI.

Modification of the facility of FBR fuel fabrication line was completed for MK-2 core fuel fabrication, and test runs have been conducted with new equipment to show reliability. Such R & D work on fuel fabrication study and fuel design evaluation by computer codes were performed for MONJU fuel, of which fabrication is supposed to undertaken in near future.

In the general study on MOX fuel, miscellaneous studies have been made covering plutonium recycle economy and strategy, and preparation work for the over-power experiments in NSSR.

Regarding development of co-conversion process of Pu-U nitrate solution to MOX powder, installation of process equipment with a conversion capacity of 2Kg MOX/day was completed, and thereafter the co-conversion experiment was begun for MOX powder with one to one ratio between uranium and plutonium.

R & D works were also continued for the treatment of plutonium contaminated waste.

1. Heavy Water Reactor Fuel

Twenty-four fuel assemblies for both 1st and 2nd reloadings of FUGEN were fabricated, and then shipped to the reactor site on March 6th, 1980. Also two-hundred sixty-one fuel rods of 0.55% Pu-fissile content were finished in the following fabrication campaign of the 3rd reloaded fuel. Meanwhile thirty-five special type fuel rods were fabricated and shipped to DCA in October.

Regarding the irradiation tests, the following activities were conducted. The results in IFA-423 irradiation test were evaluated with ATFUEL code and the data of SGHWR-type D irradiation test were analyzed. In R & D of ATR fuel, measurements of high-temperature strength of MOX pellet and friction coefficient between pellet and zircalloy cladding were conducted, whose data are to be used for the evaluation of PCMI.

2. Fast Breeder Reactor Fuel

Regarding MK-2 core fuel fabriction, modification of the FBR fuel fabrication line was at last completed with installation of the fuel assembling machine. The plutonium test run for pellet preparation began after a series of uranium test runs, and a series of experiments was conducted for dry recovery of rejected MK-2 pellets of 30% plutonium-oxide content by oxidation and reduction treatment. End-plug welding tests were continued for fuel pin fabrication and an automatic machanism was developed for replacement of weld electrodes. Also the design was developed for the MK-2 special fuel, aiming to make a series of irradiation experiments on both FBR fuel and structural materials. There are contained three types of special fuels, A type, B type and C type among which design proceeded most actively for the C type.

For the development of MONJU fuels technology, fabrication tests were continued on the pellets with low O/M ratio and low gas content. Dry recovery of rejected pellet of 30% plutonium-oxide content was tested with promising results. For automatically assembling of fuel bundle, much effort was made for the survey of both shape and dimensional precision of assemble parts. Basic studies of fuel design evaluation and of fuel irradiation performance were conducted along with measurements of such pellet characteristics as thermal conductivity, high temperature strength and sintering shrinkage. Fuel irradiation tests were continued at JMTR and EBR-2. Fuel specimens were prepared for irradiation test at JRR-2, and twenty fuel pins, which were fabricated last year, were shipped to the Phenix reactor in France for irradiation test (called Phenix PNC-3). Considerable effort was made in order to develop computer codes "CEDAR", DIRA and DFR, which are to make the prediction of fuel irradiation performance.

For development of a container for fuel assembly shipment, transportation tests was successfully conducted including measurements of vibration characteristics of the assembly with a dummy MK-2 fuel assembly. The data obtained from the tests

will be used for "Safety Analysis Report" in the licensing application of the MK-2 fuel container. Also the specifications were compiled for designing a container for MONJU fuel assembly.

3. General study of MOX fuel

In regard to study of LWR fuel, irradiation of IFA-514 fuel rods were initiated on July 10th at Halden reactor (HBWR) of Norway and then twelve fuel rods of IFA-529 project were shipped to Halden reactor. For pellet-densification observation, irradiation of five capsules in JRR-2 was completed and neutron radiographs were taken on two capsules.

A new programme related to safety evaluation of MOX fuel was initiated in collaboration with JEARI. In this programme, a series of pulse irradiation tests in NSSR is scheduled for the observation of fuel pin failure behaviour under excessive heating of reactivity excursion.

Since a series of criticality experiments at TCA of JEARI was finished, the analysis of experimental data was performed as to "Reactivity effect of ^{241}Pu decay" and "Effect of corner rods".

In the field of plutonium utilization study, a survey was conducted on re-enrichment of uranium recovered by reprocessing and on an effective plutonium use. Cost estimation of MOX fuels was continued using WAGIRI code on JOYO fuel, FUGEN fuel and ATR demonstration fuel.

4. Plutonium Facilities and Supporting Works

Detailed design of planned Plutonium Fuel Production Facililty (PFPF) was continued, in which both MONJU fuel and Demonstration ATR fuel are to be fabricated. Relating to the designing, automatic equipment for pellet preparation and chemical analysis have been developed with the cooperation of equipment manufacturing companies.

A governmental permission was obtained for renewal of the fuel fabrcation facility in PFDF, and the work for scrapping the old facility was started in early November.

The construction was started toward the end of August for a large storage faclity of plutonium-contaminated waste, having space to accommodate about six thousand drum containers. For treatment of plutonium-contaminated waste, various

approaches have been investigated to obtain basic and engineering information. They covered the treatment of such various waste as HEPA filter, metallic scrap, neoplene glove and vinyl chloride sheet. Especially, a micro-wave heating process was designed to treat a contaminated liquid from the chemical laboratory, and the construction was ordered to a manufacturing company. Based on the information from the R & D, the work was initiated to make a configuration design of a waste treatment facililty.

In the development of co-conversion process for Pu-U nitrate solution, the equipment of both ammonium co-precipitation process and denitration process were completely installed, and then test operation was made with uranium nitrate solution. In early July, co-conversion test started with Pu-U nitrate solution. It was confirmed that the property of the MOX powder obtained by denitration process of micro-wave heating was as good as that of powder by ammonium coprecipitation process. About 860Kg of Pu was co-converted by denitrtion process to the MOX powder from September through June.

Increase in O/M Ratio of Sintered Pellet of Uranium-Plutonium Mixed Oxide Stored at Room-Temperature *

Susumu SASAKI, Youzi OCHIAI
Sadamitsu KASHIMA and Yutaka HONDA

A number of investigations have been reported so far to reduce the oxygen-to-metal ratio (O/M) of sintered pellets of uranium-plutonium mixed oxide for prevention of fuel-cladding chemical interaction during irradiation.

Little attention, however, has been paid to a phenomenon that the O/M ratio of sintered pellets gradually increases in a usual glove-box atmosphere. This phenomenon is due to a room-temperature oxidation reaction termed O/M increases and is generally accelerated by the humidity in the atmosphere of pellet storage. In order to investigate this phenomenon, periodic O/M measurements were carried out on the pellets stored in three types of atmospheres shown in Table 1. Pellet specimens used in this study were made of hypostoichiometric mixed-oxide, $(U_{0.7}\cdot Pu_{0.3})O_{2-x'}$ which was fabricated as FBR type fuel pellets by a process illustrated in Fig. 1. Table 2 shows the characteristics of the pellet specimens. The O/M increase is expressed by the equation

$$\Delta W = \Delta(O/M)\frac{W}{M}\times 1.6 \quad \text{----------(1)}$$

where ΔW=weight increment of specimen equivalent to the

O/M change, $\Delta(O/M)$

W = specimen weight

M = molecular weight of the specimen

and 16= atomic weight of oxygen

*Presented at the Annual Meeting of the Atomic Energy Society of Japan (March,1979).

The increment Δ(O/M) can be calculated from the equation

$$\Delta(O/M) = (O/M)_t - (O/M)_s \text{ ----------(2)}$$

where $(O/M)_t$ and $(O/M)_s$ indicate the O/M ratios at the start and the time t, respectively.

Substituting (2) into (1),

$$(O/M)_t = (O/M)_s + \frac{\Delta W}{W} \cdot \frac{M}{16} \text{ ------- (3)}$$

According to continuous measurements of the specimen weight, the O/M increment was estimated for the total storage time up to 130 days. The O/M ratio is determined by heating the specimens to 800°C, exposing to air flow for 0.5 hr and then to N_2-5%H_2 gas flow for 4.0 hr (Fig. 2). The variations of the O/M ratio with storage time in the three types of atmospheres (see Table 1) are illustrated in Figs. 3, 4 and 5 respectively. It is seen from the figures that the rate of O/M increment apparently depends on the moisture content of running atmosphere. Using the data of Figs. 3 to 5, the value of the O/M ratio at a storage time t can be derived from the equation

$$(O/M)_t = (O/M)_i + A\left\{1-\exp\left[-\frac{(P_{H_2O})^{0.43}.t}{1.03}\times 10^{-4}\right]\right\} \text{--------(4)}$$

where $(O/M)_t$ = O/M ratio after storage time t (day)

$(O/M)_i$ = initial O/M of fuel pellet

A = constant

P_{H_2O} = water content of storage atmosphere (vpm)

The comparisons of O/M ratio between measured values in this study and ones calculated by Eq. (4) are illustrated in Fig.6. The figure shows that Eq. (4) is instructive to presume the increment of O/M ratio of sintered pellet during preservation.

Table 1. Test condition and starting date.

No.	Atmosphere	Water content ($\times 10^4$vpm)	Starting date
A	2.4N HCl (Wet box)	2.0 ~ 2.5	14,Sep.1977
B	Air	1.0 ~ 1.3	1,Apr.1978
C	Silicagel (Dry box)	0.2 ~ 0.4	1,Mar.1978

Table 2. Characteristic of specimen.

MOX	: $(U_{0.7}\cdot Pu_{0.3})O_{2-x}$
Diameter	: 5.41 (mm)
Height	: 9.92 (mm)
Density	: 85.3 (%T.D.)
O/M ratio	: $a_1 = 1.950$ $a_2 = 1.940$ $a_3 = 1.936$ $a_4 = 1.929$ $b_1 = 1.964$ $b_2 = 1.952$ $b_3 = 1.944$ $b_4 = 1.931$ $c_1 = 1.957$ $c_2 = 1.950$ $c_3 = 1.941$

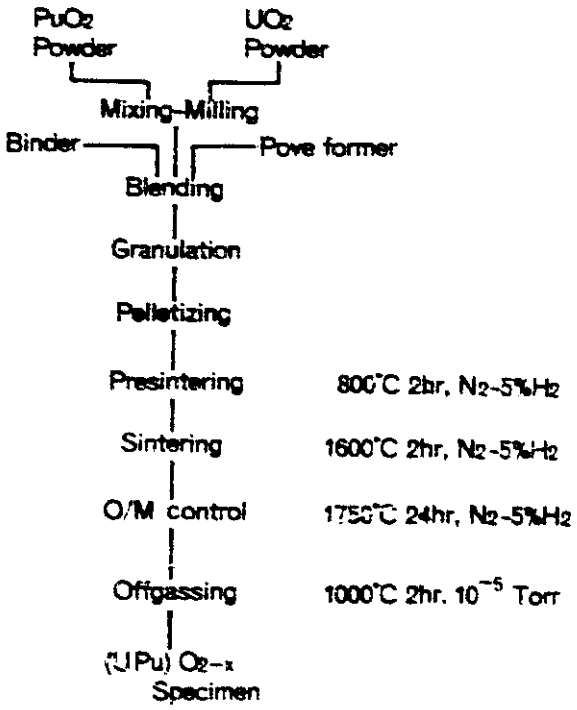

Fig. 1. FBR fuel pellet fabrication flow sheet.

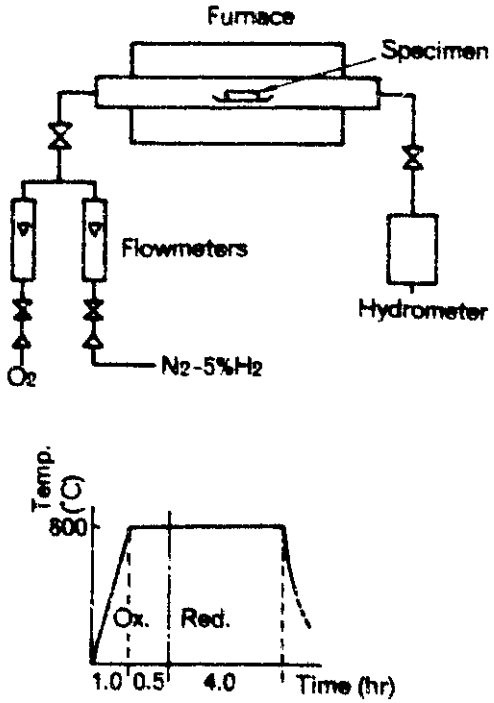

Fig. 2. Schematic drawing of oxidation-reduction process for measurement of O/M ratio.

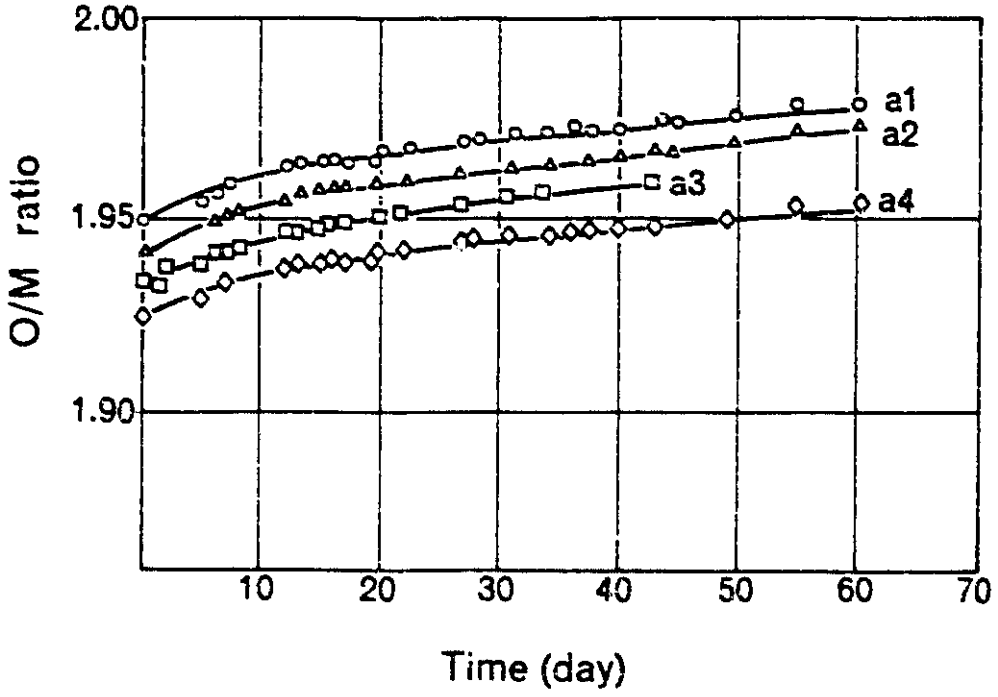

Fig. 3. O/M drift data under 2.0-2.5x10^4 Vpm H_2O (test-A).

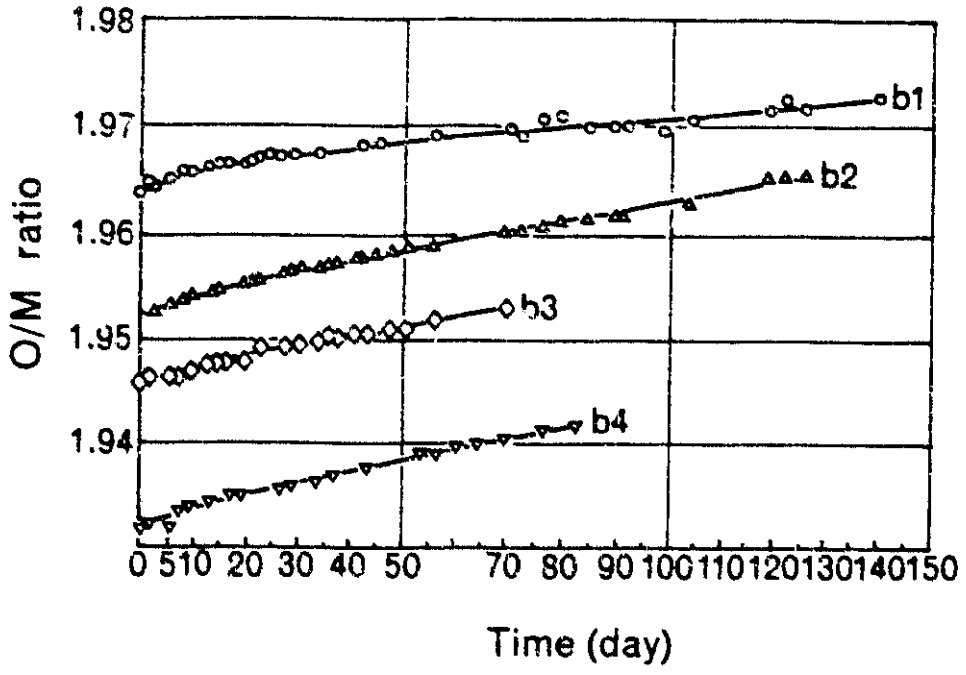

Fig. 4. O/M drift data under 1.0-1.3x10^4 Vpm H_2O (test-B).

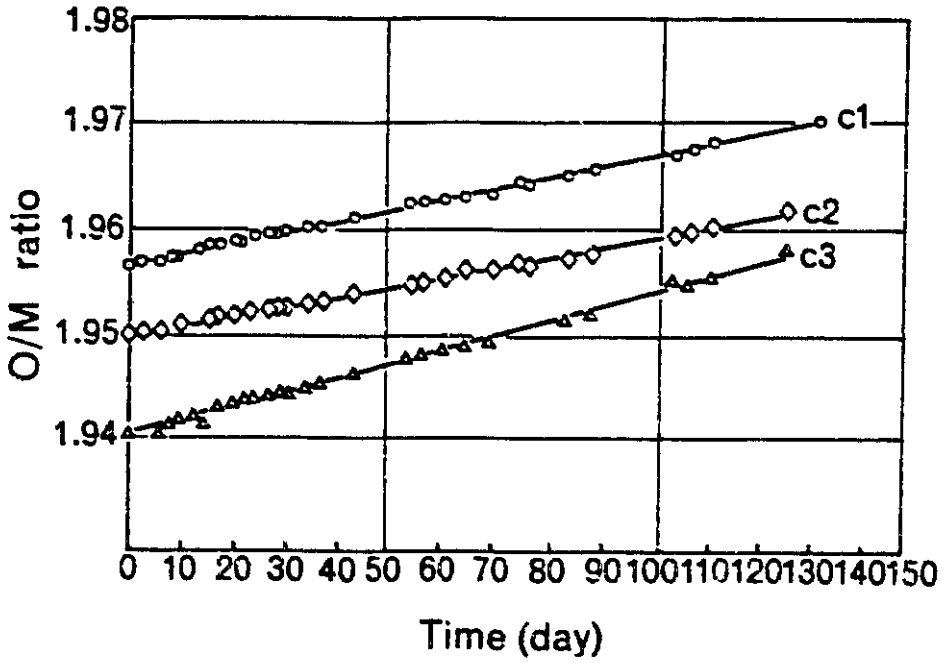

Fig. 5. O/M drift data under 2.0-4.0x10^3 Vpm H_2O (test-C).

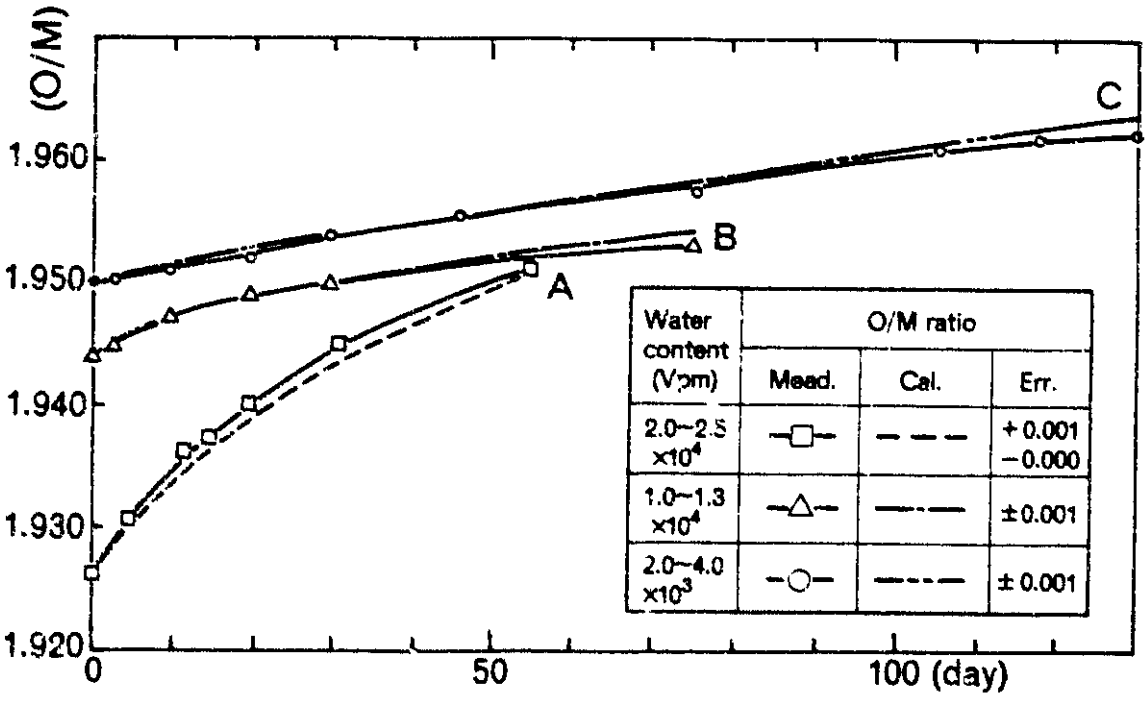

Fig. 6. Comparison of measured O/M ratio with calculated O/M ratio.

Measurements of Thermal Conductivity for $(U_{0.7}, Pu_{0.3})O_{2-x}$ Fuels*

Toshihiro YAMAGUCHI, Hiromitsu KANEKO
and Yutaka HONDA

1. Introduction

The UO_2-PuO_2 mixed oxide is used as a driver fuel in LMFBR. The design for the prototype fast breeder reactor "Monju" indicates that the mixed oxide fuel could contain a maximum of 30 wt% plutonium and the balance of uranium as fuel. It is necessary to know the thermal conductivity of (U, Pu)O_2 fuel for predicting thermal behaviour of fuel pins in LMFBR operation.

The thermal conductivities of (U, Pu)O_2 were measured and reported by many workers [1],[2],[3],[4],[5],[6], but their results were almost limited to the plutonium content up to 20 wt%. To the best of our knowledge, only a literature by Gibby[2] reported the thermal conductivity of 30 wt% plutonium content in the temperature range up to 1200°C.

In the present study, thermal conductivity measurements were made on specimens of $(U_{0.7}, Pu_{0.3})O_{2-x}$ sintered pellets with various densities and O/M ratios in the temperature range of 800 to 2400°C. Using the results obtained in this work, an empirical equation was proposed for representing the thermal conductivity of $(U_{0.7},Pu_{0.3})O_{2-x}$ as a function of temperature, fuel density and O/M ratio.

2. Experimental

2.1 Specimen Preparation

An outline of the specimen preparation process was shown in Fig.1. The

---

* Presented at the Fall Meeting of the Atomic Energy Society of Japan (October ,1979).

specimens of $(U_{0.7},Pu_{0.3})O_{2-x}$ pellets were prepared by sintering at 1750°C for 4 hrs in a N_2-5%H_2 atmosphere. Six kinds of $(U_{0.7}, Pu_{0.3}))O_2$ pellets were prepared for this study as shown in Table 1. The densities of the pellets were 85, 90 and 95% T.D.. The O/M ratios were controlled to 1.94, 1.96, 1.98 and 2.00 for the pellets with a density of 95%T.D., and 1.98 for the pellets with 85 and 905T.D. Figure 2 shows the shape and dimension of the pellets used in the experiment. As shown in the same figure, the pellet has a central hole of 5.0 mm in diameter to accomodate the tungsten rod heater. It also has logitudinal slit of 1 mm in width which has been expected to prevent a cracking caused by the thermal stress. The specimen pellet also has four black-body holes with different depths in radial directions for optical temperature measurement. The ratios of depth to diameter of the holes are in the range of 3 to 8 and are considered to satisfy a black-body condition.

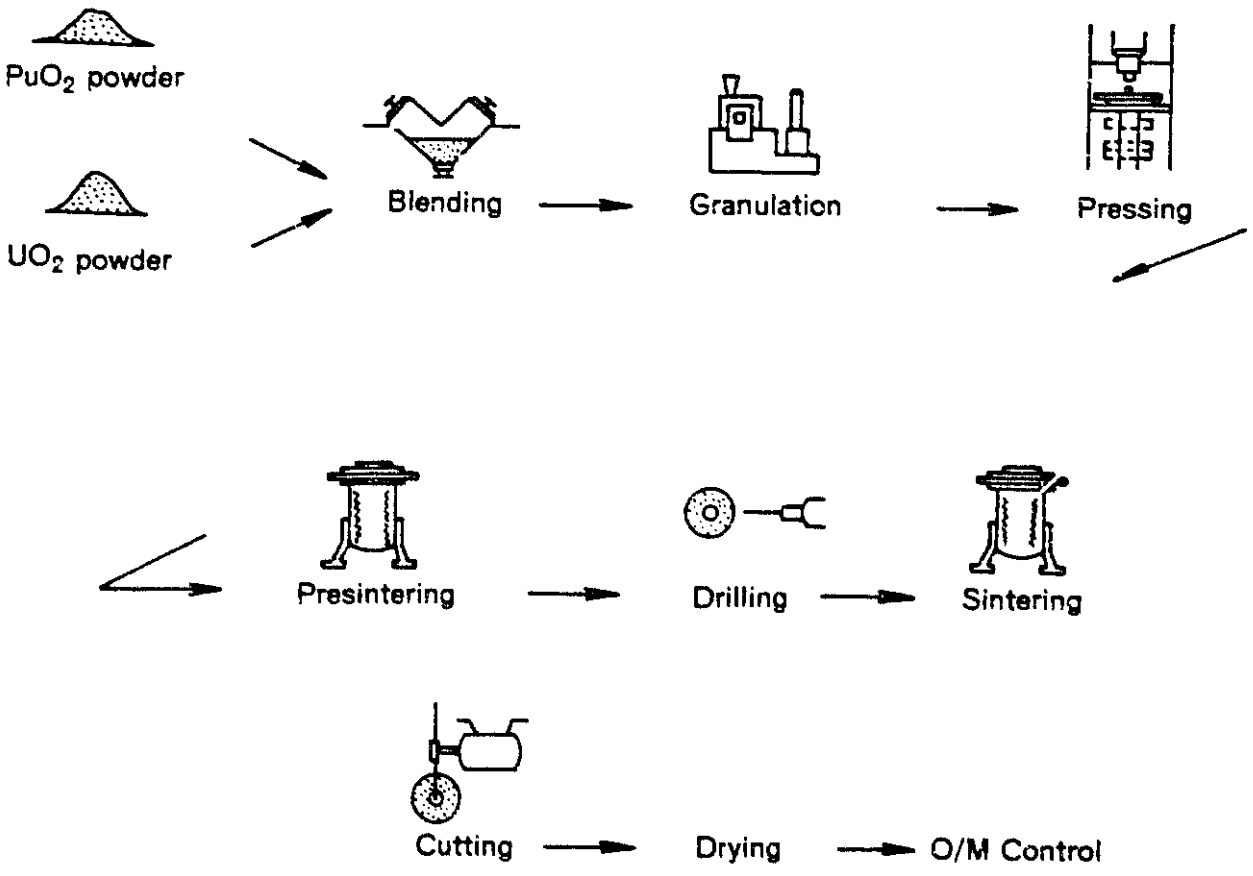

Fig. 1. An outline of specimen preparation process.

Table 1. Parameters of specimen used in the experiments.

Density (%T.D.)	O/M Ratio			
95	2.00	1.98	1.96	1.94
90		1.98		
85		1.98		

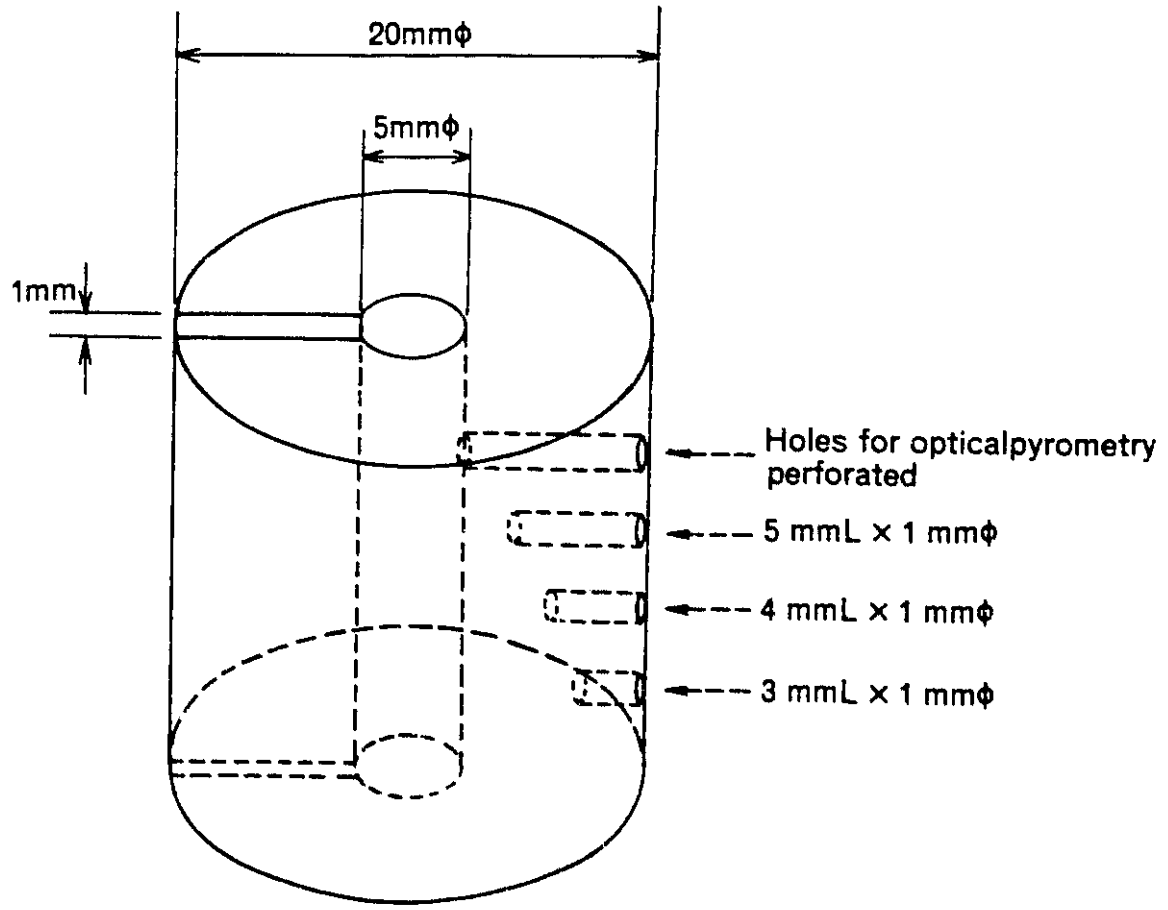

Fig. 2. Shape and dimension of the pellets used for thermal conductivity.

2.2 Apparatus

Apparatus for the thermal conductivity measurement is schematically shown in Fig. 3. It consists of a tungsten rod heater, a tungsten mesh heater, reflectors and a vacuum system. A tungsten rod heater with 4.9mm diameter is inserted through the center hollow of pellet. Since an electrical contact between the tungsten rod and the bottom electrode is provided by an In-Ga eutectic liquid metal pool, the movement of the rod is kept free even when the rod expands at high temperatures. To obtain a radial temperature gradient at high temperatures, hollow pellets are heated by both the tungsten rod and the surrounding tungsten mesh heaters. The operating temperature attains to 3000°C at the tungsten rod heater and 2800°C at the tungsten mesh heater.

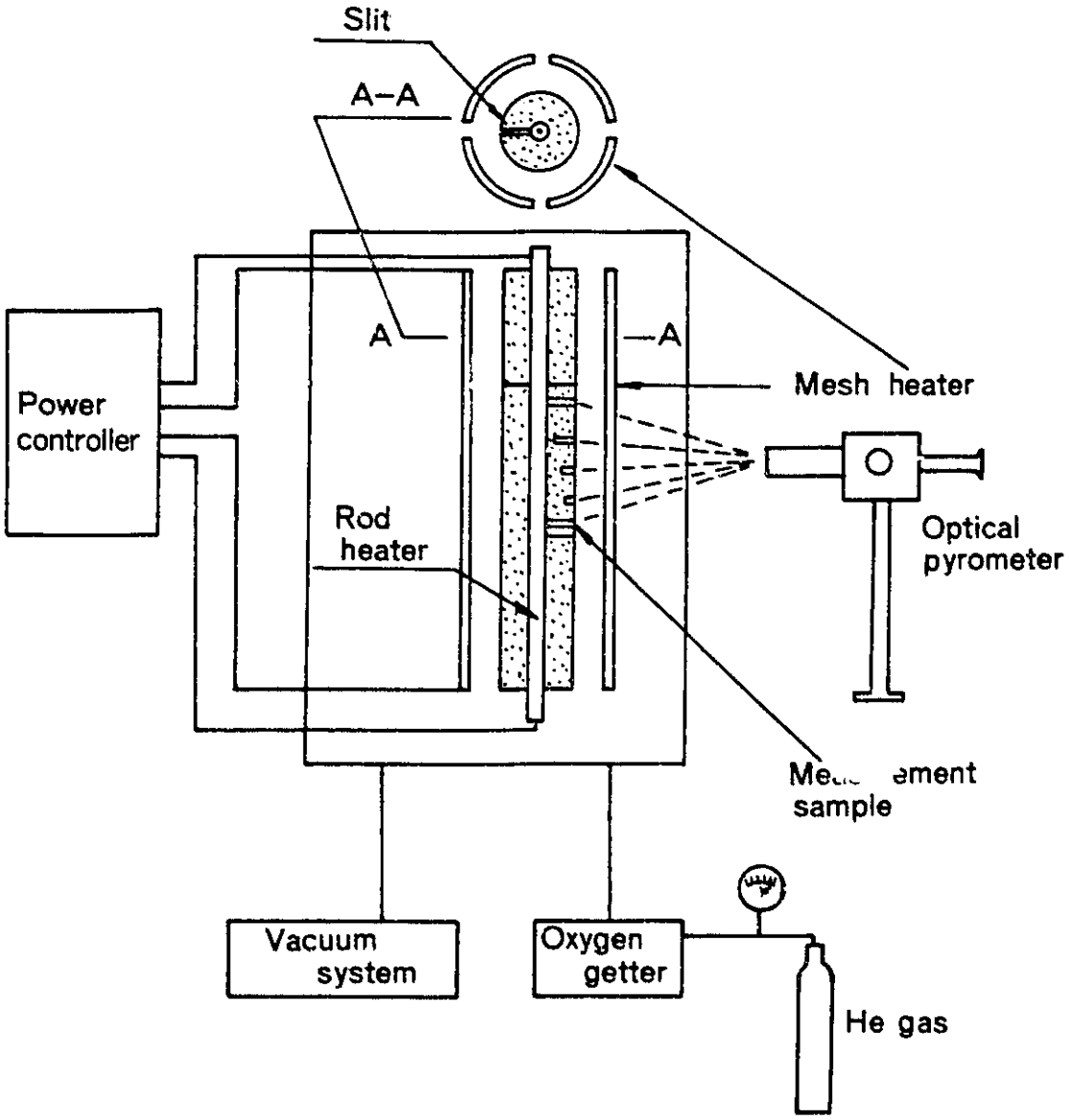

Fig. 3. Thermal conductivity measurement apparatus.

2.3 Procedure

Two specimens of $(U,Pu)O_2$ pellets were sandwiched by twelve UO_2 insulator pellets in a manner that six UO_2 pellets were placed beneath and the remaining six on the test specimens. Because of this configuration, axial heat loss from the specimens was minimized. The specimens were heated in the apparatus by high purity-helium gas ($1kg/cm^2$). Moisture in the helium gas is controlled to be less that 10 ppm by using a titanium getter. Temperature at the four black-body holes was measured with an optical pyrometer calibrated by a standard lamp in the temperature range of $800^{\circ}C$ to $2,400^{\circ}C$. The radial temperature gradient in the specimen was limited to be less than $1,000^{\circ}C/cm$ to prevent plutonium and oxygen redistribution.

Thermal conductivity is determined by the use of the following equation (1) which is based on the heat conduction through a homogeneous cylindrical wall,

$$K = \frac{Q/L}{2\pi(T_2 - T_1)} \ell n \frac{r_2}{r_1} \quad \text{-----} \quad (1)$$

where K is an average thermal conductivity ($w/cm\text{-}^{\circ}C$) between T_1 and T_2, and Q/L a linear power (w/cm). Then T_1 and T_2 are temperatures ($^{\circ}C$) at radii r_1 and r_2 (cm), respecitvely ($T_2 > T_1$ and $r_2 < r_1$). The values of generated power (Q) and electrical resistance (R) of the tungsten rod heater were calculated from the relations

$$Q = I^2R \quad \text{----------} \quad (2)$$

and

$$R = \rho \frac{L}{S} \quad \text{----------} \quad (3)$$

where I is the current (A), S the cross-section area (cm^2), and p the specific resistivity of tungsten rod heater (Ω .cm). L is the distance between penetration holes of the highest and lowest test specimens (cm).

In order to check validity of the apparatus used in this study, measurements of thermal conductivity were preliminary performed by using UO_2 specimens. The results were in good agreement with those of UO_2 thermal conductivity reported previously by others[4,5,6]. Figure 4 shows the conductivities in the temperature range of 950 to $2,150^{\circ}C$ for UO_2 with density of 93.4%T.D. After the confirmation of the validity, measurements on the $(U_{0.7},Pu_{0.3})O_{2-x}$ pellets were conducted.

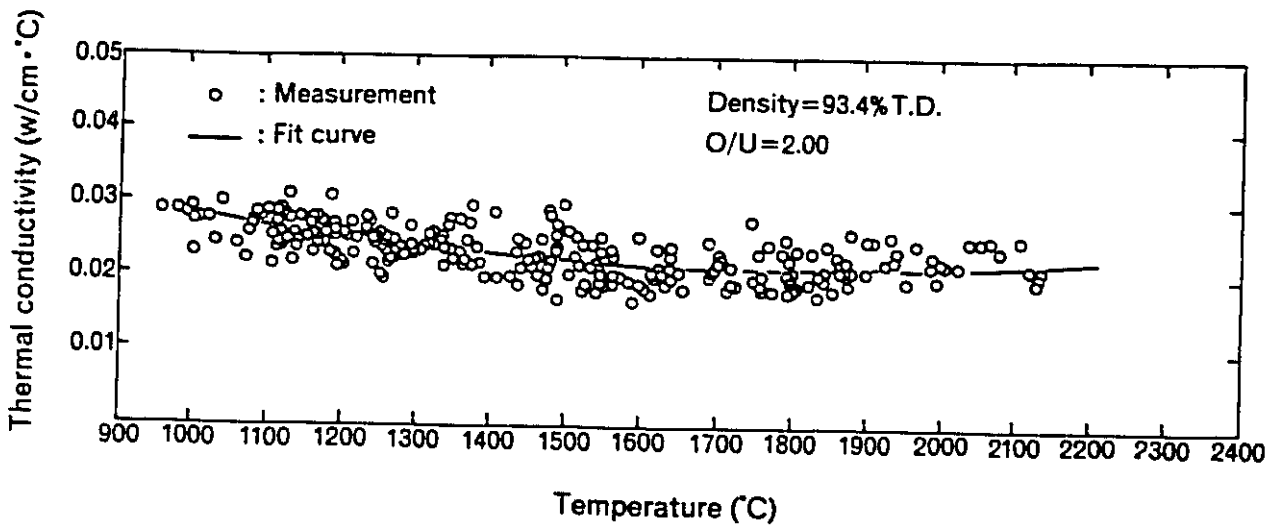

Fig. 4. Thermal conductivity of UO_2 as a function of temperature.

3. Results and discussion

The temperature dependence of thermal conductivity on the pellets is shown in Figs. 5, 6 and 7. The conductivity gradually decreases with increasing the temperature up to 1,800°C and then increases in the temperature range higher than 1,800°C for all kinds of specimens tested. This trend is in good agreement with that of UO_2 which is shown in Fig. 4. The difference of the conductivity between UO_2 and $(U_{0.7}, Pu_{0.3})O_2$ exists over the limit of experimental erros. This result shows that the conductivity change due to plutonium content in mixed oxide is negligible at the temperatures over 1,000°C. Baily et al.[1] also suggested that no significant change of the conductivity occurred in mixed oxide with different plutonium contents.

In Fig. 8 the thermal conductivities are plotted as a function of O/M ratios between 1.94 and 2.00 for $(U_{0.7}, Pu_{0.3})O_{2-x}$ with a density of 95%T.D. Negligibly small changes were found in the O/M ratios before and after the thermal conductivity measurements as shown in Fig. 9. Figure 8 shows that the higher conductivities are obtained in the pellets with higher O/M ratio for all temperature range examined. For instance the conductivity of $(U_{0.7}, Pu_{0.3})O_{2.00}$ is about 20% higher than that of $(U_{0.7},Pu_{0.3})O_{1.94}$ at a temperature of 1,000°C. Figure 8 also indicates that the effect of O/M ratio on the conductivity becomes notable with decreasing temperature.

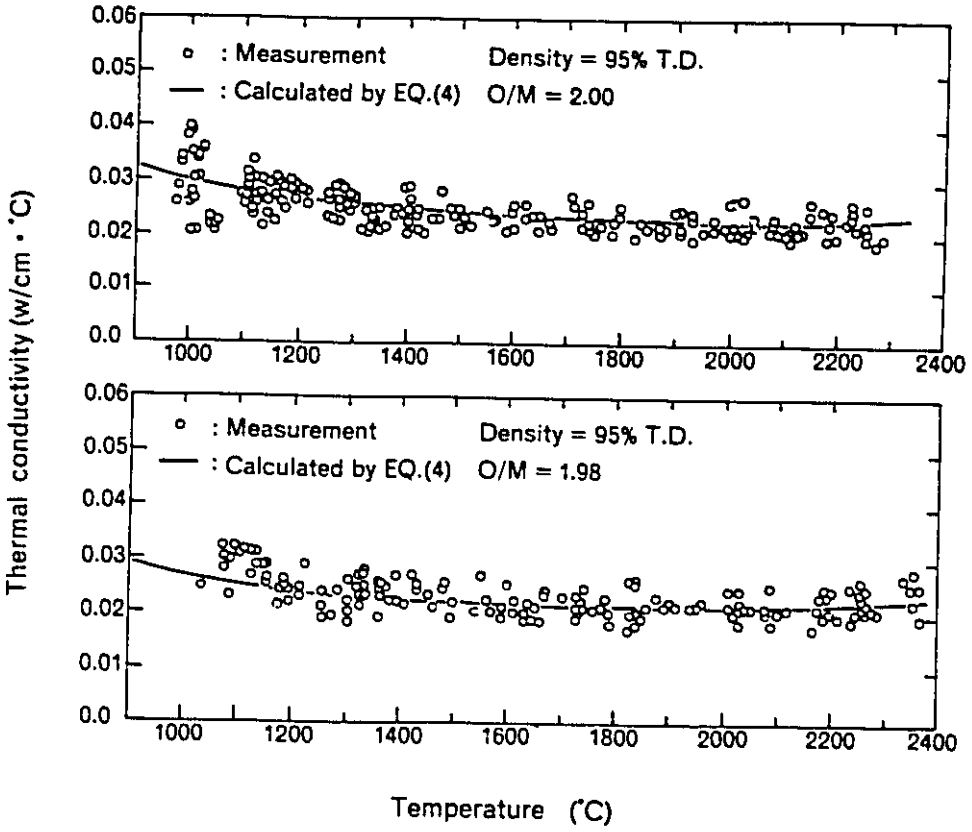

Fig. 5. Thermal conductivity of $(U_{0.7}, Pu_{0.3})O_{2-x}$ as a function of temperature.

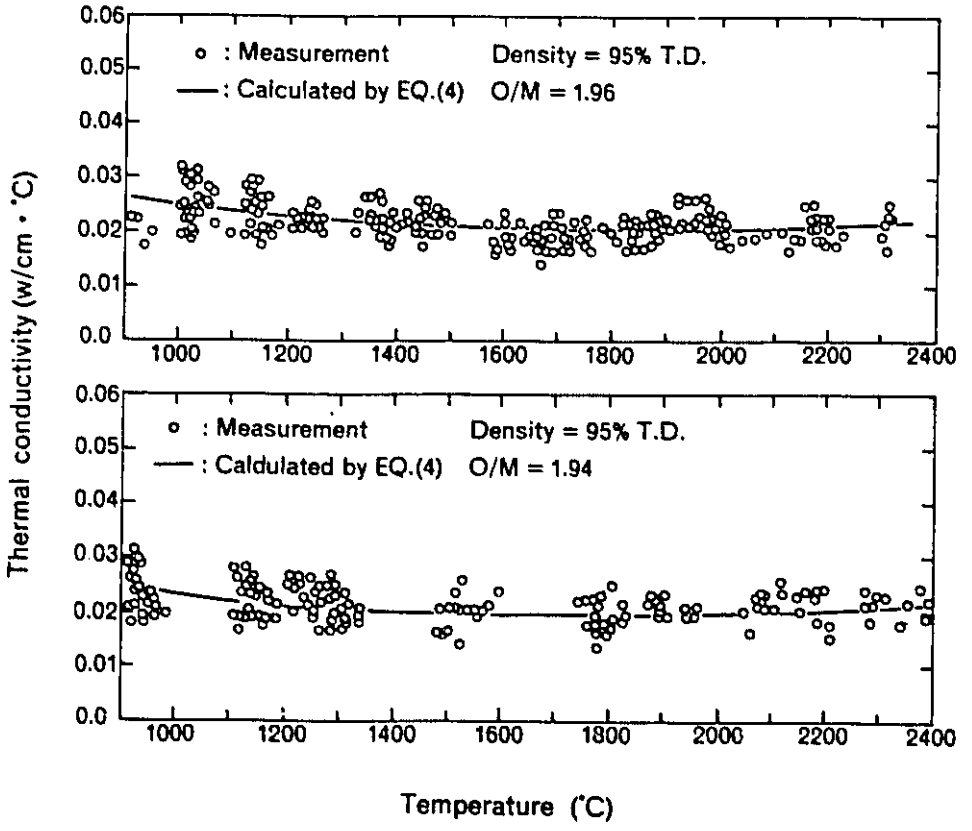

Fig. 6. Thermal conductivity of $(U_{0.7}, Pu_{0.3})O_{2-x}$ as a function of temperature.

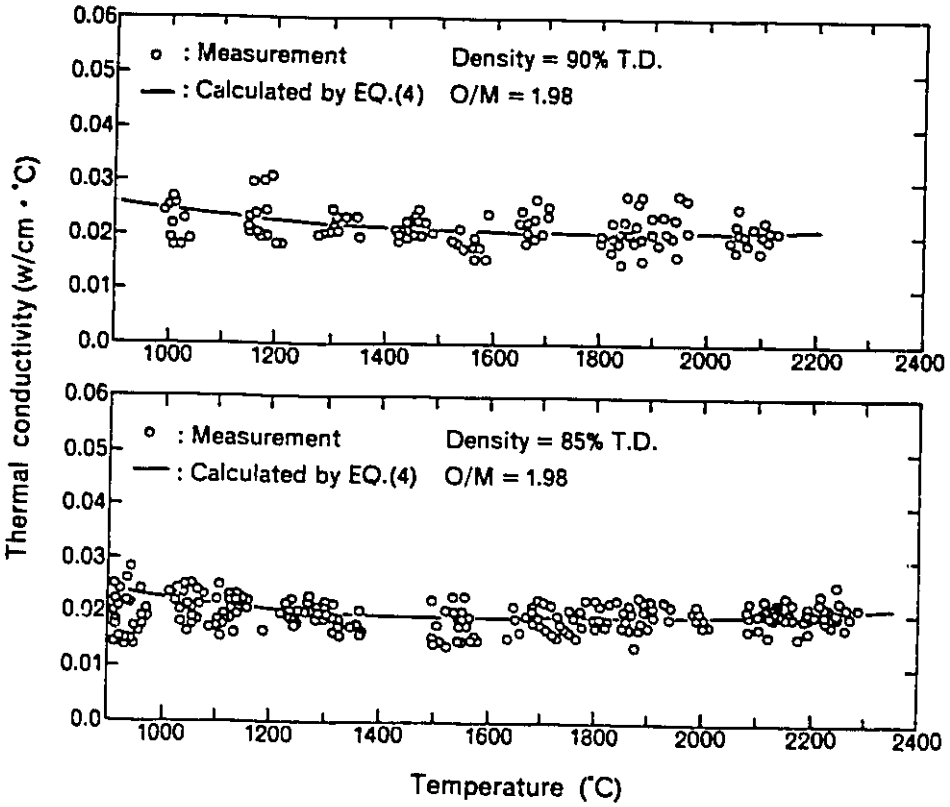

Fig. 7. Thermal conductivity of $(U_{0.7}, Pu_{0.3})O_{2-x}$ as a function of temperature.

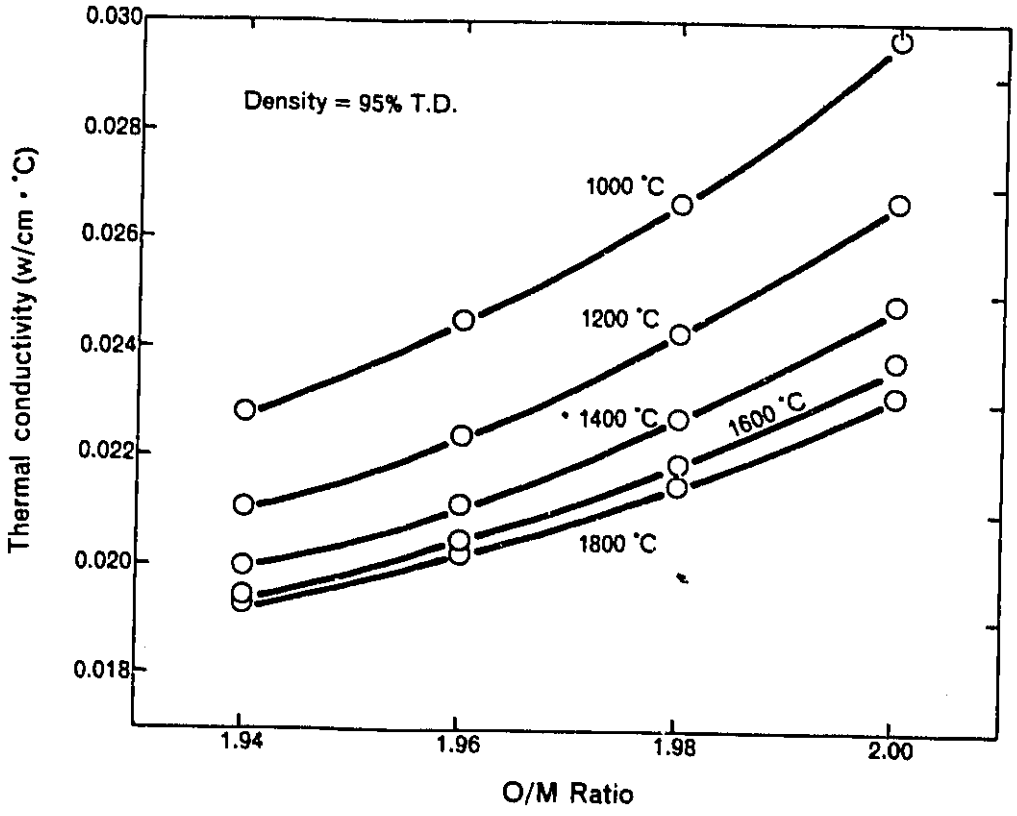

Fig. 8. Thermal conductivity of $(U_{0.7},Pu_{0.3})O_{2-x}$ as a function of O/M ratio.

The density dependence of conductivity is shown in Fig. 10 for $(U_{0.7},Pu_{0.3})O_{1.98}$. The conductivity increases with density of pellets, and this trend is observed in the temperature range of 1,000 to 1,800°C. Large differences between the conductivities of low (85%T.D.) and high (95%T.D.) density pellets are observed in the lower temperature region. Both results of density and O/M dependences of conductivity show that porosity and phonon scattering at oxygen vacancies take an important role on the thermal conductivity especially at a low temperature of 1,000°C.

An empirical equation representing the thermal conductivity of $(U_{0.7}, Pu_{0.3})O_{2-x}$ is given by means of a least square fit of the results obtained above. The equation is expressed by

$$K_f=9.855\times10^{-3}+\frac{1}{(0.04094+0.455\times(2.0-O/M)+0.1998\times(1.0-\rho)).T}+4.6518\times10^{-13}.T^3 \quad ...(4)$$

where K_f is the thermal conductivity of $(U_{0.7},Pu_{0.3})O_{2-x}$ (w/cm.°C), O/M the oxygen to metal ratio, ρ the fractional density and T temperature (°C). The curves represented in Figs. 5, 6 and 7 were obtained from Eq. (4) and the equation has an error of 15% with 90% confidence level.

The thermal conductivity evaluated from Eq.(4) is compared with those of Gibby[2] and Laskiewicz et al.[3] in Fig. 11. The conductivity obtained in the present study is slightly higher than those shown in the above study in the temperature range from 900°C to 1,600°C. At the higher temperature range of 1,600°C to 2,400°C, little difference of the conductivity values are seen between the two studies.

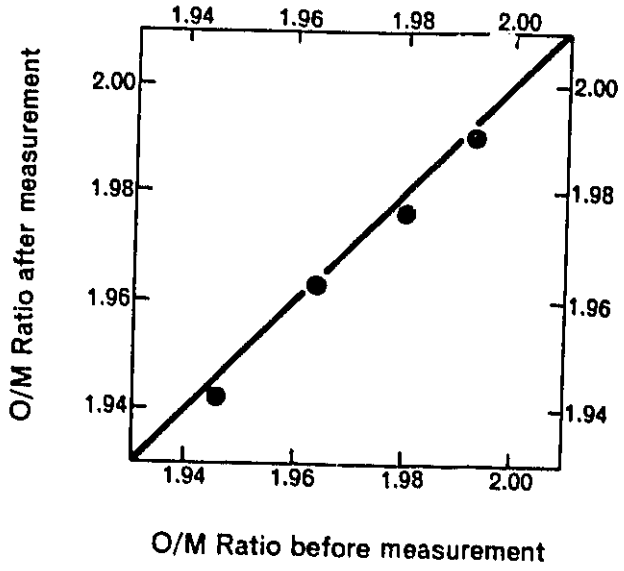

Fig. 9. Comparison of O/M ratio between before and after the test.

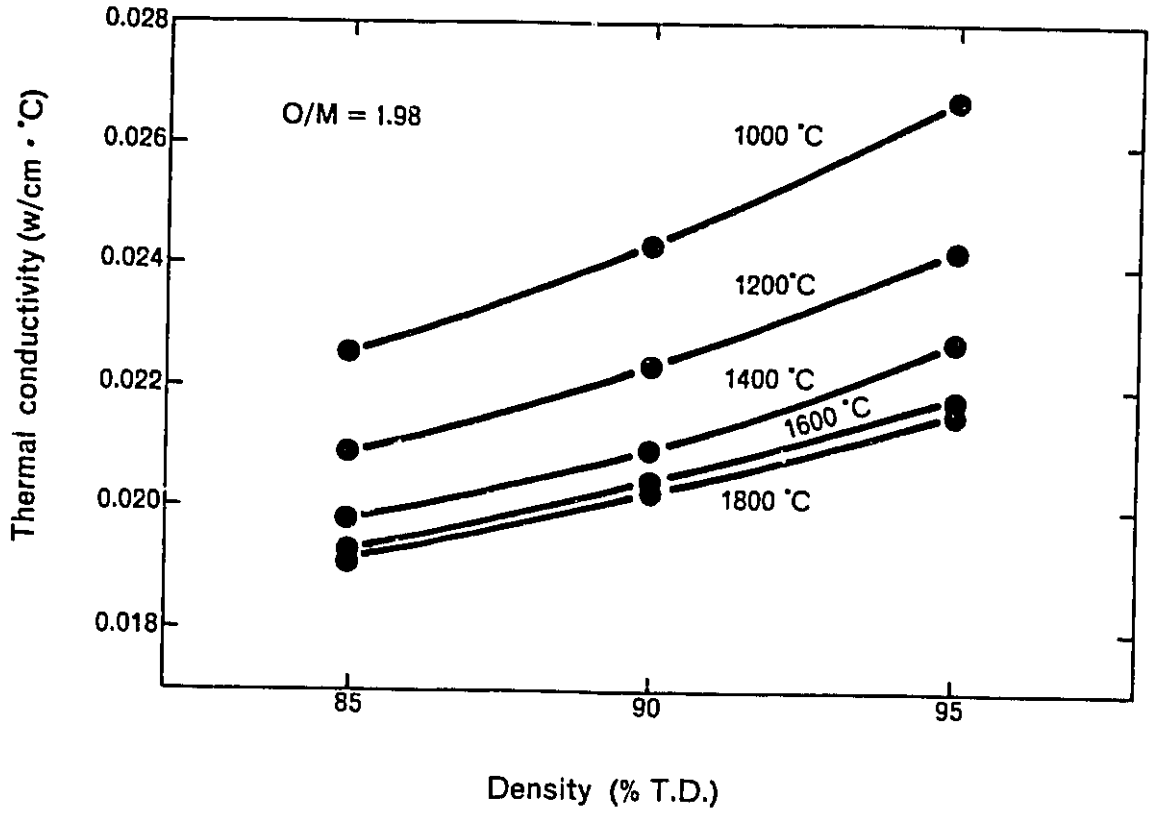

Fig. 10. Thermal conductivity of $(U_{0.7}, Pu_{0.3})O_{2-x}$ as a function of density.

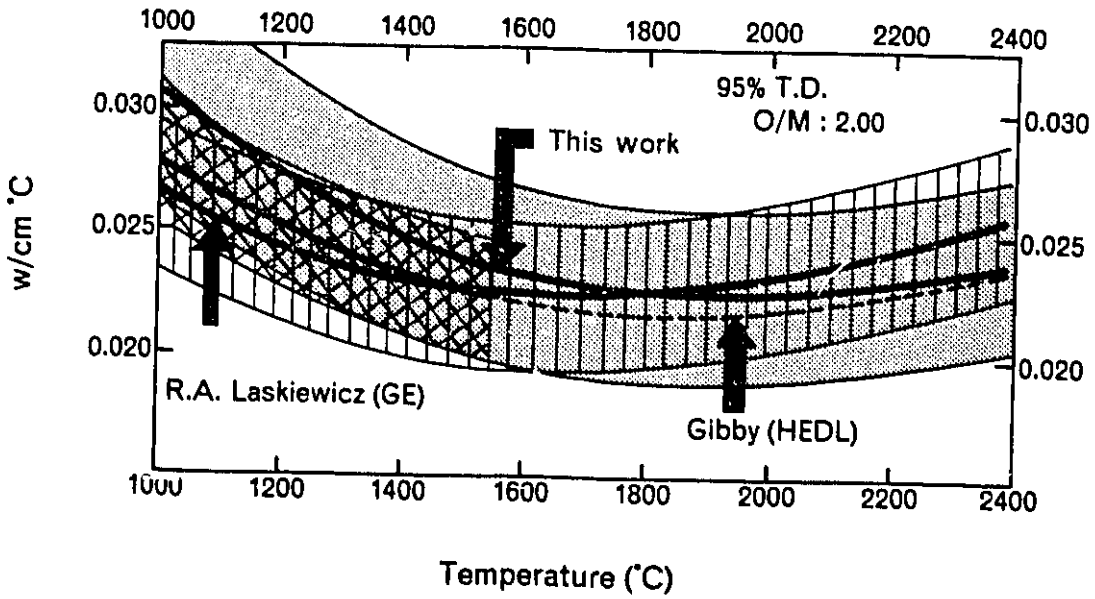

Fig. 11. Comparison of the present result with previous ones.

Reference

(1) Baily, W. E. , Aitken, E. A. : AIME (1967), Thermal Conductivity of Uranium-Plutonium.

(2) Gibby, R. L. : J. Nucl. Mat. , 38 (1971), The Effect of Plutonium Content on the Thermal Conductivity of $(U,Pu)O_2$ Solid Solutions.

(3) Laskiewicz, R. A. et al. : GEAP-13733 (1971), Thermal Conductivity of Uranium-Plutonium Oxide.

(4) Asamoto, R. R. et al. : GEAP-5493 (1968), The Effect of Density on the Thermal Conductivity of Uranium Dioxide.

(5) Lyons, M. F. et al. : GEAP-5100-1 (1966), UO_2 Power and Pellet Thermal Conductivity During Irradiation.

(6) Yamaguchi, T. et al. : PNCT831-79-02 (1979), Thermal Conductivity of $UO_{2.00}$ and $(U_{0.7}, Pu_{0.3})O_{1.98}$.

Measurement of Stress-Strain Curves for (U, Pu) O_2 *

Toshimichi TACHIBANA, Daisuke NARITA,
Hiromitsu KANEKO and Yutaka HONDA

1. Introduction

The plastic deformation in $(U,Pu)O_2$ which results from thermal stress is a phenomenon having an important influence on fuel performance in fast breeder reactors[1]. It is, therefore, necessary to obtain the stress-strain relation curve of mixed oxide fuel in the wide range of stress and temperature, in order to predict the response of fuel column to variation of reactor power. The stress-strain curves of UO_2 have been studied extensively[2)~9)], but basic measurements have never been made on the stress-strain curve of $(U,Pu)O_2$ at high strain rate. The purpose of this paper is to describe results obtained to date by compressing test of $(U,Pu)O_2$ at a constant strain rate of $0.1 \sim 10.0 min^{-1}$ in the temperature range of $1000 \sim 1800^{\circ}C$.

2. Test specimens and testing procedure

Pellets of $(U_{0.7},Pu_{0.3})O_2$ were prepared by press-forming of fine 30 w/oPuO_2-UO_2 powder and by the subsequent sintering in a reducing atmosphere (N_2-5%H_2) at $1650^{\circ}C$ for 2hrs. The dimensions of the as-sintered pellet were 5.4 mm in diameter and 9.5mm in height. The O/M ratio and density of the specimen pellets were 1.98 and 88 ±1%T.D., respectively.

Compression tests were performed of the specimens placed in a vacuum of about 10^{-5} torr at temperatures between 1000 and $1800^{\circ}C$, using an Instron type compressing machine[7)] with cross-head speeds suitable for strain rates in the range of $0.1 \pm 10.0\ min^{-1}$. The heating furance is composed of Ta band heaters and Ta band reflectors. The temperature of the furnace was raised at a constant rate of about $50^{\circ}C$/min to the desired value, and then maintained for 30 min before starting the compression test. The temperature of the specimen was measured with a micro-

*Presented at the Annual Meeting of the Atomic Energy Society of Japan (March, 1979).

pyrometer calibrated at the melting point of Ag, Au, Cu, Fe, Pt and Al_2O_3.

The standard compression tests were performed at a speed of 1 mm/min. corresponding to a strain rate of 0.1 min^{-1}. Some additional runs were also conducted at 10 and 100 mm/min for determining the effect of strain rate on the plastic deformation in $(U, Pu)O_2$.

3. Results and Discussion

The stress-strain curves were obtained with an X-Y recorder. Figure 1 shows the curves of $(U_{0.7}, Pu_{0.3})O_2$ obtained at a strain rate of 0.1 min^{-1} in the temperature range of 1000 to 1800°C. The curves displays a continious variation above proportional limit. The temperature dependence of the curves obtained is similar to that found in compression test of UO_2[6)~9)].

The effects of temperature and strain rate on proportional limit can be obtained from the stress-strain curves. They are shown in Fig. 2 and 3, respectively. Figure 2 and 3 show that the proportional limit decreases with temperature and increases with strain rate. The behaviour is in good agreement with that previously reported for UO_2[6) ~ 8)].

In order to study the deformation mechanism of $(U, Pu)O_2$, the value of strain rate sensitivity (n) was estimated from the following equation. Thermally activated deformation of ceramic materials has been frequently interpreted in terms of a well-known equation[7),8)]

$$\dot{\varepsilon} = A/T \cdot \sigma^n \exp(-\Delta H/R \cdot T) \quad \text{----------(1)}$$

where $\dot{\varepsilon}$ is the strain rate, σ the stress, n the strain rate sensitivity (stress exponent), ΔH the activation energy and A a constant. The value of n can be obtained from the equation[8)].

$$n = \left(\partial \ln \dot{\varepsilon} / \partial \ln \sigma \right)_T \quad \text{----------(2)}$$

Previous workers[6)~9)] reported that plastic deformation of UO_2 at low strain rate is caused by dislocation climb (n=3 to 5) and Nabarro-Herring diffusional creep or grain boundary sliding mechanism (n=1). In the present study, the value of n for $(U,Pu)O_2$ was calculated by substituting $\dot{\varepsilon}$ and σ p (proportional limit) into Eq.(2). Those

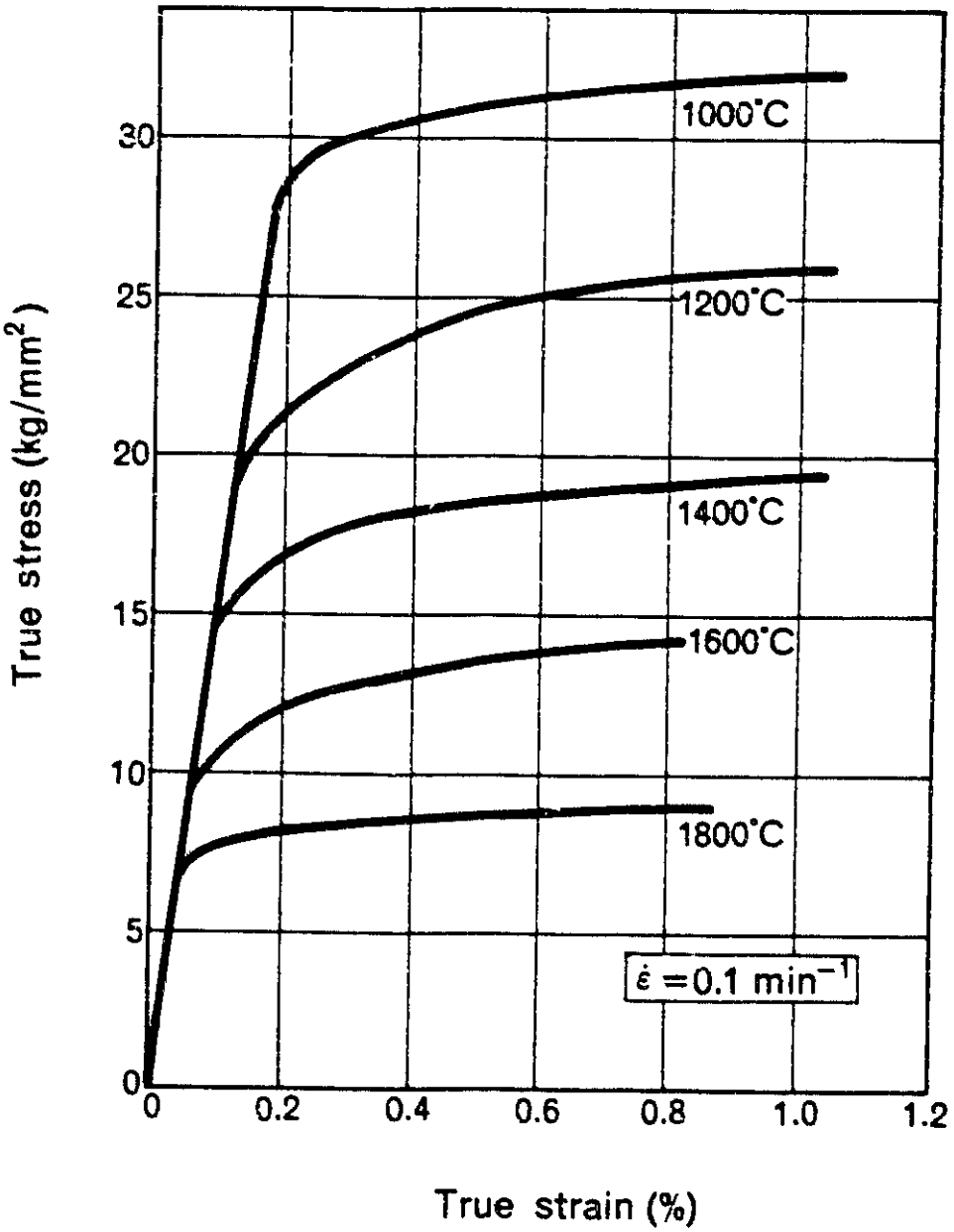

Fig. 1. Stress-strain curve of $(U_{0.7}, Pu_{0.3})O_{2-x}$.

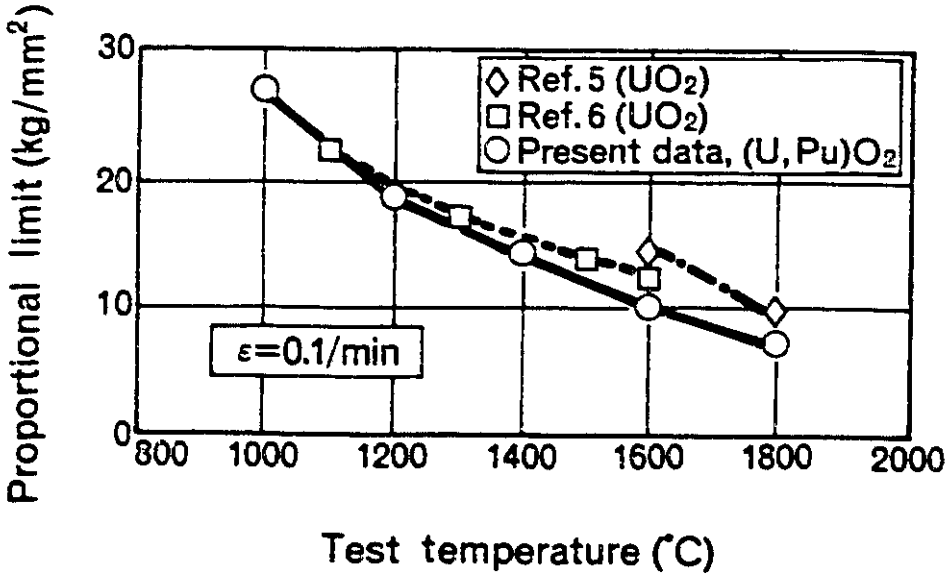

Fig. 2. Temperature dependence of the proportional limits for UO_2 and $(U_{0.7}, Pu_{0.3})O_{2-x}$.

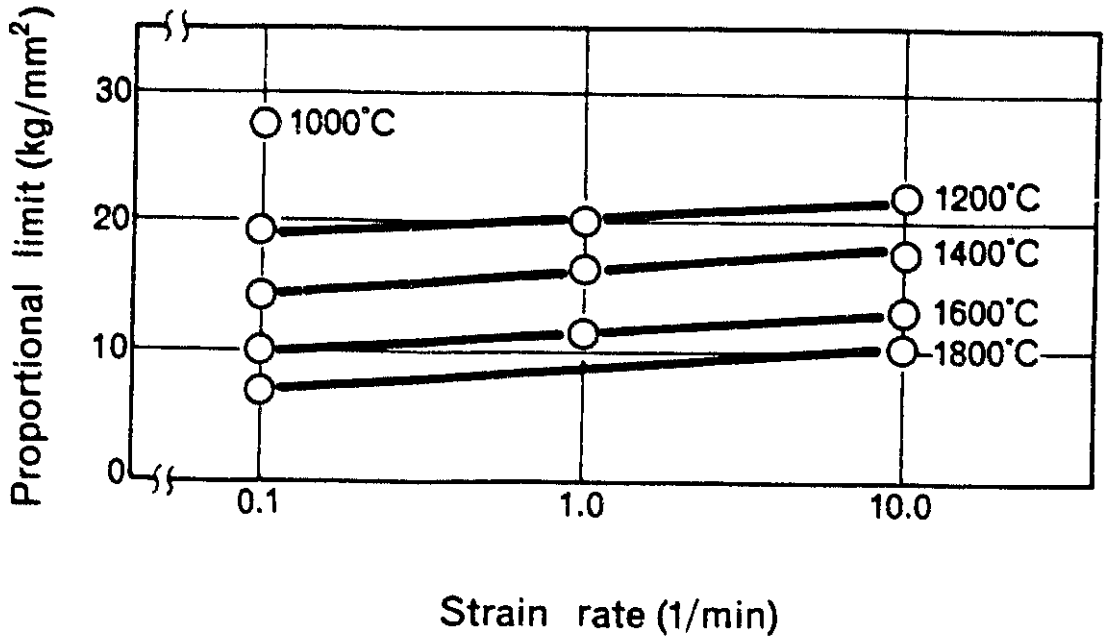

Fig. 3. Stran rate dependence of proportional limit for $(U_{0.7}, Pu_{0.3})O_{2-x}$ Pellet.

values were estimated to be 50 at 1200°C, 19 at 1400°C, 14 at 1600°C and 10 at 1800°C, and 1 to 5 times as large as those of UO_2 at the same temperatures. Though calculated n-values are too large to be compatible with deformation models mentioned above, those are in good agreement with previous data (10 to 32) obtained at high strain rate for UO_2[6) ~ 8)]. The results can not identify the deformation mechanism at high strain rate for (U, Pu)O_2, but the high n-values obtained in the present study suggest that the deformation mechanism of (U, Pu)O_2 at high strain rate is analogous to that of UO_2.

4. Conclusion

Pellets of $(U_{0.7},Pu_{0.3})O_2$ were compressed in the high-strain rate of 0.1, 1.0, and 10.0 min^{-1} at temperatures ranging from 1000 to 1800°C. The test results are summarized as follows.

(1) The stress-strain curves of mixed oxide were successfully obtained at constant strain rates.

(2) The strain rate sensitivity (n) of the mixed oxide ranges from 10 to 50.

(3) Those strain rate sensitivities suggest that the deformation mechanism of (U,Pu)O_2 at high strain rates and high temperatures is analogous to that of UO_2.

References

(1) Janks, V. Z. , Week, R. W. : Nucl. Eng. Design, 18, 91 (1972).

(2) Byron, J. F. : J. Nucl. Mater. , 27, 48 (1968).

(3) Nadeau, J. S. : J. Amer. Ceram. Soc. , 52, 1 (1969).

(4) Evans, A. G. , Davidge, R.W. : J. Nucl. Mater. , 33, 249 (1969).

(5) Canon, R. F. , Roberts, J. T. A. , Beals, R. J. : J. Amer. Ceram. Soc. , 54, 105 (1971).

(6) Guerin, Y. : J. Nucl. Mater, 56, 61 (1975).

(7) Tachibana, T. , Furuya, H. , Koizumi, M. : J. Nucl. Sci. and Tech. 13, 9 (1976).

(8) Radford, D. C. , Terwilliger, G. R. : J. Amer. Ceram. Soc. , 58, 7 (1975).

(9) Mordike, B. L. : J. Nucl. Mater. , 60 (1976) 223 - 226.

Out-of-Pile Experiments of Fuel-Cladding Chemical Interaction (II)*

Kenji KONASHI, Tadao YATO
Hiromitsu KANEKO and Yutaka HONDA

1. Introduction

Cesium is considered to be one of the most important fission products in fuel-cladding chemical interaction (FCCI) of LMFBR fuel pins. However, the FCCI under irradiation cannot always be explained by considering only the cesium-oxygen system as a corrodant, since no attack occurs in the cesium-oxygen system unless oxygen potential is sufficiently high. Adamson[1] has proposed the cesium-tellurium-oxygen system to account for the heavy cladding attack which was sometimes found in hypostoichiometric mixed oxide fuel pins. Therefore, fundamental data of cladding attack by tellurium are needed. Attack by tellurium has been reported by Lobb[2], Hofmann[3] and Batey[4], but detailed data are not reported for attack by liquid tellurium. The present report describes an experiment on the reaction between liquid tellurium and stainless steel.

2. Experimental Procedure

Type 316 stainless steel claddings for Monju type fuel pin were used as experimental specimens. Tellurium was encapsulated into a cladding tube with stainless steel end plugs, as shown in Fig. 1, in an argon filled glove box. Two series of experiments were planned with the capsules. The purpose of the first series is to examine the temperature dependence of attack by tellurium in the range of 450°C to 900°C for 30 min, and that of the second to examine the heating-time dependence in the range of 5 min. to 200 hr at 725°C. The capsules were heated in an infrared lamp

*Presented at the Fall Meeting of the Atomic Energy Society of Japan (October,1979).

furnace for short time experiments within 7 hr, and in a registance furnace for longer time experiments. After heating, the capsules were sectioned and examined metallographically with an optical microscope, an SEM and an electron-probe micro-analyzer.

3. Results and Discussion

The results of the first experiments are illustrated in Fig. 2 using Arrhenius type plots of matrix attack depth for the reciprocal of temperature. Figure 3 shows a typical result of metallography. It was observed that the character of corrosion was a matrix attack for every temperature. The electron probe microanalysis (EPMA) reveals that the reaction products on stainless steel surface consisted of two different phases, i.e., a chromium rich inner phase, and an iron- and nickel-rich outer phase (see Fig. 4). It is believed that the iron- and nickel-rich phase was liquid during heating, since the dendrites were formed in the latter phase. On the other hand, the former phase obviously remained solid. From the second experiments, the following results were obtained:

(1) Attacked area initially located at the lower part of the tube spreads toward the upper part of the tube with increase of heating period (see Fig.5)

(2) After a 100-hr heating, tellurium was observed to penetrate into the cladding.

The experimental results were summarized as follows:

(1) Primarily, components of stainless steel, mainly iron and nickel, are dissolved in liquid tellurium, so that the wall thickness of stainless steel decreases rapidly.

(2) In the second step of reaction, a phase of solid-reaction product is formed on the stainless steel surface. The solid phase consists of mainly tellurium and chromium. The formation of this phase prevents the increase of the attack depth, and then the area of attacked zone increases gradually.

(3) After a long time heating, the penetration of tellurium becomes significant.

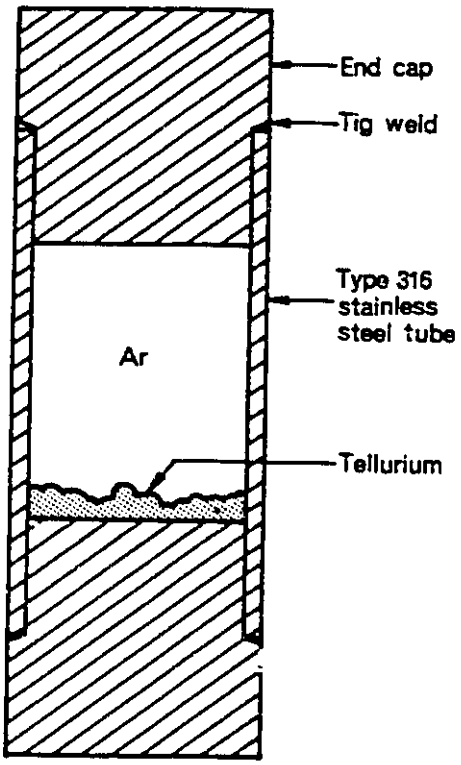

Fig. 1. Capsule.

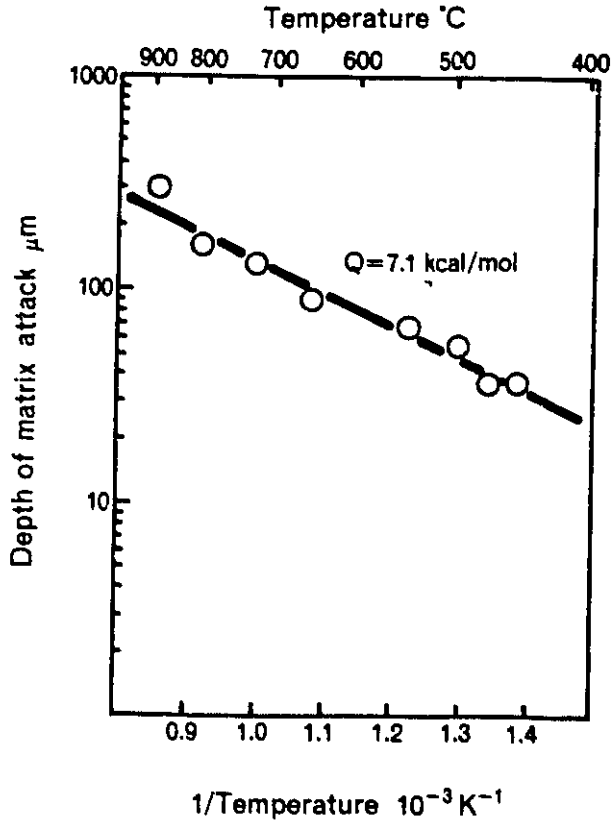

Fig. 2. Arrehenium plots of depth of matrix attack.

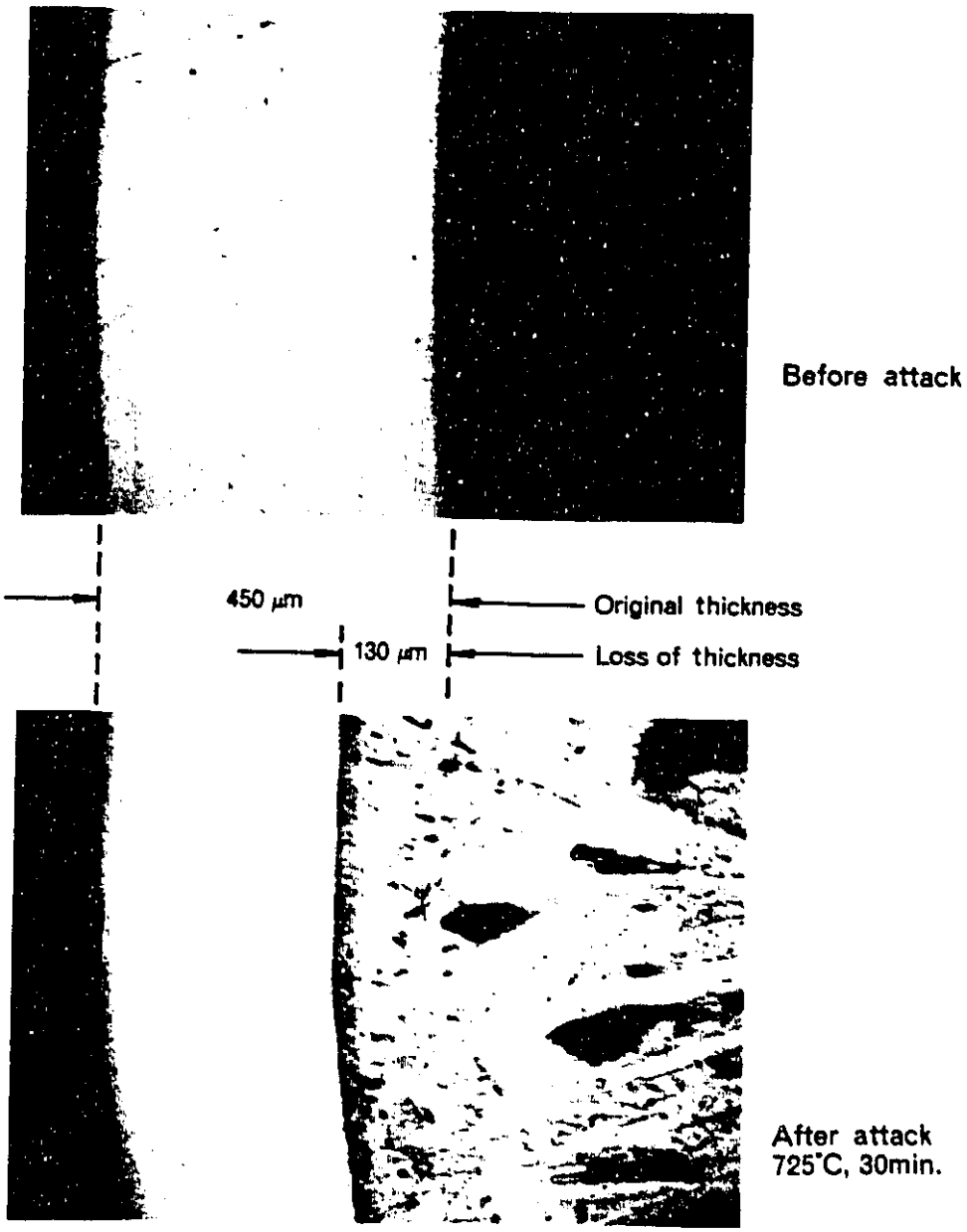

Fig. 3. Matrix attack of stainless steel by Te.

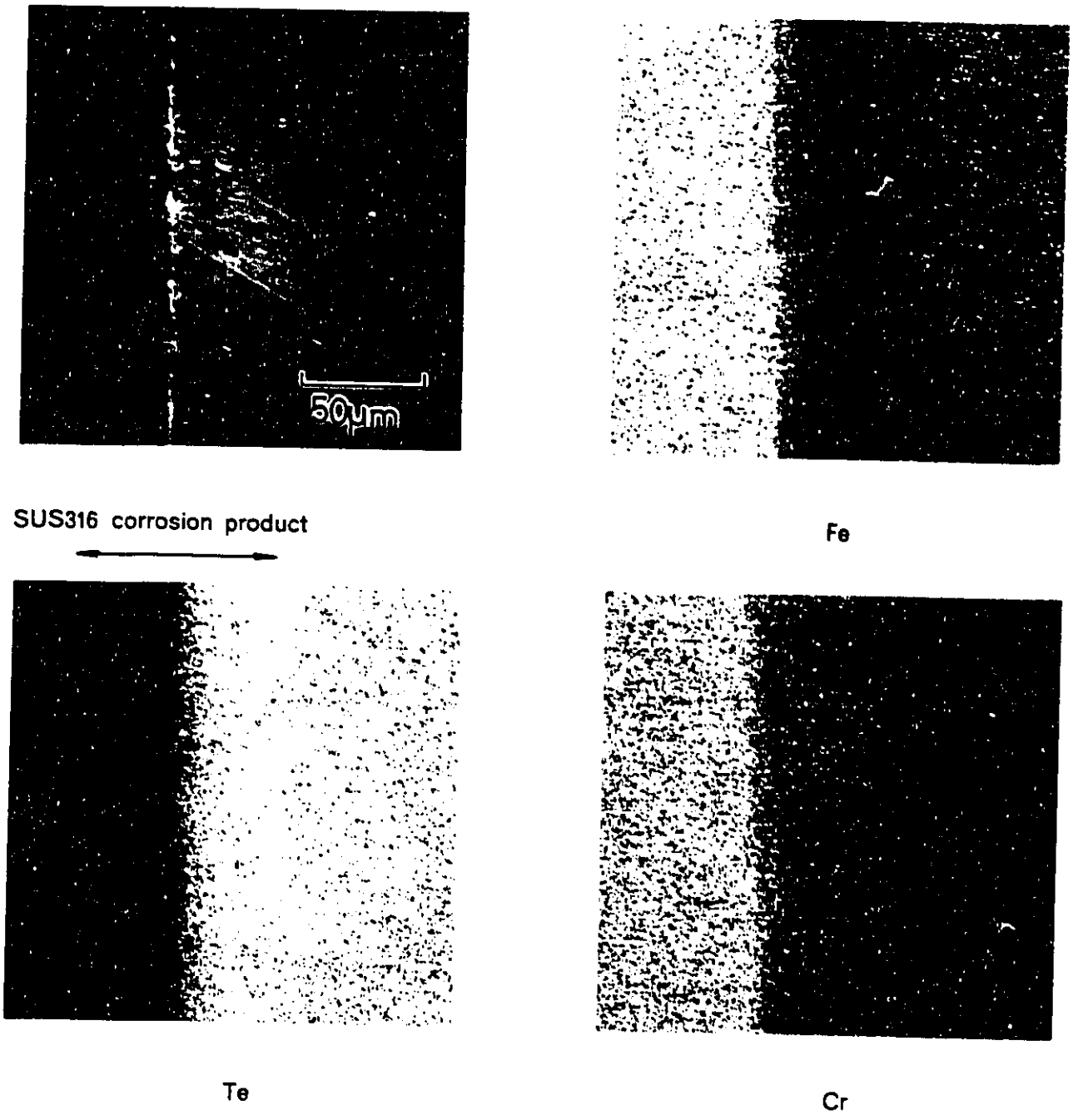

Fig. 4. EPMA of attack layer for 30 min. at 725°C.

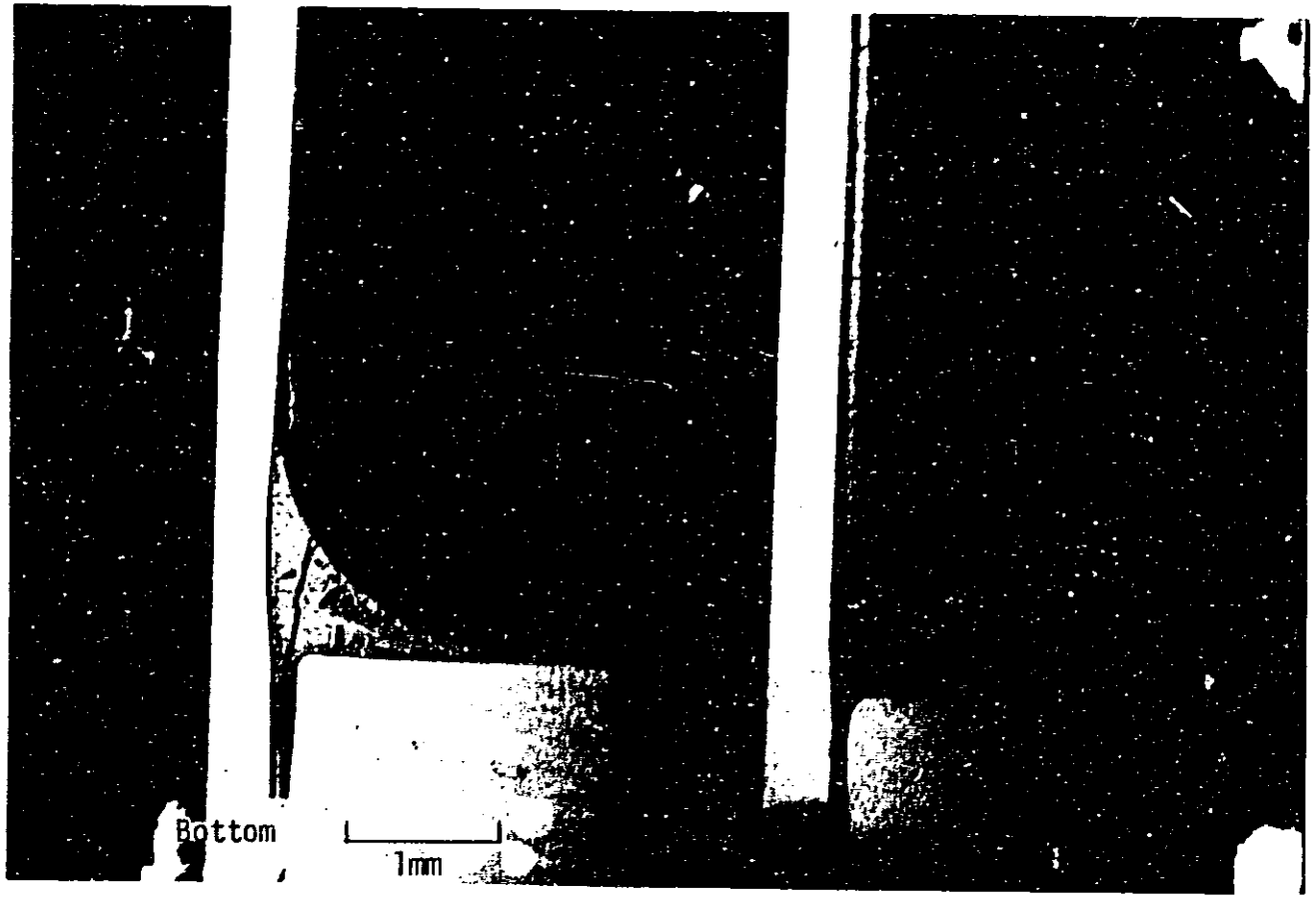

Fig. 5. Corrosion process at 725°C.

References

(1) Adamson, M. G. et al. : IAEA-IWGFR/16, 170. (1977).
(2) Lobb, R. C. et al. : J. Nucl. Mat. 62, 50 (1976).
(3) Hofmann, P. : KFK-1831 (1974).
(4) Batey, W. et al. : J. British Nucl. Eng. Soc. 13, 49. (1974).

Flow Velocity Distributions in the Wire-Wrapped Fuel Subassembly (II)*

Kazuo ITAGAWA, Masao SENZAKI, Mikio KAZITANI,
Takao YAGI and Ryozo YUMOTO

1. Introduction

An accurate prediction of the thermal-hydraulic behavior is essential for the design of LMFBR wire-wrapped fuel subassembly. The most important purpose of a thermal hydraulic model is to describe the flow field in a fuel subassembly. In the interior region of the subassembly, the flow mixing through the gaps between fuel rods results from turbulent flow exchange, sweeping crossflow and pressure-induced crossflow. In the peripheral region, a transverse flow called "a swirl flow" runs parallel with the duct wall.

Previous efforts (1) (2) have been devoted mainly to measure the fine flow velocity, its direction and the crossflow rate between the adjacent internal and peripheral subchannels. A circular flow and a decrease of axial flow velocity were observed in the subchannel containing the spacer wire.

In addition, it was found that the cross flow rate between the adjacent interior and peripheral subchannels were approximately given by a trigonametrical function.

The purpose of this experimental work is to obtain fundamental hydraulic data on the differences of coolant velocity distributions and flow rates between a single wire-wrapped subassembly and a double wire-wrapped subassembly. In the measurement was used a simulated subassembly which is five times as large as the Rapsodie fuel subassembly. The subassembly was composed of a wrapper tube, simulated fuel rods and a fuel rod support system, and mounted in the open-end air loop. The data obtained are used for improving and verifying thermal-hydraulic analysis codes applicable to LMFBR fuel subassembly design.

*Presented at the Fall Meeting of the Atomic Energy Society of Japan
(October, 1979)

2. Experimental Method and Apparatus

Figure 1 shows a schematic drawing of the air-loop equipment for this experiment. The air was blown into the wind tunnel by a 22 KW blower with a capacity of 19.2m^3/min. Then, the air traveled to the inlet of the test section provided with the subassembly.

The inlet of the test section was installed with a pitot tube and a thermometer for measuring the flow rate and the temperature of the air, respectively. The air flow passed through the test section and was discharged into the atmosphere.

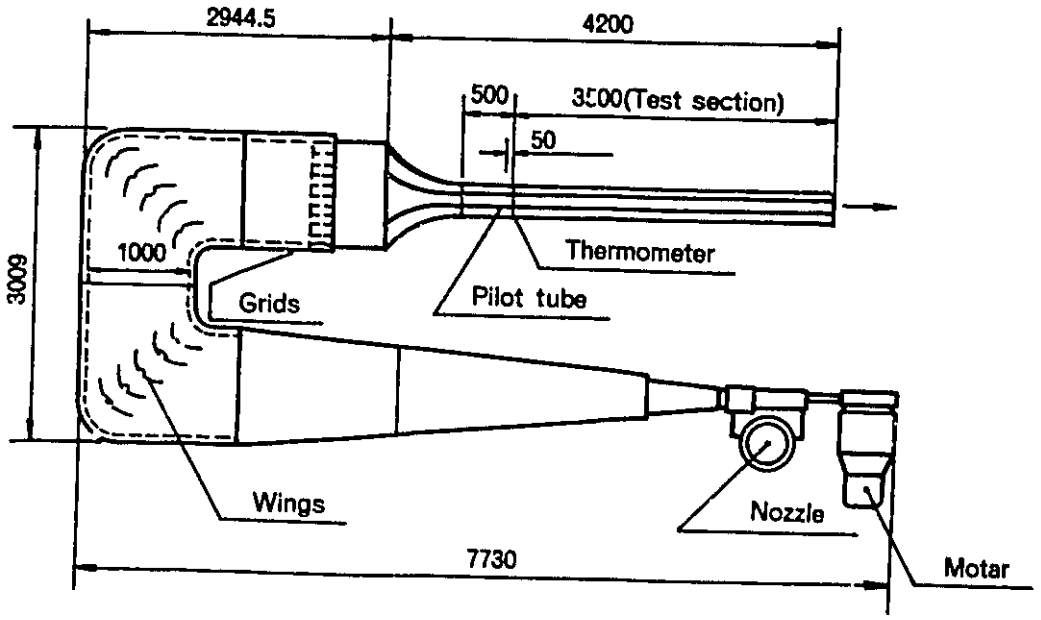

Fig. 1. Scheme of air loop.

Figures 2 and 3 show the dimensions of a simulated subassembly installed at the test section. Two kinds of pin bundles were used in this experiment. One consisted of a bundle of single wire-wrapped pin. and the other a reformed bundle of double wire-wrapped pin whose wrapping phases were shifted by a quarter of the period in the peripheral region. The rod bundle consisted of thirty-seven pins, including a detector pin for measuring the axial flow velocity in the subassembly.

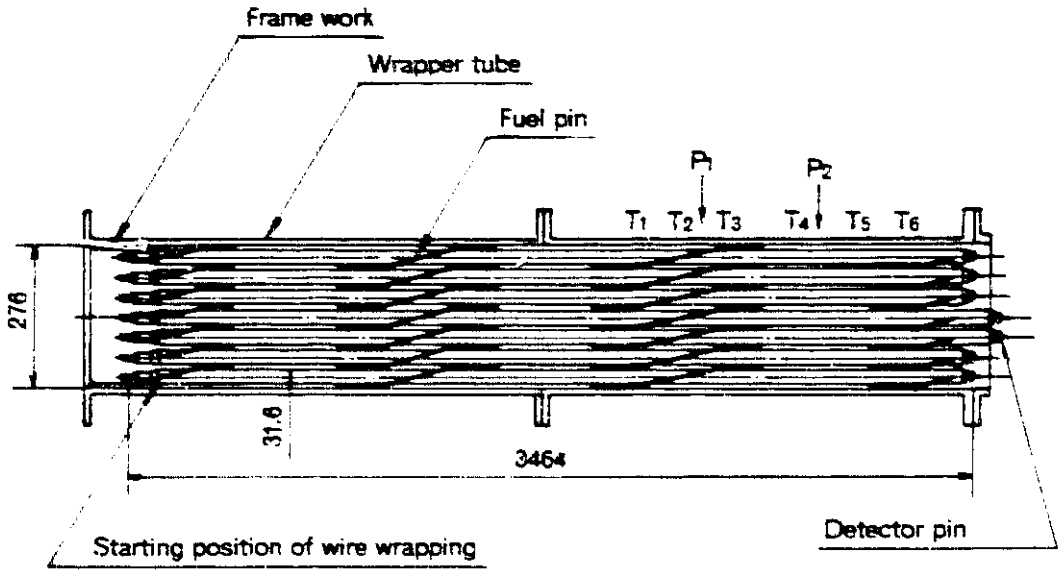

Fig. 2. Test subassembly.

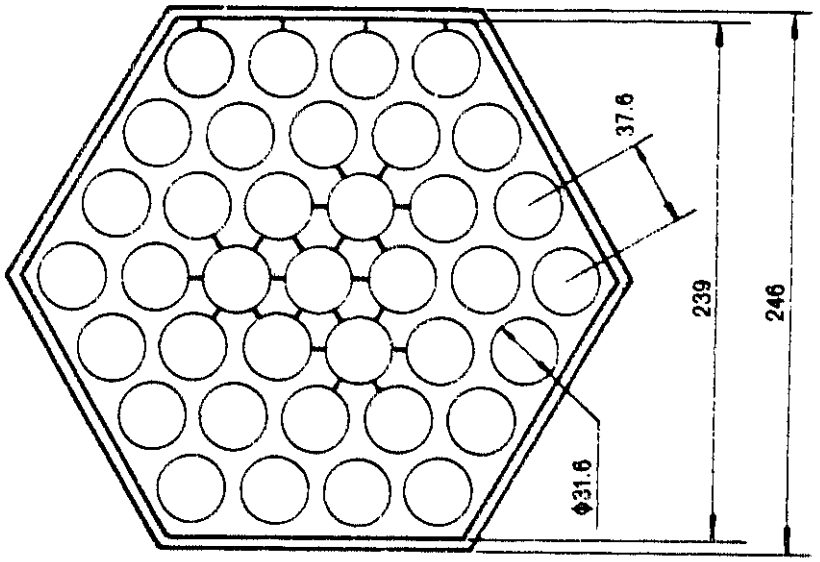

Pin length	Number of pin	Pin pitch(P)	Dia. of pin(d)	P/d	Dia. of wire	Wire lead
3464 mm	37	37.6 mm	31.6 mm	1.19	6.0 mm	1100 mm

Fig. 3. Cross section of test subassembly.

Figure 4 shows the detector pin which has two pitot tubes at the axial positions of 2,245.8(P1) and 2,704.2 (P2) mm from the starting position of wire wrapping. The diameter and the wire-wrapping pitch of the detector pin are the same as those of the normal fuel rod. The pitot tubes are of a arrow type with five holes of 2.1mm diameter, and can be moved vertically and radially by hand through the outlet of the test section.

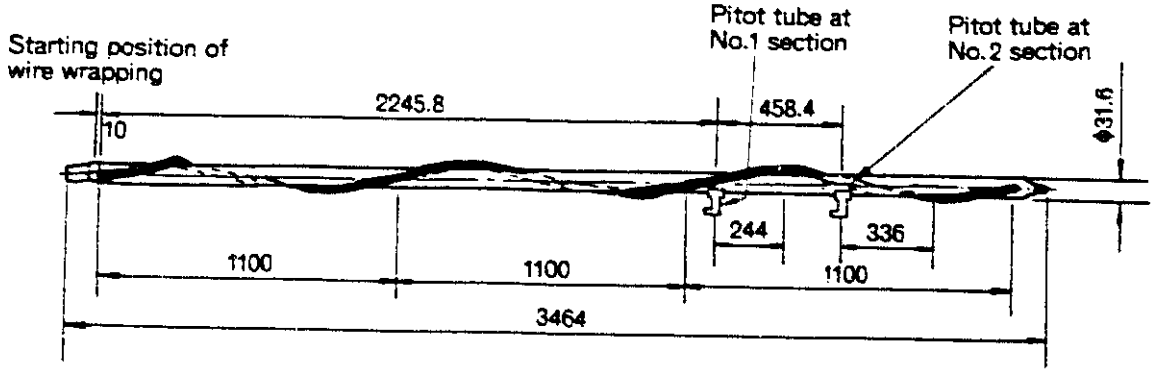

Fig. 4. Detector pin.

The upper tube wall of the downstream position was also equipped with pitot tubes for measuring the peripheral flow at six axial positions of 1,913(T1), 2,133(T2), 2,353(T3), 2573(T4), 2,793(T5) and 3,013(T6)mm from the starting position of wire wrapping.

The measuring points are indicated in Fig. 5. The measurement was made under the following conditions:

air flow rate	0.15~0.33 m^3/h
air temperature	30 to 40°C

The velocity distributions can be determined by measuring the difference of the dynamic pressure between the center hole and other four holes of the pitot tube at the measuring point in the subchannel.

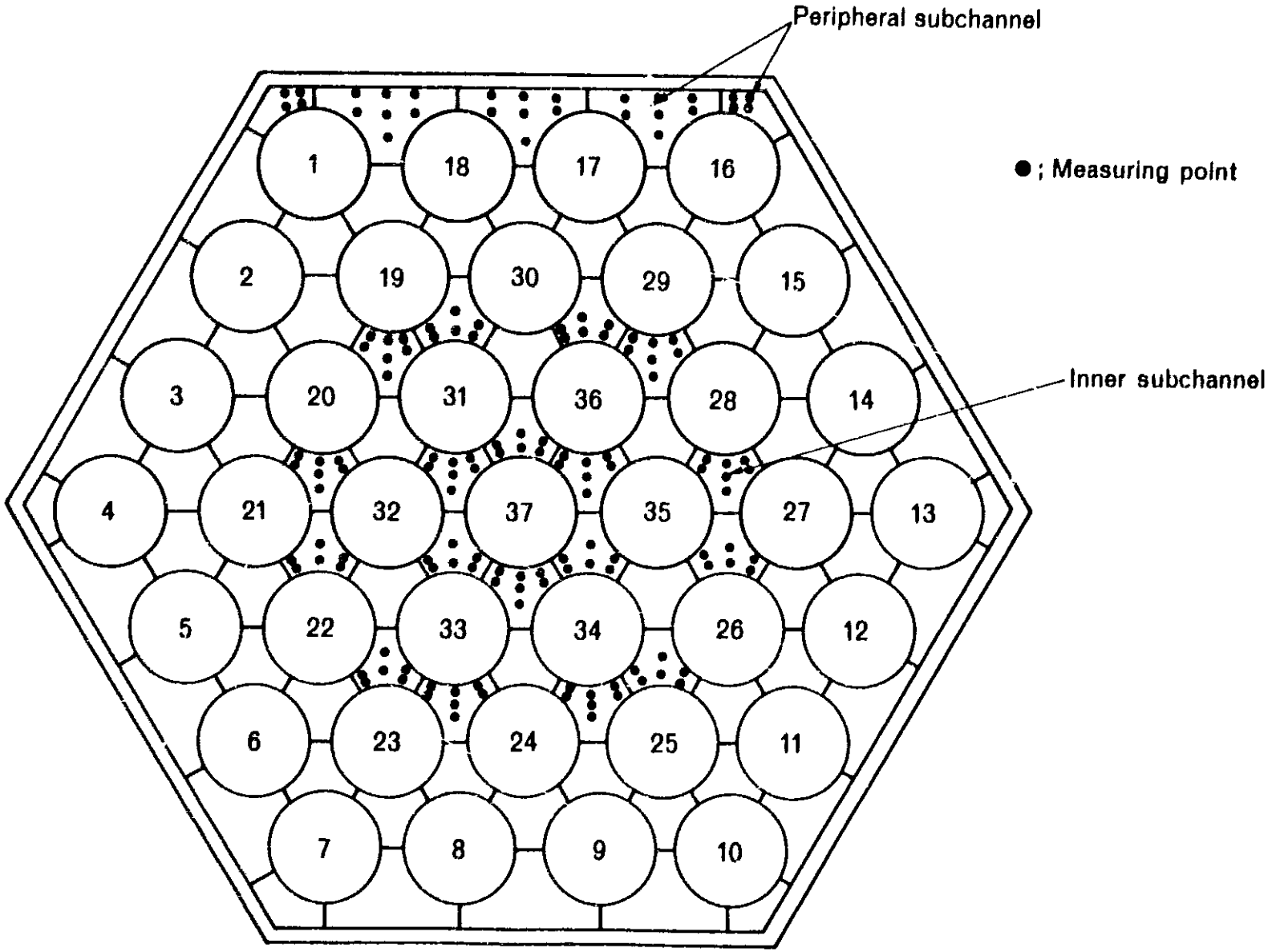

Fig. 5. Measuring points in the subassembly.

3. Experimental Results

The measured relative flow velocities in the single and double wire-wrapped pin bundles are shown in Figs.6,7,8 and 9. In the figures, Vo is the bundle average velocity and Vx is the interior or peripheral subchannel average velocity. Figure 6 shows the flow velocity at the internal and the peripheral subchannels in the single wire-wrapped pin bundle. This figure gives the experimental result that the flow velocity is about 10 percent larger in the peripheral subchannel than in the internal subchannel.

Figure 7 shows the flow velocity distribution in the double wire-wrapped pins in the peripheral pin ring. Figure 7 indicates that the peripheral subchannel velocity is larger than the internal subchannel velocity by about 3 percent. The flow velocity distribution seemed more uniform in the double wire-wrapped bundle than in the single wire-wrapped bundle.

In Figure 8 is given the comparison between the relative flow velocities the Reynolds number of the single and the double wire-wrapped bundles. This figure shows that the double wire-wrapped pins have higher flow velocities by about 5 percent.

Figure 9 gives the flow velocity change in the peripheral subchannels. The figure means that the double wire-wrapped pins have the lower peripheral subchannel flow velocity by about 2 percent.

Compared with the velocities in the single wire-wrapped pins, the effect of double wire-wrapped pins resulted in a velocity decrease in the peripheral subchannel and a velocity increase in the internal subchannel. Consequently, the flow velocity distribution becomes more uniform in the reformed bundle than in the single wire-wrapped pin bundle.

It is also important to evaluate the edge flow effect for a thermal-hydraulic design. The coefficient of edge flow effect is defined by the equation

$$fw = \frac{W^{av}}{W^{av}_{in}}$$

where W^{av} is the average flow rate in the bundle and W^{av}_{in} is the average flow rate in internal subchannels.

Figure 10 is the calculated result of the coefficient fw, showing that the double wire wrapping gives the coefficient about 7 percent of decrease in the peripheral region and makes the flow volume uniform in the bundle. The decrease of the

coefficient is considered as corresponding to that of flow area of subchannels.

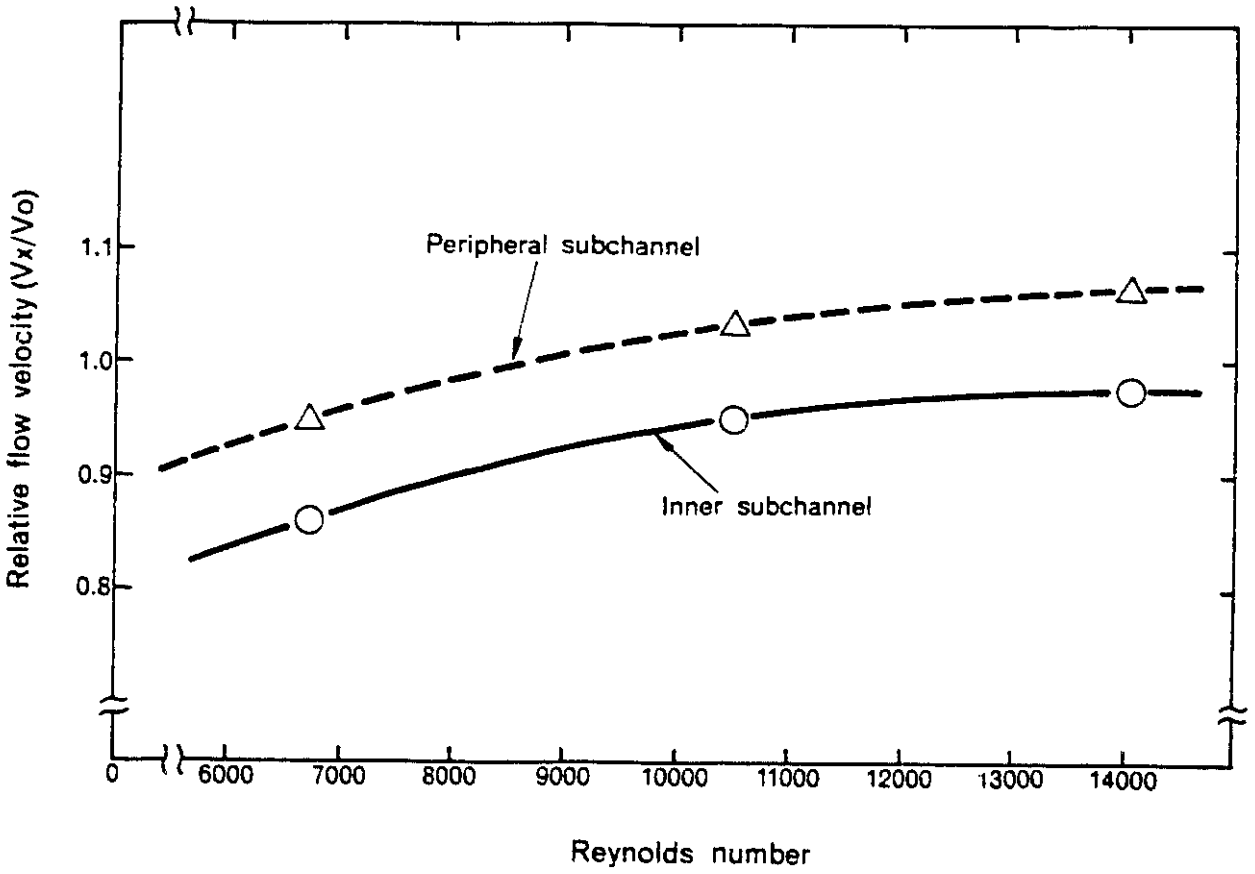

Fig. 6. Relative flow velocity distirubtion in single wire-wrapped pin bundle.

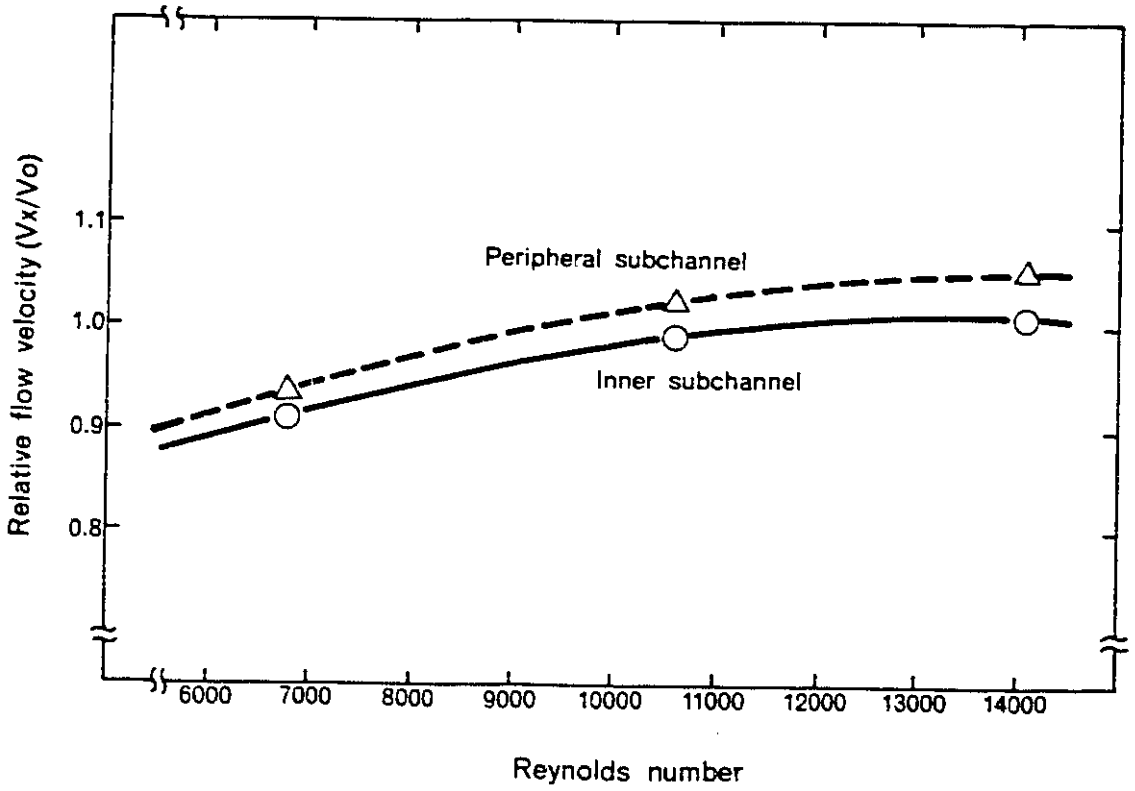

Fig. 7. Relative flow velocity distribution in peripheral double wire-wrapped pin bundle.

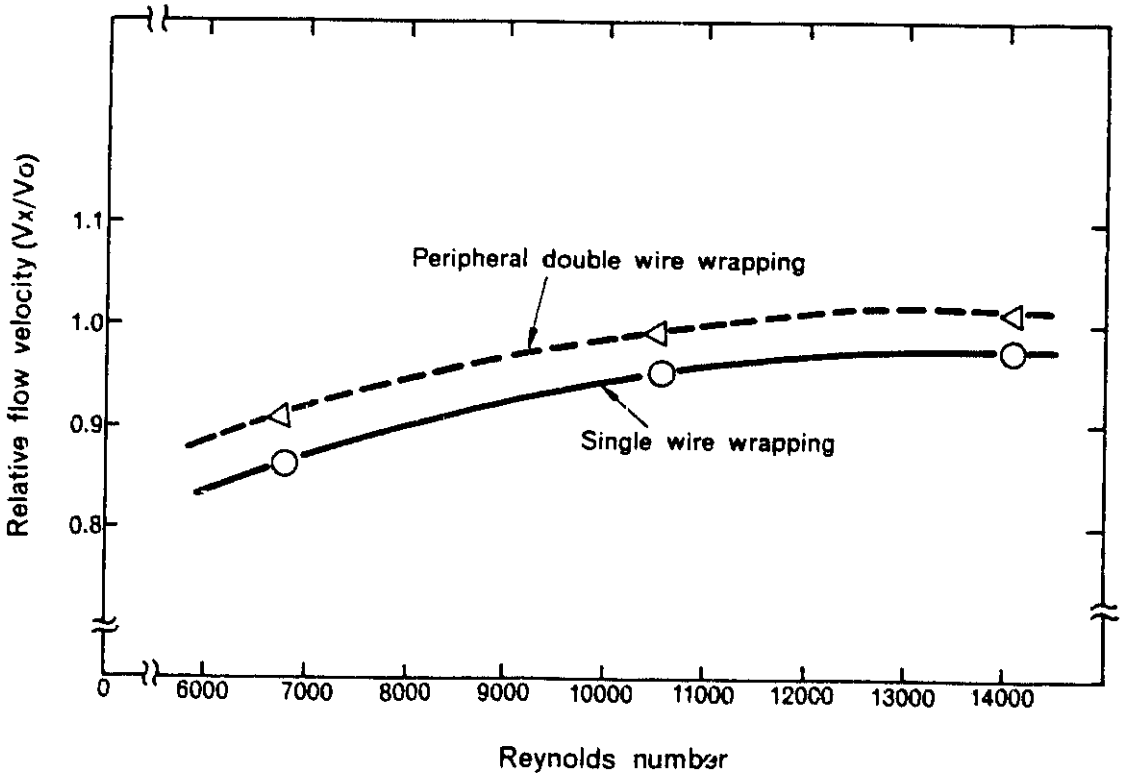

Fig. 8. Relationship between relative flow velocity and Reynolds number in inner subchannels.

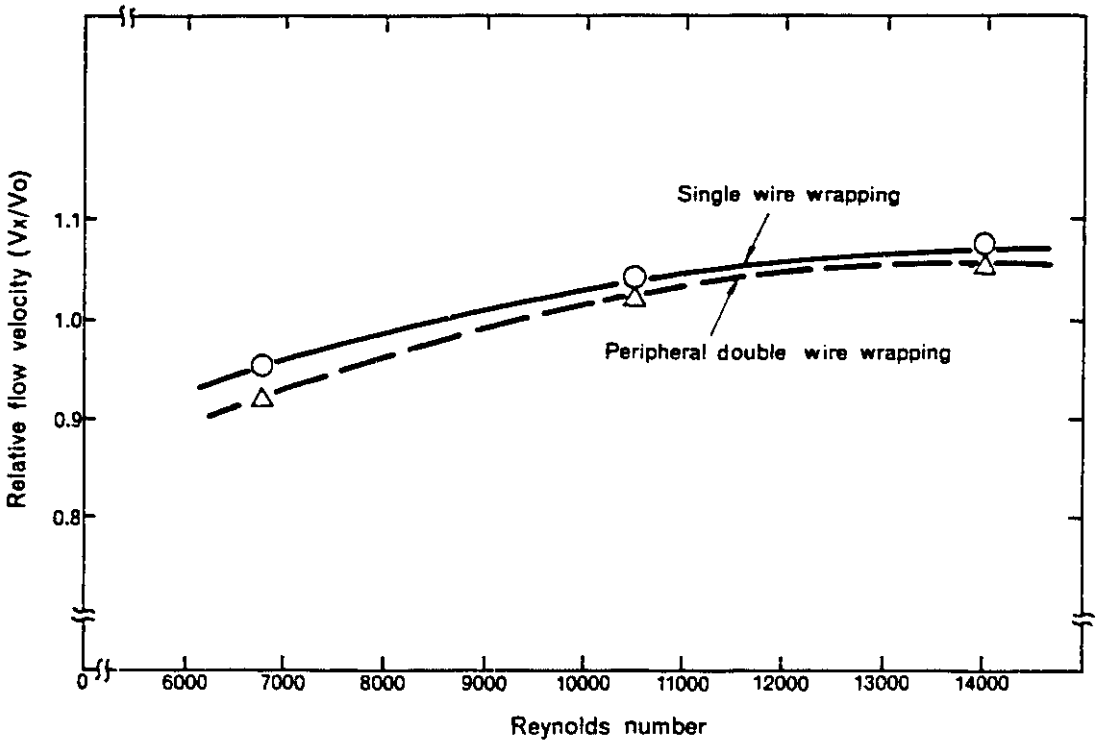

Fig. 9. Relationship between relative flow velocity and Reynolds number in peripheral subchannels.

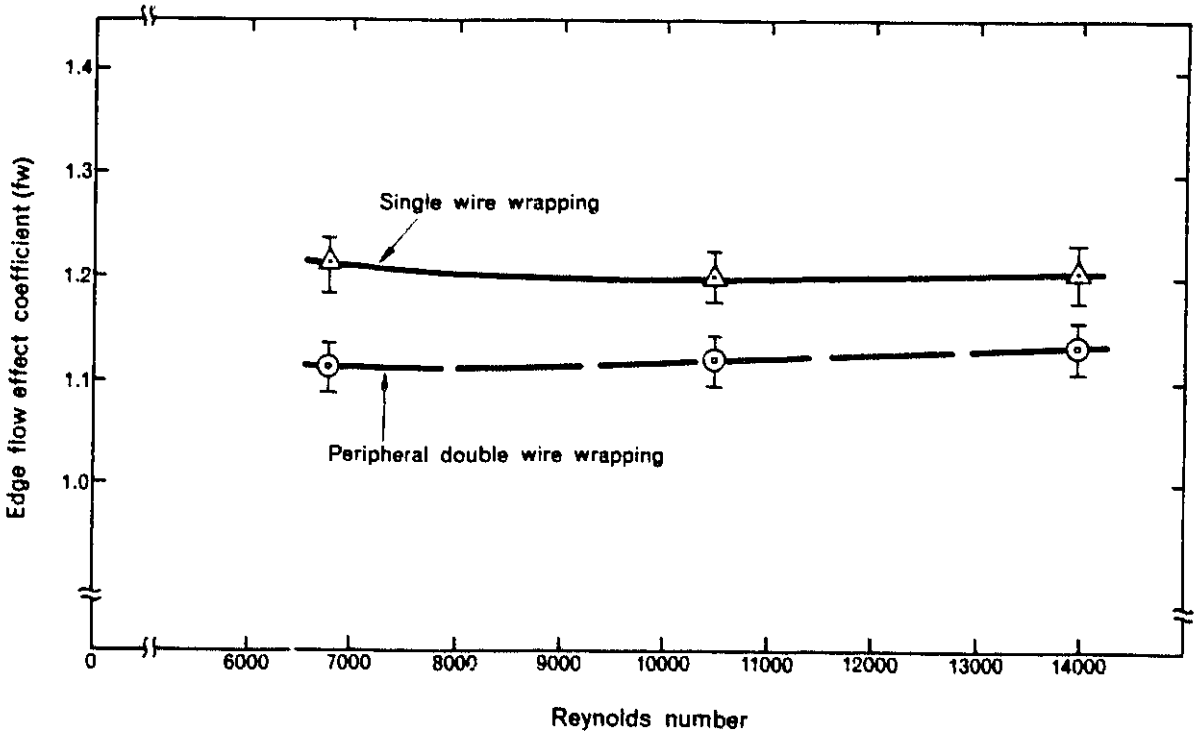

Fig. 10. Relationship between edge flow effect coefficient and Reynolds number.

4. Conclusion

The results of experiments are summarized as follows:

(1) The axial velocity in the subassembly of single wire-wrapped pins is about 10 percent larger in the peripheral subchannel than that in the internal subchannel. In double wire-wrapped pins in the peripheral pin ring, the axial velocity of peripheral subchannels is about 3 percent larger in the peripheral subchannel than that in the internal subchannel.

(2) The coefficient fw of edge flow effect is evaluated at 1.21 for the subassembly of single wire-wrapped pins and 1.12 for the reformed subassembly. The coefficient fw of the double wire-wrapped pins decreases by about 7 percent in the peripheral region of subassembly, compared that in the internal channel.

(3) Utilization of double wire-wrapped pins in the bundle makes the coefficient fw of edge flow close to unity and the flow rate distribution becomes uniform in the subassembly.

References

(1) Toshihide OHTAKE, et al. : "Velocity Measurements in subchannel of Wire Spaced Subassembly" N841-75-04 (PNC Report) (1975).

(2) Takao YAGI, et al. : "Velocity Distributions in a wire-Spaced Fuel Assembly" PNCT 831-78-01 (1978)

Irradiation Experiments of FUGEN PuO_2-UO_2 Fuel Assembly in WSGHWR*

Yoji YOKOUCHI, Naoki YOKOSAWA,
Takashi KAJIYAMA, Yoshiharu KIYONAGA,
Ryozo YUMOTO and Kazushige DOMOTO

1. Introduction

Four irradiation tests (Type-A,B,C and D) have been carried out for the development of design and fabrication for the advanced thermal reactor "FUGEN" fuel assembly.

The present report describes the irradiation conditions and the results of the post-irradiation tests for the Type-D fuel assembly which was fabricated prior to the production of mixed oxide fuel for "FUGEN" in the plutonium Fuel Fabrication Facility of PNC.

The fuel Assembly was irradiated in the Winfrith Steam Generating Water Reactor (WSGHWR) to a peak burnup of 8,690 MWd/tMO in peak pellets. The subsequent post-irradiation test was carried out in Windscale Nuclear Power Development Laboratories, UKAEA, from December, 1977 to June, 1978.

2. Description of Fuel Assembly

A summary of the fuel assembly design data is shown briefly in Table 1 in comparison with the FUGEN fuel design data.

The details of the assembly are described in previous reports.[1],[2]

3. Irradiation History Data

The assembly was loaded into the reactor on October 21, 1975. The irradiation

*Presented at the Annual Meeting of Atomic Energy Society of Japan (March, 1980).

of the assembly was performed up to 360 effective full power days for a year and half. The fuel assembly was initially loaded into the channel S07, but after the temporary discharge, it was transferred to the channel S17 in the beginning of the second year of irradiation. Figure 1 shows the locations of the assembly in the core. Figure 2 shows the relative positions of the fuel pins to the upper tie plate vee-mark together with the pin reference numbers used in the WSGHWR fuel data bank.

The channel cooling conditions were as follows:

1) Coolant pressure 68 kg/cm^2
2) Coolant flow rate 15.5 kg/sec.
3) Inlet temperature 276°C

The impurity concentration in the primary circuit water was kept below the normal operation level.

The assembly have achieved a peak pellet burnup of about 4,000 MWd/tMO in the channel S07 and then about 5,000 MWd/tMO in the channel S17. Reactor operations of 30 cycles were carried out during the irradiation of this assembly.

Figure 3 shows the progress of the irradiation of the assembly in terms of peak pellet burn-up versus time. The assembly average burnup and the pellet peak burnup reached 5,600 and 8,690 MWd/tMO at the end of irradiation respectively, whereas the target burnup was 8,500 MWd/tMO in the pellet peak.

The peak pellet linear-rating in the assembly during the irradiation was 490 w/cm, which occurred in pin C11 a few days after startup. Figure 3 gives the plot of peak linear-rating (w/cm) against time for the pin C11. During the subsequent irradiation, the peak pellet linear-rating of pin C11 did not exceed a maximum value of 490 w/cm due to a negative effect of higher burnup.

Table 2 gives the various form factors relevant to the assembly at each core state (see Fig.3 for the definition). The radial form factor (the ratio of peak to average power in the assembly) decreased from 1.243 at the beginning of irradiation to 1.161 at the end of the irradiation. The assembly tilt factor also slightly decreased from 1.027 to 1.012.

The irradiation of the assembly has been successfully completed without major problems. After the cooling for nine months, the assembly was subjected to post-irradiation examinations.

Table 1. Summary of type-D and FUGEN fuel assembly design data.

	Type-D	FUGEN
1. Assembly		
(a) Number of rods	28	28
(b) Number of spacers	11	12
(c) UO_2-PuO_2 weight (kg)	164.3	173.5
(d) Pu fiss. weight (g)	2470	1021
2. Fuel		
(a) Pu enrich. (w/o Pu fiss.)	1.7	0.55, 0.80
(b) Pellet density (% T.D.)	95	95
(c) Pellet dia. (mm)	14.4	14.4
(d) Pellet height (mm)	18	18
(e) Pellet end shape	dished, cham.	dished, cham
(f) Active length (mm)	3510	3700
3. Cladding		
(a) Material	Zr-2	Zr-2
(b) O.D (mm)	16.46	16.46
(c) I. D (mm)	14.7	14.7
(d) Plenum length (mm)		
Upper	191	251
Lower	24	24

Table 2. Form factors.

(Peak/Mean values)

Core state		Axial	Radial	Cluster tilt
(S07)	64	1.294	1.243	1.027
	65	1.275	1.231	1.027
	66	1.261	1.225	1.027
	67	1.255	1.218	1.022
	68	1.250	1.212	1.022
	69	1.240	1.206	1.022
(S17)	70	1.288	1.202	1.023
	71	1.288	1.202	1.019
	72	1.283	1.194	1.019
	73	1.301	1.187	1.012
	74	1.289	1.184	1.012
	75	1.278	1.177	1.012
	76	1.268	1.171	1.012
	77	1.257	1.167	1.012
	78	1.248	1.161	1.012

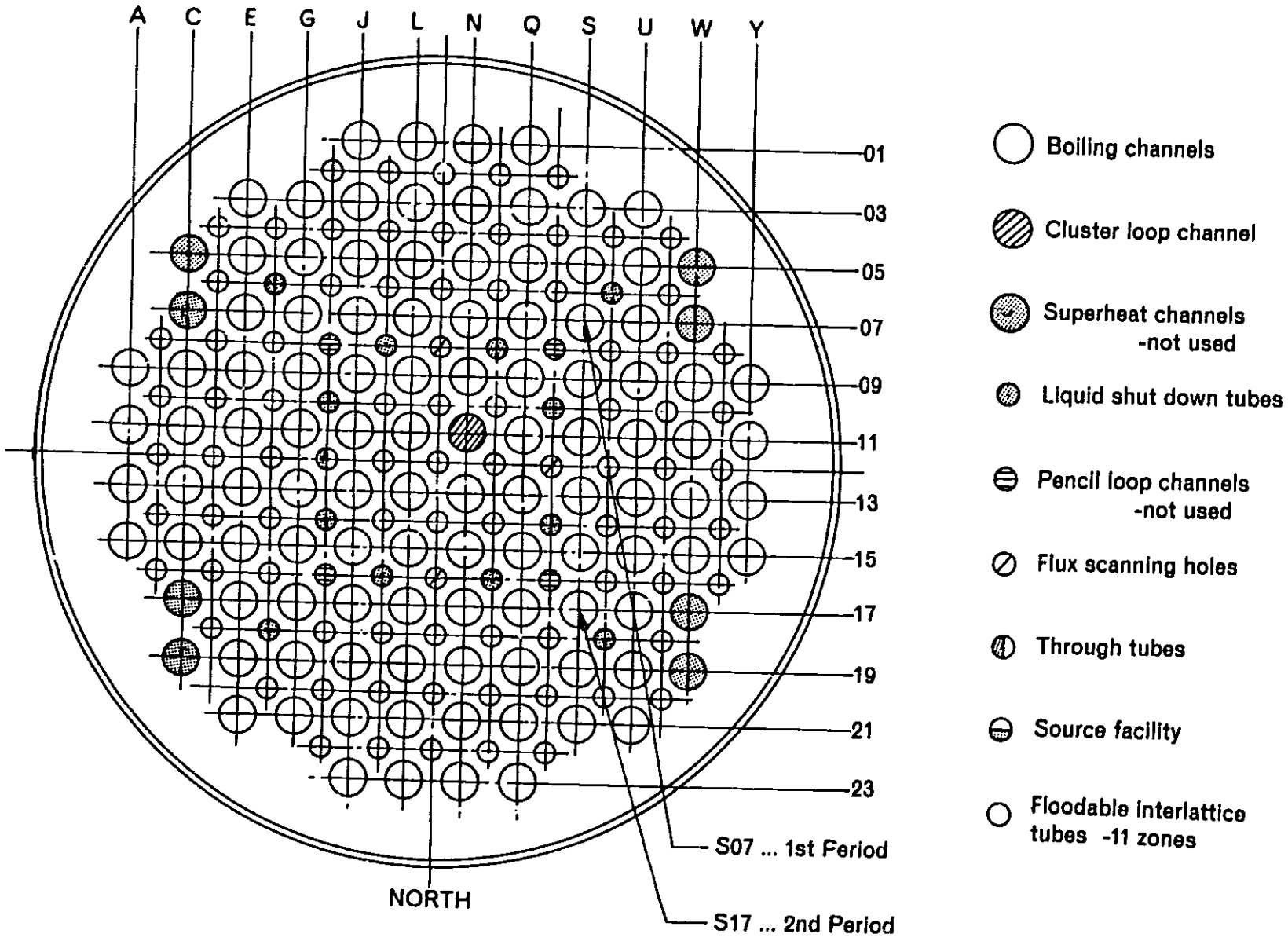

Fig. 1. SGHWR core plan and PNC cluster location.

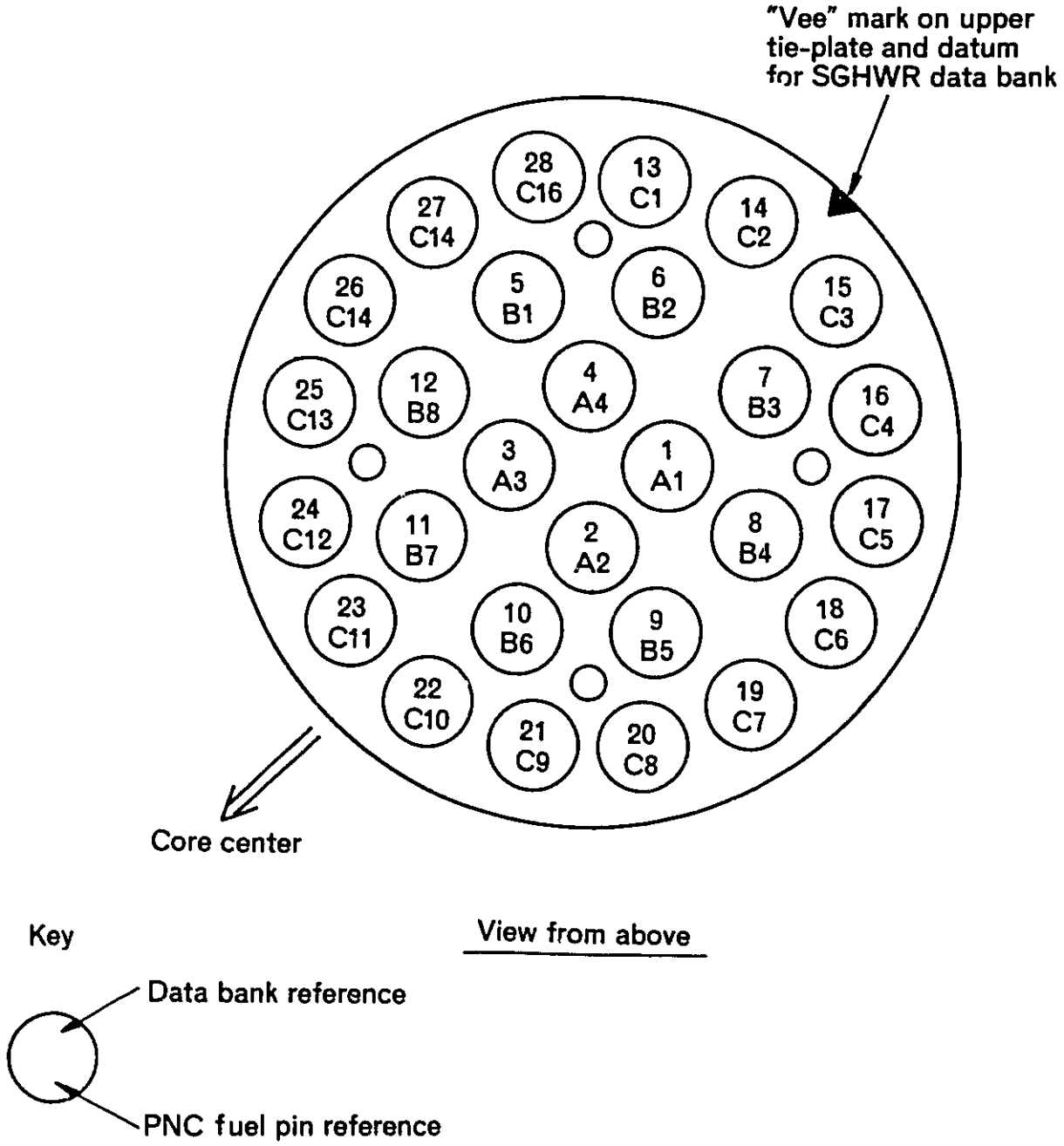

Fig. 2. Fuel pin references and cluster location.

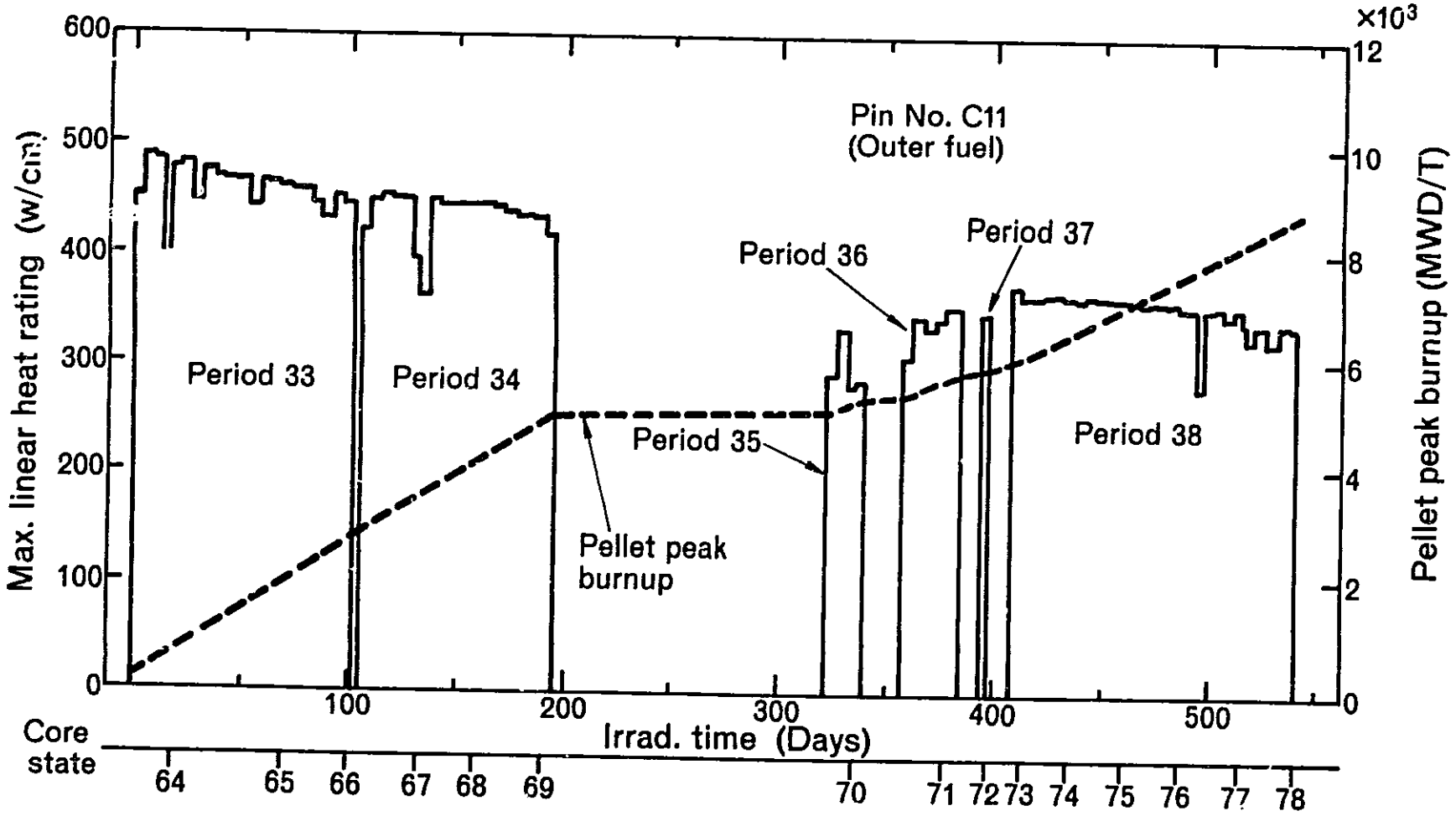

Fig. 3. Peak linear heat rating and pellet peak burnup of pin No. C11.

4. Post-irradiation Examinations

The assembly was examined by post-irradiation tests consisiting of the following points.

(1) Visual examination of assembly and pins.
(pin gap, crud, fretting corrosion of cladding by spacer grids and oxidation of cladding outer surface)
(2) Eddy-current testing (9 pins)
(3) Measurement of pin length
(4) Measurement of pin diameter (8 pins)
(5) Gamma-scanning (9 pins)
(6) Neutron radiography (4 samples)
(7) Measurement of fission gas release (8 pins)
(8) Metallography of pellet and cladding
(9) Measurement of fuel density
(10) Burnup analysis
(11) Hydraulic pressure tests
(12) Burnup analysis of fuels
(13) Measurement of pellet density
(14) Hydraulic pressure test of claddings

After visual examinations, 9 pins were selected for destructive examinations. The samples were cut from one inner ring pin, one intermediate pin and seven outer ring pins.

4.1 Non-destructive Examinations

1) Visual examination of assembly and pins

The fuel assembly was in excellent condition and no unusual crud pattern was observed. No difficulties were encountered during the pin withdrawal. The forces required for removing the fuel pins from the assembly were roughly similar between outer and imtermediate ring pins, and tended to decrease in inner ring pins. The grids were kept in good condition and their forces sustaining pins were not markedly changed by the irradiation. There were no signs of bowing of the spacer-tie rods.

(1) Pin gap

Two slip gauges 1.85 and 1.70mm thick were used for checking inter-pin spacings at midpoints between grids. At first the 1.85mm slip gauge was used for measurements at 72 points in the outer ring pins and intermediate ring pins at six mid-spacer positions. The pin gaps were about 2.2mm before irradiation, and it was possible to insert the 1.85mm gauge between the pins at all test positions. The gaps showed tight fits at five positions on the outer ring and one position on the intermediate ring after the irradiation. But the 1.70mm gauge easily entered the gaps at those six positions. The gaps are considered to remain sound in comparison with the criterion of 1.70mm before irradiation.

(2) Crud

The assembly was coated with crud in the middle region, while it was virtually free of crud in the bottom and top regions.

The crud was observed to be thinner on the intermediate ring pin and inner ring pins than on the outer ring pins. Little crud was observed on the surface of non-heat-generating components such as spacer-tie rods and spacer grids.

Some selected pins were brushed for the subsequent examinations, but only about half of the surface was observed to be black after removal of the crud. The rest part was brown-colored, and it showed that hard crud was still remaining on the surface.

For the measurement of crud thickness, a specimen was prepared from the middle of an outer ring pin after hardening the crud with a resin. A typical crud deposit photogaph is shown in Fig. 4. A maximum thickness of crud was 43 μm and the outer layer of the crud was porous, including iron as the main component. The thickness of the porous crud ranged from 10 to 25 μm. The inner layer consisted of a dense crud rich in Cu.

(3) Fretting corrosion of cladding by spacer grids

Since fretting corrosion has an important influence on the material strength, very careful observation was made on the selected pins with a periscope. The contact-marks due to fretting were so small that they could be found only by careful observation. Comparatively large contact-marks were observed at several grids in the bottom and top regions of fuel pins. The marks were evaluated to be below 10 μm in depth by metallography. Though the irradiation time has reached about one-third of the full irradiation period, the fretting corrosion depth may be expected not to exceed the criterion of 76 μm at an end of full use.

Fig. 4. Crud deposits on resin-protected region of pin No. C12.

(4) Oxidation of cladding outer surface

A lustrous black oxide surface appeared after careful removal of crud. The uniform oxide film was observed to have a thickness below 2 μ m by metallography. The oxide film under the crud layer was not thicker than that in crud-free region.

There were many tiny spots called nodular oxides near grids. In general, oxidation was greatest at bottom-ward grid positions 8,9, and 10, although it was present at all grids except the top position. On the other hand, no nodular oxide was seen between the grid positions on the inner ring pin, but small quantity of oxide was seen between grids on the intermediate and outer ring pins.

The oxidation between grids seemed to be associated with scratches formed during the element assembling.

The results of metallography showed that one of the heaviest oxidation was 43 μ m in depth, of which about one-third protruded from the surface of cladding tube (Fig. 5).

Fig. 5. Largest oxide layer on specimen at grid 4 of pin No. C14.

2) Eddy current testing

Eddy current test (ECT) was made on nine pins. Signals from pellet ends were observed on only outer ring pins generally in the region of 500 mm to 2500 mm from the bottom end shoulder, while no significant signals were observed at grids.

Three small signals were detected on pins A4, C11, and C14, but the subsequent visual examination of the regions showed no indication of defect on the outer surface although spalling of crud or oxide was found at the signal position of pin C14. Transverse micro-specimens through the signal regions failed to reveal evidence of defects. There was also no evidence to show highly concentrated hydrides, frettings and other defects.

Plenum lengths at the top and bottom ends were measured from ECT and gamma-scanning charts. In the outer ring pins, increases between 27.5 mm and 32.1 mm were observed in total plenum length, the single inner and intermediate pins involved showed lower increases of 16.2mm and 14.4mm respectively.

3) Measurement of pin length

Measurement of overall length was made on all the 28 fuel pins of the assembly. The inner ring pin increased by 0.12% in length, the intermediate 0.15% and the outer 0.21% on the average.

4) Measurement of pin diameter

The diameters of eight pins were measured using a non-contact capacitance diameter transducer (CDT) system. Two simultaneous scans after irradiation were made along the same axes ("A" and "B") of pins as those before irradiation, and the data were recorded as continuous traces on analogue charts. The values of diameters were obtained from the charts at the same 45 positions as those of pre-irradiation measurements (Fig.10 to 12).

The data clearly shows that all the pins reduced in diameter almost over the entire pin length and the greater reductions occurred in the outer ring pins. The results are summarized in Table 3.

Table 3. Changes in pin diameters.

Pin No.	Position in element	Diameter decrease (mm)					
		On axis "A"		On axis "B"		Overall	
		Max.	Mean	Max.	Mean	Max.	Mean
A 4	Inner ring	0.032	0.022	0.029	0.018	0.032	0.020
B 6	Intermediate ring	0.053	0.035	0.039	0.024	0.053	0.030
C 1	Outer ring	0.072	0.030	0.075	0.030	0.075	0.030
C 4	" "	0.095	0.042	0.085	0.046	0.095	0.044
C 7	" "	0.076	0.037	0.062	0.028	0.076	0.033
C10	" "	0.096	0.040	0.081	0.035	0.096	0.038
C11	" "	0.080	0.036	0.068	0.027	0.080	0.032
C14	" "	0.080	0.035	0.069	0.029	0.080	0.032

5) Gamma-scanning

Nine fuel pins were investigated by gamma-scanning and the results obtained are summarized in Table 4.

Relative peaks are given together with depressions at grids, interpellet gaps and fuel stack length measurements. The gamma depressions at grids were generally below 5% for outer-ring pins and a small number of inter-pellet gaps were found (maximum total gap width was below 2mm for every pin). No cesium peaking (gamma-spiking) was observed at pellet ends, but small variations below 5% were found for the gamma activity at some localized positions. Every pin decreased in the fuel stack length by a similar amount in the outer-ring region. The mean decrease X was 0.63% with a standard deviation of 0.06%. The decreases for the inner and intermediate ring pins were only about half of those for the outer ring pins.

4.2 Destructive Examination

1) Neutron radiography

Six 460 mm lengths of four pins were examined by neutron radiography at AERE Harwell. There was no evidence of the presence of large Pu particles or Pu agglomerates on the radiographs.

2) Measurement of fission gas release

Eight pins were punctured for measurement and analysis of internal gases. To obtain the ratio between released and retained gases, Xe was analyzed by mass spectrometry, assuming that all fissions occurred in Pu^{239}.

Fractional release of Xe in the inner and intermediate ring pins was low ($<$ 0.1%) as expected. The release ratios of the outer ring pins were variable from 3 to 4% except 10% in pin C12.

Table 4. Gamma scanning test results.

Pin number	Relative peak total gamma count (cps)	γ Depression at grid positions 5,6,7,8 (%)		Interpellet gaps		Fuel stack measurements				Localized variations in gamma activity between fuel pellets		Gamma-(spiking Cs peaking)
		Max	Mean	Number and position (mm from bottom end)	Total gap width (mm)	(1) Pre-irradiation length (mm)	Corrected post-irradiation length (ie less gaps) (mm)	Difference (mm)	Difference (%)	Number of pellets	(1) Fuel batch no.	
A4	381	7.7	6.6	0	0	3509.6	3496.8	−12.8	−0.36	0	6	NIL
B6	535	4.6	4.2	1 (674)	0.1	3509.8	3498.4	−11.4	−0.32	0	5, 11	NIL
C1	827	3.7	3.3	2 (1137 & 1621)	0.5	3508.9	3486.6	−22.3	−0.64	12	8	NIL
C4	815	3.5	3.1	5 (1630-2078)	1.3	3509.3	3484.1	−25.2	−0.72	1	2	NIL
C7	797	4.6	4.3	5 (1570-2163)	0.3	3511.3	3491.5	−19.8	−0.56	2	4	NIL
C10	788	5.0	4.5	9 (1390-2685)	1.0	3509.6	3488.5	−21.1	−0.60	1 (also small variations on 5 others)	8	NIL
C11	825	3.6	3.1	4 (1800-2790)	0.2	3513.4	3491.3	−22.1	−0.63	1 (also small variations on 6 others)	5	NIL
C12	810	4.2	3.2	15 (1492-2446)	1.7	3507.2	3482.7	−24.5	−0.70	0	9	NIL
C14	740	5.1	4.5	10 (1248-2613)	0.8	3506.1	3485.4	−20.7	−0.59	10	8	NIL

(1) Data supplied by PNC representative

3) Metallography of pellet and cladding

(1) Pellet

A total of 15 specimens (12 transverse and 3 longitudinal) were prepared from the selected pins.

For inner and intermediate ring pins, the grain size of pellets did not change and macropores still remained at the pellet center. On the other hand, metallographs of outer ring pins showed that the grain size in the pellet center had grown to the range from 15 μm to 30 μm.

At the center of some pellets growth of columnar grains, estimated to occur at about 1600°C, was observed.

Since the pellet had dishes of 0.2 mm in depth at the ends, a dimple should be found at each pellet end of longitudinal section specimens. But most of the dimple depth decreased with burnup. In the case of Type C irradiation test, the decrease of depth was not so significant as in Type D in spite of higher temperature at the pellet centers of Type C.

Photographs of longitudinal specimens showed that neighboring pellets sintered at the interface even in the low temperature zone fairly near to chamfers. The sintered boundaries were not flat and the fragmentation of pellets was observed at the interface of pellet end as shown in Fig. 6.

Though there were Pu spots of about 100 μm diameter, there was no evidence of elevation of temperature at Pu spots. Alpha-autoradiography showed that Pu spots at the pellet center grew to 180 μm diameter, but the diameter of Pu spots at the outer region did not amount to 120 μm.

The effect of neutron flux tilt was observed from the result of beta-gamma autoradiography. The flux tilt became more pronounced across the outer ring pins than across the inner or intermediate ring pins.

For the study of pellet deformation and pellet and cladding mechanical interaction (PCMI), the gaps between pellet and cladding were measured on longitudinal section specimens. Figure 7 shows a typical datum on a specimen in a comparatively high heating-rate region. Although the diameter of cladding at a pellet end decreased as indicated by the diametral measurement, the gaps were minimum at mid-pellet. This shows that the diameter of pellets is maximum at mid-pellets instead of pellet ends as well-known ridging. The similar behaviour could also be confirmed by other examinations such as ECT and gamma scanning.

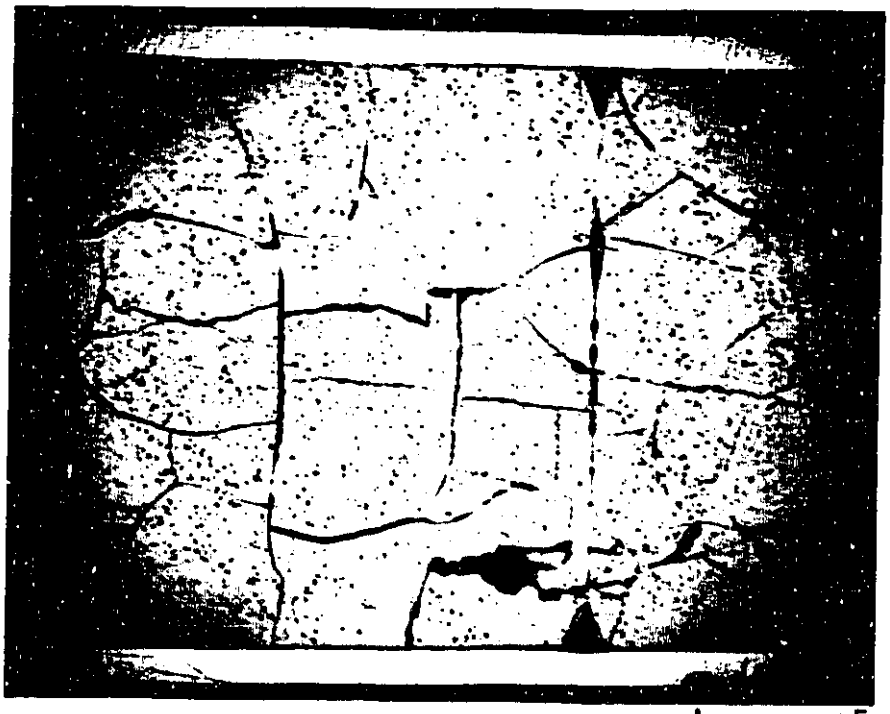

a) 1936(L) x5

Grid spring side

Pellet chamfers

b) 1936(L) x75

Pellet chamfers

c) 1936(L) x75

High interpellet pressures resulted in sintering of pellet-ends lands, and local fragmentation of pellet.

Fig. 6. Inter-pellet microstructural features of pin No.7 (Max. burnup region of 95%).

(2) Cladding

The result of PCMI is observed by metallography as oxidation of cladding inner surface or sticking of fuel fragments to cladding. Metallographs for PCMI were taken from 20 specimens. Only three specimens prepared from the high rate regions gave evidences of PCMI. One of them showed sticking of a fuel fragment, but the cladding showed no deformation. All of the three specimens showed about 8 μm of oxidation layers which extended to a limited range with layers of uneven thickness.

On the other hand, the cladding inner surface at the chamfer of pellet ends were also corroded to $\lesssim 8$ μm in thickness. It is considered that this corrosion resulted from the reaction between cladding and fission products from pellets.

There was observed no extremely hydrated zone in the cladding. The hydride inclusions tended to be circumferentially oriented with a short length. Although the cladding zone adjacent to the end-closure weld has a tendency to form hydride more easily than the non heat affected zone, there was no abnormal hydride precipitation.

4) Measurement of fuel density

Two specimens were sectioned from each of A4, B6, C4 and C11 pin for density measurements. The measurements were made on four pellets of 70mm length by mercury pycnometry. Figure 8 shows the results modified with solid swelling by solid fission products.

5) Burnup analysis

One complete pellet length was dissolved for analysis of gross burnup and isotopic compositions. The results are given in Table 5. The samples from pins A4, B6 and C10 were selected at positins about 1950mm from the top shoulder. The burnups of pins A4, B6 and C10 were estimated to be 4,696, 6,159 and 9,400 MWd/tMO respectively.

The measurements of radial burnup distribution were made on two transverse specimens - one from B6 and the other from C11 - taken at the position of 1890 mm from the top shoulder of each pin. The specimens were prepared from 5 concentric ring zones with an ultrasonic drill. The results are shown in Fig. 9.

6) Hydraulic pressure tests

(1) End-closure weld tests at room temperature (20°C)

Both top and bottom weld regions of pin C7 were hydraulically pressurized without failure up to 120 MPa at 20°C.

Table 5. Isotopic analyses, Pu/U and Nd148/U ratios and gross burn-up samples.

Pin number	A4	A4	B6	B6	C4	C4	C10	C11	C11	C11
Distance from top shoulder (mm)	1975	3585	1940	3425	2840	3505	1965	3155	1940	880
Atom % U234	0.01	0.01	0.01	0.01	0.01	0.01	0.01	0.01	0.01	0.01
U235	0.62	0.69	0.59	0.66	0.53	0.62	0.51	0.55	0.51	0.56
U236	0.02	0.01	0.03	0.02	0.04	0.02	0.04	0.03	0.04	0.03
U238	99.35	99.29	99.37	99.31	99.42	99.35	99.44	99.41	99.44	99.40
Atom % Pu238	0.24	0.16	0.28	0.20	0.34	0.22	0.37	0.30	0.36	0.30
Pu239	67.71	72.83	63.80	69.07	56.23	64.97	54.61	58.60	54.67	59.75
Pu240	24.60	21.99	27.68	24.62	33.29	27.93	33.86	31.89	33.83	30.58
Pu241	6.38	4.27	6.90	5.17	8.07	5.68	8.81	7.44	8.79	7.62
Pu242	1.07	0.75	1.34	0.94	2.07	1.20	2.35	1.77	2.35	1.75
Atom % Nd142	0.11	0.08	0.12	0.07	0.13	0.12	0.17	0.10	0.23	0.11
Nd143	26.93	27.62	26.60	27.29	25.91	27.11	25.72	26.54	26.07	26.42
Nd144	21.91	21.37	22.39	21.78	23.29	22.25	22.97	22.39	22.89	22.35
Nd145	18.97	19.21	18.89	19.10	18.81	18.99	18.81	18.99	18.74	18.96
Nd146	16.22	15.97	16.20	15.99	16.15	15.92	16.39	16.18	16.28	16.34
Nd148	10.17	10.10	10.15	10.13	10.12	10.02	10.26	10.15	10.17	10.22
Nd150	5.69	5.65	5.65	5.64	5.99	5.59	5.78	5.65	5.62	5.60
Pu/U ratio by weight	0.0202	0.0205	0.0195	0.0199	0.0183	0.0189	0.0176	0.0190	0.0176	0.0183
Nd148/U ratio by weight $\times 10^{-3}$	0.0578	0.0228	0.0758	0.0418	0.1067	0.0582	0.1157	0.1008	0.1185	0.0917
Burn-up estimate from Nd148/U ratio MWd/te MO	4696	1853	6159	3396	8670	4729	9400	8190	9628	7451

* All results corrected to January 1, 1979.

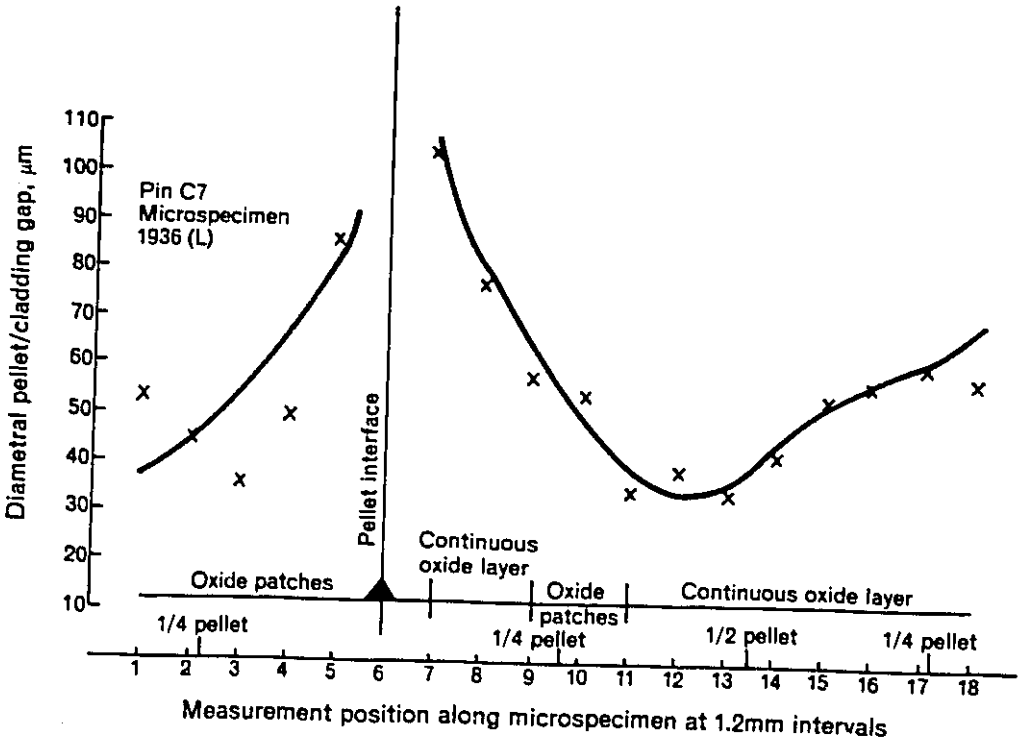

Fig. 7. Fuel pellet and cladding gaps of pin No. C7.

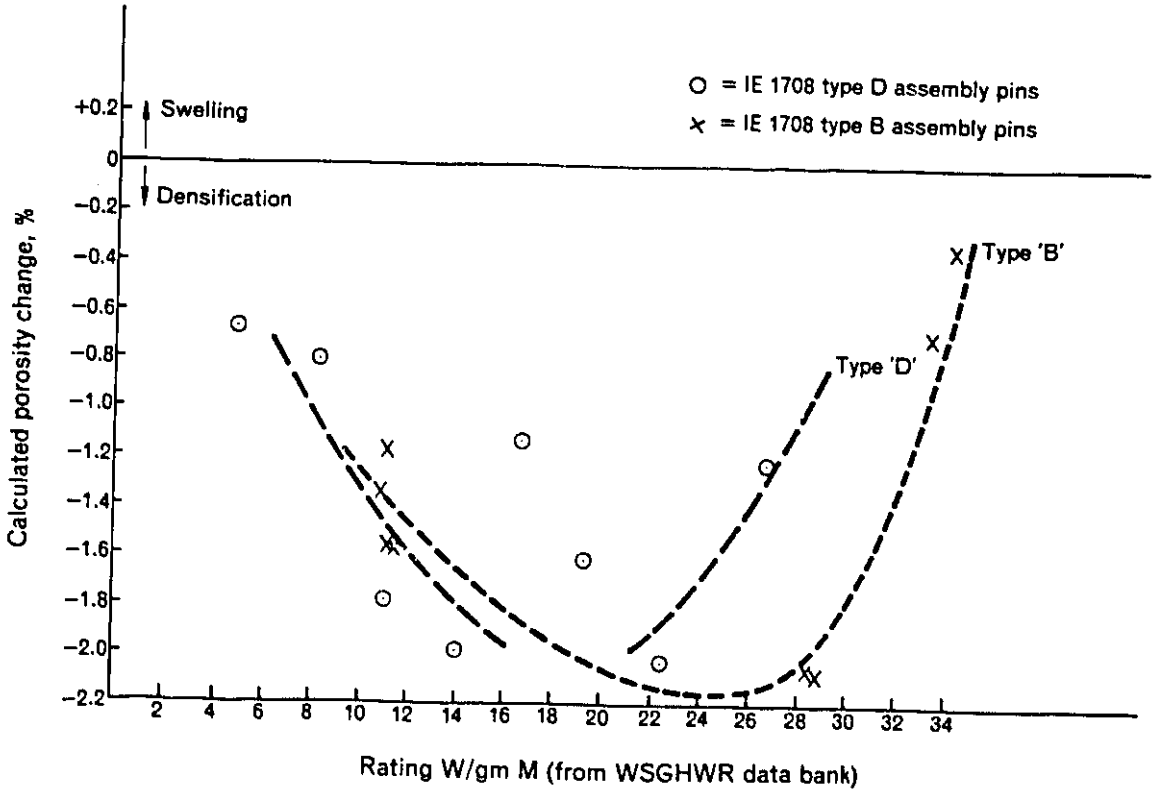

Fig. 8. Comparison of calculated fuel porosity change in type B and type D assemblies.

(2) Burst test at 340°C

One specimen from the central region of pin C7 was tested at 340°C. The cladding elongation was estimated to be 8.7% after irradiation. This value sufficiently satisfies the specification for FUGEN fuel cladding before irradiation. The ultimate burst strength and 0.2% proof stress were 654.5 MPa and 599MPa, respectively.

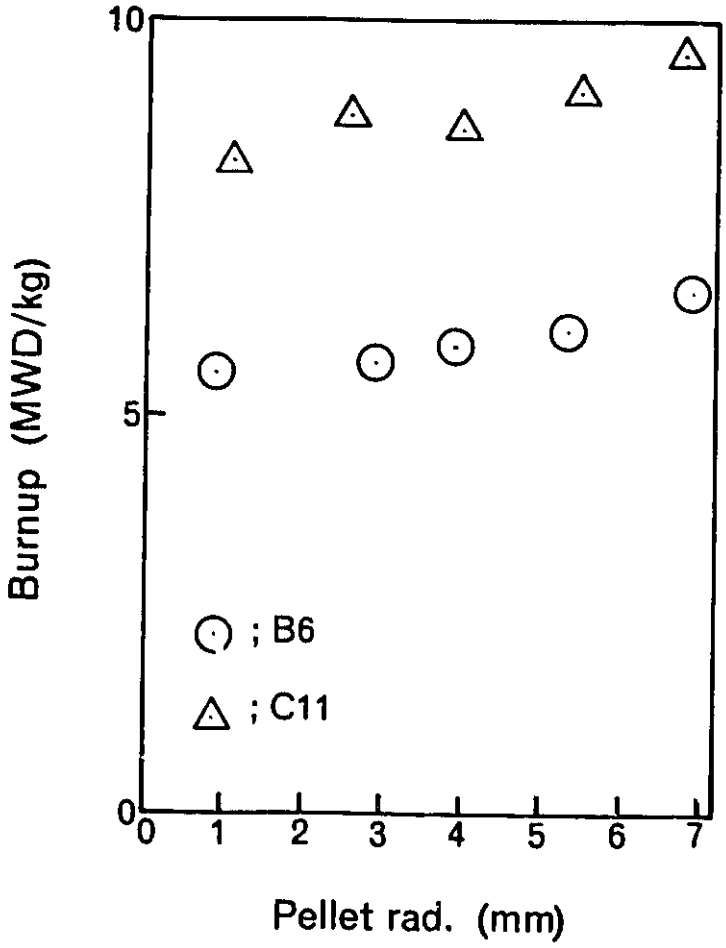

Fig. 9. Radial burnup distribution in pellet.

5. Discussion

5.1 Change of Overall Fuel Length

The fuel pin length changes of intermediate and inner rings are in good agreement with those observed on the Type B and C fuel pins, but the outer ring fuel pins gave slightly higher (~ 0.009%) values than those expected from the irradiation data of the Type B and C.

It is found from the comparison between the length changes of each ring pin that the pin length increases with increasing fuel burnup. On the other hand, the pin length changes have an opposit tendency for fast neutron flux. According to the irradiatin data of tie rods obtained from the Type C test, the change of cladding length due to fast neutron fluence is estimated at about 0.07% in the case of Type D.

5.2 Measurements of Fuel Pin Diameter

All fuel pins reduced in diameter over their whole length during irradiation and the greater reductions occurred in the outer ring pins. The ovality of cladding also occurred in all fuel pins.

Careful examination of results on ECT, gamma scanning and profilometry suggested that ridges occurred at pellet centers, but not at pellet ends. Further indirect evidence from metallography suggests that the pellets assumed a barrelled shape rather than a usual wheatsheaf shape during irradiation. There are certainly more available evidences of intimate contact between fuel and cladding at mid-pellet positions than at pellet ends. The data from diameter scanning reveal that the mean radial ridge heights amount to 18μm and a maximum radial ridge height to 28μm.

The results of measurement and predicted values from our code "ATFUEL" for diameter changes are shown in Fig. 10 to Fig. 13. Figures 10 to 12 show typical cases for the axial distribution of pin diameter changes at the inner, intermediate and outer rings. The result reveals a tendency of decrease with increasing rod power. The measured maximum and mean values of Δ D/Do of each ring are shown in Table 6.

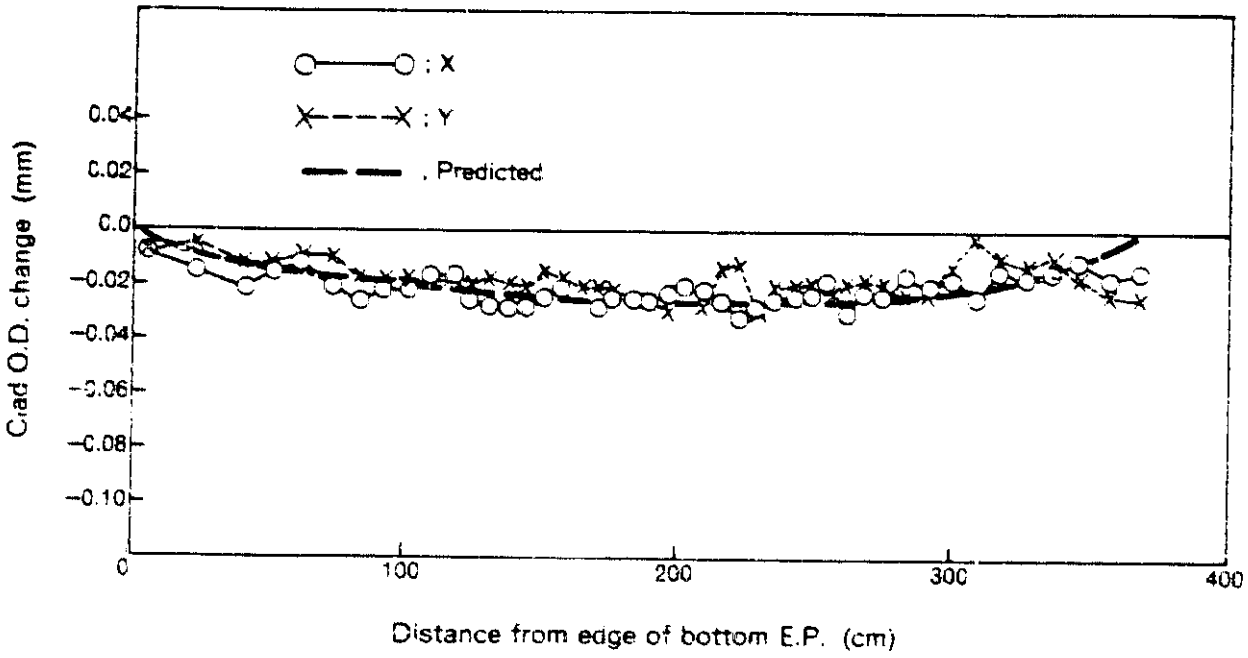

Fig. 10. Comparison of predicted and measured outer diameter changes for inner ring pin A4.

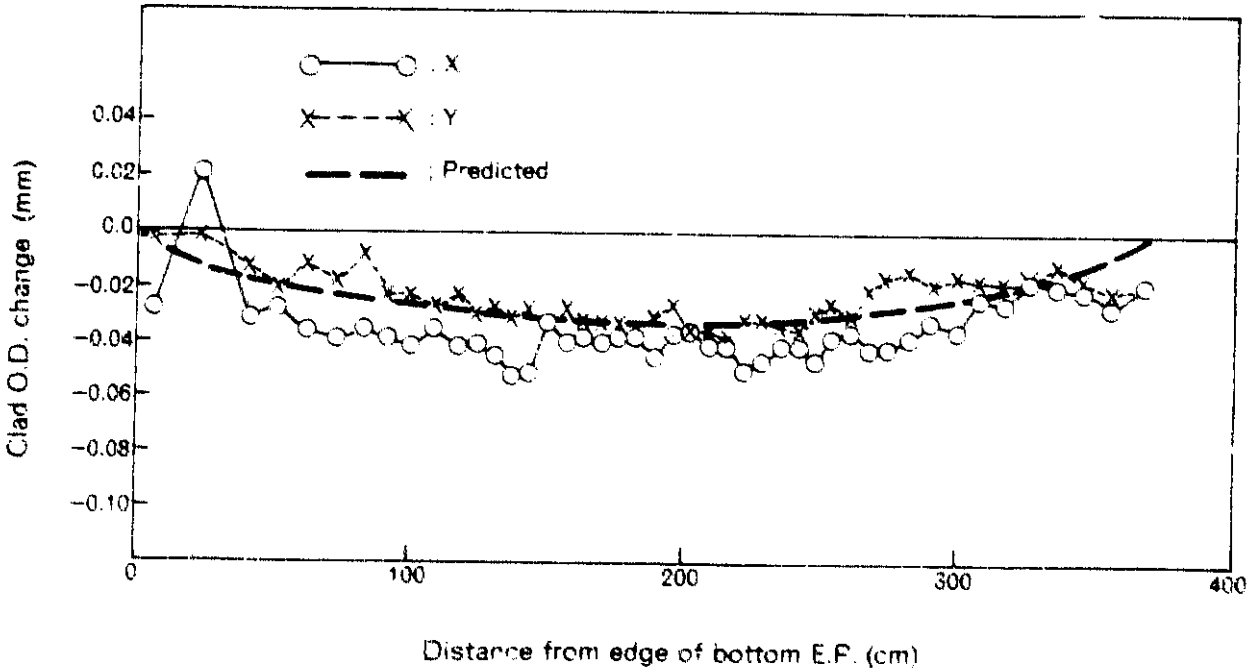

Fig. 11. Comparison of predicted and measured outer diameter changes for intermediate ring pin B6.

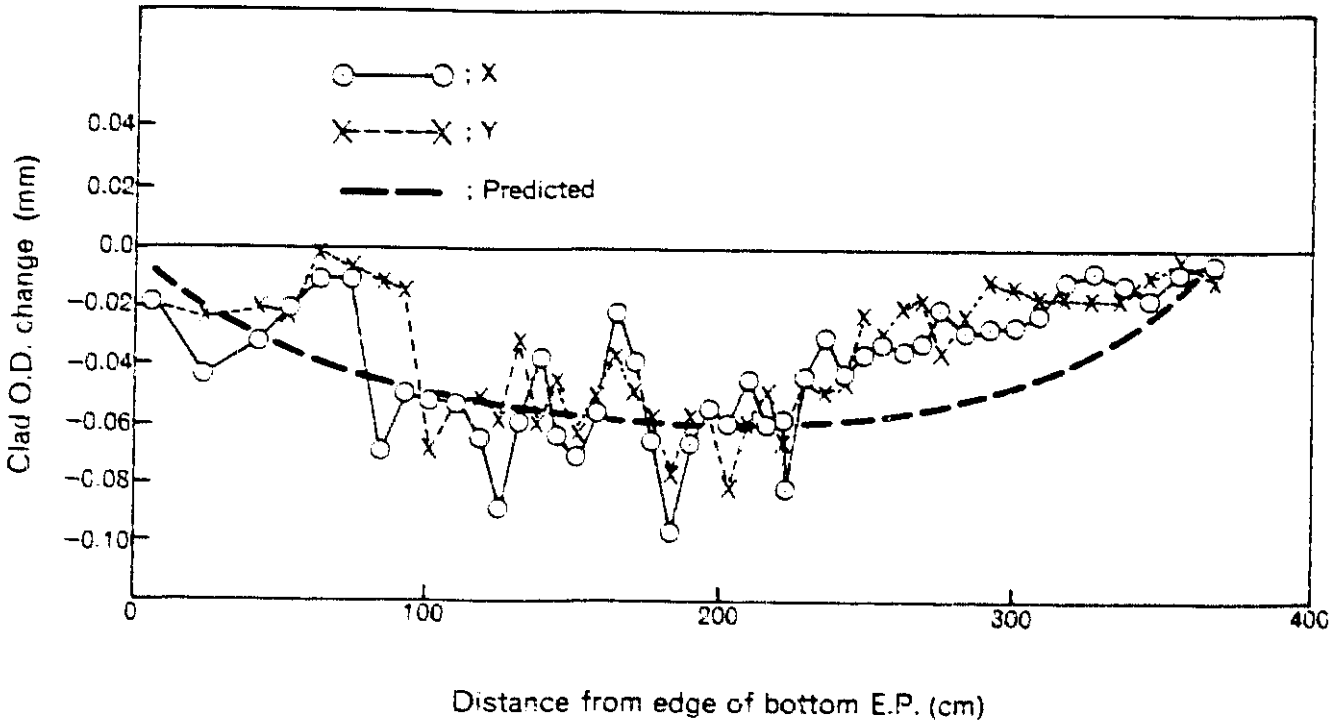

Fig. 12. Comparison of predicted and measured outer diameter changes for outer ring pin C10.

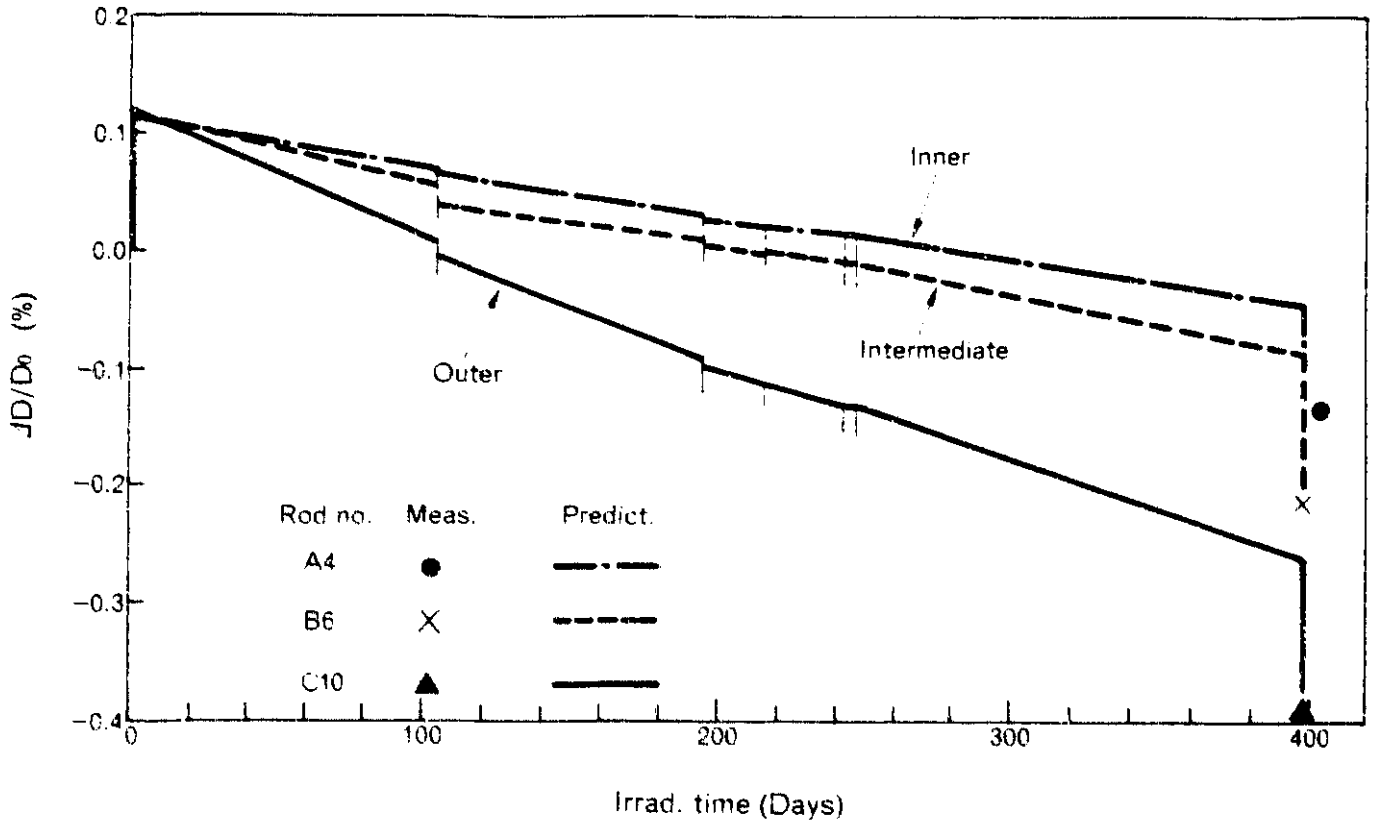

Fig. 13. Changes of cladding outer diameter at maximum linear heat generation rate location.

Table 6. Measured diameter changes in fuel pins.

	Max. ⊿D/Do (%)	Mean ⊿D/Do (%)
Inner ring pin	−0.19	−0.12
Intermediate ring pin	−0.32	−0.18
Outer ring pin	−0.58	−0.23

On the other hand, the predicted results indicate a good agreement with these measured data. Figure 13 shows calculated diameter changes at a maximum rod power position of each ring as a function of the irradiation history. The pin diameter gradually creeps down with the irradiation time. The measured values of ⊿D/Do after irradiation are in good agreement with the calculated data as shown in Table 7.

Table 7 Comparison between measured and calculated ⊿D/Do at PIE

	Measured (%)	Calculated (%)
Inner ring pin	−0.10	−0.15
Intermediate ring pin	−0.20	−0.18
Outer ring pin	−0.39	−0.37

5.3 Fission Gas Release

Figure 14 shows the results of measured values and calculated values obtained from an ATR fuel design code. The calculated results are in good agreement with the measured data except those for singular pin C12.

Comparison of the gas inventories between the pin C12 and other outer ring pins indicates that the increase in gas content in the pin C12 was entirely due to an increase in Xe and Kr contents. From the fuel ceramography it may be estimated that the pin C12 was irradiated at higher fuel temperature than fuel pins in the other outer region.

5.4 Cladding Metallography

The cladding grains assume the forms of reasonably equiaxed crystals with diameters below 6 μ m. Hydride inclusions were short in lengh and tended to be circumferentially oriented, although numerous shorter piatelets of randomly oriented hydride were observed. The hard dense crud apparently caused no overheating of the cladding, since no extraordinary oxidation was observed beneath this crud. But an evidence of slight hydrogen pick-up was detected beneath the larger surface nodules of oxide.

5.5 Measurement of Fuel Density

The change in density data was corrected for solid fission product swelling to give the claculated porosity change, i.e., the amount by which the pre-irradiation porosity had been changed by iradiation.

The results show that the densities of all the specimens have increased with irradiation. The maximum measured amount of densification was evaluated at 2.03% for the 22.4w/g specimen from pin C4.

In Fig. 8 the calculated porosity change is plotted against fuel rating with the data of Type B assembly obtained from a similar irradiation test. A reliable comparison cannot be made between the two types of fuel due to the scattered values from a relatively few measurements, but it would appear that a maximum densification occurred at a lower rating in the Type D fuel than in the Type B fuel.

5.6 Burnup Analysis

According to radial burnup analysis.the burnup depression in the fuel pellet revealed almost the same value in the average burnup between 5900 MWd/t and 8900 MWd/t. The burnup ratio of pellet surface to peilet center was about 1.18.

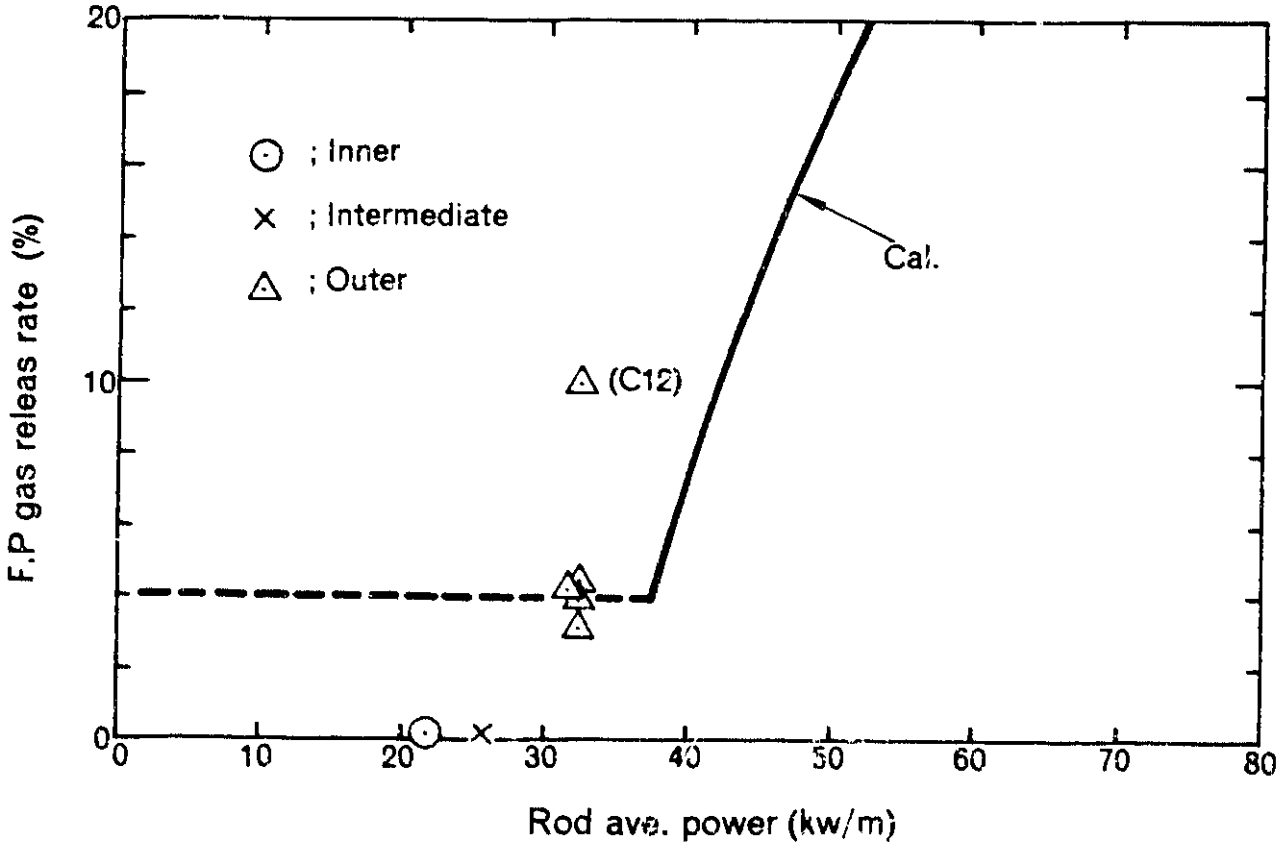

Fig. 14. FP gas release rate vs rod average power.

6. Conclusion

The irradiation of the Type D assembly in the WSGHWR has been successfully completed without any serious problems and the pellet peak burnup was 8,690 MWd/tMO.

Destructive and non-destructive examinatins on selected pins revealed no evidence of failure or incipient defects. The fuel assembly was in excellent condition for pin gap, pin straightness and other appearances.

Therefore it may be concluded that the design and fabrication of the present fuel are reasonably suitable for operation of the reactor FUGEN.

Reference

(1) KANEDA, K., YUMOTO, R., and AOKI, T.:
"Irradiation Experiment of FUGEN PuO_2-UO_2 Fuel Assembly in SGHWR (I) Design and Performance Analysis of the Fuel Assembly"
Tokai Works Semi-Annual Progress Report,
PNCT 831-77-01 (January-June 1976), P10-P16

(2) YOKOSAWA, N., NARUKI, K., et al.:
"Fabrication of a Fuel Assembly for an Irradiation Test in SGHWR"
Tokai Works Semi-Annual Progress Report,
PNCT831-77-01 (January-June 1976), P17-P23

Validation of KENO, ANISN and Hansen-Roach Cross-Section Set on Plutonium Oxide and Metal Fuel System*

Tadakuni MATSUMOTO, Koh NAKANO**
and Ryozo YUMOTO

1. Introduction

In a previous report[1] we have discussed the validity of KENO,[2)3)] ANISN[4)] and Hansen-Roach 16 group Cross-Section Set [5)] on the critical plutonium nitrate solution systems with various geometries, absorbers and neutron interactions.

The purpose of the present report is to examine the validity of the same calculation system on the homogeneous plutonium oxide and plutonium-uranium mixed oxide fuels with various densities. The critical experiment data on such homogeneous oxide systems are so limited that criticality data on plutonium and uranium metal systems are adopted as supplemental data on high density oxide system.

2. Data of Critical Experiment

Eleven experiments adopted for validation are summarized in Table 1. First six experiments were performed at Pacific Northwest Laboratory of Battelle Memorial Institute, and remaining five experiments at Los Alamos Scientific Laboratory of the University of California. Figure 1 shows a schematic view of stacked core of oxide fuel blocks reflected with plexiglas.

The characteristics of core fuel are given in Table 2, and the isotopic compositions of plutonium in Table 3. Figure 2 shows the relation between H/(Pu+U) atomic ratio and fuel density employed in these benchmark experiments and

---

*Presented at the Annual Meeting of Atomic Energy Society of Japan (Mar.,1979).

** CRC.

Table 1. List of critical experiments for benchmark calculations.

Case I.D.	Core			Reflector	Data source	Ref. No.
	Geometry	Fuel composition	Fuel density (gPu+U/CC)			
A-1	Rectang. prism	$Pu(18)O_2$	5.762	Plexiglas	Battelle (PNL)	(6)
A-2	〃	$Pu(8)O_2$-Polystyrene	1.050	〃	〃	(7)
A-3	〃	$Pu(18)O_2$-Polystyrene	0.367	〃	〃	(8)
A-4	〃	$30.0Pu(8)O_2$-$U(0.15)O_2$-Polystyrene	0.373	〃	〃	(9), (10)
A-5	〃	$14.6Pu(8)O_2$-$U(0.15)O_2$-Polystyrene	0.580	〃	〃	(9), (10)
A-6	〃	$7.9Pu(8)O_2$-$U(0.15)O_2$-Polystyrene	0.360	〃	〃	(9), (10)
B-1	Sphere	Pu(5)	19.74	H_2O	Univ. Calif. (LASL)	(11)
B-2	〃	Pu(4.8)−1.10 w/o Ga	15.53	U(nat.) metal	〃	(12)
B-3	〃	Pu(4.5)−1.02 w/o Ga	15.61	Bare	〃	(12)
B-4	〃	Pu(20)−1.01 w/o Ga	15.73	〃	〃	(12)
B-5	〃	U(93.8E)	18.75	〃	〃	(12)

Table 2. Characteristics of core fuel used for benchmark calculation.

Case I.D.	Indication of fuel composition	Fuel composition			Fuel density		Atomic ratio	
		Pu content in (Pu+U) (wt.%)	^{240}Pu content in Pu (wt.%)	^{235}U content in U (wt.%)	Pu+U (g/cc)	Pu (g/cc)	H/(Pu+U)	H/Pu
A-1	$Pu(18)O_2$	100	~18	—	—	5.762	—	0.04
A-2	$Pu(8)O_2$-Polystyrene	100	~ 8	—	—	1.050	—	15.0
A-3	$Pu(18)O_2$-Polystyrene	100	~18	—	—	0.367	—	49.6
A-4	$30.0Pu(8)O_2$-$U(0.15)O_2$-Polystyrene	30.0	~ 8	0.151	0.373	(0.112)	47.4	158
A-5	$14.6Pu(8)O_2$-$U(0.15)O_2$-Polystyrene	14.62	~ 8	0.151	0.580	(0.085)	30.62	210
A-6	$7.9Pu(8)O_2$-$U(0.15)O_2$-Polystyrene	7.89	~ 8	0.151	0.360	(0.028)	51.8	659
B-1	Pu(5)	99.9*	~ 5	—	—	19.74	—	—
B-2	Pu(4.8)−1.10 w/o Ga	98.9*	~ 4.8	—	—	15.53**	—	—
B-3	Pu(4.5)−1.02 w/o Ga	98.98*	~ 4.5	—	—	15.61**	—	—
B-4	Pu (20)−1.01 w/o Ga	98.99*	~20	—	—	15.73**	—	—
B-5	U(93.8)	—	—	93.8	18.75	—	—	—

*) Purity of plutonium metal.

**) Alloy density containing impurity Ga.

Table 3. Plutonium isotopic composition (in at. %).

Case I.D.	Composition of core fuel	Isotopic composition of Pu (at.%)					$Pu^{239}+Pu^{241}$ (at.%)	Comments
		Pu^{238}	Pu^{239}	Pu^{240}	Pu^{241}	Pu^{242}		
A-1	$Pu(18)O_2$	0.23	75.32	18.31	5.01	1.13	80.33	**
A-2	$Pu(8)O_2$-Polystyrene	<0.01	91.16	8.06	0.75	0.034	91.91	
A-3	$Pu(18)O_2$-Polystyrene	0.23	75.88	18.44	4.31	1.14	80.19	**
A-4	30.0 $Pu(8)O_2$-$U(0.15)O_2$-Polystyrene	0.0	91.22	8.13	0.61	0.04	91.83	**
A-5	14.6 $Pu(8)O_2$-$U(0.15)O_2$-Polystyrene	0.0	91.43	7.97	0.56	0.04	91.99	**
A-6	7.9 $Pu(8)O_2$-$U(0.15)O_2$-Polystyrene	0.0	91.25	8.12	0.58	0.05	91.83	**
B-1	Pu(5)	<0.01	94.5	5.18	0.30	0.02	94.8	Purity=99.9%
B-2	Pu(4.8)−1.10 w/o Ga	—	(94.9)*	(4.80)*	(0.30)*	—	(95.2)*	***
B-3	Pu(4.5)−1.02 w/o Ga	—	95.2	4.5	0.3	—	95.5	***
B-4	Pu(20)−1.01 w/o Ga	—	76.4	20.1	3.1	0.4	79.5	***
B-5	U(93.8)	—	—	—	—	—	—	

*) in wt.%.

**) calculated from atomic number densities shown in references.

***) Ga : Impurity.

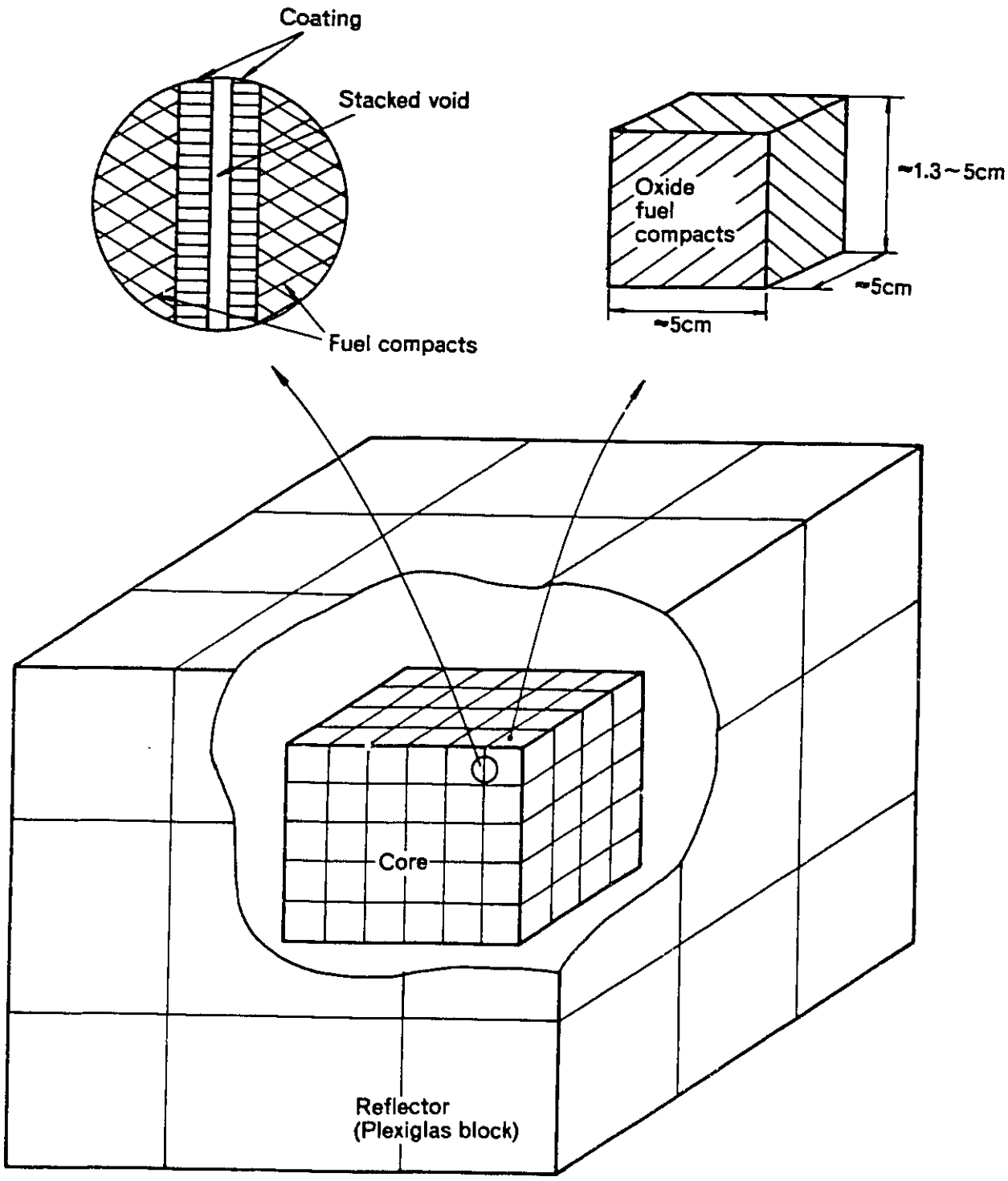

Fig. 1. Schematic view of plexiglas reflected core and details of block of fuel compacts.

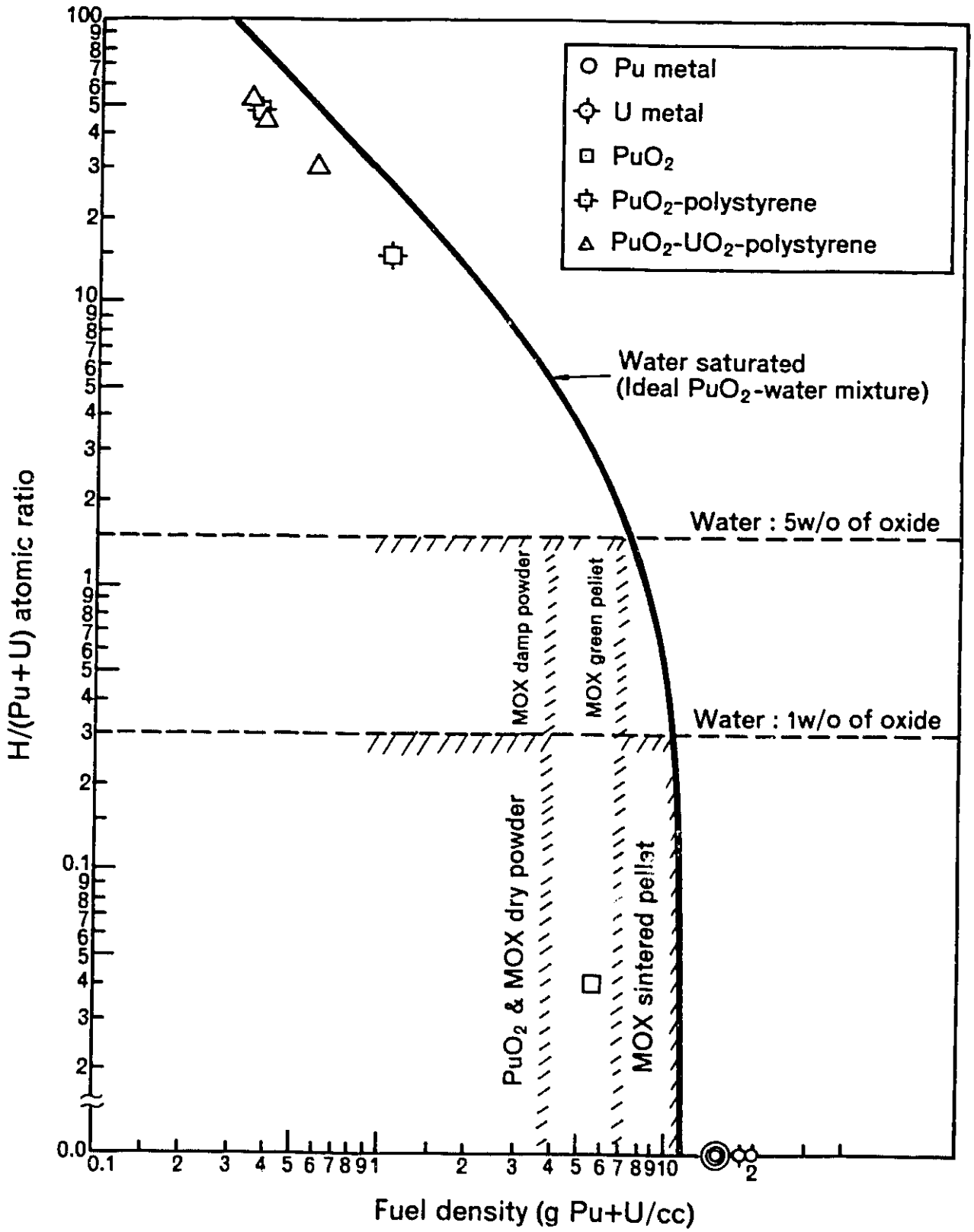

Fig. 2. Benchmark calculations compared with various forms of PuO_2 and mixed oxide in storage and fabrication processes.

compared with their atomic ratios of PuO_2 and mixed oxides in powder storage and pellet fabricatin processes. Validation of calculation is not sufficient in the range of unmoderated mixed oxide fuel with intermediate density for lack of critical experiment data.

3. Calculation Conditions

Critical core dimensions and reflector conditions are given in Table 4. Two types of core with maximum volume (slab) and minimum volume (near cubic) were selected for each composition of oxide fuel. The atomic number densities of oxide fuels, metal fuels and reflectors are shown in Table 5, 6 and 7 respectively.

4. Results of Calculation

The effective multiplication factors k_{eff} were calculated with the KENO code and are listed in Table 8. In the case of metal fuels with simple sphere geometry, addtional calculations with the ANISN code were performed for comparison and the results are also shown in Table 8.

The calculated k_{eff}'s of homogeneous oxide fuel cores are about 1 ~ 3 per cent larger than the measured values (= unity). Relatively large differences are observed between the calculated k_{eff}'s for the two cores with maximum and minimum critical volume in unmoderated PuO_2 core as shown in Fig. 3. There seems to remain some problem in the method for evaluating experimental correction. The calculated k_{eff} slightly depends on plutonium enrichment for the PuO_2-UO_2 systems, but there seems to be no significant dependence for the PuO_2-polystyrene systems.

Relatively excellent agreements are obtained on metal fuel cores, but k_{eff}'s calculated with the ANISN code are slightly larger than those with the KENO code.

5. Discussions

The calculated k_{eff}'s are illustrated in Fig. 4 as a function of fuel density together with the results of the previous report [1]. Relatively good agreements were obtained in the sphere geometry of plutonium metal and nitrate solution, but the calculated k_{eff}'s are scattered in other systems-oxide systems and French plutonium solution systems. Detailed reevaluation of fuel and structure composition and experimental conditions are required for more excellent agreement.

Table 4. List of critical core dimensions for benchmark calculations.

Case I.D.*	Composition of core fuel**	Core dimension (cm)			Core volume (l)	Reflector
		Length	Width	Height		
A-1S	$Pu(18)O_2$ [H/Pu=0.04]	25.65	25.65	10.03	6.60	Plexiglas (15 cmt)
" -1L		41.05	41.05	5.95	10.03	
A-2S	$Pu(8)O_2$-Polystyrene [H/Pu=15]	25.65	25.65	25.03	16.47	Plexiglas (15 cmt)
" -2L		51.31	68.25	10.36	87.65	
A-3S	$Pu(18)O_2$-Polystyrene [H/Pu=50]	40.72	30.54	29.64	36.86	Plexiglas (15 cmt)
" -3L		61.08	61.08	16.35	61.00	
A-4S	30.0 $Pu(8)O_2$-$U(0.15)O_2$-Polystyrene	30.54	30.54	30.89	28.81	Plexiglas (15 cmt)
" -4L		66.17	61.08	14.43	58.32	
A-5S	14.6 $Pu(8)O_2$-$U(0.15)O_2$-Polystyrene	30.54	40.72	29.81	37.07	Plexiglas (15 cmt)
" -5L		61.08	61.08	16.63	62.04	
A-6S	7.9 $Pu(8)O_2$-$U(0.15)O_2$-Polystyrene	40.72	40.64	36.42	60.27	Plexiglas (15 cmt)
" -6L		61.08	66.04	22.09	89.10	
		Radius of spherical core (cm)				
B-1	High purity Pu(5) metal (α-phase)	4.122			0.293	H_2O (>30 cmt)
B-2	Pu(4.8) metal, 1.10 w/o Ga	4.533			0.390	U(nat.) metal (19.609 cmt)
B-3	Pu(4.5) metal, 1.02 w/o Ga	6.385			1.090	(Bare)
B-4	Pu(20) metal, 1.01 w/o Ga	6.660			1.237	(Bare)
B-5	U(93.8) metal	8.732			2.789	(Bare)

* "S" denotes the smallest core, i.e. a near-cubic geometry, in the serial experiments.
"L" denotes the largest core, i.e. a thin slab geometry, in the serial experiments.

** The value in "( )" after Pu denotes the rough content of Pu^{240} in Pu, and the value in "( )" after U denotes the U^{235} enrichment in U.

Table 5. Atomic number densities of oxide fuels.

[atoms/b·cm]

Fuel composition	$Pu(18)O_2$	$Pu(8)O_2$ -Polystyrene	$Pu(18)O_2$ -Polystyrene	30.0 $Pu(8)O_2$ -$U(0.15)O_2$ -Polystyrene	14.6 $Pu(8)O_2$ -$U(0.15)O_2$ -Polystyrene	7.9 $Pu(8)O_2$ -$U(0.15)O_2$ -Polystyrene
H^1	5.511×10^{-4}	3.966×10^{-2}	4.575×10^{-2}	4.468×10^{-2}	4.489×10^{-2}	4.719×10^{-2}
C^{12}		3.966×10^{-2}	4.505×10^{-2}	4.537×10^{-2}	4.412×10^{-2}	4.540×10^{-2}
O^{16}	3.094×10^{-2}	5.288×10^{-3}	2.082×10^{-3}	1.974×10^{-3}	3.023×10^{-3}	1.830×10^{-3}
U^{235}	—	—	—	1.008×10^{-6}	1.904×10^{-6}	1.285×10^{-6}
U^{238}	—	—	—	6.604×10^{-4}	1.252×10^{-3}	8.376×10^{-4}
Pu^{238}	3.383×10^{-5}	2.644×10^{-7}	2.125×10^{-6}	0.0	0.0	0.0
Pu^{239}	1.092×10^{-2}	2.410×10^{-3}	6.952×10^{-4}	2.578×10^{-4}	1.954×10^{-4}	6.528×10^{-5}
Pu^{240}	2.654×10^{-3}	2.131×10^{-4}	1.689×10^{-4}	2.257×10^{-5}	1.702×10^{-5}	5.941×10^{-6}
Pu^{241}	7.269×10^{-4}	1.983×10^{-5}	3.952×10^{-5}	1.756×10^{-6}	1.211×10^{-6}	3.481×10^{-7}
Pu^{242}	1.632×10^{-4}	8.990×10^{-7}	1.045×10^{-5}	0.0	0.0	0.0
Am^{241}	0.0	0.0	7.345×10^{-6}	3.511×10^{-7}	4.036×10^{-7}	1.741×10^{-7}
Comments (Case I. D.)	(A-1)	(A-2)	(A-3)	(A-4)	(A-5)	(A-6)

Table 6. Atomic number densities of metal fuels.

[atoms/b•cm]

Fuel composition	Pu (5)	Pu(4.8)–1.10 w/o Ga	Pu(4.5)–1.02 w/o Ga	Pu(20)–1.01 w/o Ga	U (93.8)
Ga*)	0.0	1.476×10^{-3}	1.375×10^{-3}	1.372×10^{-3}	—
U^{234}	—	—	—	—	4.921×10^{-4}
U^{235}	—	—	—	—	4.506×10^{-2}
U^{238}	—	—	—	—	2.456×10^{-3}
Pu^{238}	0.0	0.0	0.0	0.0	—
Pu^{239}	4.699×10^{-2}	3.672×10^{-2}	3.705×10^{-2}	2.994×10^{-2}	—
Pu^{240}	2.575×10^{-3}	1.850×10^{-3}	1.751×10^{-3}	7.876×10^{-3}	—
Pu^{241}	1.492×10^{-4}	1.151×10^{-4}	1.168×10^{-4}	1.215×10^{-3}	—
Pu^{242}	9.944×10^{-6}	0.0	0.0	1.567×10^{-4}	—
Am^{141}	0.0	0.0	0.0	0.0	—
Comments (Case I.D.)	(B-1)	(B-2)	(B-3)	(B-4)	(B-5)

*) Impurity, (Gallium).

Table 7. Atomic number densities of reflectors.

Reflector composition	Plexiglas	H_2O	U (natural)
Density (g/cc)	(~1.2)	0.9982	19.00
Atomic density (at./b·cm)			
H^1	5.712×10^{-2}	6.674×10^{-2}	—
C^{12}	3.570×10^{-2}	—	—
O^{16}	1.428×10^{-2}	3.337×10^{-2}	—
U^{235}	—	—	3.457×10^{-4}
U^{238}	—	—	4.770×10^{-2}
Comments (Case I.D.)	(A-1~A-6)	(B-1)	(B-2)

Table 8. Results of benchmark calculations.

Case I.D.	Reflector	Composition of core fuel	Core volume (ℓ)	Calculated k_{eff}	Comments*
A-1S	Plexiglas	$Pu(18)O_2$ [H/Pu=0.04]	6.60	1.02830±0.00850	KENO, H=7800, T=10
-1L			10.03	1.00788±0.00962	" , H=7800, T=10
A-2S	Plexiglas	$Pu(8)O_2$-Polystyrene [H/Pu=15]	16.47	1.01019±0.00768	KENO, H=10800, T=10
-2L			87.65	1.01369±0.00935	" , H=8400, T=10
A-3S	Plexiglas	$Pu(18)O_2$-Polystyrene [H/Pu=50]	36.86	1.02667±0.00617	KENO, H=13200, T=10
-3L			61.00	1.01746±0.00748	" , H=12600, T=10
A-4S	Plexiglas	30.0 $Pu(8)O_2$-$U(0.15)O_2$-Polystyrene	28.81	1.00928±0.00787	KENO, H=10200, T=10
-4L			58.32	1.00150±0.00822	" , H=10500, T=10
A-5S	Plexiglas	14.6 $Pu(8)O_2$-$U(0.15)O_2$-Polystyrene	37.07	1.01634±0.00901	KENO, H=10800, T=10
-5L			62.04	1.01465±0.00815	" , H=11700, T=10
A-6S	Plexiglas	7.9 $Pu(8)O_2$-$U(0.15)O_2$-Polystyrene	60.27	1.03198±0.00898	KENO, H=9600, T=10
-6L			89.10	1.02878±0.00612	" , H=10500, T=10
B-1	H_2O	High purity Pu(5) metal	0.293	1.00353±0.00855	KENO, H=12000, T=10
				1.00644	ANISN, T*=81 sec
B-2	U(nat.) metal	Pu(4.8) metal, 1.10 w/o Ga	0.390	0.99999±0.00394	KENO, H=50700, T=10
				1.00121	ANISN, T*=80 sec
B-3	Bare	Pu(4.5) metal, 1.02 w/o Ga	1.090	1.00395±0.00188	KENO, H=264600, T=5
				1.00602	ANISN, T*=13 sec
B-4	Bare	Pu(20) metal, 1.01 w/o Ga	1.237	1.00783±0.00194	KENO, H=255300, T=5
				1.00979	ANISN, T*=13 sec
B-5	Bare	U(93.8) metal	2.789	1.00235±0.00186	KENO, H=201300, T=5
				1.00336	ANISN, T*=14.7 sec

* H : Number of neutron histories, T : Calculation time by CDC 6600 (min.).

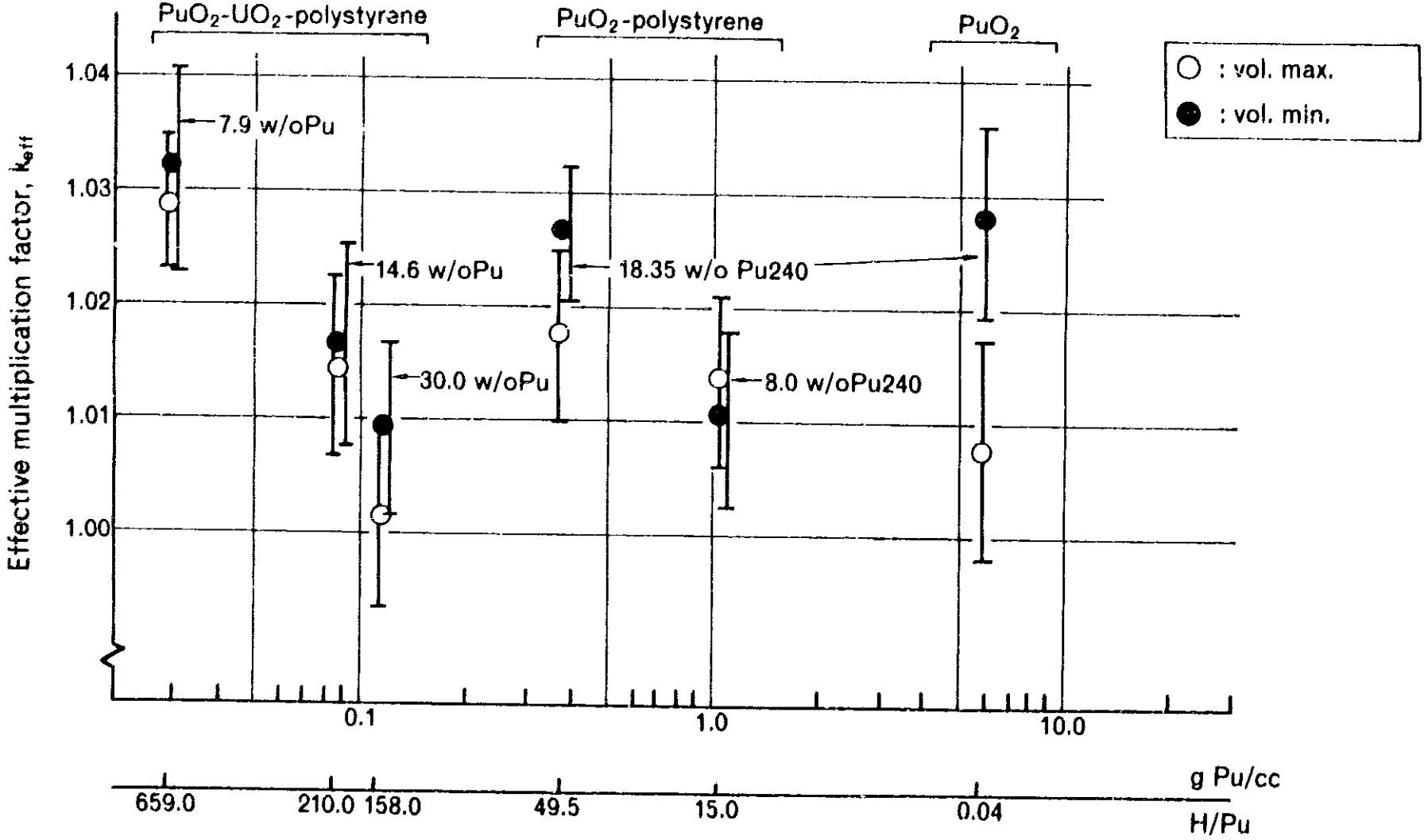

Fig. 3. Calculated k_{eff} on PuO_2 and PuO_2-UO_2 fuel systems.

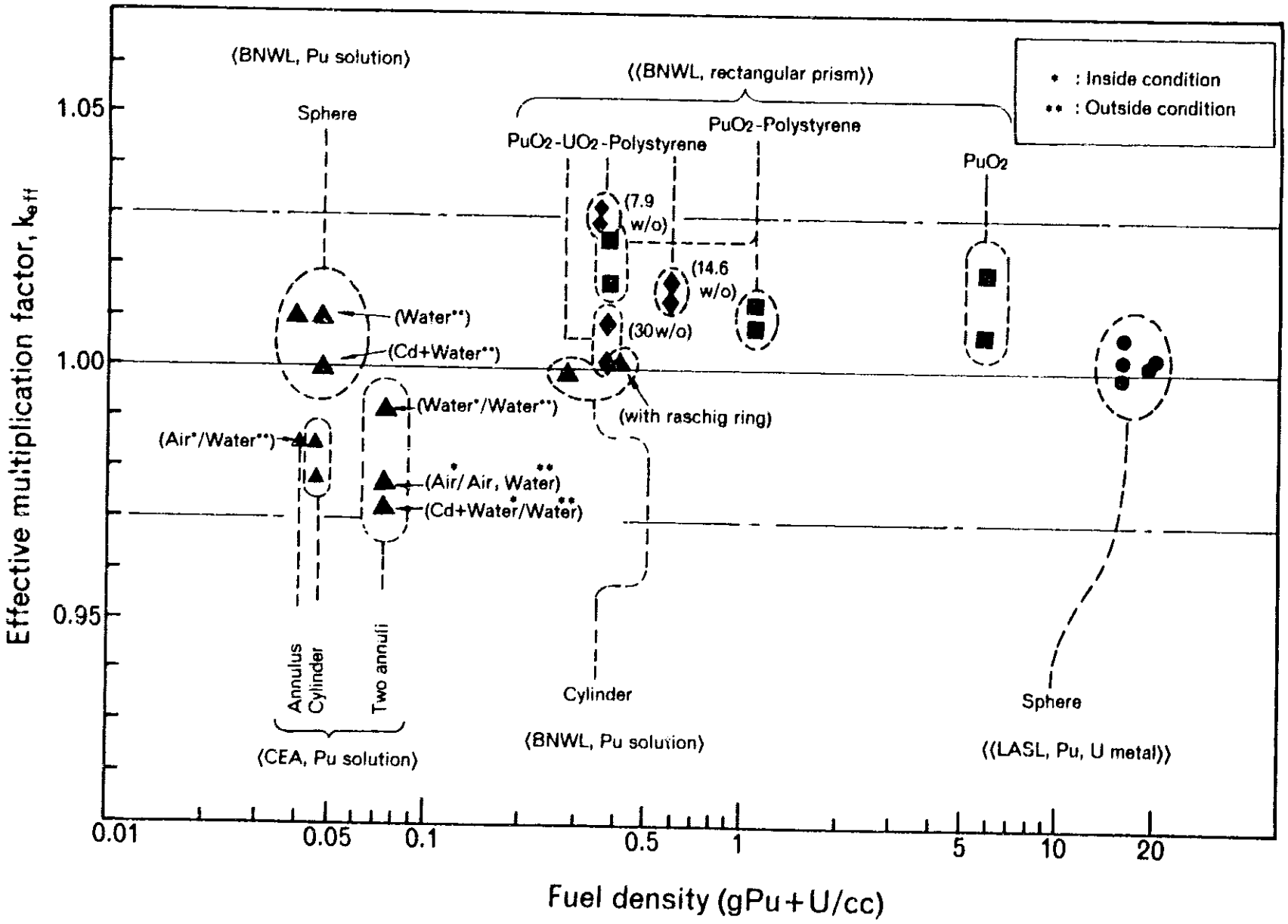

Fig. 4. Calculated k_{eff} on various Pu fuels with KENO, ANISN and H.R. cross-section set.

The calculated k_{eff} on oxide fuel cores was compared with those calculated with other methods performed in Canada, U.K. and U.S.A. as shown in Table 9. Bias of each method has similar magnitude except for the results of U.K. calculation.

6. Conclusions

The criticality calculation system composed of KENO, ANISN and Hansen-Roach cross-section set was found to be valid for calculating the criticality on plutonium oxide, plutonium-uranium mixed oxide, plutonium metal and uranium metal fuel systems as well as on plutonium solution systems with various geometries, absorbers and neutron interactions.

More refined experiments and benchmark calculations are considered desirable for application to the systems with complicated fuel compositions and core geometries.

Table 9. Comparison of calculated K_{eff} on the critical oxide fuel.

Case I.D.	Composition of fuel	This work (PNC)	Canada (CRNL)	U.K.*)	U.S.A. (BNWL)	U.S.A. (BNWL)
A-1S	$Pu(18)O_2$ [H/Pu=0.04]	1.028±0.009		0.993±0.018		
-1L		1.008±0.010				
A-2S	$Pu(8)O_2$-Polystyrene [H/Pu=15]	1.010±0.008		1.030±0.013		
-2L		1.014±0.009				
A-3S	$Pu(18)O_2$-Polystyrene [H/Pu=50]	1.027±0.006		1.040±0.012		
-3L		1.017±0.007				
A-4S	30.0 $Pu(8)O_2$-$U(0.15)O_2$-Polystyrene	1.009±0.008	1.024±0.006	1.064±0.012	1.011±0.008	1.021±0.008
-4L		1.002±0.008	1.006±0.007		1.022±0.007	
A-5S	14.6 $Pu(8)O_2$-$U(0.15)O_2$-Polystyrene	1.017±0.009	1.027±0.006	1.061±0.013	1.007±0.008	1.033±0.008
-5L		1.015±0.008	1.015±0.006		1.008±0.008	
A-6S	7.9 $Pu(8)O_2$-$U(0.15)O_2$-Polystyrene	1.032±0.009	1.004±0.005	1.036±0.012	1.032±0.007	1.027±0.007
-6L		1.029±0.006	1.033±0.006		1.029±0.007	1.034±0.008
Calculation method	Code	KENO-II	KENO-I	MONK	KENO-I	KENO-I
	Cross section	Hansen-Roach (16 groups)	Hansen-Roach (16 groups)	U.K. data	from GAMTEC-II (18 groups)	from ENDF/B-II (18 groups)
Reference No.		(This report)	(13)	(14)	(9)	(9)

*) Actual arrangement of fuel compacts for these calculations are not apparent.

References

(1) Matsumoto, T. , et al. : "Validation of KENO-II, ANISN and Hansen-Roach Cross-Section Set on Plutonium Solution Systems", PNCT 831-79-02, P42-52, (1979).

(2) Whitesides, G. E. , Cross, N. F. : "KENO-a Multigroup Monte Carlo Criticlity Program", CTC-5.

(3) Petrie, L. M. , Cross N. F. : "KENO-IV, An Improved Monte Carlo Criticality Program", ORNL-4938 (Nov. 1975).

(4) Soltesz, R. G. , Disney, R. K. : "ANISN-W, Nuclear Rocket Shielding Methods, Modification, Updating and Input Data Preparation Vol. 4", WANL-PR-(LL)-034.

(5) Hansen, G. E. , Roach, W. H. : "Six and Sixteen Group Cross Sections for Fast and Intermediate Critical Assemblies", LAMS-2543.

(6) Bierman, R. S. , Clayton, E. D. : "Critical Experiments with Unmoderated Plutonium Oxide", Nucl. Tech. , 11, 185-190 (June 1971).

(7) Richey, C. R. , et al. : "Criticality of Homogeneous Plutonium Oxide-Plastic Compacts at H Pu=15", Nucl. Sci. Eng. , 23, 150-158 (1965).

(8) Bierman, S. R. , Clayton, E. D. , : "Critical Experiments with Homogeneous PuO-Polystyrene at 50 H/Pu", Nucl. Tech. , 15, 5-15 (July 1972).

(9) Bierman, S. R. , et al : "Critical Experiments with Homogeneous Mixtures of Plutonium and Uranium Oxides Containing 8, 15 and 30 wt% Plutonium", Nucl. Sci. Eng. , 50, 115-126 (1973).

(10) Bierman, S. R. : "Critical Experiments-Benchmarks (Pu-U Systems)", Nucl. Tech. , 26, 352-381 (July 1975).

(11) Smith, D. R. , Geer, W. U. : "Critical Mass of a Water-Reflected Plutonium Sphere", Nucl. Appl. Tech. , 7, 405-408 (Nov. 1969).

(12) Hansen, G. E. , Paxton, H. C. : "Reevaluated Critical Specifications of Some Los Alamos Fast-Neutron Systems", LA-4208 (Sept. 1969).

(13) Keller, N. A. : "Calculation of Fourteen Pu-U Critical Experiment Benchmarks using KENO and Su-HAMMER" AECL-5539 (July 1976).

(14) Clayton, E. D. , et al. : "Basis for Subcritical Limits in Proposed Criticality Safety Standards for Mixed Oxides", Nucl. Tech. , 35, 97-111 (Mid-Aug. 1977).

Experiment and Analysis on Reactivity Decrease due to ^{241}Pu Decay in Light-Water Moderated PuO_2-UO_2 Lattices*

Hideyoshi SASAJIMA, Tadakuni MATSUMOTO,
Ryozo YUMOTO, Harumichi TSURUTA+
and other members of Pu-thermal critical experiments group**

1. Introduction

The decay of ^{241}Pu with a half-life of 14.89 years results in a corresponding accumulation of ^{241}Am. Both thermal capture cross sections of ^{241}Pu and ^{241}Am are of the same orders in magnitude, but the thermal fission cross section of ^{241}Pu is about 300 times larger than that of ^{241}Am. The reactivity by plutonium contained in the lattice, therefore, will be reduced with decrease of ^{241}Pu.

A series of critical experiments have been carried out to obtain the data for reactivity variations of light-water moderated PuO_2-UO_2 lattices in the Tank-type Critical Assembly (TCA) at JAERI. Variations in reactivity of uniform lattices were traced over a period of seven years ranging from June 1972 to May 1979.

The present paper describes the critical experiments and calculational analysis on the reactivity decrease due to decay of ^{241}Pu.

---

* This is a joint research program between PNC and JAERI. Presented at the Fall Meeting of the Atomic Energy Society of Japan (Oct., 1979).

** I. Kobayashi+, T. Suzaki+, A. Ohno+, K. Murakami+.

\+ JAERI

2. Experiments

Critical experiments were performed for four kinds of lattices, using fuel rods containing 3.0 w/o PuO_2-UO_2 oxide which were fabricated by PNC. The volume ratios of water to fuel in the lattices range from 2.42 to 5.55, such as 2.42, 2.98, 4.24 and 5.55. Table 1 shows a specification of the PUO_2-UO_2 fuel rod. The fuel rods were designed on reference to current BWR rods, but were not longer than those of BWR.

The lattices were assembled to form a rectangle or a square in a horizontal cross-sectional view. Figure 1 shows horizontal and vertical cross-sectional views.

The critical size of each lattice was determined by measuring the moderator water level at its criticality. The reactivity of the lattice with an effective fuel length of 70.6cm was derived from both critical water level and water-level worth at the water temperature of 20°C.

Table 1. Fuel specification and atomic number density.

Fuel specification		Atomic number density on May 16, 1972($\times 10^{24}$ at./cm^3)	
Fuel		Fuel	
Enrichment, w/o	3.01 ± 0.05	^{235}U	9.4018×10^{-5}
Isotope ratio, w/o		^{238}U	1.2963×10^{-2}
Uranium	Natural	^{238}Pu	1.9928×10^{-6}
Plutonium (71/8/19*)		^{239}Pu	2.7539×10^{-4}
^{238}Pu	0.494	^{240}Pu	8.8585×10^{-5}
^{239}Pu	68.18	^{241}Pu	2.8099×10^{-5}
^{240}Pu	22.02	^{242}Pu	8.1251×10^{-6}
^{241}Pu	7.26	^{237}Np	3.5502×10^{-9}
^{242}Pu	2.04	^{241}Am	1.2357×10^{-6}
Americium (71/8/16*)		0	2.7864×10^{-2}
^{241}Am	530 ppm in PuO_2	Cladding #	
Pellet		Zircaloy-2	3.840×10^{-2}
Fabrication method	Mechanically blended and pre-sintered	Moderator	
		H_2O	3.338×10^{-2}
Diameter, mm	10.65		
Density, g/cm^3	6.056±0.076		
Stack length, mm	706 ± 3		
Cladding			
Material	Zircaloy-2		
Inner dia., mm	10.83±0.06		
Thickness, mm	0.7±0.07		

*) Date of assaying

#) Including air gap region

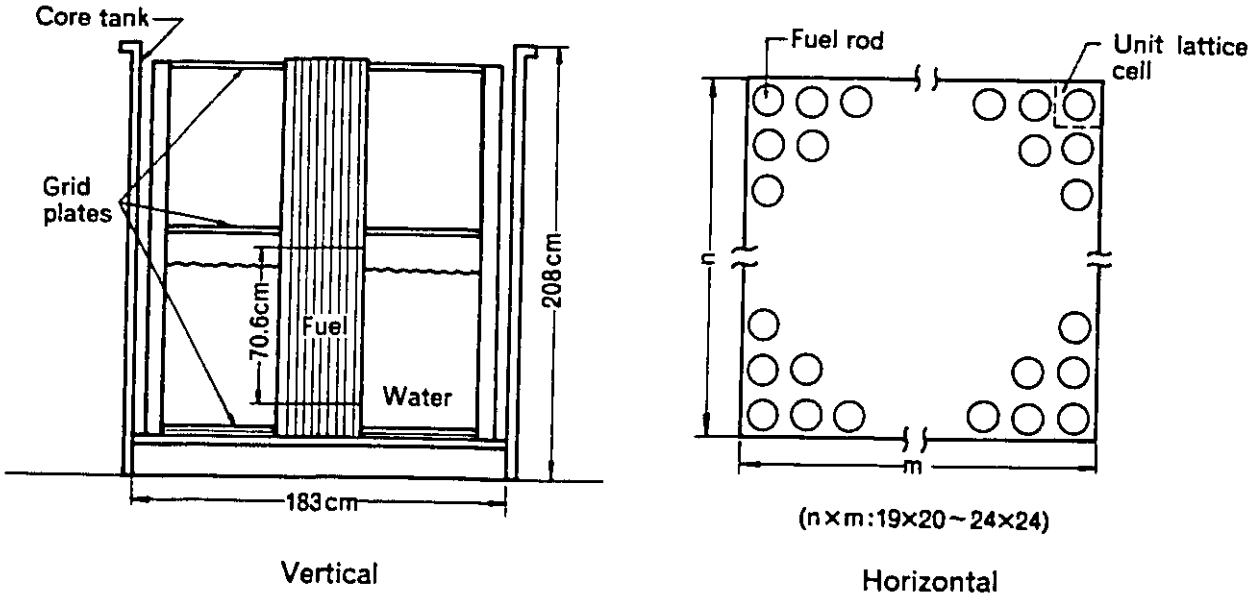

Fig. 1. Vertical and horizontal cross-sectional views of lattice.

3. Calculations

The block diagram of calculational scheme is shown in Fig.2. Neutron spectrum and three-group microscopic constants were calculated with the code GTB-2[1]. This code originates from the GAM-II code for fast neutrons and the THERMOS code for thermal neutrons. The cross section library of GTB-2 was formed with the GGC-4 library. The thermal energy cut-off is assumed to be 1.86eV in this calculation.

Burnup calculations during zero-power operation were performed for calculating the variation of effective multiplication factor (k_{eff}) due to decay of ^{241}Pu, using a two-dimensional diffusion code, CITATION[2] and three-group microscopic constants. Two kinds of decay chains, as shown in Fig. 3, were taken into consideration for the burnup calculation. Table 2 gives the conditions adopted for calculation of k_{eff} for each lattice. Vertical bucklings were obtained from effective water levels and vertical reflector savings[3]. The reactivity conversion from unit in $\Delta k/k$ to unit in dollar was calculated by using the value β_{eff}[3] obtained from perturbation calculation with four-group constants.

Table 2. Calculation condition.

Water-to-fuel volume ratio (V.R.)	Lattice pitch (cm)	n × m*	Vertical buckling(cm^{-2})	H/Pu atom ratio
2.42	1.825	22 × 22	1.4903×10^{-3}	402
2.98	1.956	21 × 21	1.8274×10^{-3}	494
4.25	2.224	20 × 20	1.8746×10^{-3}	703
5.55	2.474	21 × 21	1.7922×10^{-3}	921

* Fuel rod array, refer to Fig. 1.

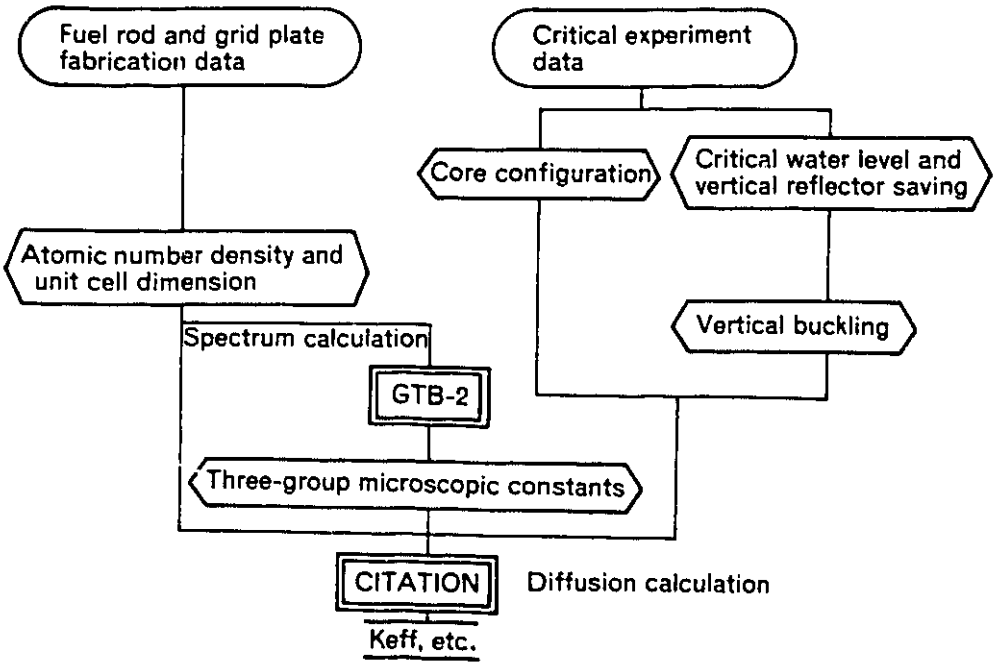

Fig. 2. Claculational scheme.

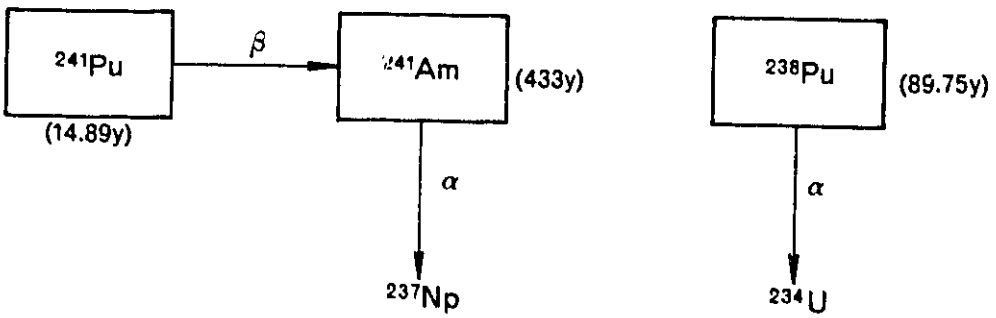

Fig. 3. Decay chains.

4. Results of experiments and calculations

Figures 4 to 7 show the experimental results of reactivity decrease of various lattices. The solid line in the figures was determined by the least square fittings of the measured values to an exponential form

$$\rho(t) = C \cdot (1-e^{-\lambda t}) \quad \cdots\cdots\cdots\cdots \quad (1)$$

where C : constant

λ : decaly constant of ^{241}Pu

t : elapsed time from standard date.

The experimental error shown in the figures was derived from the water-level worth, but it can be disregarded in about 2,000 days. Table 3 shows the calculational results and Figure 8 the variations of k_{eff}'s for each lattice.

The experimental and calculational results show that the decreasing rate of reactivity against time is about 1.0 $/year at the begining of the experiment for the lattice with a water-to-fuel volume ratio of 2.98, and the value reduces to about 0.5 $/year after 3,000 days. The decreasing rate depends on the water-to-fuel volume ratio and becomes larger with increase of the volume ratio. The calculated values indicate the smaller dependence than the measured.

Figure 9 shows a comparison of reactivity decrease between experiments and calculations. In general, the calculation for decrease of reactivity is in relatively good agreement with the experiment. But for the smaller values of the water-to-fuel volume ratio, the calculation overestimates the decreasing rate of reactivity by 10% after 3,000 days.

Table 3. Calculated K_{eff} and reactivity variation.

Volume ratio	β_{eff}	Elapsed time, years	0	1	3	5	7
2.42	0.003635		0.993765 0.0 0 0	0.990262 −0.003537 −0.9730	0.983711 −0.010220 −2.812	0.977731 −0.016399 −4.511	0.972275 - 0.022103 −6.081
2.98	0.003597	k_{eff} $\Delta\rho_A$ (Δk/k) $\Delta\rho_B$ ($)	0.996314 0.0 0.0	0.992849 −0.003490 −0.9703	0.986373 −0.010078 −2.802	0.980463 −0.016167 −4.495	0.975072 −0.021785 −6.056
4.24	0.003526	k_{eff} $\Delta\rho_A$ (Δk/k) $\Delta\rho_B$ ($)	0.998065 0.0 0.0	0.994617 −0.003467 −0.9833	0.988172 −0.010011 −2.839	0.982284 −0.016066 −4.556	0.976908 −0.021657 −6.142
5.55	0.003453	k_{eff} $\Delta\rho_A$ (Δk/k) $\Delta\rho_B$ ($)	0.996957 0.0 0.0	0.993490 −0.003490 −1.011	0.987007 −0.010081 −2.919	0.981083 −0.016180 −4.686	0.975674 −0.021814 −6.317

Note ; $\Delta\rho_A = \frac{k_{eff}(i) - k_{eff}(0)}{k_{eff}(i)}$.

$\Delta\rho_B = \Delta\rho_A / \beta_{eff}$.

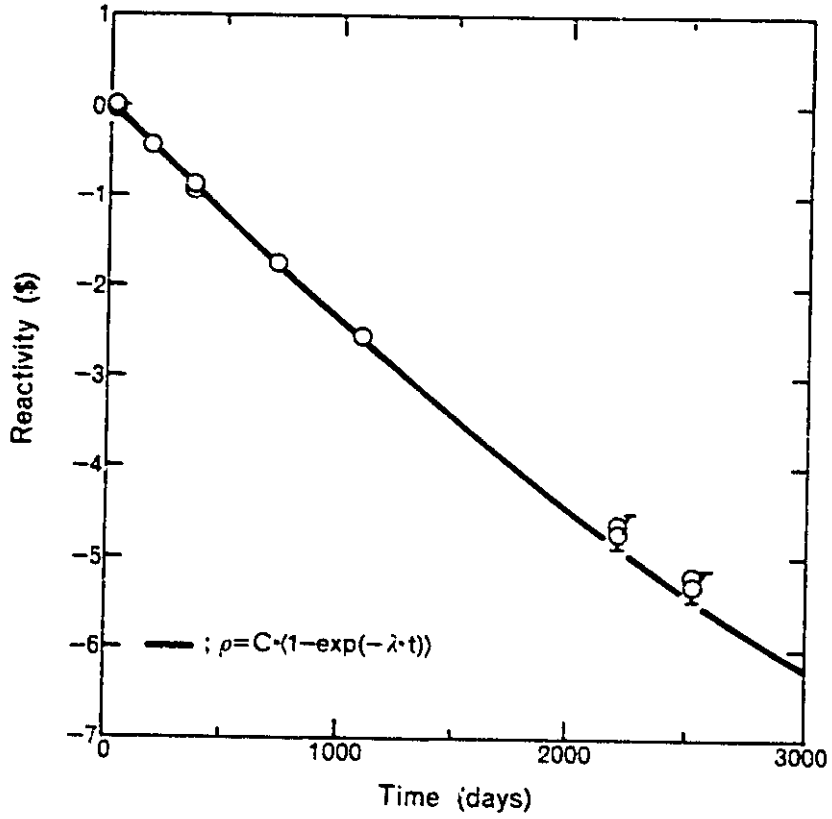

Fig. 4. Decrease in reactivity of lattice with a volume ratio of 2.42.

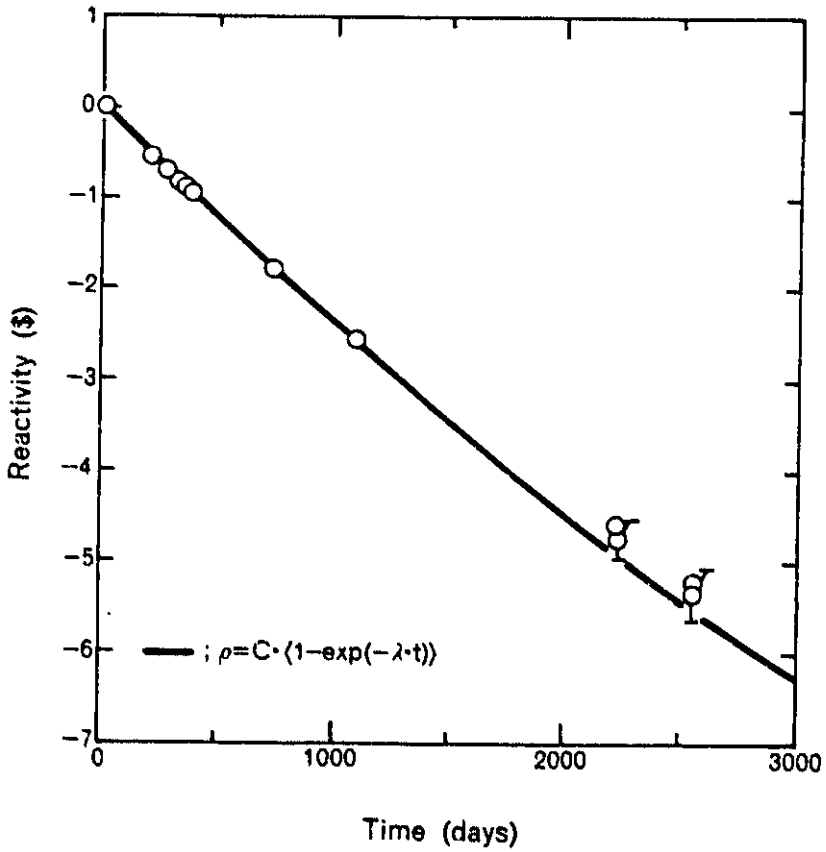

Fig. 5. Decrease in reactivity of lattice with a volume ratio of 2.98.

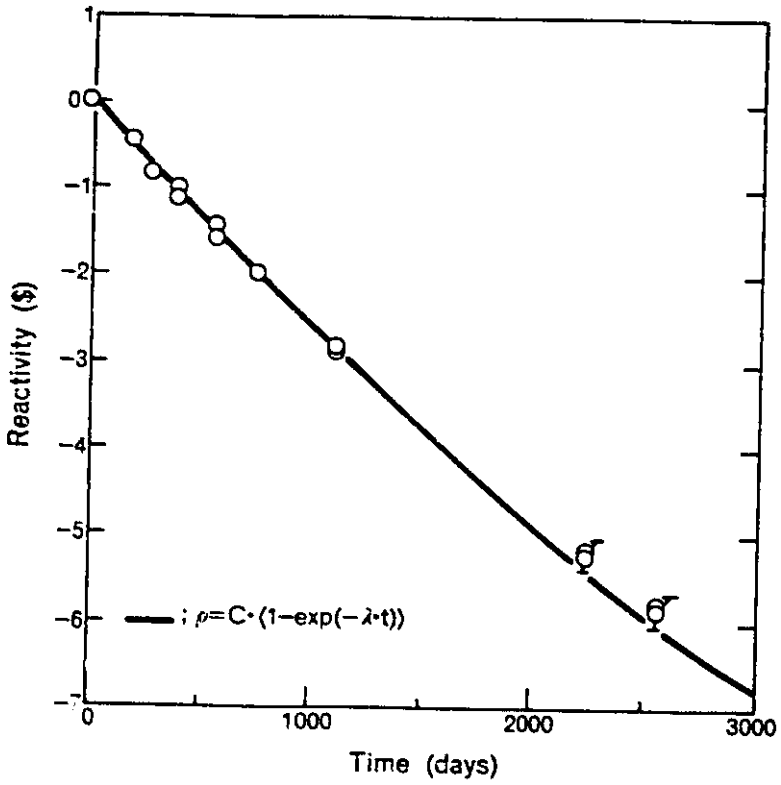

Fig. 6. Decrease in reactivity of lattice with a volume ratio of 4.24.

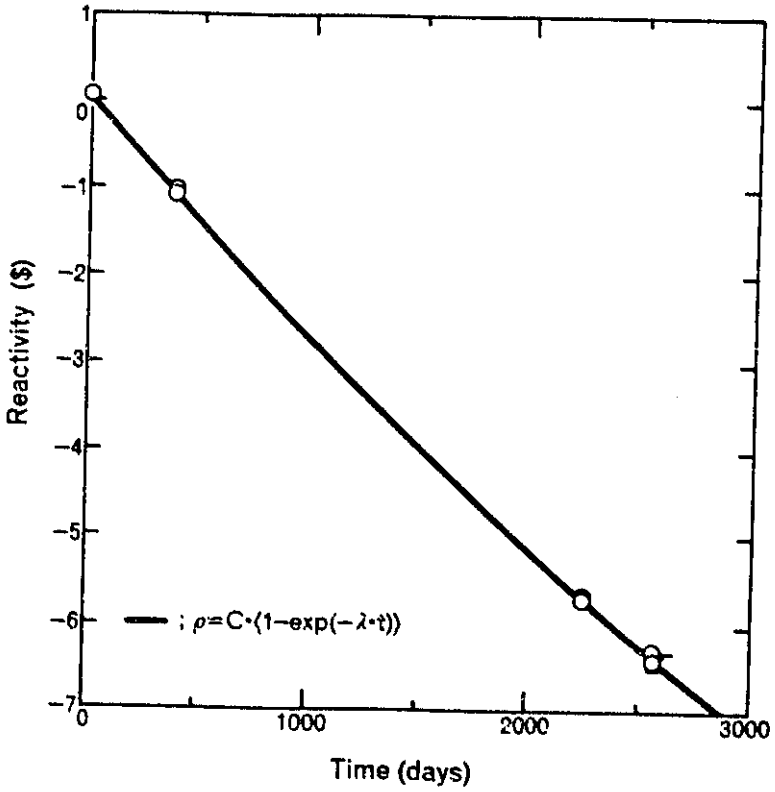

Fig. 7. Decrease in reactivity of lattice with a volume ratio of 5.55.

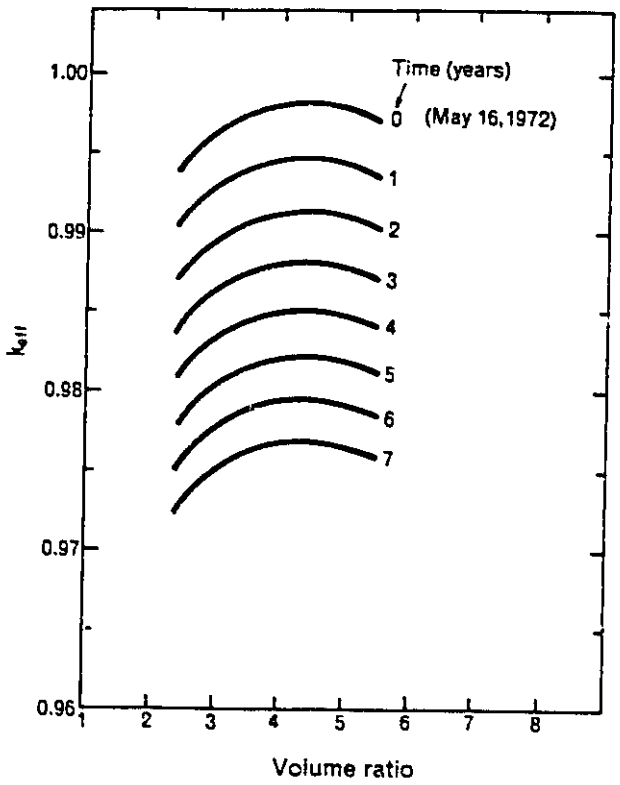

Fig. 8. Variation of k_{eff} with lapse of time.

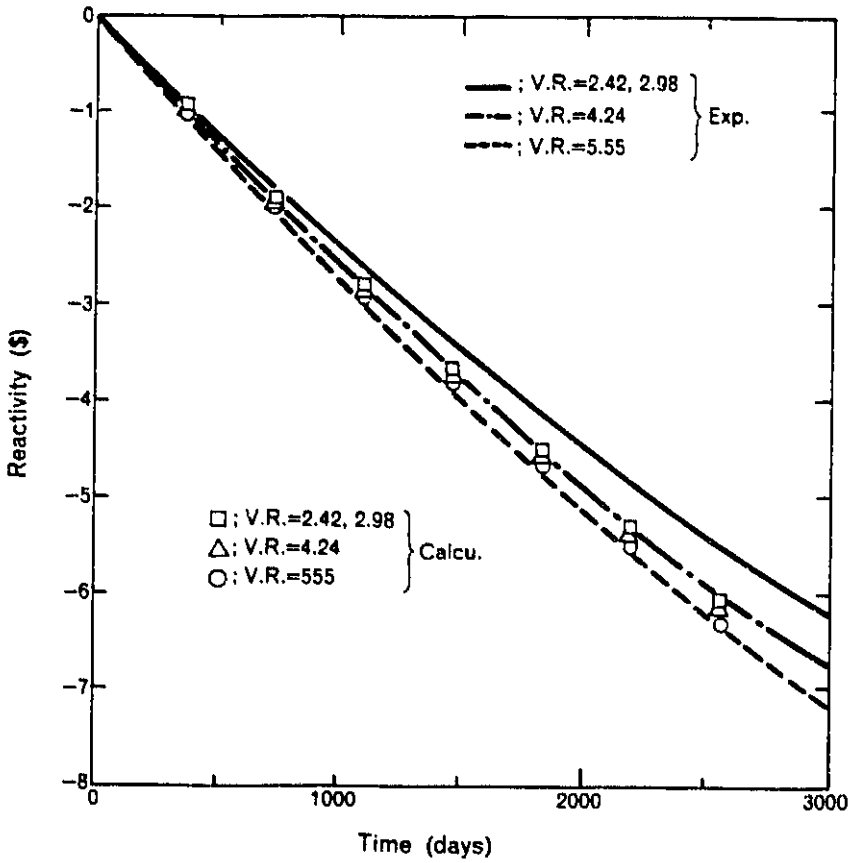

Fig. 9 Comparison between calculated and measured reactivity variations.

The value V.R. indicates the volume ratio of water to fuel.

5. Discussion

Table 4 gives the variations of calculated $\Delta k/k$ and $\Delta \eta f/\eta f$ in the thermal group against time. The comparison between $\Delta k/k$ and $\Delta \eta f/\eta f$ indicates that the reactivity decrease depends almost on the decrease of ηf. Both loss of ^{241}Pu by decay and buildup of ^{241}Am have influence to the variation of ηf. Figure 10 shows an example for the effect of ^{241}Am absorption cross sectin on the variation of ηf. The contribution of the thermal neutron absorption of ^{241}Am to the variatin of ηf amounts to about 50% and depends on the volume ratio of water to fuel as shown in Fig. 11.

Table 4. Comparison between calculated $\Delta K/K$ and $\Delta \eta f/\eta f$.

Volume ratio	Elapsed time, years	0	1	3	5	7
2.42	$\Delta k/k$	0.0	−0.003537	−0.010220	−0.016399	−0.022103
	$\Delta \eta f/\eta f$	0.0	−0.003427	−0.009887	−0.015863	−0.021377
2.98	$\Delta k/k$	0.0	−0.003490	−0.010078	−0.016167	−0.021785
	$\Delta \eta f/\eta f$	0.0	−0.003379	−0.009763	−0.015656	−0.021099
4.24	$\Delta k/k$	0.0	−0.003467	−0.010011	−0.016066	−0.021657
	$\Delta \eta f/\eta f$	0.0	−0.003370	−0.009734	−0.015621	−0.021058
5.55	$\Delta k/k$	0.0	−0.003490	−0.010081	−0.016180	−0.021814
	$\Delta \eta f/\eta f$	0.0	−0.003407	−0.009851	−0.015811	−0.021316

Note ; ηf is $\nu\Sigma f/\Sigma a$ in thermal group.

Thermal cut off energy is 1.86 eV.

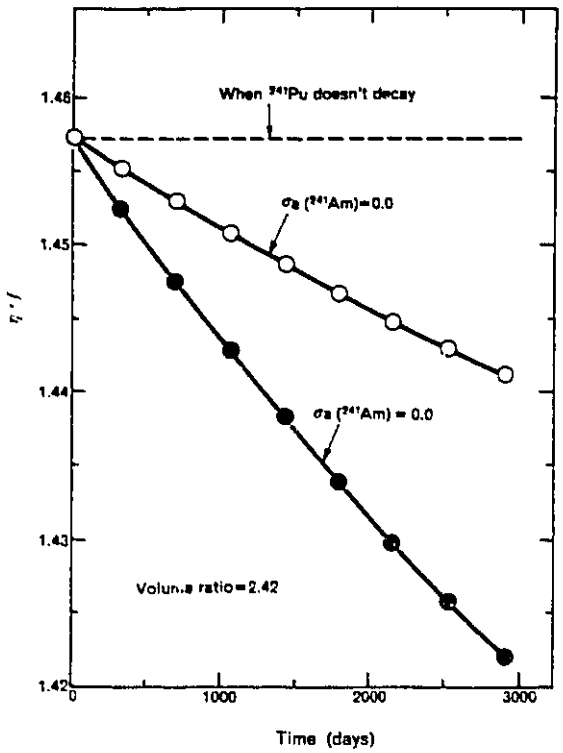

Fig. 10. Effect of ^{241}Am absorption cross section on variation of η f.

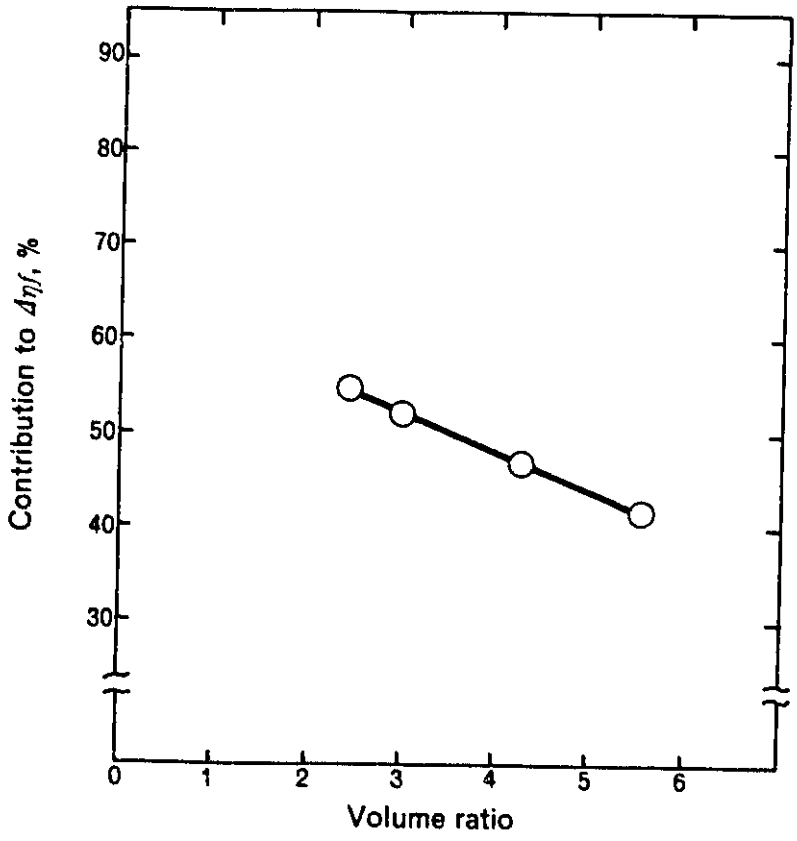

Fig. 11. Contribution of ^{241}Am to variation of η f.

6. Conclusions

The results of the study are summarized as follows:

1) The reactivity of the lattice decreases with loss of ^{241}Pu by natural decay and buildup of ^{241}Am.
2) The calculated values for decrease of reactivity are in relatively good agreement with the measured.
3) The results of experiments and calculations show that the decreasing rate of reactivity against time is about 1.0 $/year at the begining of the experiment for the lattice with a water-to-fuel volume ratio of 2.98 and the value reduces to about 0.5 $/year after 3,000 days.
4) The decreasing rate depends on the volume ratio of water to fuel and becomes larger with increase of the volume ratio. The calculated values indicate the smaller dependence than the measured.
5) At the water-to-fuel volume ratio of 2.42 and 2.98, the calculation overestimates the decreasing rate of reactivity by 10% after 3,000 days.
6) The reactivity decrease depends almost on the variation of ηf in the thermal group, and the contribution of the thermal neutron absorption of ^{241}Am to the variation of ηf amounts to about 50% and depends on the volume ratio of water to fuel.

References

(1) Yumoto, R. & Matsumoti, T. : "A One-Dimensional Neutron Spectrum Burnup Calculation Code, GTB-2, for PuO_2-UO_2 Light Water Lattices," SN841-78-12 (1978).
(2) Fowler, T. B. , et al. : Nuclear Reactor Core Analysis Code : CITATION, ORNL-TM-2496, Rev. 2 (1971).
(3) Tsuruta, H. , et al. : Critical Sizes of Light-Water Moderated UO_2 and PuO_2-UO_2 Lattices, JAERI-1254 (1978).

In-Situ Dismantling of Plutonium-Contaminated Glove Box*

Koji NUMATA, Hisashi WATANABE,
Hisashi ISHIKAWA, Hiroaki MIYO
and Katsuyuki OHTSUKA

1. Introduction

A plutonium-contaminated glove box was dismantled along with the development of treatment techniques for plutonium-bearing waste. The objectives of this in-situ dismantling of glove box were:

- To make more efficient reuse of the Plutonium Fuel Fabrication Facility
- To reduce the volume of waste generated during box dismantling
- To acquire dismantling techniques for decommissioning of Plutonium Fuel Fabrication Facility in the future.

Up to date, several glove boxes have been dismantled in the Plutonium Fuel Facility of the Tokai Works, and they could be contained into the package for storage without being dismantled in-situ due to their small size. But recently it is becoming more necessitated to dismantle a large glove box in-situ for enclosing into a container and reducing the waste volume.

2. Glove Box Dismantling in-situ

2.1 Dismantling Procedures

Figure 1 shows a flow-sheet of procedures for dismantling a glove box in-situ. Prior to the dismantling works, a greenhouse for decontamination is installed for

---

* Presented at the Annual Meeting of the Atomic Energy Society of Japan (March, 1979).

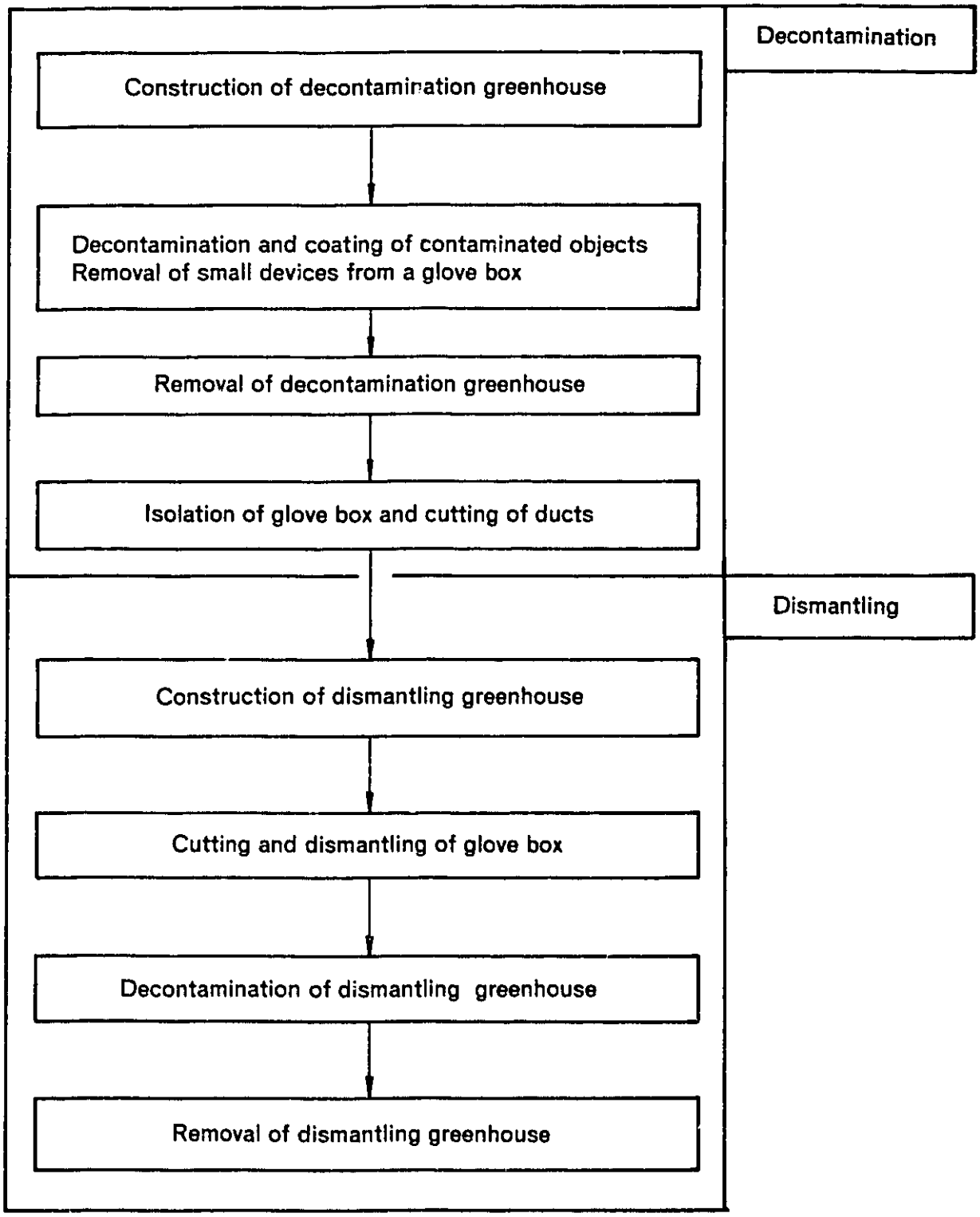

Fig. 1. Flow-sheet for dismantling in-situ.

prevent from plutonium contamination in the case of glove failure, during the work. Small devices provided in the glove are removed to ease decontamination work.

Then, decontamination with surfactants is performed to lower the surface activity detected by the smear method below 4.5×10^{-4} μ Ci/100cm^2. Unremovable contamination is coated with paint before removal of the greenhouse. Air-supply/exhaust ducts and other pipes are cut off to isolate the glove box from the surrounding equipment.

After removing the decontamination greenhouse, another greenhouse for dismantling is assembled again to contain the box as shown in Fig. 2. This greenhouse is ventilated over10 times per hour under the negative pressure of 5 to 10 mmH_2O.

The greenhouse No.1 is a large area for dismantling work, and No.2, No.3 and No.4 are areas for contamination control.

For the works, each area can admit:

4 main workers in Greenhouse No. 1,

1 assistant worker in Greenhouse No. 2,

1 assistant worker in Greenhouse No. 3,

1 assistant worker in Greenhouse No. 4,

and several workers are watching and waiting outside the greenhouse.

In the greenhouse, the main workers wearing protective devices are engaged in cutting of devices inside the glove box into smaller pieces, using electric nibbler, electric diskgrinder and other tools. Sectioned glove box materials are packed into a waste container through a PVC tunnel installed at the greenhouse. The main workers are permitted to work inside the greenhouse for 4-5 hours a day.

2.2 Protective Devices and Cutting Tools

The protective devices used in the dismantling greenhouse are shown in Table 1.

In the greenhouse, a main worker wears an anorak type PVC suit over an air-line mask. The assistant worker in Greenhouse No.2 wears a Howell-type pressurized suit as well as PVC pants, and the assistant worker in No.3 and No.4 wears a respiratore.

Figure 3 shows the outline of the air-line suit. The suit is made of specially processed PVC fabrics. Air is supplied from head, arms and legs, and exhausted from the back.

Table 2 shows the tools used for the dismantling. When a plasma cutter is used, fire retardment sheets are laid over PVC sheets for prevention of fire due to spark generation. A notable disadvantage of plasma cutting is that the generated heat

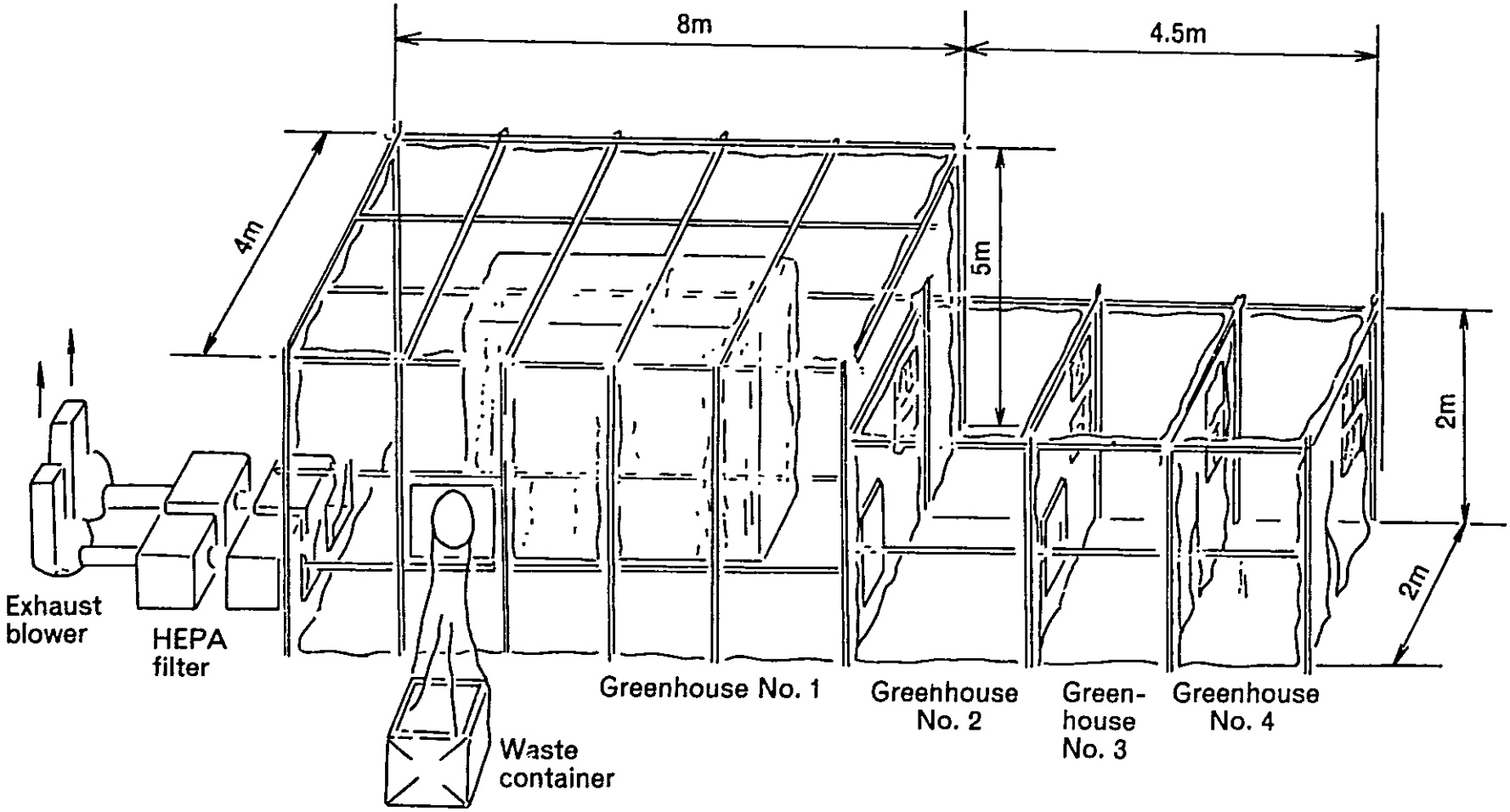

Fig. 2. Outline of dismantling greenhouses.

makes the worker so sweaty as to interrupt his working. A plasma cutter is not suitable for continuous operation for a long period. An electric nibbler secures safety of worker without spark and heat generation even in cutting twice as fast as plasma cutting. An electric diskgrinder is not suitable for cutting glove box of stainless steel, since a blade wears off very fast, for example, at each 0.5m cutting of 4mm stainless steel. An electric diskgrinder generating no sparks is more useful for cutting corners of glove box and supports of inner devices as compared with a plasma cutter. An electric circular-saw or a jigsaw is suitable for cutting acrylic resin sheets of the glove box.

2.3 Comparison of Dismantling Procedures

The results of dismantling in-situ were compared with two previous cases of dismantling carried out by different procedures.

In Table 3, the term "whole removal" means that a used glove box is accomodated into a waste container without in-situ dismantling after removing tools and box decontamination. The volume of waste generated in the case of whole removal was 4.1 - 4.6m^3 per cubic meter of glove box, slightly depending on whether the glove box is made of PVC or stainless steel.

In the case of dismantling, the volume of waste was 1.6 - 1.8 m^3 per cubic meter of glove box. It was evident that the glove box can be removed with less waste by in-situe dismantling.

Table 1. Protective devices provided in each area.

Work areas / Types of devices	Greenhouse No.1	Greenhouse No.2	Greenhouse No.3	Greenhouse No.4
Air-line mask	Coverall Anorak PVC suit	Pressured suit Coverall PVC pants	Respirator Coverall	Respirator Coverall
Air-line suit	Suit cover (double) Coverall	Air-line suit Suit cover (single) Coverall	Respirator Coverall	Respirator Coverall

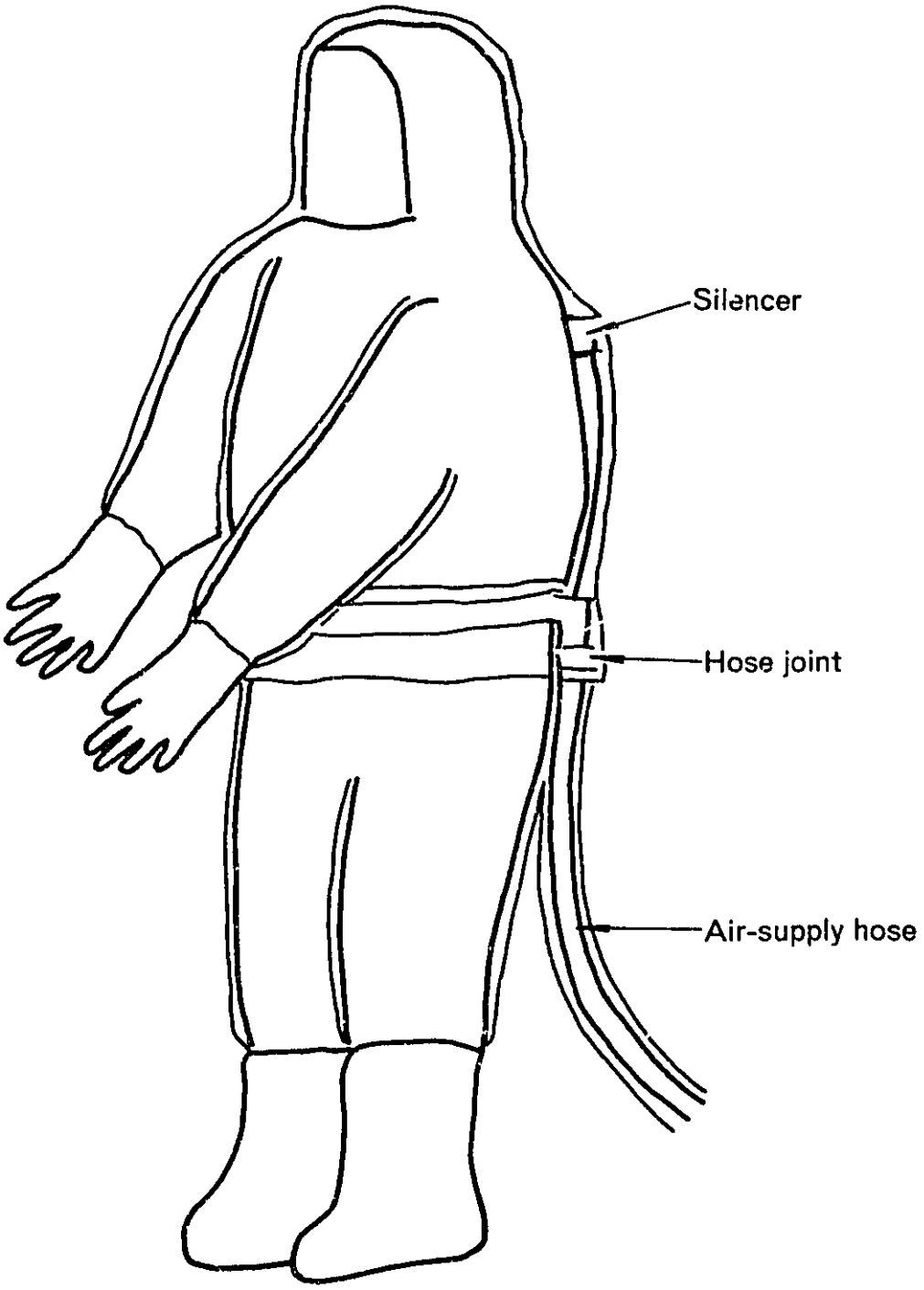

Fig. 3. Worker wearing air-line suit.

Table 2. Comparison of cutting tools.

Item / Types of tools	Objective	Cutting speed (m/min)	Note
Plasma cutter	SUS-304 4mm thick	1.0	Sparks generated Receivers Problem in safety
Electric nibbler	SUS-304 4mm thick	2.0	No thermal problem Slight overweight for handling
Electric diskgrinder	Angles, etc. U-shaped/T-shaped 4mm thick	—	Some sparks generated but no effect on greenhouse
Electric circularsaw	Acrylic resin sheet sheet 4mm thick	0.5	Scattering of chips
Electric jigsaw	〃	0.5	〃

Table 3. Comparison of waste volume reduction rate.

No.	Material	Glove boxes capacity (m^3)	Removal procedure	Volume of radioactive waste (m^3)	Volume ratio of waste to glove box
1	PVC	4.0	Whole removal removal	18.5	4.6
2	SUS	10.0	〃	40.9	4.1
3	SUS	4.0	In-situ dismantling	7.4	1.8
4	SUS	88.6	〃	146.7	1.6

3. Conclulsion

In-situ dismantling of used glove boxes were successfully conducted without any trouble. Almost half of the waste generated by dismantling was composed of combustible materials such as rag and paper, and noncombustible materials such as PVC suit-cover. Considerable reduction of waste volume could be realized by in-situ dismantling works with protective devices under high contamination level. Based on the experiences of these dismantling works, further improvement will be also realized on dismantling devices and protective devices in the greenhouses.

Acid Digestion of Chlorine-Containing Wastes (II)
Engineering Tests of the Pilot Plant*

Kazutoshi MIYATA, Hitoshi MIYAZAKI
Ryukiti MIZUNO and Katsuyuki OHTSUKA

1. Introduction

Approximately 40% of the alpha-contaminated solid wastes generated at the Plutonium Fuel Fabrication Facility of PNC contains organic chlorides-mainly PVC sheets and chloroprene rubber gloves.

At PNC, acid digestion has been developed to reduce the volume of alpha-contaminated wastes, while converting the waste into a stable nonreactive residue.

For a nonradioactive chlorine-containing waste, basic studies on acid digestion have already been conducted with digesters of 2 ℓ and 20 ℓ. Based on the results from the basic studies, a nonradioactive pilot plant equipped with a 200 ℓ digester was designed and constructed to confirm the performance in a scaled-up process and the engineering problems.

2. Pilot Plant of Nonradioactive Acid Digestion

A process diagram of the pilot plant of nonradioactive acid digestion is shown as Fig. 1.

(1) Feedstock storage vessels

The nonradioactive chlorine-containing wastes used for the experiments are reserved for a while in the feedstock vessels and fed to the digester in quantity as required. The sulfuric acid is stored in a proper storage vessel made of SUS-316, but other chemicals such as nitric acid, hydrogen peroxide and sodium hydroxide are stored in each shipping vessel connected with the system by feed pipes.

* Presented at the Fall Meeting of the Atomic Energy Society of Japan (October, 1979).

(2) Waste crushing and feeding unit

To promote contact with sulfuric acid, wastes are supplied to the digester after crushed. The crusher has rotary blades and the sizes of crushed pieces varies with the screen. The feeding is made by vibration as well as piston motion, continuously or batch-wise as required.

(3) Digester

Polyvinyl-chloride and chloroprene gloves are dechlorinated and oxidized with sulfuric and nitric acids. The digester has a volume of 200 ℓ and the agitator are glass-lined. It is also equipped with a Messonde P [R] sensor for detecting a glass-lining failure and an electric heater. The operation of the digester is usually made under a negative pressure of -100mm aq.

(4) Off-gas treatment module

Three gases of HCl, SOx and NOx generated from the system are recovered as HCl, H_2SO_4 and NHO_3 respectively.

i) Separation of hydrochloric acid

The treatment system is provided with glass-lined absorption columns, tanks and pipes. After heated gases are cooled, HCl and NOx are separately absorbed into water.

ii) Recovery of sulfuric and nitric acids

The gases of SO_2 and NO in the exhaust gas are oxidized and recovered as H_2SO_4 and HNO_3 respectively. This unit are made of SUS-316, including pipes.

(5) Separation of residue

The residue in the digester is removed and distilled after operation. The residue after distillation contain inorganic materials from chloroprene gloves, which is vitrified for storage.

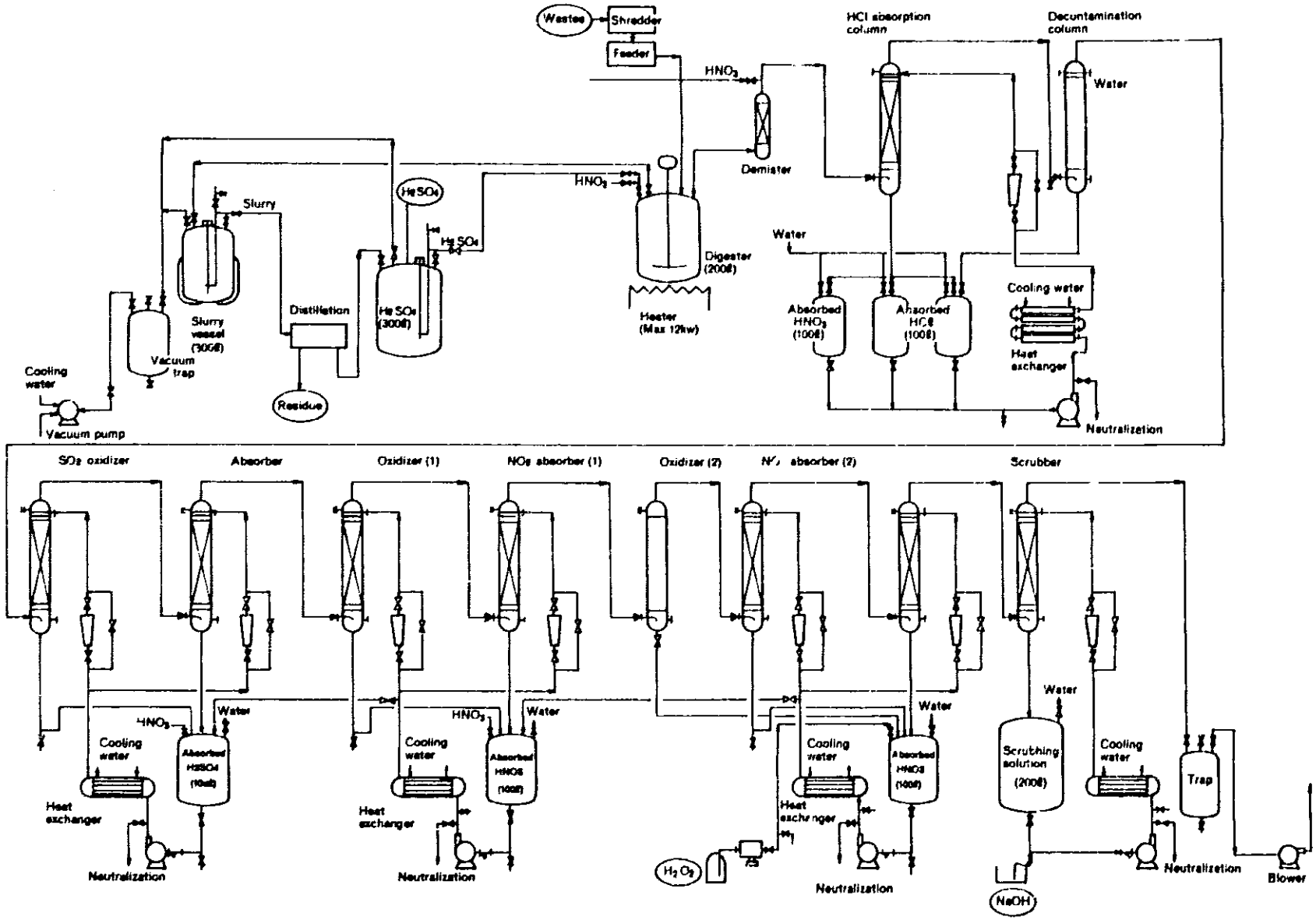

Fig. 1. Acid Digestion Pilot Plant.

3. Experiments

The objectives of the experiments with the pilot plant of acid digestion were to confirm reproducibility of the results obtained from basic studies and to verify safety of the processes.

The primary chemical reactions involved in the acid digestion process can be represented by the four formulas;

$$1/p(C_mH_nCl)_p + (n-1/2)H_2SO_4 \longrightarrow HCl + (n-1)H_2O + (b-1/2)SO_2 + mC \quad (1)$$

$$C + 2H_2SO_4 \longrightarrow 2H_2O + 2SO_2 + CO_2 \quad (2)$$

$$3C + 4HNO_3 \longrightarrow 4NO + 2H_2O + 3CO_2 \quad (3)$$

$$5C + 4HNO_3 \longrightarrow 2N_2 + 2H_2O + 5CO_2 \quad (4)$$

The basic processes are based on decomposition with sulfuric acid in Eq. (1) and oxidation with nitric acid in Eq. (3). These processes have been adopted to preliminarily separate hydrochloric acid, but they cannot separate and recover nitric acid for re-use. Another reason for the adoption is to prevent formation of nitrosylchloride which may be generated in the presence of hydrogen chloride and nitric oxide. It is also expected that nitration can be prevented by the preliminary carbonization reaction by sulfuric acid.

The process of acid digestion for chlorine - containing waste is shown in Fig. 2. Figure 3 shows a comparison between the rates in 200 ℓ and 20 ℓ digesters for oxidation of PVC with nitric acid.

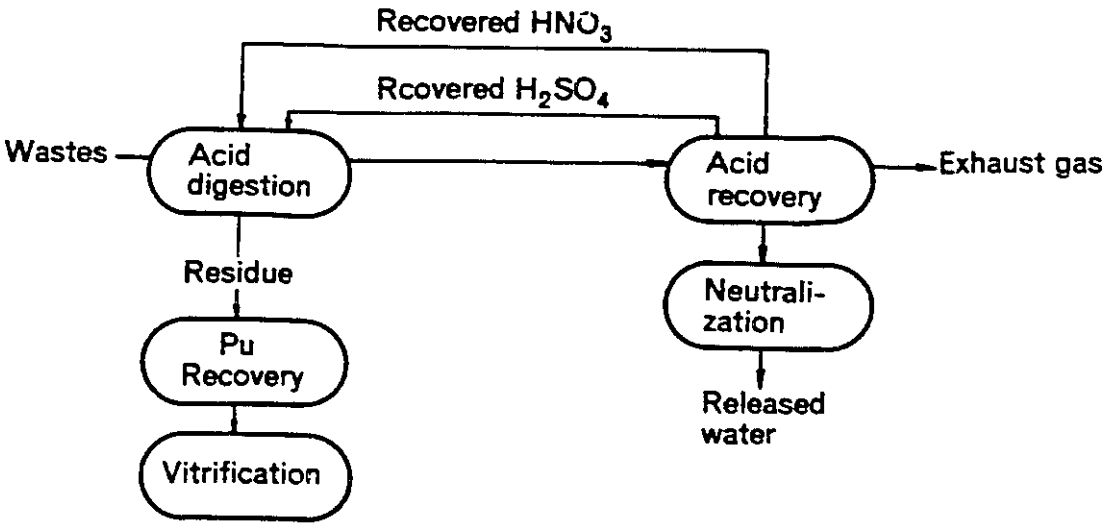

Fig. 2. Process flow sheet for acid digestion.

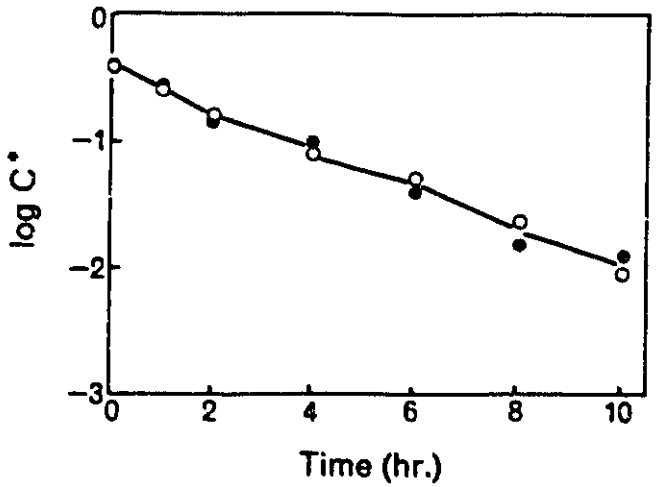

	PVC	H_2SO_4	HNO_3	Test unit
•	10kg	80 ℓ	150mol/hr	200 ℓ
○	1kg	8 ℓ	15mol/hr	20 ℓ

*: C ; the initial total organic carbon concentration

Fig. 3. HNO_3 oxidation rate.

The constants of the oxidation rates are the same value, k=-0.3/hr both for 200 and 20 ℓ l scales as shown in Fig. 3. It indicates that the scale of the acid digestion plant has little influence on the oxidation rate.

A correlation between the initial total organic carbon (TOC) concentration and the oxidation rate of PVC is shown in Fig.4. Both oxidation rates are nearly the same value, k=0.7/hr. No effects on the oxidation rate were observed in the range of the concentration.

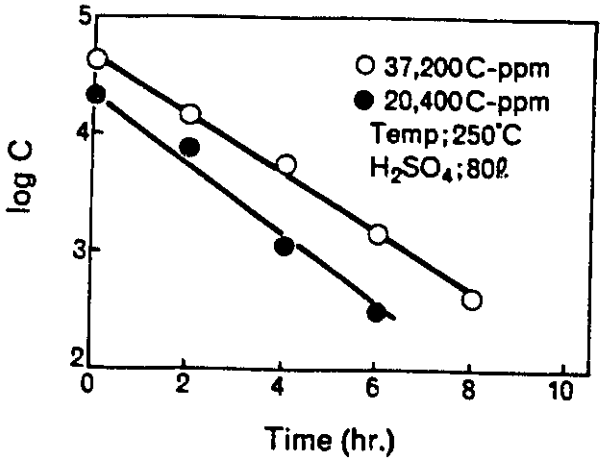

Fig. 4. Effects of temperature on HNO_3 oxidation of PVC.

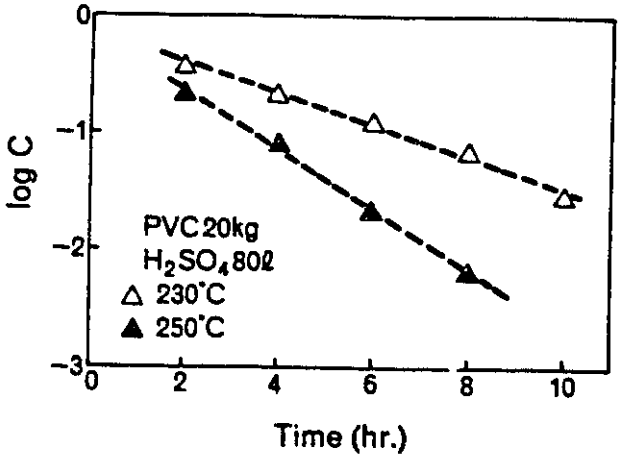

Fig. 5. Effects of temperature on HNO_3 oxidation of PVC.

Effects of temperature on the oxidation with nitric acid is shown in Fig. 5. The comparison between the oxidation rates at 230°C and 250°C reveals that the oxidation at 250°C becomes faster than that at 230°C by 2 to 4 hours. This well coincides with the results in the basic studies carried out by using 20 digester. Table I gives typical conditions of experiments carried out in the pilot plant.

The samples tested are PVC commonly available. As the rate of feeding, we used a value of 4kg/hr obtained from testings at variable rates of 4kg/hr to 8kg/hr.

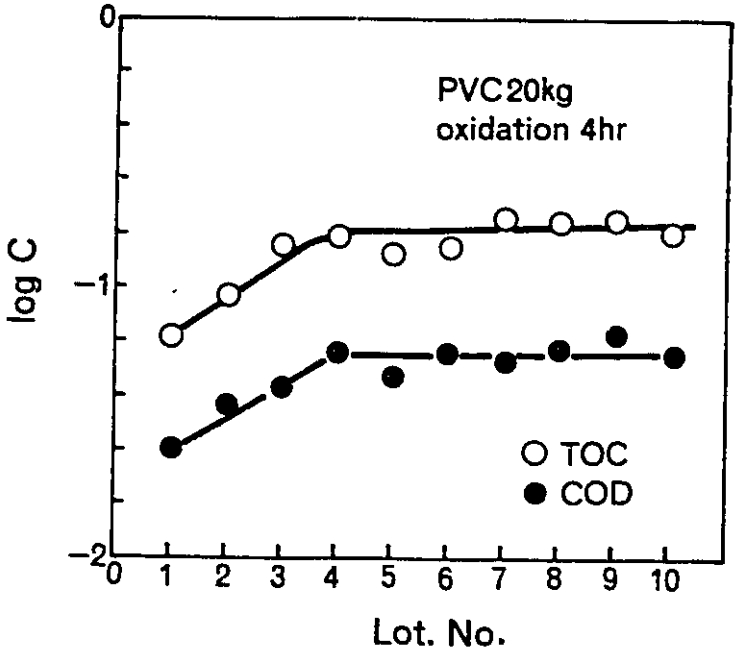

Fig. 6. Accumulation of organic materials in the digester.

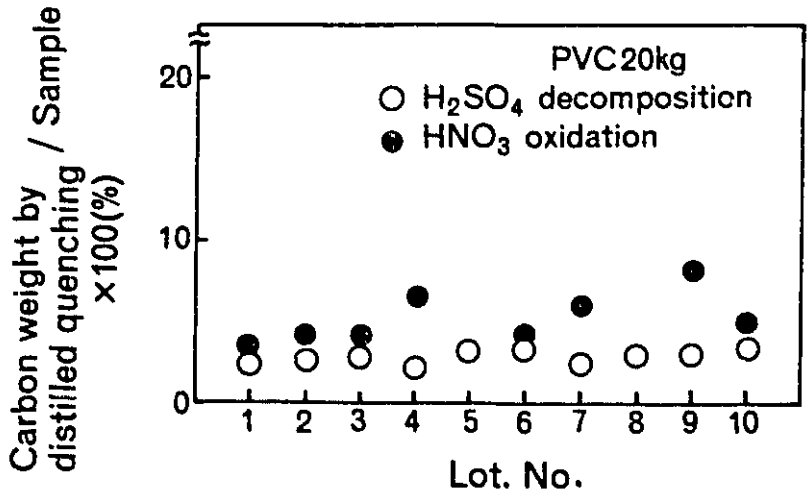

Fig. 7. Distilled organic materials transferred from the digester to the off-gas treatment module.

Figure 8 shows a chart of gas chromatography which results from the liquid absorbed during PVC digestion. The analysis reveals that the liquid contains acetic acid, phthalic acid and lower fatty acids including propionic aicd, butyric acid and stearic acid. This fact may prove that aliphatic acids are formed as by-products of the PVC acid digestion reactions.

Table 1. Typical experimental conditions.

	H_2SO_4 decomposition	HNO_3 oxidation
Samples	PVC sheets	
Feed rate	4 kg PVC/hr	
Reaction time	5 hours	
Digested volume	230 ~250°C	250 °C
H_2SO_4 volume	80 lit.	
HNO_3 volume	—	1000 mols

Figure 6 shows the accumulation of organic materials in the digester after repeated reactions of acid digestion. In the experiments, the nitric acid oxidation time was fixed at 4 hrs. It was confirmed that accumulation of organic materials reaches the equilibrium after 3-4 times of repeated digestions as shown in Fig. 6. The quantity of the residual organic materials was estimated to be 14.4% of the total sample weight in terms of carbon, i.e. 1,289 gr-C.

Figure 7 shows distilled organic materials transferred from the digester to the off-gas treatment module as a function of the lot number. Repeated application of acid digestion reaction does not very increase the quantity of distilled organic materials. The proportions of organic materials sublimated were evaluated to be 2-3% for sulfuric acid decomposition and 4-5% for nitric acid oxidation.

The quantity of nitro compounds, which may directly be concerned explosion reaction, was found to be negligibly small from the results of UV absorption study.

The compositions of gases decomposed from the acid digestion reaction are shown in Table 2. From these facts we can conclude that risk of gas explosion is very small during PVC acid digestion.

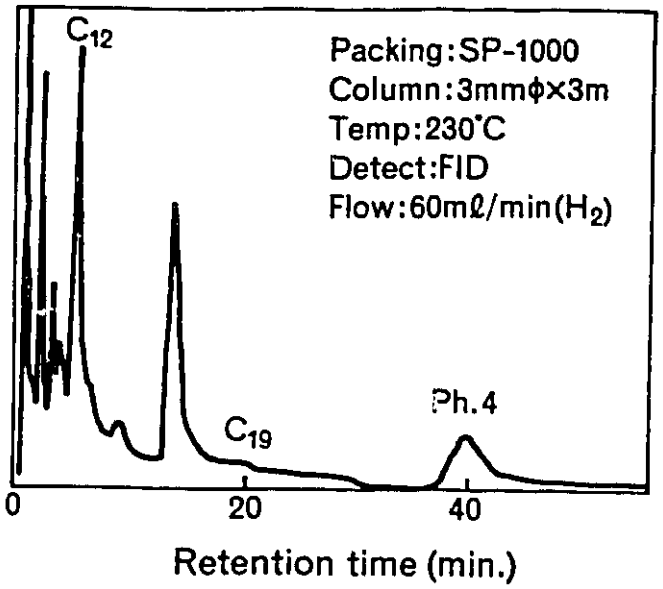

Fig. 8. Chromatogram of gas generated by liquid decomposition with acid.

Table 2. Compositions of exhaust gas from PVC acid digestion at 250°C*).

	Time	O_2	N_2	NO	CO	N_2O	CO_2	SO_2	Cracking gas
H_2SO_4 Decomposition	0 (hr)	14.1	74.6	0.0	0.83	2.0	7.5	0.0	0.0
	1	3.56	23.9	0.0	4.17	3.33	16.51	48.3	0.0
	2	3.05	20.15	0.1	3.3	1.09	15.90	55.86	0.0
	3	1.8	18.83	0.1	4.14	0.27	14.59	48.81	0.0
	4	3.1	20.64	0.0	3.7	0.19	14.90	52.79	0.0
	5	1.08	11.08	0.63	4.53	0.18	25.7	48.93	0.0
HNO_3 Oxidation	0	5.79	43.21	6.67	0.86	4.92	20.98	22.51	0.0
	1	0.17	9.9	21.96	9.75	1.29	43.34	13.9	0.0
	2	0.25	10.89	12.25	7.36	6.55	64.44	0.0	0.0
	3	0.2	11.74	13.55	3.91	2.51	61.08	0.0	0.0
	4	0.32	13.05	15.55	3.01	2.93	54.68	0.0	0.0

*) Off-gas from quenching column.

4. Conclusion

From about one-year experiments in the pilot plant, many useful results were obtained for the nitric acid oxidatin processes. The next purpose of the experiment is to evaluate the reaction rate of sulfuric acid decompoisition which has an important influence to the capacity of the equipment.

Technical Services Division

Activity of Technical Services Division (Jan. 1979—Mar. 1980)

The Technical Services Division consists of Technical Information Service, Developmental Research Laboratory, Waste Treatment Technology Laboratory, Fuel and Material Inspection Section, Fuel and Material Assessment Section, and Chemical Analysis Section, including the Chemical Processing Facility under construction. This division extends technical assistance to each project of PNC.

Each section of the Technical Service Division has displayed the following activities and achievements during the period from January 1979 to March 1980.

1. Developmental Research Laboratory

Development of technologies and design of the pilot plant for FBR fuel reprocessing have been advanced for the purpose of reprocessing spent fuels from the reactors, "Joyo" and "Monju".

The Chemical Processing Facility (CPF) has been under construction for performing basic hot tests of reprocessing using irradiated fuels from the Joyo. The construction has proceeded on schedule and the building will be completed in August, 1980. Construction of the Engineering Demonstration Facility (EDF) was also started for full pilot-scale tests of reprocessing by using unirradiated uranium and radioactive isotopes, and the building is expected to be completed this summer.

Design and technical development for the pilot plant are outlined as follows.

1.1 Design of the Pilot Plant

A preliminary design of the pilot plant was completed in June 1979. After a careful review of the design basis and philosophy in the preliminary design, a conceptual design of the pilot plant with a capacity of 120kg HM/day has been started on the basis of a revised design guide under actual conditions.

1.2 R & D

Programmes for research and development of the Purex Process are now in progress, since this process has been chosen for a pilot plant, but some improvements are required for application of technologies to commercial FBR fuel reprocessing.

The items of R & D programms are indicated below.

(1) Head end process
- Disassembling and chopping machines
- Sodium deactivation system
- Volume reduction system of hulls and hardwares
- Dissolver system
- Voloxidation system (Voloxidation and off-gas treatment)

(2) Main separation process
- Feed clarifier system (centrifugal type)
- Pulse column extractor
- Rapid contactor (centrifugal type)
- Solvent regeneration system (vacuum distillation method)

(3) Reducing techniques for radioactive materials release
- Off-gas treatment system (IODOX method)
- Iodine behaviour test
- Tritium removal system (Distillation method)

(4) Common Process technologies
- Remote maintenance technology (construction of mock-up cell and components)
- Material test for redissolver
- Transfer equipment (air-lift method)

2. Waste Treatment Technology Laboratory

The present status of development of HLLW solidification process is as follows.

1) Study of glass melting

A Joule-heated ceramic melter constructed in 1977 was operated successfully

from May 15th, 1979 to December 20th, 1979, and about 13.5 tons of simulated waste glass was melted and flowed out. At present, molten glass has been completely drained out and tests have been conducted for evaluation of life time of the melter components.

2) Engineering-scale testing of the process

The cold engineering facility has been installed with the equipment necessary for the main process. This process by means of simulated wastes is composed of denitration, concentration, slurry transportation, glass melting, flowing-out of molten glass, canister handling, seal welding, leak testing of weld, decontamination and off-gas treatment. Two types of Joule-heated ceramic melters have been installed in this facility. The initial test working of this facility was started in February, 1980. The melters will be operated at intervals under low temperatures condition.

3) Evaluation of the glass

In a long term testing, the simulated waste glass was heated at high temperatures (450°C-650°C) for 114 days and some studies were made on the physical and phase changes of the glass. Another long term leaching test (50-200 days) is now continued to find out the mechanism of leaching.

4) Target of next year's R & D

Operation test of the facility will be continued for evaluation of the process equipment. Development of remote maintenance of the process equipment will also be performed for installation of the equipment in the hot cell. A conceptual design will be started for construction of a pilot plant.

3. Fuel and Material Assessment Section

The section has performed extensive series of tests on the fuel cladding tubes for the reactors, JOYO MK-II, FUGEN, and MONJU. They included creep test, mechanical property test, burst test and metallographic examination, and contributed to the safety evaluation of fuel designs.

Especially various tests have been conducted on the test fuels for MONJU, and quality of the MONJU's fuel subassemblies was examined by exposure to water and sodium flows. The effects of hydriding of the FUGEN's pressure tube on its

brittleness was also studied. The acoustic emission technique were examined as means of monitoring brittle rupture of pressure tube and detecting crack initiation of cladding tube in the stress corrosion cracking test for the Advanced Thermal Reactor.

For nondestructive inspection techniques of fuel cladding tubes, developmental studies were made on ultrasonic and eddy current testing, and surface detection of defects by laser beam reflection.

Out-of-pile tests were performed on compatibility between FBR fuel and Type 316 stainless-steel cladding tube to obtain design data of FCCI for the MONJU fuel.

4. Fuel and Material Inspection Section

Purchasing audit and technical checking have been conducted for manufacturing cladding tubes, spacers, end plugs, and other materials used as exchange-loaded FUGEN and first-loaded JOYO MK-II fuels.

Adjustment of the data base system for the FUGEN and JOYO MK-II fuels was continued by using TOKAI central computer system and satellite terminals.

For nondesctructive inspection of JOYO MK-II core fuel cladding tube, the automatic equipment has been regulated on electronic units and scanning mechanisms. Maintenance and improvement have been made on the inspection and testing equipment for fuel assembling parts.

5. Chemical Analysis Section

In this section, chemical analyses have been made of reactor materials and fuels which were purchased for the PNC's development projects, and other analyses have also been done for the development work of various projects.

Uranium enrichment process analysis and the related various chemical analysis have been carried out for the uranium enrichment technology development. This section is now engaged in the development of an automatic measuring equipment for uranium enrichment.

For the inspection of the international safeguards, this section has participated in the SALE (Safeguards Analytical Laboratory Evaluation) program.

6. The Chemical Processing Facility

The Chemical Processing Facility, CPF, is now under construction as basic research facility for downstream of nuclear fuel cycle. This facility includes hot laboratories where fundamental research will be carried out for reprocessing of FBR spent fuels and treatment of high-level radioactive wastes.

This facility consists of a research building and an administration office with the total floor area of 7,400m^2. The former is three stories with a basement, and the latter two stories.

The research building is composed of two lines of laboratories, A-line for reprocessing and B-line for waste treatment. It is provided with hot cells in each line and storage equipment for liquid and solid wastes under the ground.

Construction of the facility was started in July 1978. After civil engineering works for the underground part, building construction was started in April, 1979. Fabrication of in-cell equipment, analyzing and measuring instruments, liquid waste storage, ventilation and utility have been simultaneously advanced with construction.

This facility will be completed early in 1981. After several inspections and tests, hot operation is expected to start immediately.

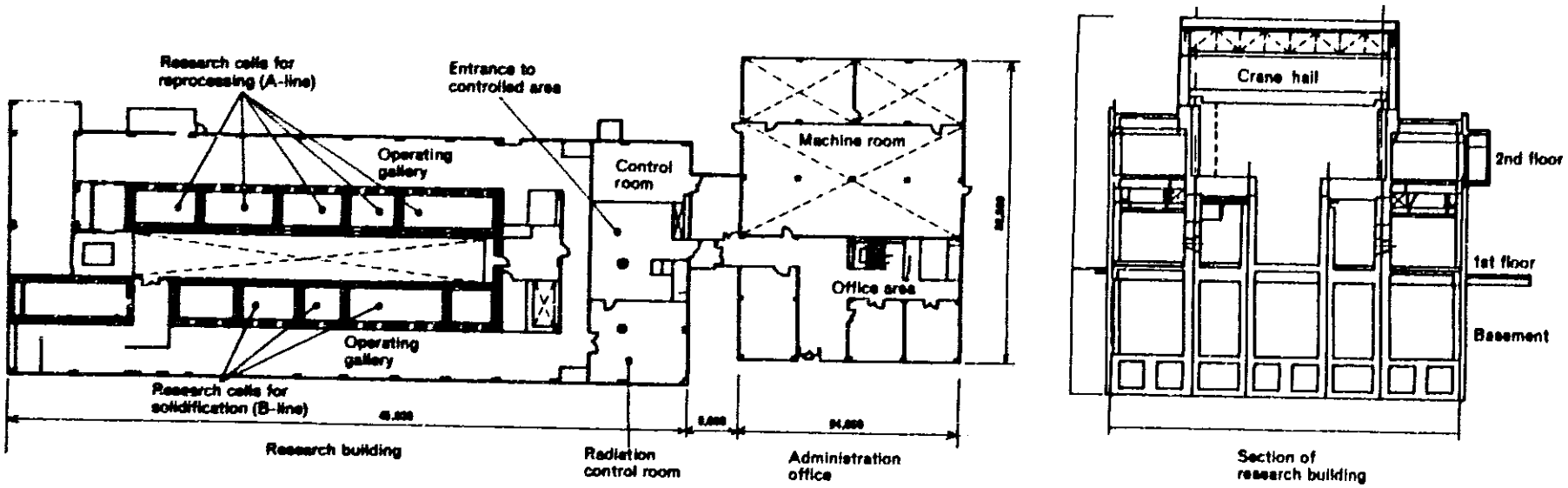

Fig. Floor plan and elevation of CPF

Removal of Iodine Species with Concentrated Nitric Acid (VII) Iodine Treatment by Nitric Acid Decomposition*

Hisao KANEKO, Jun KOMAKI,
Hideaki MURAMOTO, Hiroshi TAKEDA
and Tadaya HOSHINO

1. Introduction

The Iodox process[1] is attractive for iodine removal from off-gas stream in nuclear fuel reprocessing, because organic iodides like CH_3I can be eliminated with high decontamination factor as elemental iodine can.

The Iodox process consists of four steps including absorption-oxidation, iodine concentration/solidification and HNO_3 recovery as shown in Fig. 1. The authors have studied on the absorption-oxidation step through laboratory-scale experiments [2)-4)] and engineering-scale tests[5]. Some studies have also been performed on the concentration and solidification steps on a laboratory scale[6-7]. There was a problem that the material of the equipment was corroded by hot concentrated nitric acid. It also turned out that the solidified product (HI_3O_8) is not suitable for long term iodine storage because of its high solubility in water or thermal decomposition.

So it is necessary to develop a new substitutional treatment process for the conventional concentration and solidification steps.

In the previous studies, it was observed that IO_3^- was reduced to I_2 by NOx originated from nitric acid and resulted in I_2 evolution. The purpose of the present study is to confirm that in a laboratory scale iodine can be stripped from a solution by reduction of IO_3^- to I_2 with NOx, which is produced from nitric acid decomposition with some decomposing agents such as formaldehyde, formic acid and sucrose.

*Presented at the Annual Meeting of the Atomic Energy Society of Japan (March, 1979).

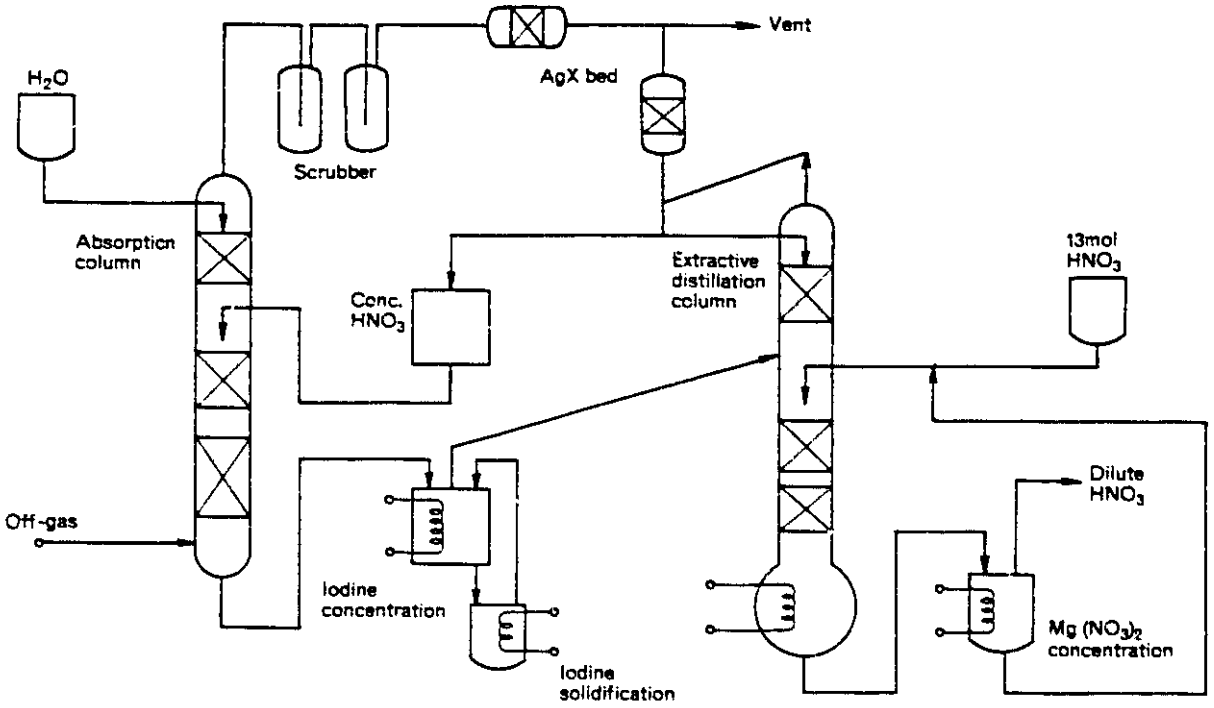

Fig. 1. Schematic diagram for iodox process.

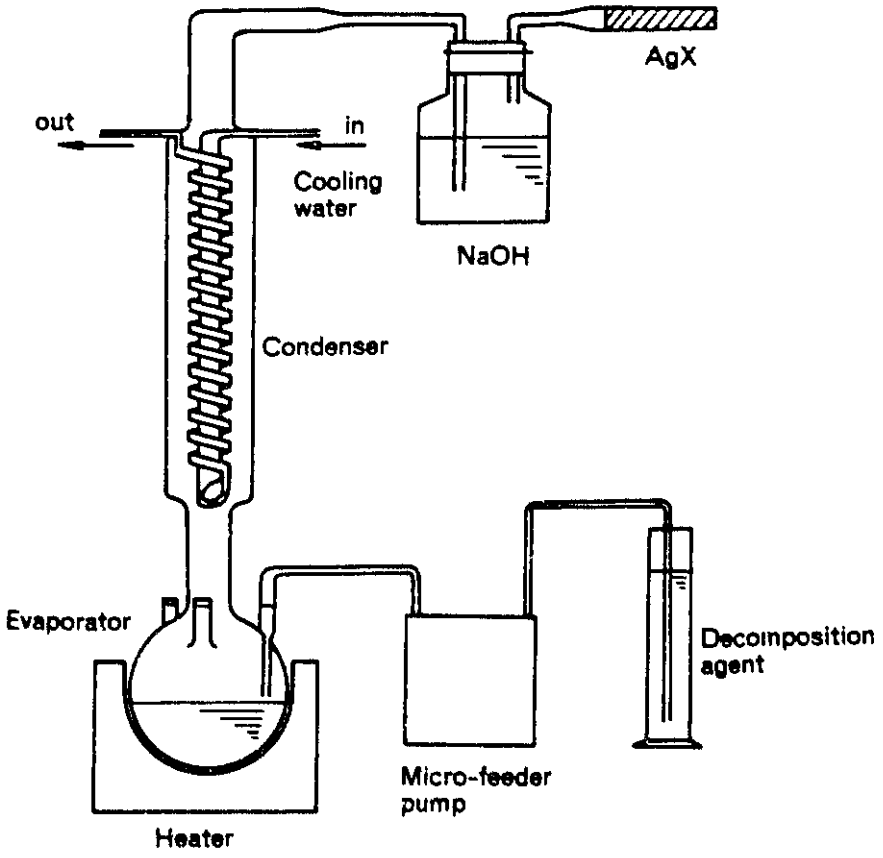

Fig. 2. Schematic drawing of apparatus.

2. Experiment

A simulated waste solution used in this experiment contained 15.2N (almost azeotropic) and 6 g/litre IO_3^- (about 20% of saturation) similar to solution obtained in the iodine concentration step of Iodox process. As a tracer, ^{131}I was added to the solution in the chemical form of IO_3^-, which was prepared by oxidation of $Na^{131}I$ with 22N fumic nitric acid.

A schematic drawing of experimental apparatus is shown in Fig. 2. After the simulated solution of 200ml was charged in a pyrex-glass flask (1 litre), a decomposing agent such as formaldehyde (HCHO), formic acid (HCOOH) and sucrose ($C_{12}H_{22}O_{11}$) was fed through a micro-feeder-pump at a constant rate into the reflux system.

The solution was heated to 80°C before addition of formic acid or surcrose. But folmaldehyde was added to the solution at room temperature, since the solution begins to boil easily by a great reaction heat and the reaction rate of the system can not be controlled.

A condenser and a silver-zeolite (AgX) bed were used for iodine cold trap and adsorption respectively. To prevent the adsorption ability of AgX from the toxic effect of nitric acid fume, NaOH scrubber (5N and 0.5 litre) was provided before AgX bed.

In order to determine the amount of iodine deposited, the condenser was perfectly washed out with ethanol after the run. Then the ^{131}I concentration in ethanol solution was measured with NaI (Tl) well-type scintillation detector. Amounts of iodine adsorbed in AgX and absorbed in NaOH scrubber were also determined by measurement of ^{131}I.

3. Results and Discussions

The reaction between nitric acid and three agents are shown in Table 1[8-10]. The production of I_2 by NOx is expressed by the equations

$$IO_3^- + H^+ + 2N_2O_4 + H_2O \longrightarrow I^+ + 3\,HNO_3 + NO_3^-$$

$$2I^+ + 2NO_3^- + N_2O_4 + 2H_2O \longrightarrow I_2 + 4HNO_3$$

These correspond to reversal reactions of iodine oxidation with concentrated nitric acid in Iodox process, and the reaction apparently proceeds to the right direction with increasing NO_2.

Table 1. Chemical reaction of HNO_3 and decomposition agent.

Decomposition agent	Reaction	HNO_3 conc.
HCHO [8]	$4HNO_3+HCHO \rightarrow 4NO_2+CO_2+3H_2O$	8 N
	$4HNO_3+3HCHO \rightarrow 4NO_2+3CO_2+4H_2O$	2 to 8 N
	$2HNO_3+HCHO \rightarrow HCOOH+2NO_2+H_2O$	2 N
HCOOH [9]	$2HNO_3+3HCOOH \rightarrow 2NO+3CO_2+4H_2O$	1 to 4 N
	$2HNO_3+HCOOH \rightarrow 2NO_2+CO_2+2H_2O$	14 to 16 N
$C_{12}H_{22}O_{11}$ [10]	$C_{12}H_{22}O_{11}+48HNO_3 \rightarrow 48NO_2+12CO_2+35H_2O$	Not described

Prescribed amounts of decomposition agents were fed into simulated waste solutions of 200 ml at a rate of 0.05 mol/min for formaldehyde and formic acid, and at a rate of 0.005 mol/min for sucrose. Due to initial high concentration of nitric acid, no induction period (as seen in dilute nitric acid) was observed in any reaction.

Figure 3 shows the effects of HNO_3 concentrations on iodine distributions after the reaction. Following denitration to 12N, nearly 90% of initial iodine content is evolved as I_2 in each experiment.

Using formaldehyde or formic acid as decomposing agent, iodine residue in the solution decreased as increasing amount of the added agents and finally reduced to less than 1% of initial content with denitration to 2N. The amount of iodine deposited in the condenser decreased with the progress of reaction, while the amount of iodine trapped in NaOH scrubber and AgX showed a tendency to increase.

In the addition of sucrose, the decomposition reaction being mild, the solution was heated for 1-2 hr to ensure termination of the reaction. In this process, iodine was observed to return from the condenser to decomposer.

As iodine was scarcely evolved due to a small amount of NOx generation, iodine seems to be accumulated in the solution.

Figure 4 shows the relations of nitric acid and iodine concentrations with heating period after addition of sucrose. Lasting decrease of nitric acid concentration means that the reaction continues after addition. In the addition of 0.3 mol sucrose, increase of iodine concentration in the solution shows the reflux and accumulation from the condenser.

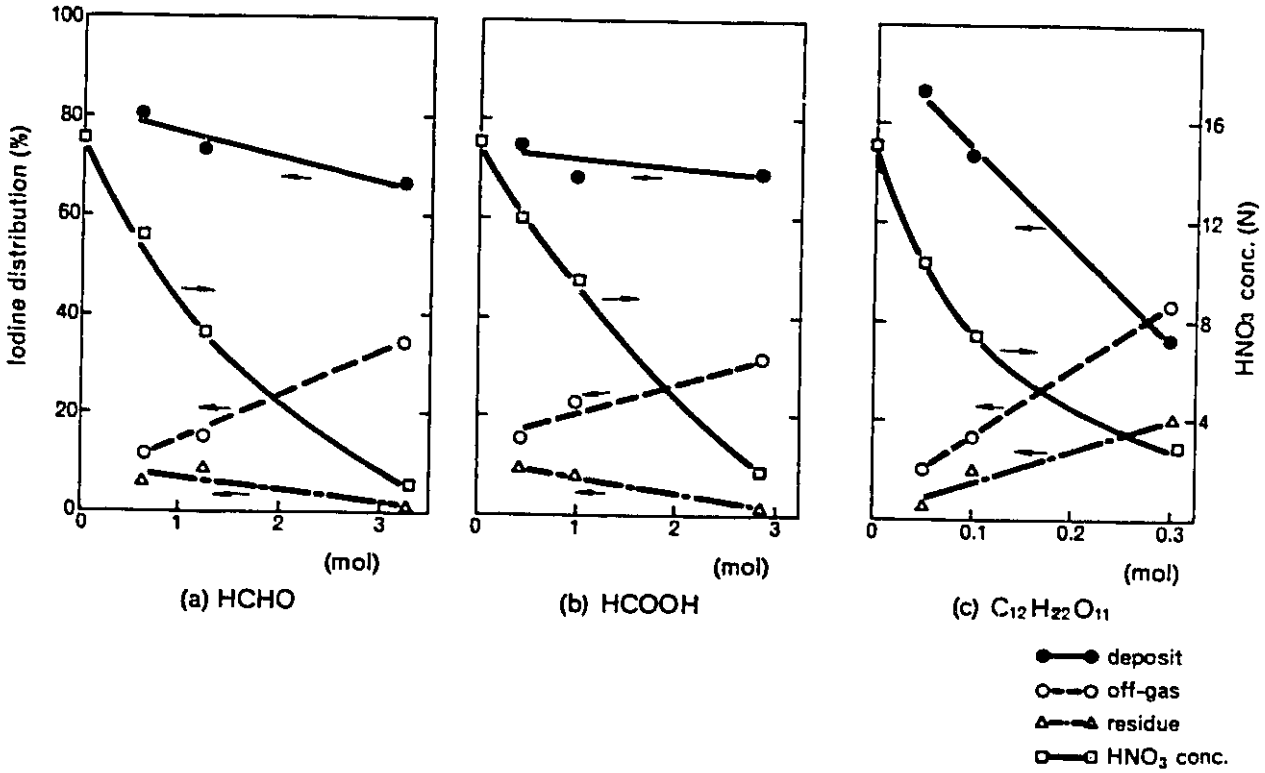

Fig. 3. Iodine distributions and HNO_3 concentration after denitration with three agents.

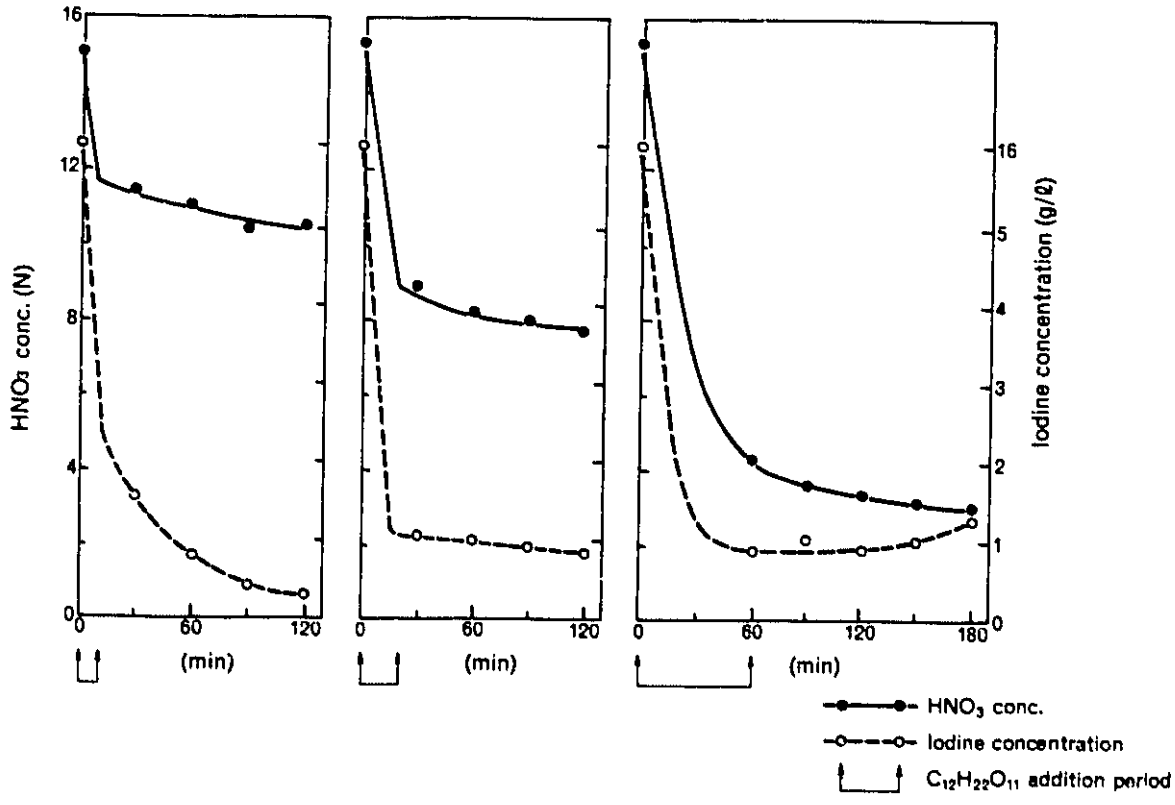

Fig. 4. Variation of HNO_3 and iodine concentrations after addition of sucrose

Based on these results, a consideration is made on a new iodine treatment process by denitration with formaldehyde and others as follows.

It seems that iodine can be perfectly evolved from the solution after denitration to 2N. But higher concentrations of nitric acid is desired to remain for useful regeneration on recycle. In an more attractive process, iodine should be evolved up to 90% with about 12N of nitric acid and remaining nitric acid should be returned to the iodine concentration step.

Iodine reflux will be stopped by adoption of two or three condensers in series. The first condenser is used for condensing only nitric acid vapor at 50°C or over, and next for iodine trap at lower temperature. After the end of decomposition, I_2 collected in cold trap is vaporized and adsorbed into Pb-zeolite or activated carbon as a final storage form.

Formaldehyde or formic acid as decomposing agent is superior to sucrose due to rapid rate, provided that the reaction of the system can be controlled. But there is another problem that NOx absorber must be added to recover nitric acid.

As a result, a modified Iodox flow is proposed as shown in Fig. 5.

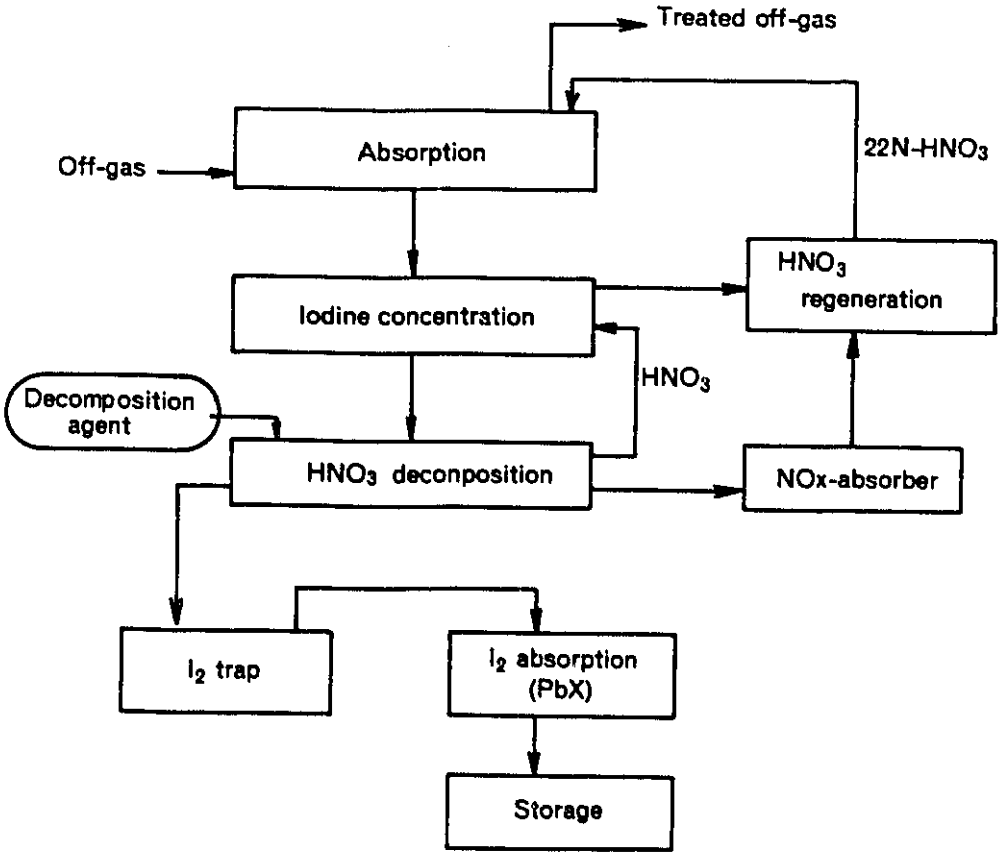

Fig. 5. Flow of modified iodox process

4. Conclusion

For the Iodox process, a new iodine treatment process was examined by laboratory scale experiment. This process includes a step of iodine evolution from solution by NOx produced from nitric acid with formaldehyde, formic acid or sucrose.

The results obtained are summarized as follows.

1) As nitric acid is decomposed from azeotropic composition to 12N, about 90% of I_2 can be evolved from the solution of IO_3^-.

2) Addition of formaldehyde or formic acid as decomposing agent lowers iodine residue in the solution to the less than 1% with progressing decomposition of nitric acid to about 2N.

3) In the case of sucrose as decomposing agent, it takes a few hours to complete the reaction. This treatment results in iodine reflux from the condenser.

Reference

(1) Yarbro, O. O. , et al. : 13th AEC Air Cleaning Conference, (1974).
(2) Yoshiki, N. et al. : PNC Report N841-77-16 (1977).
(3) Kaneko, H. et al. : PNC Report N841-78-21 (1978).
(4) Muramoto, H. et al. : PNCT831-79-02, 90-98 (1979).
(5) Yoshiki, N. et al. : PNCT831-79-01, 84-90 (1979).
(6) Kaneko, H. , et al. : PNCT831-79-01, 78-83 (1979).
(7) Kaneko, H. , et al. : PNCT831-79-02, 99-104 (1979).
(8) Forsman, R. C. et al. : HW-79622 (1963).
(9) Bradley, R. F. et al. : DP-1299 (1972).
(10) Bray, L. A. : HW-76973 REV. (1963).

Development of Vitrification of HLLW by Joule-Heated Ceramic Melter Process Testing and Components Examination of the Equipment*

Shin-ichiro TORATA, Nobuo KAWANISHI
Hiroshi NAGAKI and Naomi TSUNODA

1. Introduction

In order to establish the vitrification process of HLLW, development of Joule-heated ceramic melter has been performed for three years. This ceramic molter can cotinuously convert a mixture of nuclear waste and glass formers into a stable glass product.

To perform the process testing with simulated calcined waste as well as simulated denitrated liquid waste, an engineering scale melter was made and five running tests have been carried out for about 300 days.

The lives of refractories and electrodes were evaluated from the results of these tests. Improvement of the glass flowing-out system has also been carried out in this period.

2. Operation test of Joule-heated ceramic melter

(1) Melter description

Figure 1 shows the engineering-scale ceramic melter. The equipment consists of the melting cavity for melting of raw material which is a mixture of waste and glass additives, the riser and the forehearth for glass refining. Electrofused-cast refractories of ZrO_2-SiO_2-Al_2O_3 (AZS) are used for walls and bottoms, which are in contact with glass.

---

*Presented at the Annual Meeting of the Atomic Energy Society of Japan (March,1980).

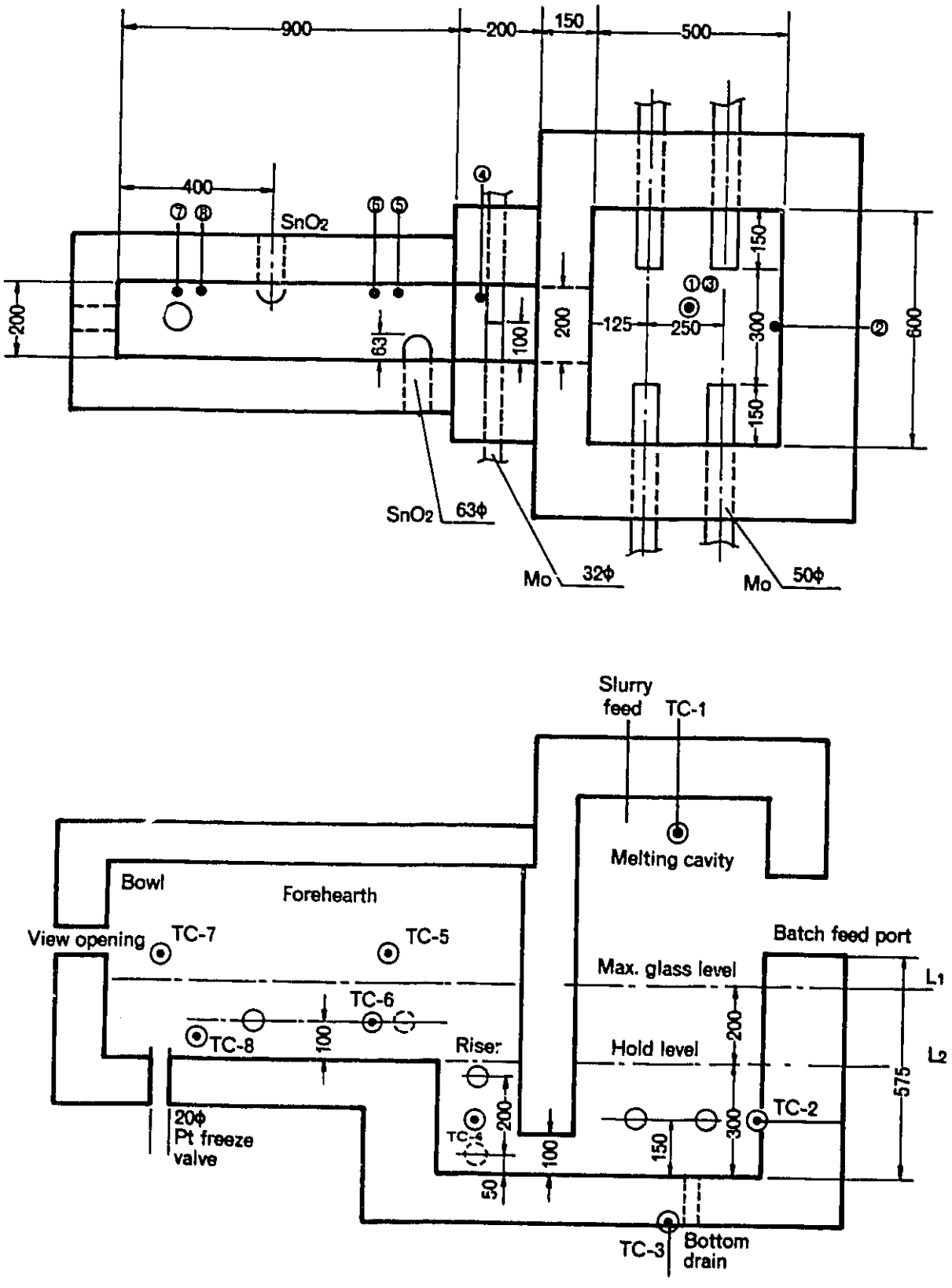

Fig. 1. Joule-heated ceramic melter.

The melting cavity is equipped with two pairs of metallic molybdenum electrodes of 50mm in diameter; the riser is also installed with a pair of molybdenum electrodes of 32mm in diameter and the foreihearth with a pair of SnO_2 electrodes of 62mm in diameter.

The total holding capacity of the melter amounts to about 200 lilters, always keeping at minimum 100 liters to maintain the Joule-heating.

A mixture of calcined waste and glass additives is supplied by a vibrational feeder through the batch feed port. Liquid raw material is supplied through the feed nozzle at the ceiling of the melting cavity.

When raw material is fed into the melter, the surface of the molten glass is covered with the raw material and kept at a lower temperature (cold top), to prevent volatile materials from vaporizing from molten glass. This layer also contributes to reduction of radiation from the surface and effective operation of the equipment.

Table 1 shows the glass composition used in the operating test. The compositions, G-2 and GB-series, were selected as basic glasses which have melting temperatures of 1200°C and 1350°C respectively.

Usually molten glass flows out through the freeze valve at the end of the forehearth. Besides this freeze valve drain, the melting cavity is installed with a bottom drain hole for shutdown.

(2) Start-up and steady runs

For the start-up operation, it is necessary to heat the glass up to the temperatures at which the glass becomes conductive. The melter was heated up to about 900°C by Sic heaters in melting cavity and by $MoSi_2$ heaters in forehearth to melt the pre-charged glass cullet between the electrodes, and then steady-state operation by Joule-heat was started.

In a steady run, a raw mixture of simulated calcined waste and glass additives was charged and melted to the maximum capacity of the melter. Then the half of the molten glass was poured into the canister, and the next raw material was charged to the melter again.

The feed rate of dry raw material was about 20Kg-glass equivalent per hour on the average (Fig. 2). Operational conditions of material feeding and idling (without feed) are indicated in Table 2. The power supplies in feeding decreased to nearly the same power as in idling due to heat loss reduction by the raw material overing the molten glass.

Table 1. Glass compositions.

Glass series / Oxide components	G-2	GB-1	GB-2	GB-3	GB-4
	WT%				
SiO_2	44.6	55.6	54.35	52.72	51.36
B_2O_3	14.6	9.77	9.80	11.24	13.60
Li_2O	3.13	1.95	1.95	1.95	1.01
Na_2O	1.04	1.05	0.29	2.02	2.01
K_2O	2.09	/	/	/	/
MgO	/	/	2.00	/	/
CaO	2.09	/	/	/	/
ZnO	2.09	/	/	/	/
Al_2O_3	3.50	5.09	5.09	5.60	5.56
Waste total	26.68	26.68	26.68	26.68	26.68
Na_2O	9.18	-	-	-	-
K_2O	0.15	-	-	-	-
SrO	0.55	-	-	-	-
BaO	0.91	-	-	-	-
ZrO_2	2.67	-	-	-	-
Fe_2O_3	1.79	-	-	-	-
NiO	0.51	-	-	-	-
Cr_2O_3	0.17	-	-	-	-
MnO_2	0.39	-	-	-	-
CoO	0.16	-	-	-	-
TeO_2	0.36	-	-	-	-
MoO_3	2.69	-	-	-	-
R.E. oxides	6.90	-	-	-	-

(3) Direct feeding of liquid raw material in a slurry state

Instead of feeding dry raw material of calcined-HLLW, a mixture of liquid waste and powdered glass additives can be fed directly into the melter as slurry. This method is expected to make the pretreatment process simple.

The liquid raw material as shown in Table 3 was prepared and fed by pump or airlift into the melter. Figure 3 shows a schematic of liquid feeding.

Temperature and power supply during liquid feeding are shown as functins of time in Fig.4. Under a power supply of 60KW, the optimum feed rate was estimated at about 25 ℓ /hr (7.5Kg-glass/hr). A continuous feed of 50 ℓ /hr resulted in the formation of thick calcine bridge, and the temperature varied due to intermittent blowing of decomposition gas.

Table 4 shows a comparison between thermal efficiencies during liquid feeding and idling. From measurement of heat loss through refractories and water-cooling of electrodes, the heat necessary for glass melting was theoretically estimated. The total efficiency of liquid feed process is evaluated at about 40%.

Table 2. Steady-state operational conditions of ceramic melter.

	Rising level (Feeding)				Idling			
	Power KW	Volt	Amp.	Temp. °C	Power KW	Volt	Amp.	Temp. °C
Melter	46.8	85	550	1150	40.9	95	430	1140
Riser	6.0	63	95	980	3.2	45	70	1020
Forehearth (SnO_2)	0.5	21	23	1100	/	/	/	/
Forehearth super	8.4	43	195	1030	9.9	44	225	980
Bowl super	6.5	33	197	850	4.2	24	172	940

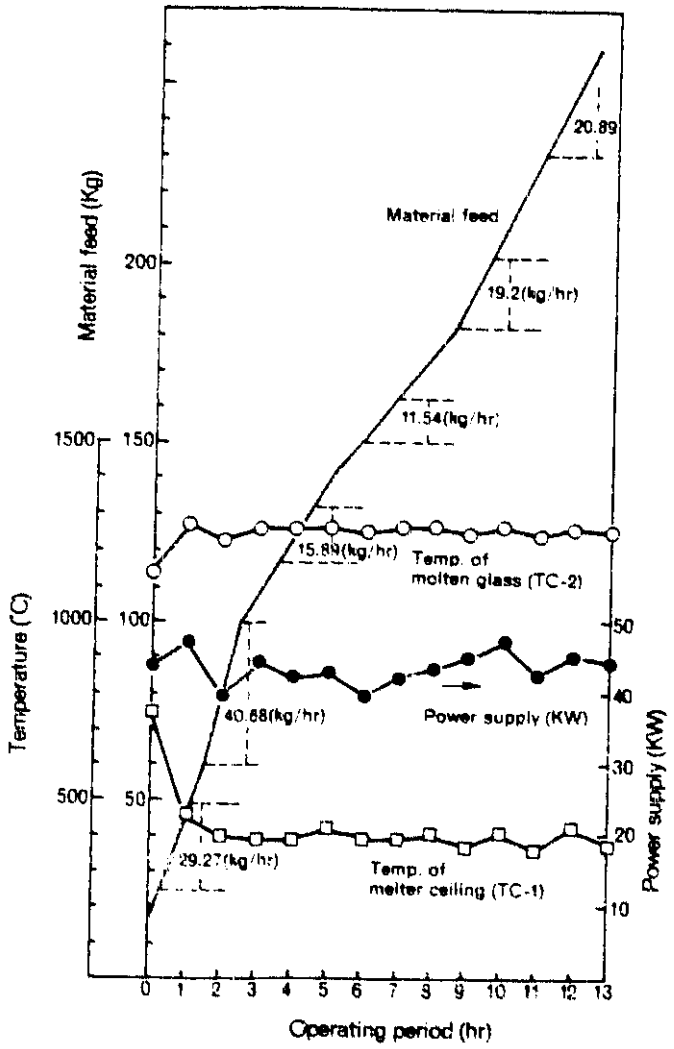

Fig. 2. Operation of melter.

(4) Flowing-out and stopping system of molten glass

In the first stage, a few types of freeze valves made of ceramics and platinum heater were used for flowing-out of molten glass. But they were not very resistant to the thermal shock at frequent heating-up and cooling.

In the 4th and 5th running tests, and improved device made of platinum nozzle and shear-cutter was introduced into the flowing-out system. The platinum nozzle was heated by Joule-heat to the temperature of 800°C, and then glass flowed out. The glass flow rate could be controlled within the range of 50 Kg/hr to 200 Kg/hr by varying the nozzle temperature.

At stopping of flowing-out, the platinum nozzle was cooled by blowing air and the flow rate was decreased simultaneously. Then stringy glass was cut by a shear-cutter and a water-cooled cap was set at the outlet of the nozzle at the same time.

By this method, stoppings of flowing-out glass were tested 230 times, and the freeze valve has proved to be durable for a long time use.

(5) Examination of melter after operation

After 288 days of operation, the glass-contact refractories and electrodes were examined in respect of erosion. The erosion of refractory was determined by measuring the change of the inside dimension. As a result, the maximum of the sidewall erosion was observed at a position higher than the electrode-projecting level where the temperature reached the maximum.

The erosion depth of the sidewalls are shown in Fig. 5. The maximum value of erosion in the sidewalls amounted to 42mm after 288 days operation.

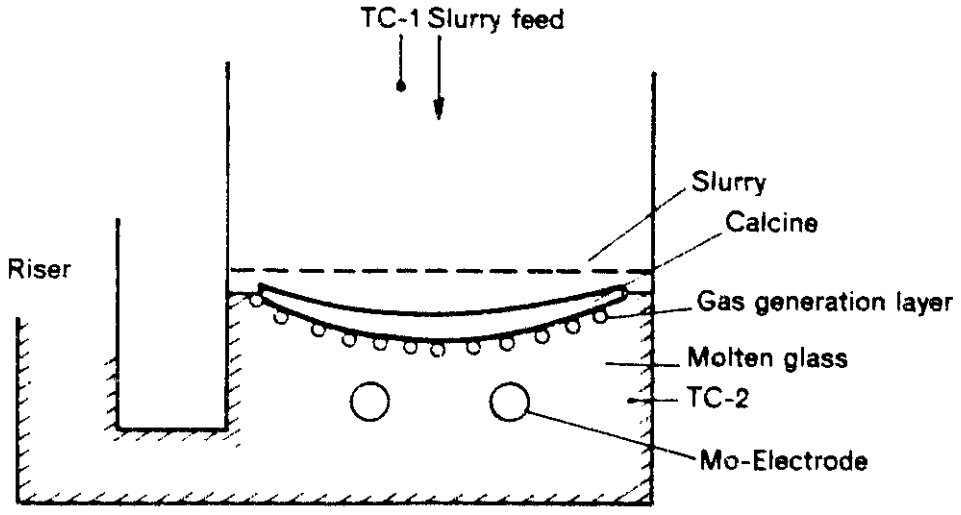

Fig. 3. Schematic of direct liquid feed operation.

Table 3. Preparations of slurry (100 kg as glass).

Reagents	
K_2CO_3	0.816 (Kg)
$SrCO_3$	0.78
$BaCO_3$	1.167
$ZrO_2 \cdot SiO_2$	3.981
$Na_2MoO_4 \cdot 2H_2O$	4.475
$Na_2TeO_3 \cdot 5H_2O$	0.670
MnO_2	0.39
R.E. oxides	6.80
Fe_2O_3	1.792
Cr_2O_3	0.172
NiO	0.513
CoO	0.157
Na_2CO_3	13.5
Al_2O_3	3.5
Powder of glass additives	69.82
Water	305 (ℓ)
Total slurry volume	350 (ℓ)
Glass yield	286 g/ℓ

Table 4. Thermal balances during liquid feed and idling.

	Liquid feed (T.C.2 ; 1150 °C)	Idling (T.C.2 ; 950 °C)
Radiative heat loss		
Sidewalls	12.3 KW	10.5 KW
Ceiling	0.8	1.5
Base (Floor)	0.73	0.73
Water cooling of electrodes	8.0	8.0
Glass melting from liquid raw materials	23.2 (25 ℓ/hr)	0
Total	45.03 KW	20.73 KW
Actual power supply	60 KW	27 KW

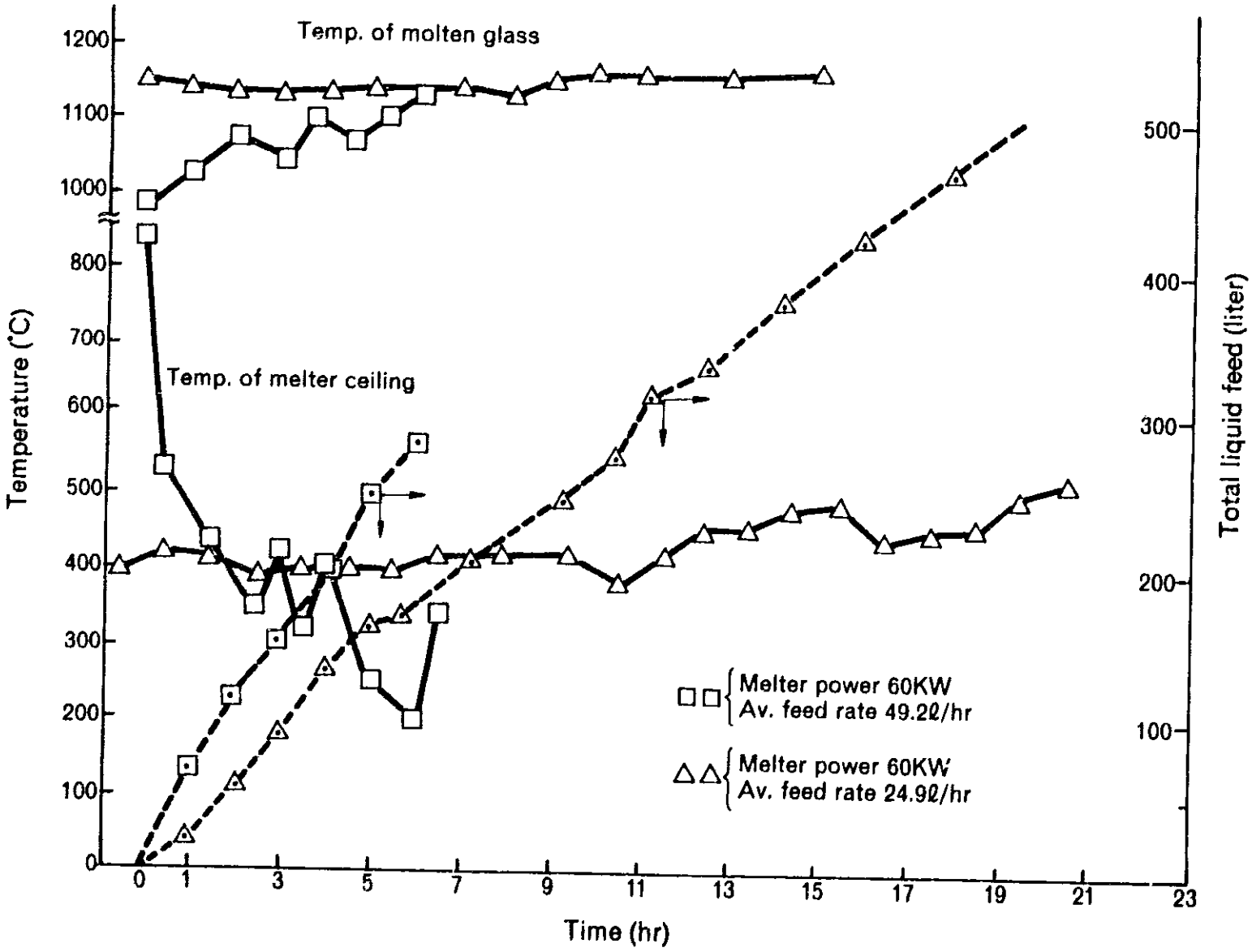

Fig. 4. Operation by direct liquid feed.

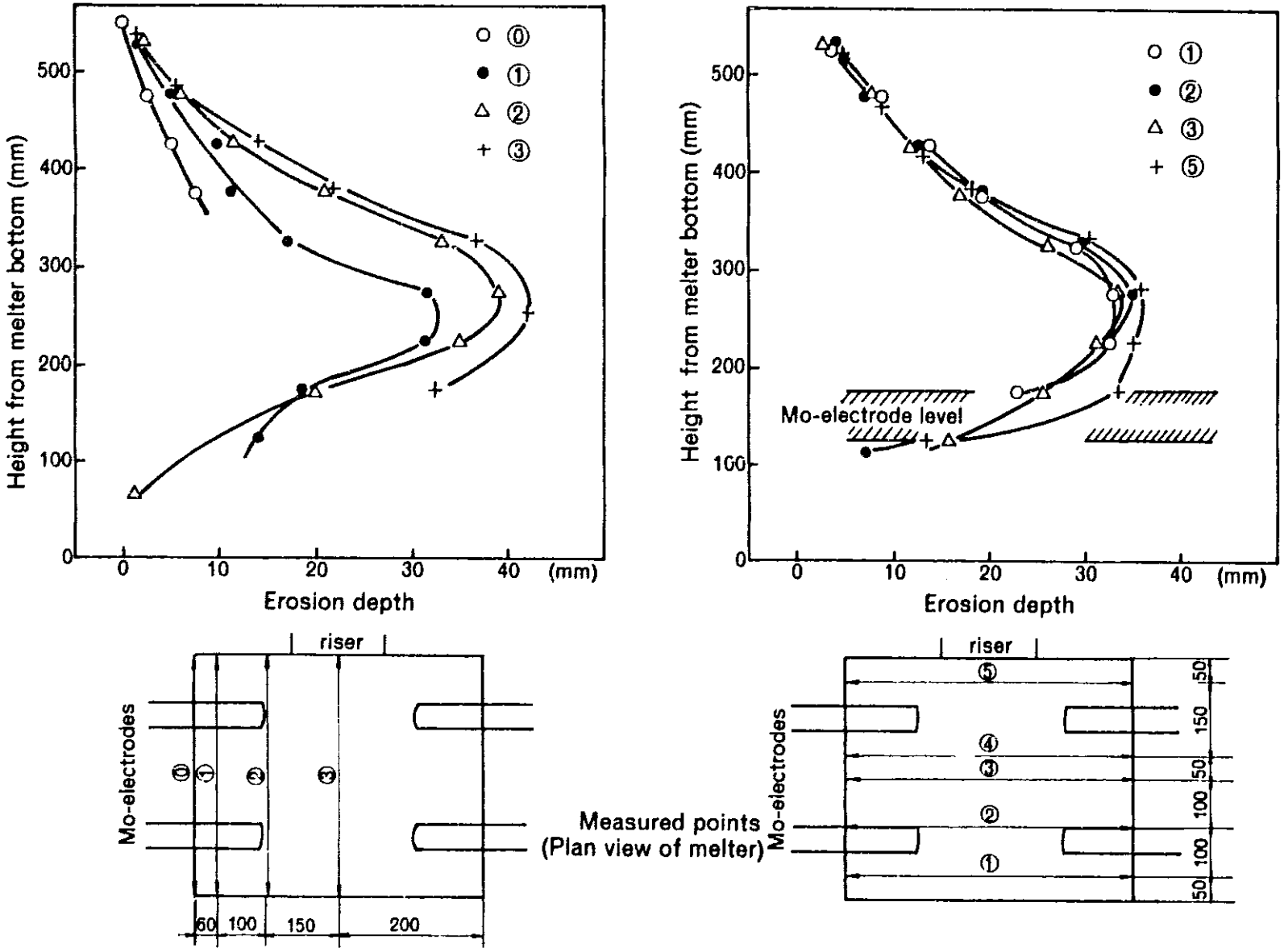

Fig. 5. Erosion of melter sidewalls (after operation of 288 days).

3. Conclusion

The melter was operated for about 300 days through five running tests. It produced about 21.5 tons of glass containing 30wt% equivalent simulated waste.

The glass melting rate was about 20Kg-glass/hr for dry raw material and 7.5Kg-glass/hr for liquid raw material on the average. This capacity is equivalent to the waste from a reprocessing plant of 1 to 3 MTU/day capacity.

Evaluation of the melter after the operation suggests that the melter can be safely operated for more than two years. The use of platinum nozzle has proved to improve the thermal-shock resistance during glass flowing out and be capable of controlling the glass flow-rate.

Compared with the long-life refractories of the melter, the electrodes and some of the electric sensors would not be used so long and the periodical maintenance must be needed. Based on the information obtained from this operation, further development is expected to be made on the enclosed type of melter including the design for remote operation.

Reference

(1) OGUINO, N . et al : PNCT831-79-02 Tokai Works Semi-annual Report "A Development of Vitrification of HLLW by Joule Heated Ceramic Melter; An Experimental Melting Operation".

(2) NAGAKI, H . et al : PNCT841-79-54 Development of Vitrification Technique of HLLW in Engineering-Scale at PNC, Nov. 10, 1979.

Leaching Test on Chemical Durability of Glasses Containing Simulated High Level Wastes*

Nobuo KAWANISHI, Hiroshi IGARASHI
Horoshi NAGAKI and Naomi TSUNODA

1. Introduction

It is required that glass containing HLW has various stable physical and chemical properties for its long-term storage. Especially chemical durability is important to prevent the release of radionuclildes into the biological environment.

The purpose of this study is to evaluate chemical durability of waste glass by leach tests. In PNC, the leach tests have been conducted by two methods, the Soxhlet test and the two stagnant phases leach test. Another long-term leach test has been performed, using the Soxhlet apparatus. The surface of glass used in the tests was also analyzed by the following methods; optical microscopy, electron probe microanalysis (EPMA) and Auger electron spectroscopy (AES).

2. Experimental

2.1 Sample Preparation

The compositions of glasses investigated in the present study are given in Table 1. Each glass contains 27wt% of simulated waste oxides. To study chemical durability, ground samples (-40, +60 ASTM mesh) and polished blocked (10x10x20mm) were made from each glass.

---

* Presented at the Annual Meeting of the Atomic Energy Society of Japan (March,1980).

2.2 Experimental Procedure

The Soxhlet apparatus and the two stagnant phases test appratus are schematically described in Figs.1-(a) and (b), respectively. The test appratus shown in Fig.1-(b) is made according to Japanese Industrial Standard (JIS-R-3502) prescribed for evaluation of the chemical durability of apparatus ware. Experimental conditions are given in Table 2.

2.3 Calculations of Leaching Rate

Leaching rates are defined either as weight loss per unit surface area or as amount of ion dissolved from unit surface area in a unit time. Leaching rates are calculated by the following formulas;

Weight loss;

Leaching rate $(g/cm^2.day) = (W_i - W_f)/W_i \; S \; t$

W_i = initial sample weight (g)

W_f = final sample weight (g)

S = specific surface area of sample (cm^2/g)

t = leaching time (days)

Chemical analysis;

Leaching rate $(g/cm^2.day) = A_t/A_o \; S \; t$

A_t = amount of ion removed in time t (g)

A_o = initial amount of ion in sample (g)

Leachant was analyzed by the following methods;

B^{3+} by curcumin photometric determination

Cs^+ and Si^{4+} by flameless atomic absorption spectrometry

Na^+ and Sr^{2+} by flame atomic absorption spectrometry.

The specific surface area of glass grains (-40, +60 mesh) was estimated at $131 cm^2/g$ by means of B.E.T. method using Kr gas as absorbate.

Table 1. Compositions of glasses.

Glass	Components (wt%)										
	SiO_2	Al_2O_3	B_2O_3	Na_2O	K_2O	Li_2O	CaO	ZnO	SrO	Cs_2O	Waste oxide
G-2	43.9	4.1	14.3	0.8 (9.98)	2.0	3.1	2.0	2.0	(0.55)	(1.37)	(27.8)
GB-1	54.7	5.0	9.6	1.0 (10.18)		1.9			(0.55)	(1.37)	(27.8)
GB-4	50.5	5.3	13.4	2.0 (11.18)		1.0			(0.55)	(1.37)	(27.8)

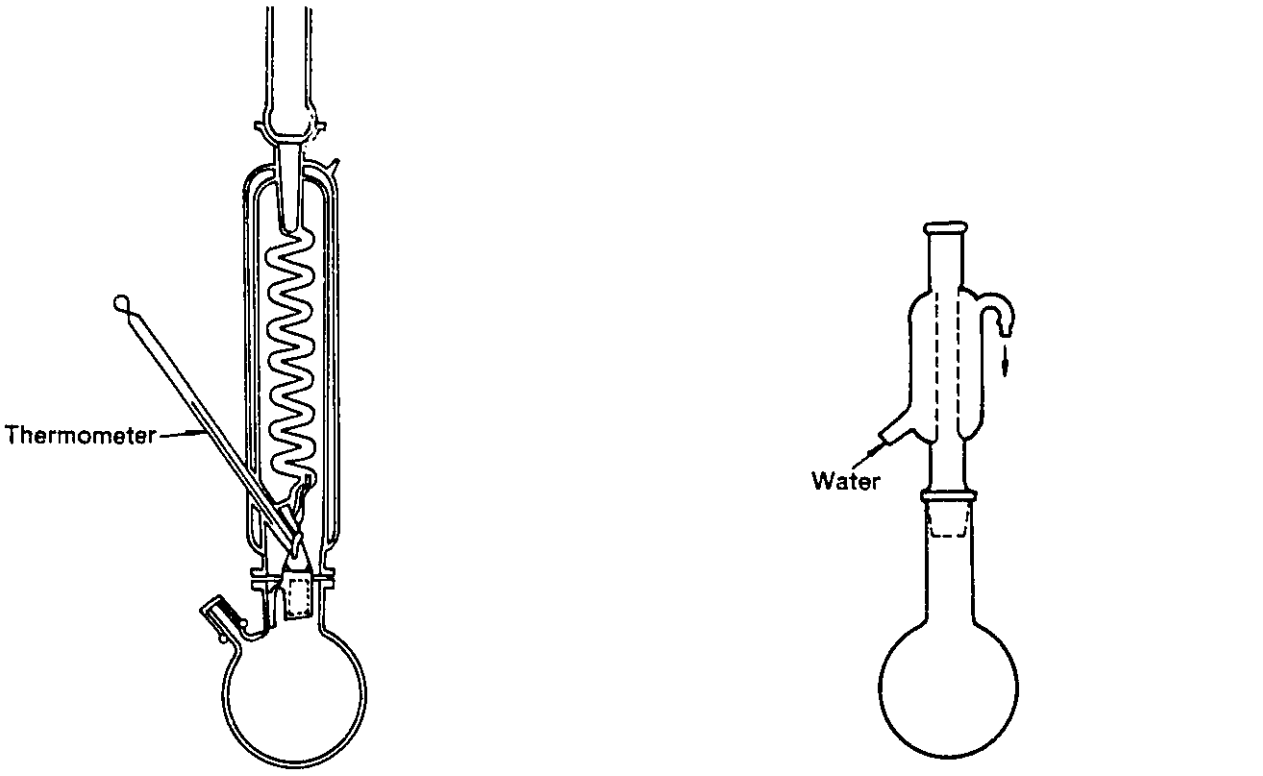

(a) Soxhlet apparatus (b) Two stagnant phases leaching apparatus

Fig. 1. Leaching apparatus.

3. Results

3.1 Two Stagnant Phases Leach Test (JIS type)

(1) The influence of sample weight on leaching rate.

To evaluate the influence of ratio between leachant volume and sample surface area (sample weight) on leaching rate, a grain sample (0.1-2.0g) was put in a 50ml distilled water and digested at 95°C for 24 hours (Table 2).

The pH value of solutions after leaching and the leaching rate are given in Fig. 2. The results indicate that the pH value of solution increases with the sample weight until pH is saturated nearly at 9.5 above a sample weight of 0.5g. On the other hand, there is a marked tendency for the leaching rate to decrease with increasing sample weight.

When a 1.0g portion of glass grain was leached in 50ml of distilled water at 95°C, the value of leaching rate for G-2 glass was 2.5×10^{-5} (g/cm^2.day) on the average and its standard deviation was 0.38×10^{-5} (g/cm^2.day)

(2) Acid-base leach test

The pH of solution before leaching was adjusted by addition of lithium hydroxide or acetic acid. The leaching rates of three glasses at pH3 and pH10 are given in Table 3.

The leaching rates of SiO_2, Na_2O and Cs_2O as functions of pH values are shown in Fig.3. The G-2 glass is more soluble in aqueous acid than GB-1 and GB-4 glasses, since it contains more basic oxide. There is no significant difference of leaching rate among three glasses in the alkaline region above pH8.

(3) The influences of ions in solutions on leaching rate.

To study the influence of ions in solution on chemical durability of glass, Al^{3+}, Si^{4+} or Fe^{3+} was added to leachant before leaching. Table 4 and Figure 4 show the results obtained. It is found from these results that even addition of a small amount of Al^{3+} (25 μ g oxide/ml) reduced the leaching rate to one-third of that without addition to leachant, and addition of Si^{4+} (300 μ g oxide/ml) reduced it to one-twentieth.

Table 2. Experimental conditions.

Apparatus	Leach tests	Leaching conditions						
		sample type	Sample weight	Leachant	Leachant vol.	Leach time	Temp.	Evaluation
Two stagnant phases apparatus [JIS type]	Effect of leachant vol. /surace area	Grain [250~420μ]	0.1~2.0g	Distilled water	50 mℓ	24 hr	95±1°C	Weight loss
	pH test		1.0 g	pH3~7 (CH_3COOH) pH7~11 (LiOH)	50 mℓ			Weight loss chemical analysis
	Effect of solute ions		1.0 g	Si^{4+}・B^{3-} Na^{+}・Fe^{3+} Al^{3+}	50 mℓ			Weight loss
Soxhlet apparatus	Long-term leach test	Bulk [10×10×20]	5.6 g	Distilled water	10 cycle/hr [100mℓ/hr]	~228 days	100°C	Weight loss chemical analysis
	Surface analysis		5.6 g	Distilled water		~20 days	100°C	EPMA* AES**

* Electron-probe microanalyzer
** Auger electron spectroscope

3.2 Soxhlet Leach Test

Figure 5 shows the results of long-term Soxhlet leach test made at 100°C for 182 days (G-2 glass) and 229 days (GB-4). An approximately linear relationship exists between the weight loss (wt%) and leaching time. Comparing these data with the results from chemical analysis in more detail, it is found that the curves can be considered as composed of a number of successive parabolas.

Table 5 shows the concentrations of various elements on the typical surface of G-2 glass for two different leaching times. The data were obtained by the electron-probe micro-analysis method. Iron, zirconium and rare earths are concentrated in the surface layer. The Auger electron spectroscopy method was also used for analyzing the depth profile of each element. These elements were concentrated even at the surface of the glass leached at 100°C for 24 hours. Figure 6 shows depth-compositional profile (Auger Electron Spectroscopy-Ar ion milling) of G-2 glass leached for 2-days at 100°C. These results show the trend of Fe ion which is particularly concentrated even at the outer layer leached for 2-days at 100°C. From further experiments (leaching time: 1-20 days), it was found that the thicknesss of the leached layer increased with leaching time, and then the layer of several microns peeled off in about ten days.

Table 3. Leaching rate at pH 3 and 10 of leachout.

[$\times 10^{-5}$ g/cm^2·day]

pH \ Glass	G-2	GB-1	GB-4
3	13.5	1.35	2.01
10	3.13	1.34	2.10

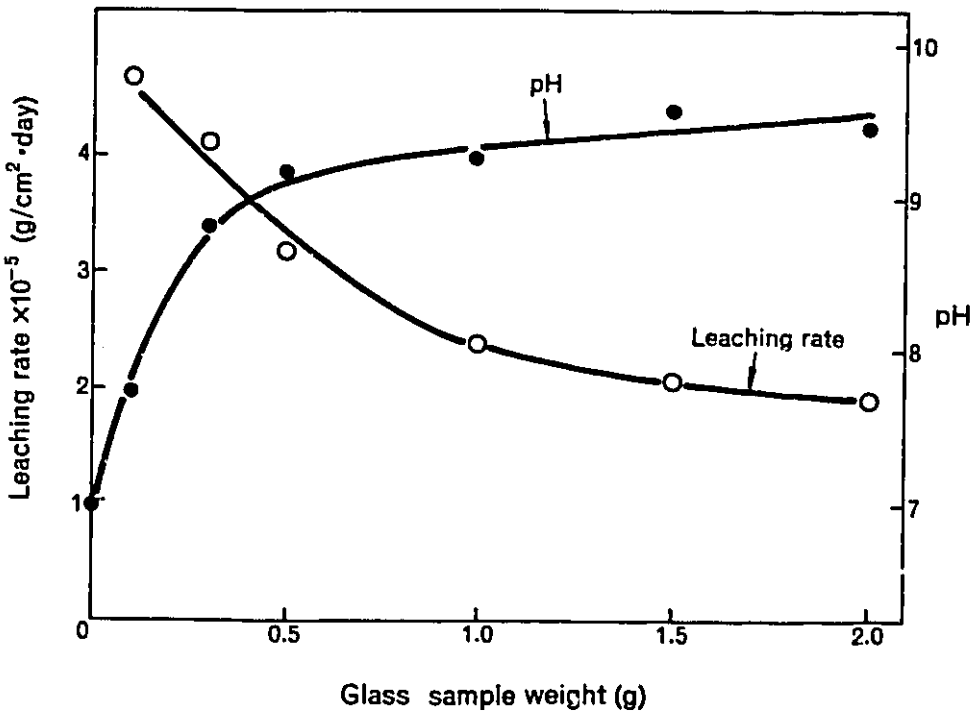

Fig. 2. Leaching rate and pH vs. sample weight.

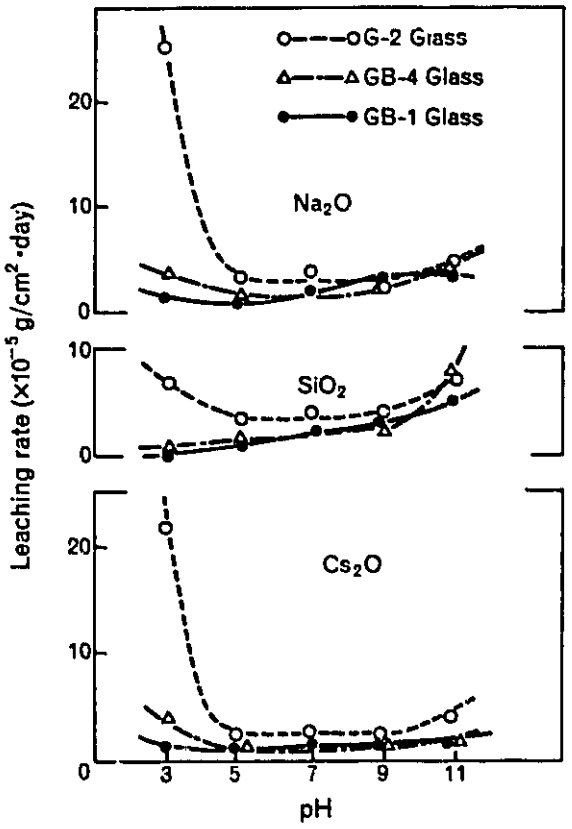

Fig. 3. Leaching rate vs. pH of leachant.

Table 4. The variation of leaching rate with amounts of ions.

Ion	Amount of ion (μg oxide/mℓ)					Leaching rate (10^{-5} g/cm^2·day)	pH of leachant	
	Li_2O	Na_2O	B_2O_3	SiO_2	Al_2O_3		initial	final
dist. H_2O						2.9	7	9.2
Li	1.5					3.0	10.0	9.0
Na		307				3.0	10.7	10.5
Na・B		307	172			2.4	11.8	11.5
Na・Si		133		305		0.3	9.9	9.7
Na・Al		27			25	0.9	9.5	9.2
Na・Si・B		307	172	188		1.7	10.4	10.9

Table 5. Variation in composition of the surface layer on G-2 glass.

Analyzed elements	Initial	Leached suface for	
		47 days	182 days
SiO_2	43.6	10.7	15.6
Al_2O_3	4.2	0.6	0.5
B_2O_3	14.3	—	—
Na_2O	9.8	0.4	0.7
K_2O	2.0	0.2	0.4
Li_2O	3.1	—	—
CaO	2.0	0	0
ZnO	2.0	1.8	1.8
SrO	0.5	0	0
Cs_2O	1.4	0.5	0.6
Fe_2O_3	1.9	19.7	4.0
ZrO_2	2.7	14.7	33.1
CeO_2	1.7	8.7	4.8
BaO	0.9	0	0.1
MoO_3	2.8	1.7	3.8
Nd_2O_3	2.6	14.6	6.9
La_2O_3	1.5	5.7	2.3

(calculated in first approximation) (wt%)

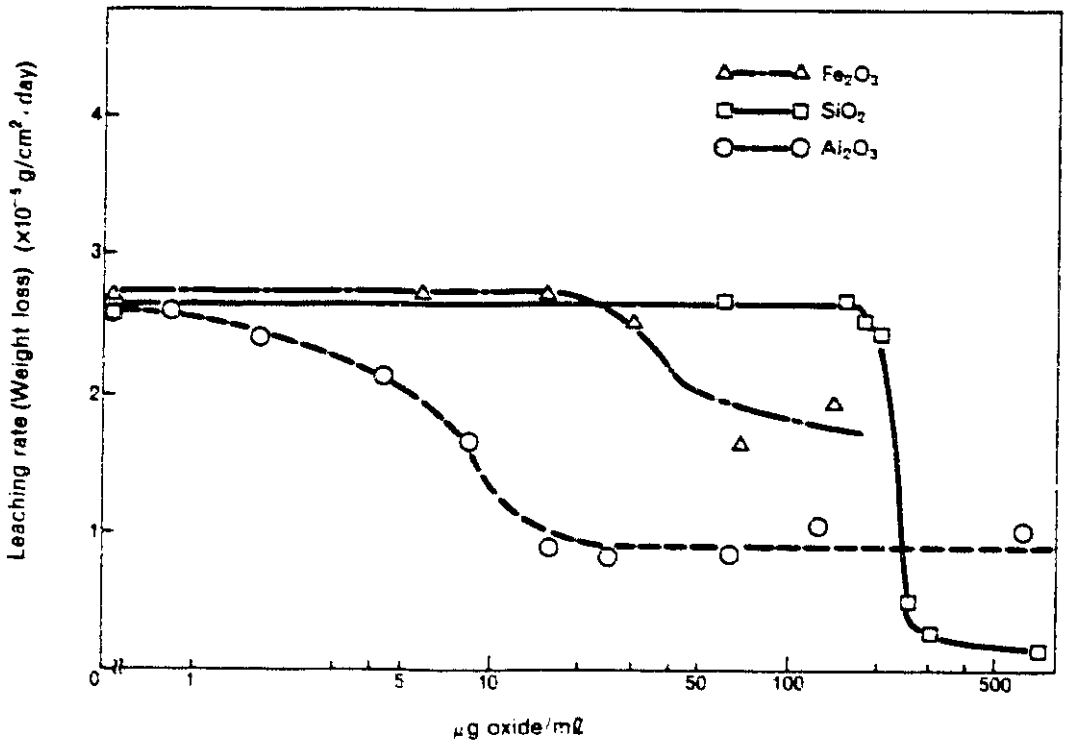

Fig. 4. Leaching rate vs. amount of ions in leachant for G-2 glass.

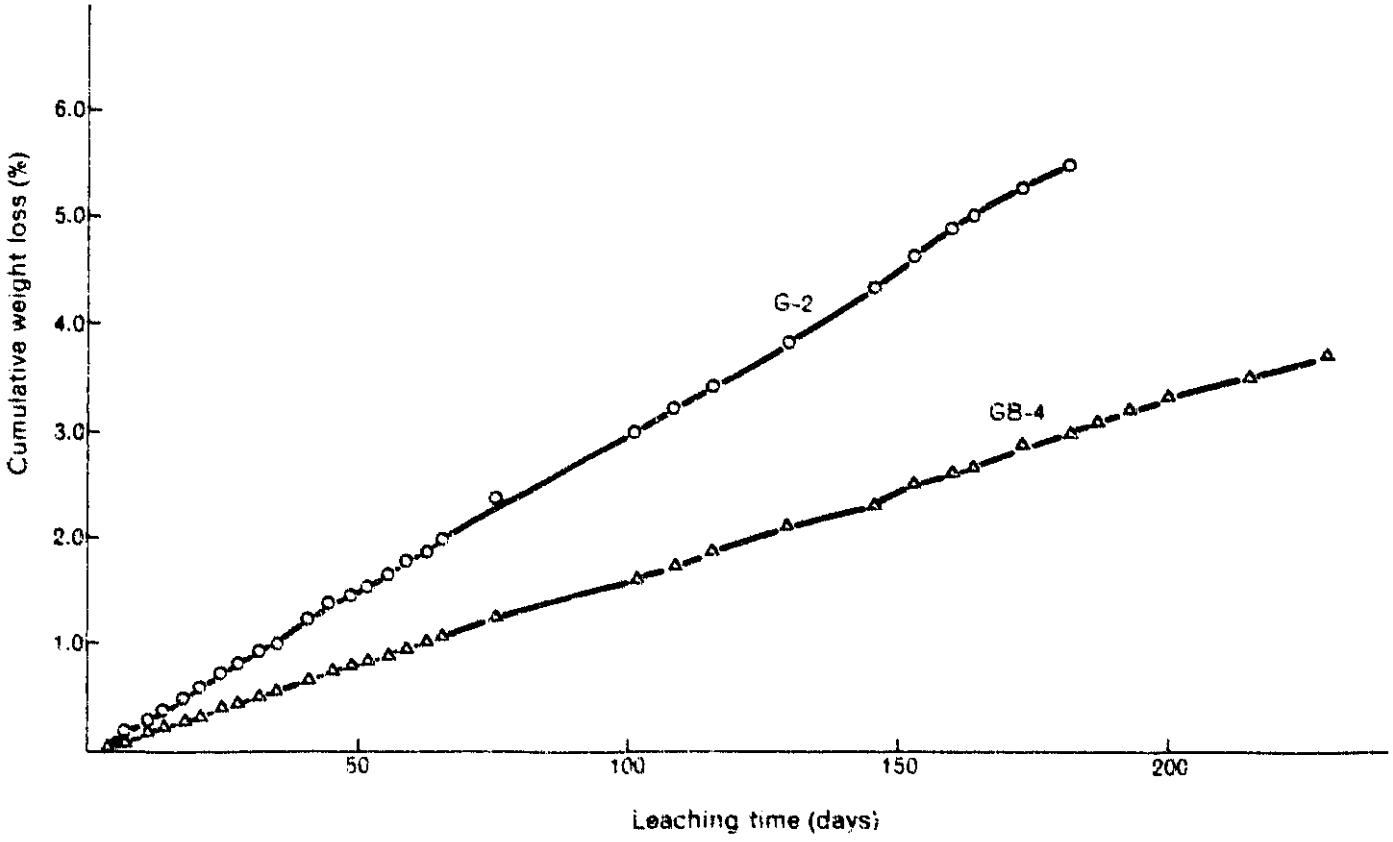

Fig. 5. Cumulative weight loss vs. leaching time for G-2 and GB-4.

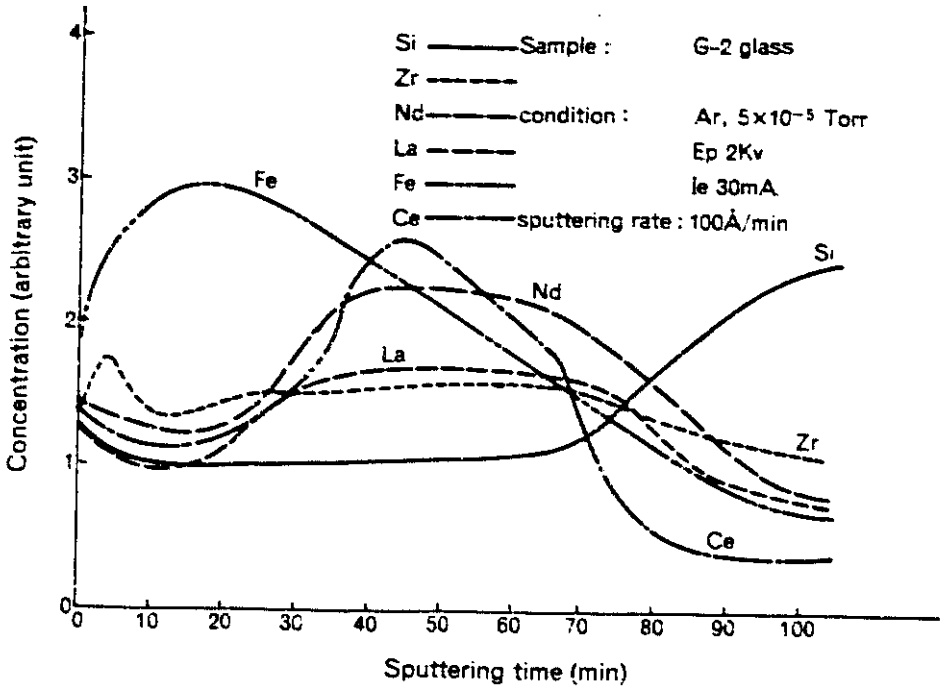

Fig. 6. Depth-compositional profile for a surface of G-2 glass leached for 2 days.

4. Summary and discussion

It was found that leaching rate decreases gradually with increasing sample weight in two stagnant phases test. It may be considered that this phenomenon results from the formation of hydrated layer composed of extracted ion in solution. It is necessary to choose an optimum ratio of leachant to surface area, for experiments.

The influence of pH on leaching rate is very small in the alkaline region ($7 < pH < 10$) for three glasses. On the other hand, as GB-1 and GB-4 glasses contain more SiO_2 than G-2 glass, GB-1 and GB-4 glasses are expected to be more durable than G-2 glass in the acid region.

In long-term leach tests with the Soxhlet appratus, the results show a linear dependence of weight loss with time. But a detailed analysis showed that the curves could be considered as composed of a number of successive parabolas.

These phenomena could be explained by the following mechanism; iron, zirconium and rare earths (La, Ce, Nd) gradually concentrated at the surface of the glass and the thickness increases with exposure time. This reaction layer seems to consist mostly of oxides or hydroxides of these metals and act as a diffusion barrier to migration of other elements. Then, the peeling of this layer was observed as the thickness of the layer increases up to several microns.

Subsequently the two steps of layer formation and peeling seem to take place alternately.

References

(1) Tymochowicz, S. "A Collection of Results and Methods on the Leachability of Solidified High Level Radioactive Waste Forms", HMI-B-241, April, (1977).

(2) "Characterization of Solidified High-Level Waste Products" Technical Reports, No.187, IAEA, Vienna, (1979).

(3) Mendel, J. E. et al.: "Annual Report on the Characteristics of High-Level Waste Glasses "BNWL-2252, June, 1977).

Preparation of SUS-316 Working Standards (2) *

Akira KAYA, Yoshifusa OHUCHI, Tohru SONE,
Shigeo AKIYAMA and Fumiaki SAKAI

The analysis of chemical composition of materials used as fuel cladding, plug, and other assembly parts are very important for quality control of the fuel fabrication process and evaluation of reactor safety.

Recently most of these analyses by wet methods have been replaced by X-ray fluorescence because of its rapidness and accuracy. But this X-ray fluorescence method depends on a comparative method with Standard Reference Materials (SRMs).

We can purchase similar SRMs of stainless steel from JSS-series of the Iron and Steel Institute of Japan and from the National Bureau of Standard of U.S.A. But both the institute and the bureau do not have many kinds of SRMs and besides their compositions are different from the application range for specifications of FBR type materials.

We reported previously the preparation of some working standards on zirconium alloys and stainless steels for X-ray fluorescence method. The present describes the preparation of working standards on stainless steel SUS-316 of which alloy are used as FBR type materials.

The working standard samples were prepared from nickel, chromium, silicon, molybdenum and manganese as alloying elements as well as carbon, phosphorous, sulfur, nitrogen, boron, arsenic, zirconium, tantalum, tin and tungsten as impurities, using high frequency-vacuum melting process.

---

* Presented at the Annual Meeting of the Japan Society for Analytical Chemistry (Cot. 1979).

The prepared sample ingots were at first examined on the homogeneity by X-ray fluorescence analysis, and they were comfirmed to have sufficient homogeneity.

The tentative methods of the analysis for these materials were studied at the analytical technique workshops consisting of three members, Power Reactor and Nuclear Fuel Development Corporation, Central Research Laboratory of Sumitomo Metal Industries Co., Ltd., and Central Research Laboratory of Kobe Steel Co. Ltd. The analytical methods were chosen for each element as shown in Table 1.

The target elements of these working standards were co-analyzed by these three members, and the certified values were decided as shown in Table 2.

These working standards were analyzed by X-ray fluorescence, using the JSS and NBS standards in the joint works.

Thus, it was confirmed that these samples could be used satisfactorily as working standards.

Table 1. The methods used for analysis of the working standards.

Element	Analytical method	Element	Analytical method
C	Coulometry Conductometry	Mo	Photometric determination with thiocyanate
Si	Gravimetry Photometric determination as molybdenum blue	B	Photometric determination with curcumine after distillation Extraction-photometric determination with methylene blue
Mn	Photometric determination as permanganate Atomic absorption spectrochemical analysis	N	Distillation and neutralization titration
P	Photometric determination as molybdenum blue	As	Photometric determination as molybdenum blue
S	Combustion and coulometry Combustion and neutralization titration	W	Photometric determination with TAPC-thiocyanate after chloroform extraction
Ni	EDTA titration after precipition with dimethylglyoxime	Sn	Extraction-photometric determination with TOP
Cr	Ammonium ferrous sulfate titration	Ta	Extraction-photometric determination with victria blue B
		Zr	Photometric determination with aresenazo-Ⅳ after TTA extraction

Table 2. Certified value of the working standards (SUS-316).

Unit ; %

Element / Sample	C	Si	Mn	P	S	Cu	Ni	Cr	Mo	V	Co	Ti	Al	As	Sn	Nb	Zr	W	Ta	Sb	B	N	O
SS-1	0.041	0.036	1.00	0.028	0.010	0.001	9.04	14.91	3.89	0.001	0.007	0.003	<0.002	0.009		<0.002					0.0022	0.0041	
SS-2	0.053	0.49	1.47	0.029	0.009	0.082	11.05	16.82	2.85	0.055	0.052	0.061	0.035	0.008		0,025					0.0022	0.0046	
SS-3	0.011	1.05	2.09	0.030	0.015	0.210	13.37	19.86	2.09	0.114	0.207	0.100	0.037	0.007		0.052					0.0031	0.0122	
SS-4	0.049	1.49	2.45	0.026	0.009	0.394	15.17	19.89	1.05	0.303	0.208	0.240	0.118	0.007		0.119					0.0028	0.0051	
SS-5	0.042	0.50	1.70	0.011	0.007		13.39	17.36	2.47					(<0.003)	0.001		0.008	<0.005	<0.001	(<0.0002)	(<0.0001)	0.0049	0.0064
SS-6	0.078	0.50	1.67	0.020	0.012		13.52	17.39	2.50					0.011	0.010		0.017	0.010	0.004	0.0010	0.0013	0.0126	0.0053
SS-7	0.101	0.51	1.67	0.031	0.024		13.47	17.42	2.51					0.018	0.020		0.020	0.022	0.008	0.0185	0.0025	0.0204	0.0036
SS-8	0.13'	0.51	1.68	0.040	0.032		13.50	17.42	2.50					0.033	0.029		0.058	0.030	0.014	0.0030	0.0037	0.0312	0.0041

Health and Safety Division

Activity of Health and Safety Division (Jan. 1979—Mar. 1980)

1. Organization and Personnel (March 31, 1980)

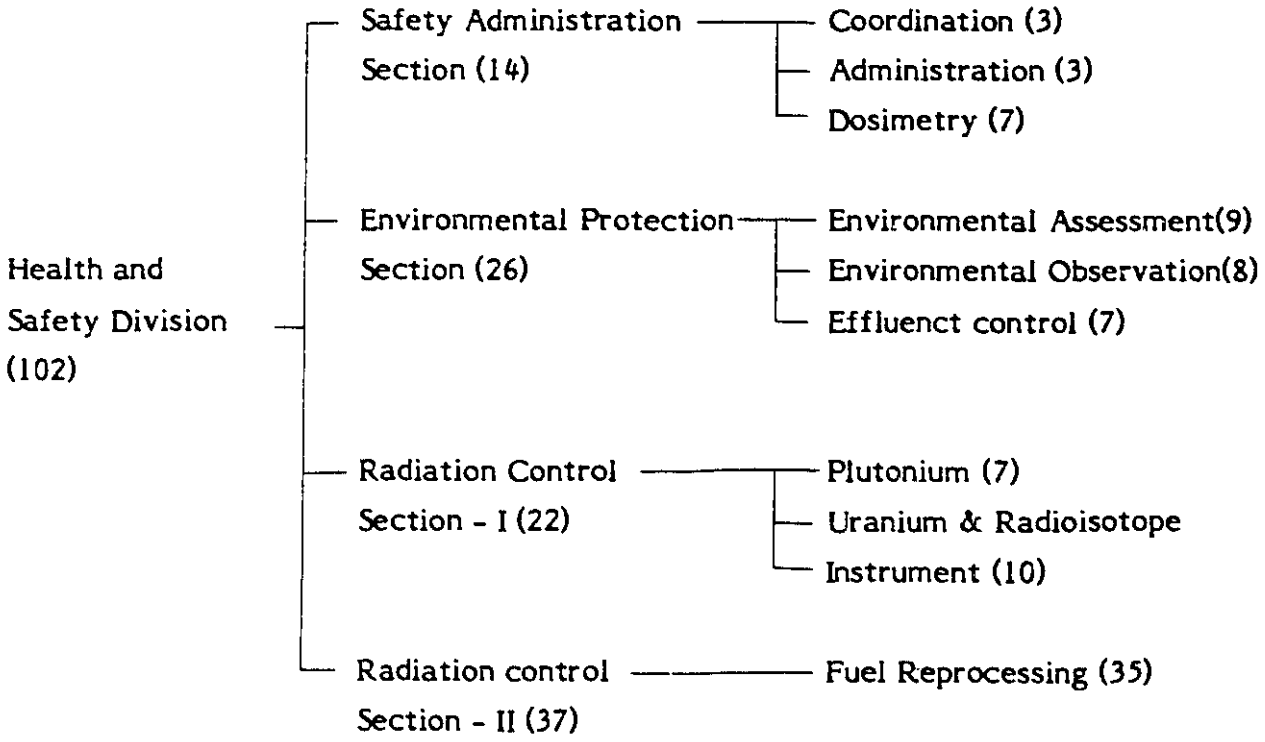

2. Safety Adminstration Section

2.1 Dosimetry

All radiation workers have been routinely monitored by using TLD badges and finger rings. Measurements are made of gamma, beta and neutron radiation for the whole body, and of gamma and beta radiation for the fingers. The period for wearing routine dosimeters is 3 months, and doses are measured and recorded every 3 months.

The maximum external radiation doses of the personnel for the whole body were 480 mrem for 3 months, and 680 mrem for the fisical year 1979 (from April 1979 to

March 1980). The total exposure by individual monitoring at PNC Tokai Works was 111 man-rems for the fisical year 1979.

The internal radiation monitoring of the personnel was carried out by means of urine bioassay, lung monitoring or whole body counting once a year. The type of monitoring depends on the kind of radiation work.

In the fiscal year 1979, the numbers of employee, non-employee and visitors in controlled areas of Tokai Works totalled to 1,134, 6,306 and 5,346 respectively, but no radioactive materials have been detected in them by the routine monitoring.

We have sent the history of personnel radiation dose to the Radiation Dose Registration Center for Workers. We have distributed a radiation control pocketbook to all our radiation workers so that they always have their own radiation dose records and medical examination records.

A new TLD badge system for personal dosimetry based on photon counting method was developed under the cooperation with Matsushita Co. Ltd. In 1979, a method of neutron and beta dosimetry was studied by using $Li_2B_4O_7$ TLDs.

A data processing system has been operated in PNC Tokai Works to process and keep the personnel exposure records since January 1979.

2.2 Health and Safety

The Advisory Committee meeting on Health and Safety and the Technical Committee meeting on Safety were held monthly to evaluate the safety of the newly planned operations and manuals or new ideas for the promotion of safety.

3. Environmental Protection Section

3.1 Environmental Monitoring

The environmental monitoring has been continued as before; samples of sea water, soil, selected agricultural products and marine products have been collected and analyzed periodically in the environs of the Tokai Works.

The environmental gamma-dose rate has been continuously measured at many points inside and outside of the site by using NaI scintillation detectors and TLD dosimeters. The results obtained have shown no radioactivity attributable to the activities of Tokai Works.

3.2 Effluent Release Control

Liquid effluent released from the facilities of Tokai Works has been collected

at each pit of the facilities and discharged to the site environs after confirming that radioactive nuclides, suspended substances, oil, fluorine, color bacilli, heavy metal ions, pH-value, and other pollutants were less than the authorized limits.

At the end of each month, composite effluent samples have been analyzed for ^{239}Pu and U contents.

4. Radiation Control of Facilities

4.1 Plutonium Facilities

Following the previous period, the radiation control for the fabricating facility of ATR "Fugen" fuel has been carried out. Also several glove-boxes have been dismantled and removed. There has been no case of radiation levels exceeding those specified in the regulations.

4.2 Uranium Facilities

The radiation control for uranium facilities has been carried out. Some equipment has been dismantled and removed. There has been no case of radiation levels exceeding those specified in the regulations.

4.3 Reprocessing Plant

The radiation control has been carried out as previously. A new evaporator for the acid recovery process was installed and inspected successfully. Decontamination and repair works at the low-active pipeline-connecting cell in the Auxiliary Active Facillity were completed by the end of September 1979. Following these remedial works, test operation was resumed, and two campaigns, i.e., the Pre-Guarantee campaign (Oct.30~Dec. 24, 1979) and Guarantee Test campaign with PWR fuels (Jan. 7 ~ Feb. 20, 1980) were carried out. Occupational exposure related to these operation was controlled and kept under the specified limits set by the regulatory body.

An abnormal air-contamination occurred in the plutonium operation area on October 1, 1979. The maximum air concentration of alpha activity amounted to 1×10^{-8} μ Ci/cm^3 (one-hour average), but no personnel inhaled plutonium from the contaminated air.

Design specifications for radiation control equipment and instruments have continually been reviewed for new facilities such as krypton recovery pilot process, plutonium conversion test facility, cask management facility.

4.4 Instrumentation

Radiation monitoring instruments used in the Health and Safety Division have been periodically inspected and calibrated. Tracerbility to the national standard was established for the γ -ray measuring instruments.

4.5 Protection Techniques Against Radioactive Aerosols.

Routine "Mask-Man Test" has been performed for the workers in controlled area.

Determination of Iodine-129 in Environmental Samples by Neutron Activation Analysis*

Aiji YAMATO, Hiromi KATAGIRI
Tamotsu NOMURA and Yoshihisa KITAHARA

1. Introduction

Iodine-129 has an extremely long half-life (1.7×10^7Y), and decays with beta emission (100%, β^- of max. 150KeV) to ^{129}Xe followed by emission of a 39KeV gamma-ray. The nuclide exists in the environment brought about from natural and man-made sources. The natural sources are spontaneous fission in uranium ores, spallation reactions on xenon in the upper atmosphere, and neutron capture reactions on tellurium. Various estimates of the natural abundance have been[1) ~ 6)] made, leading to values which range from 10^{-15} to 10^{-12} atoms of ^{129}I per atoms of ^{127}I in the hydrosphere, the atmosphere and the biosphere. The major artificial nuclide originates from nuclear weapons tests and fuel reprocessing plants. Especially as a result of the recent growth of nuclear industry, ^{129}I has been released into the environment[7) ~ 15)]. Once it is released to the environment, it tends to persist there for a long duration because of its long half-life. The radiation dose received by man from the environmental presence of ^{129}I should be evaluated in connection with the long-term survey of public dose commitment from artificial radionuclides. Although some methods have been developed for measuring ^{129}I, direct measurements of ^{129}I in environmental samples were difficult because of the low specific activity, the low environmental level and the low-energy γ radiation of ^{129}I. To date, all methods used practically for determining ^{129}I in environmental samples are those based on neutron activation by the nuclear reaction ^{129}I (n,γ) ^{130}I, and successive γ - spectrometry of ^{130}I or mass spectrometry of ^{130}Xe, the daughter of ^{130}I.

*Presented at the Annual Meeting of the Japan Radiation Research Society (November , 1979).

The present paper describes a method for the determination of ^{129}I in environmental samples by means of neutron activation method with γ -ray spectrometry.

2. Experimental

2-1 Samples and Pretreatment

Seaweeds, vegitables, rice grains, soils and milk were sampled in Tokai-mura in 1979. The collected samples were dried in a low-temperature oven or a freeze dryer. The dried samples were ground and passed through a 8-mesh sieve. To a 20g aliquot of ground sample, ^{125}I was spiked as a yield monitor. The spiked sample was rolled into a cigar-shape with small amounts of silica wool. The roll was placed in an inner tube of quartz combustion apparatus (Fig. 1a) and ignited at 1000°C in the oxygen stream for sublimation of iodine. During the combustion, dry oxygen was passed through the sample at a rate of 0.2 liter per minute. Furnace 1 was moved from the one end of the tube slowly to the sample placed in the midway of the tube for combustion. The off-gas passed through a higher temperature part of the tube, where the rest of organic matter in the off-gas from the sample was burned completely, and then was introduced into a small bed of a activated charcoal of about 3g. Iodine in the off-gas was adsorbed on the charcoal. Then the iodine absorbed on the charcoal was transferred to another small activated charcoal bed of about 0.5g with combustion of the first charcoal. The oxygen flow during the combustion was controlled at a rate of 0.1 liter per minute. The second activated charcoal bed was transferred into a quartz tube of 8mm ϕ, and the tube was evacuated as it contained the charcoal. The end of the quartz tube containing the activated charcoal was heated by a furnace at 1000°C, while the other end of the tube was cooled by liquid nitrogen (Fig. 1b). The tube was thus heated for about an hour and then sealed off at the cooled end of the tube to make an irradiation ampoule.

2.2 Neutron Irradiation

The neutron irradiation for the prepared ampoules were made in the T-pipe of a JAERI reactor "JRR-4" during 40 minutes in a thermal neutron flux of $8 \times 10^{13} n/cm^2 \cdot sec$. Each set of the samples was irradiated with comparator standards containing known amounts of ^{129}I.

Neutron capture reactions for iodine take place during the irradiation according to the formulas.

(1) $^{127}I(n,\gamma)\ ^{128}I$ (β^-, γ, 25 min)
(2) $^{127}I(n, 2n)\ ^{126}I$ (β^-, γ, 13d)
(3) $^{129}I(n,\gamma)\ ^{130}I$ (β^-, γ, 12.5h)
(4) ^{127}I (multi-neutron capture) ^{130}I
(5) $^{81}Br(n,\gamma)\ ^{82}Br$ (β^-, γ, 36h)

The reactions (4) and (5) may interfere with measurements for determination of ^{129}I.

2-3 Decontamination and Measurement

The ampoule was opened in a sealed plastic bag containing CCl_4, and the contained iodine was dissolved with CCl_4. Two milligrams of iodine was added here for easy handling in the following chemical separation. The ^{130}I with carrier iodine was extracted into CCl_4, then was back-extracted into SO_3-water and finally was precipitated as AgI at pH < 1, and the precipitate was mounted on a millipore filter paper. The activity of iodine was measured with a Ge(Li) detector. Each activity of ^{126}I, ^{128}I and ^{130}I was calculated from the gamma-ray spectrum. The chemical yield of this method was calculated by counts of ^{125}I.

3. Results and discussion

The gamma spectra obtained for the ^{129}I standard and the sample are shown in Figs.2a and 2b respectively. While the peaks corresponding to ^{130}I are clearly shown in Fig. 2a, no ^{130}I peaks are detected in Fig. 2b. The peaks for ^{128}I, which must have been produced during irradiation through the reaction (1), are also not present in the spectrum shown in Fig. 2b, probably due to the quick decay of this isotope during the cooling period (half life of ^{128}I: 25min). On the contrary, the peaks for ^{126}I which was produced through the reaction (2), are shown in Fig. 2b. No peaks for other iodine isotopes were observed. Table 1 gives a comparison of values observed for several types of samples collected at Tokai-mura. No ^{129}I concentration was found to exceed the detection limit by this method, which is about 0.01 pCi for a dry sample of 10g.

The results mentioned above demonstrate that the removal of foreign radio-isotopes before and/or after irradiation is very important for measurements by a high resolution γ -spectrometer with Ge(Li) detector, since low-level ^{129}I and other iodine isotopes in environmental samples may be contaminated by foreign elements giving many γ -rays after irradiation. The method described here was proved to be sufficiently capable of purifying iodine from interferring elements except for bromine.

Bromine-82 is produced by the reaction (5). Although the photo-peaks of ^{82}Br obtained with the high-resolution Ge(Li) detector is not overlapped by those of iodine isotopes, the compton-scattered γ-rays from ^{82}Br may notably interfere with the low-level counting of iodine isotopes. Elimination of ^{82}Br is required before measurements, since it has a harmful influence to determination of the activity a low-level ^{130}I.

Table 1. Results of anslysis.

Sample	I-127 * ($\mu g/g$)	I-129 (10^{-3} pCi/g)	$^{129}I/^{127}I$ Atom ratio (10^{-7})
Seaweed	210 ± 11	<5.1	<1.5
Cabbage	4.2 ± 1.3	<0.9	<15
Rice	34 ± 1.2	<2.1	<3.6

* Determined by counting of I-126

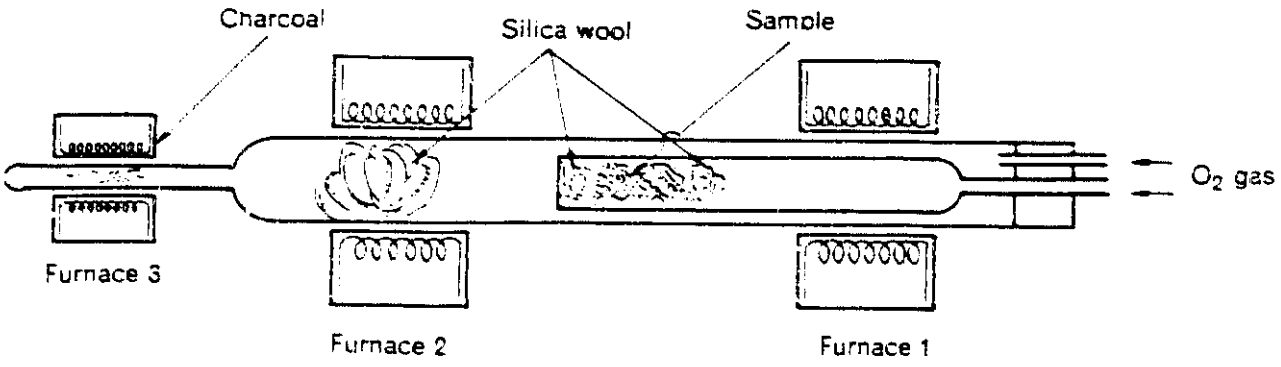

Fig. 1a. Diagram of sample combustion apparatus.

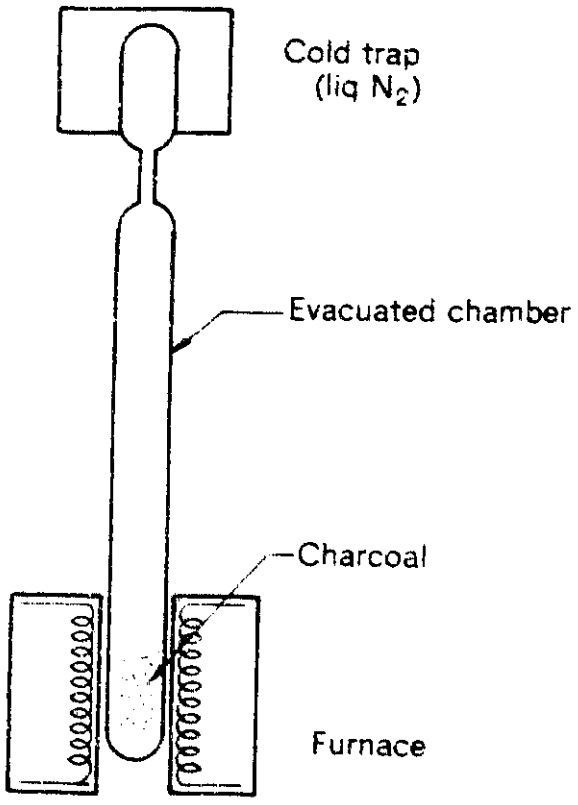

Fig. 1b. Distrillation assembly.

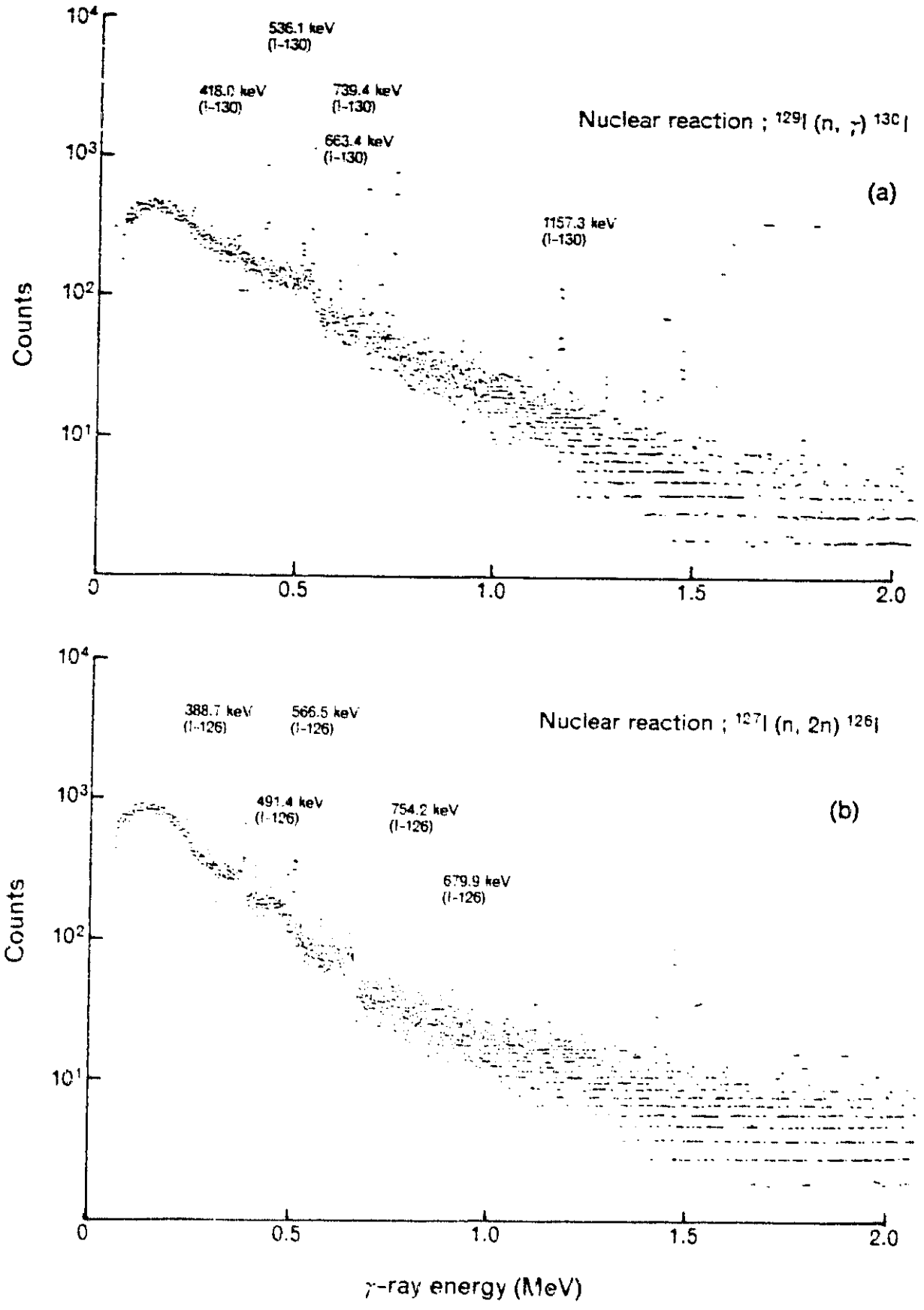

Fig. 2. Gamma ray spectra of irradiated reference sample (a) and brown algae (b).

References

(1) Purkayastha, D. C. and Martin, G. R. : Can. J. Chem Vol. 34, 293 P299 (1956)

(2) Studier, M. H. , Postmus, C. , Mech, Jr. , J., Walter, R. R. and Sloth, E. H. : J. Inorg. Nucl, Chem. , Vol. 24 P755 P761 (1962)

(3) Edwards, R. R. : Science, Vol. 137 P851 P853 (1962)

(4) Takagi, J. , Hampei, W. and Kiratn, T. : Earth planet Sci. Lett. Vol. 24, 141 (1974)

(5) Srinivasan, B. , Alexander E. C. , Jr. and Manuel O. K. : Science, Vol.173, 327 (1971)

(6) Cochran J. A. , Smith D. G. , Magno P. J. and Shien B. : HEW Report PRH/NERHL 70-3 (1970)

(7) Bryant P. M. : Health physics, Vol. 19 P611 P616 (1970)

(8) Matuszek J. M. , Paly J. C. , Goodyear S. , Paperielle C. J. and Gabay J. J. : IAEA/SM 180-39 (1973)

(9) Daly J. C. , Goodyear S. , Paperiello C. J. and Matuszek J. M. : Health physic, Vol. 26, P333 P342 (1974)

(10) Brauer F. P. , Soldat J. C. , Tenny H. and Strebin R. S. , Jr. : IAEA/SM 180/34 (1974)

(11) Brauer F. P. and Ballou N. E. : IAEA/SM 191-20 (1974)

(12) Brauer F. P. : BNWL-SA-4983

(13) Soldat J. K. , Brauer F. P. , Cline J. E. , Fager J. E. , Kleppar B. , Rickard W. H. , Vaughan B. E. and Watson D. G. BNWL-1783 (1973)

(14) Soldat J. K. : BNWL-SA-4879 (1974)

(15) Brauer F. P. and Tenny H. : BNWL-SA-5287 (1975)

Preliminary Estimation for Derived Working Limit of Tritium Concentration in Sea Water off the PNC Tokai Fuel Reprocessing Plant*

Kunihiko SHINOHARA, Yoichiro KISHIMOTO
and Yoshihisa KITAHARA

Tritium is the most abundant radionuclide in the liquid waste discharged from the PNC Tokai fuel reprocessing plant to the Pacific coastal water. The discharged quantity of tritium, which is mainly in a chemical form of tritiated water (HTO or T_2O) behaving like H_2O, should not exceed 1.89×10^{15} Bq (5.11×10^{4} Ci) per year.

Tritium has been considered to be one of the least hazardous radionuclides, because it emits only a beta-particle with an average energy of 0.0057 MeV and it is excreted from the human body with a short biological half-life of about 10 days.

Recent studies, however, showed that a few percent of the nuclide in the form of tritiated water was incorporated into the various components of the cell of animals and subsequently eliminated with a half-life of the order of one-third of the life-span.(1)

Since tritium in the sea water will be incorporated into marine organisms, important foodstuff for Japanese people, we can not absolutely exclude the potential risk of tritium discharged into the sea.

The present paper proposes an estimation on the derived working limit (DWL) in the sea water off the PNC Tokai fuel reprocessing plant.

The exposure pathway considered here is shown in Fig. 1, where TFWT means the Tissue-Free-Water Tritium and TCT the Tissue-Combined Tritium.

---

* Presented at the 14th Annual Meeting of Japan Health Physics Society (April, 1979).

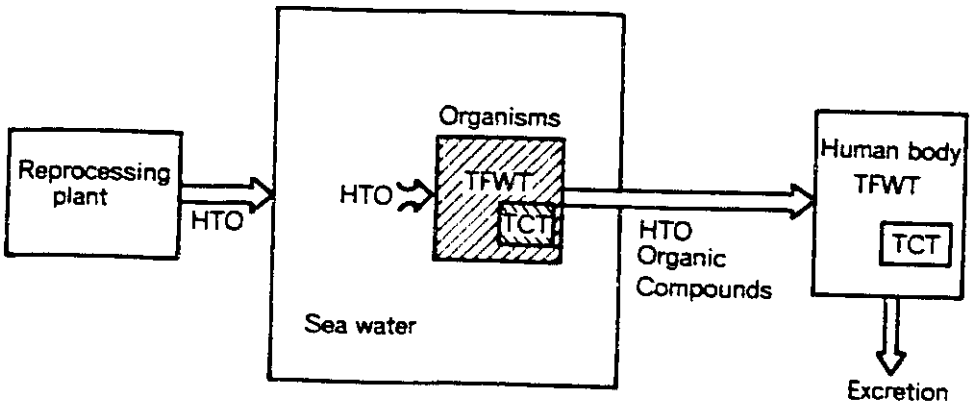

Fig. 1. Assumed pathway for calculating DWL of tritium concentration in sea water.

The concentration factor of tritium is assumed to be unity for all species of marine organisms. Strand et al[2] conducted experiments on the tritiation of aquatic animals, and the final concentration factors of 0.89, 0.87, 0.82, 0.92, 0.77 and 0.88 were calculated for TFWTs of carp, clam, crayfish, snail, periphyton and pondweed, respectively. In the Regulatory Guide 1.109 of U.S.NRC, the concentration factors of 0.9 and 0.93 are proposed for the fish and the invertebrate in saltwater, respectively.[3]

A metabolic model of tritiated water in man can be presented as a simple three-compartment model shown in Fig. 2.[4]

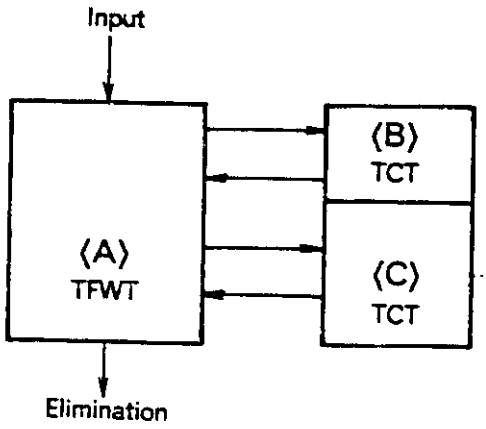

Fig. 2. Three-compartment model of tritium dynamics in human body.

In this model, <A> is the compartment of TFWT with a mean elimination half-time of 9 days, and <B> and <C> are the compartments of TCT with mean half-times of 30 and 450 days, respectively.

Ingested tritiated water is assumed to be completely and instantaneously absorbed from the gastrointestinal tract, and to mix rapidly with the total body water.[5] A small fraction of the water is combined with tissue components and eliminated slowly.

If organic compounds of tritium are ingested, a considerable fraction may be dissolved into tritiated water in the gastrointestinal tract.[5] Orally ingested organic compounds can be treated in the same way as tritiated water, using the concept of average whole organ dose.[6]

Tritium burden in the human body was calculated for chronic ingestion by the three-compartment model, and the result is shown in Fig.3. Assuming that the ingestion rate is 1 Bq per day (2.7×10^{-11} Ci per day), the equiblium body burden of tritium is 14.5 Bq (3.92×10^{-10} Ci) and the annual dose equivalent to total body is calculated to be 6×10^{-9} Sv (6×10^{-7} rem).

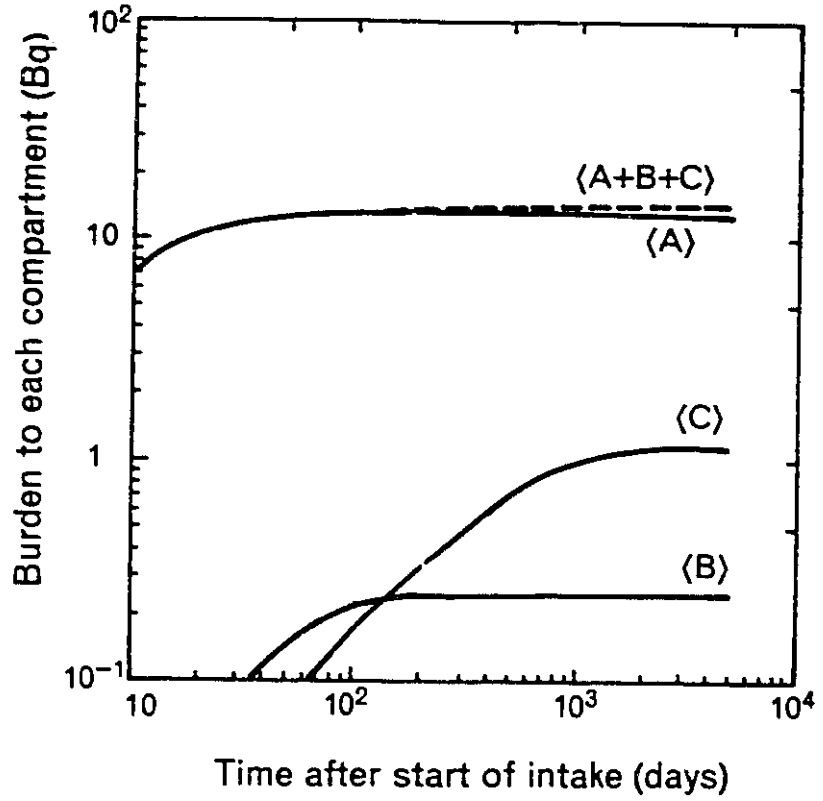

Fig. 3. Tritium burden to each compartment of human body for chronic intake rate of 1 Bq/day.

The ICRP recommends a value of 5 mSv (500 mrem) as the annual dose equivalent limit to an individual of the public,[7] so that the annual limit of intake (ALI) of tritium can be calculated from the formula;

$$ALI = \frac{\text{annual dose equivalent limit}}{\text{annual dose equivalent by ingestion of unit activity}}$$

$$= \frac{5 \times 10^{-3}}{6 \times 10^{-9} \times \frac{1}{365}}$$

Thus, ALI for an individual of the public becomes 3×10^{8} Bq (8×10^{-3} Ci).

The daily intake of marine foodstuff were estimated for the critical group near the reprocessing plant, and the values of 170, 40, 30, 10 and 10 grams per day were obtained for fish, algae, mollusca, shellfish and crustacea, respectively.

Assuming that marine foodstuff is only one carrier of discharged tritium, the DWL can be calculated according to the formula;

$$DWL = \frac{ALI}{\text{annual marine foodstuff intake} \times \text{concentration factor}}$$

$$= \frac{3 \times 10^{8}}{(170+40+30+10+10) \times 365 \times 1}$$

Thus, the value of 3×10^{9} Bq per m^3 (8×10^{-2} Ci per m^3) can be obtained as the DWL of tritium concentration in the sea water off the Tokai fuel reprocessing plant.

References

(1) Silini, G. , Metalli, M. and Vulpis, G. : Radiotoxicity of Tritium in Mammals, Critical analysis of the extraporation to man of the results of tritium incorporation into animal tissue, EUR 5033e (1973).

(2) Strand, J. A. and Thompson, R. C. : Biological Effects of Tritium Release from Fusion Power Plants, BNWL-2022 (1976).

(3) U.S.NRC : Regulatory Guide 1. 109, Calculation of Annual Doses to Man from Routine Releases of Reactor Effluents for the Purpose of Evaluating Compliance with 10 CFR Part 50, Appendix I, Revision 1 (1977).

(4) Bennett, B. G. : Radiation Dose due to Acute Intake of Tritium by Man, HASL-253 (1972).

(5) ICRP Publication 30 Part I : Limits for Intakes of Radionuclides by Workers, Annals of the ICRP, vol.2 , No.3/4 (1979).

(6) Lambert, B. E. and Clifton, R. J. : Radiation Doses resulting from the Ingestion of Tritiated Thymidine by the Rat, Health Physics, vol.15, pp.3-9 (1968).

(7) ICRP Publication 26 : Recommendations of the International Commission on Radiological Protection, Annals of the ICRP, vol. 1, No.3 (1977).

Reprocessing Plant

Activity of the Reprocessing Plant (Jan. 1979—Mar. 1980)

The Hot Test from JPDR to GTP campaign was finished on February 24, 1980.

Throughout these campaigns, the plant was obliged to stop the operation in August 1978 because of the failure of the acid-recovery evaporator. However the installation of a new evaporator substituting the old one was very successfully performed without any significant trouble and the operation was resumed in October 1979. For the confirmation of the new evaporator capacity and operator's skill after one year of operation stoppage, Pre-Guarantec Test (called PGT) was carried out in November 1979, using 5.1 tons of spent fuel (2.3 tons from Fukushima BWR and 2.8 tons from Mihama PWR). After these steps, the final stage of the Hot Test-Guarantee Test (called GTP) was started in January 1980, using 6.8 tons of spent fuel from Mihama PWR. The GTP campaign was executed very smoothly and it was confirmed that the plant can be safely and successfully operated.

1. Hot Test

The summary records of Hot Test are shown in Table 1 and 2. From 31 tons of spent fuel, about 28 tons of uranium and 168kg of plutonium were recovered and the following items were proven through the whole period of Hot Test.

1) The workability, safety and processing capacity were certified to be satisfactory.
2) Purities of plutonium and uranium product were within the specifications (See Table 3 and 4).

3) Product recovery ratios were within the regulated value. (The recovery ratios of plutonium and uranium during Hot Test were 98.6% and 98% respectively.)
4) MUFs of plutonium and uranium were 0.5 ~ 1.1% and 0.2 ~ 1.7% respectively. (See Table 2)
5) Radioactivities of liquid wastes discharged into the sea were under the designed values.
6) Dose rate and concentration of radioactivities in water and air effluents were controlled under the regulated value.

Table 5 shows the radioactivities released into the environment. Though 1.2×10^5 Ci of krypton-85 was released during the Hot Test, in the near future Krypton Removal Demonstration Facility is to be constructed and operated for reduction of released radioactivity. Moreover about $70m^3$ of HALW (high active liquid waste) with about 6.1×10^6 Ci of retained activities has been already stored in the tanks.

2. Utilization of the Plutonium Product

About 45kg out of plutonium product was shipped to Plutonium Conversion Facility for fabricating mixed oxide fuel for the advanced thermal reactor "FUGEN". PNC will in this way contribute largely for the establishment of nuclear fuel cycle by the utilization of plutonium product from its own reprocessing plant.

3. Reception of Spent Fuel

About 44 tons of spent fuel were transported into the facility from August 1979 to March 1980 for post-hot-test operation. Most of these fuels were transferred with the domestic cask-HZ-75T, which was confirmed to be treated as safely as Excellox-3A cask. The former contains 7 assemblies of PWR type of 14 assemblies of BWR type per cask, while the latter can hold 5 assemblies of PWR of 10 assemblies of BWR type.

Table 1. Results of Hot Test.

Campaigns	1977	1978	1979	1980
JPDR	Sep.22~Dec.24 3.3tU			
BWR	Hot test started	Jan.24~Mar.27 4.7tU		
PWR		May.8~Jun.14 6.4tU		
GT·BWR		Aug.1~24 4.7		
Repair of acid-recovery evaporator		Aug.24 Failure of acid-recovery evaporator	Oct.30 Cell closing	
P·GT			Nov.19~Dec.24 5.1tU	
GT·PWR			Jan.19~Feb.15 6.8tU Hot test finished	

Table 2. Summary of Hot Test.

Campaign		JPDR	BWR	PWR	GT BWR	PGT		GT PWR	Total
						BWR	PWR		
Reactor		Japan power Demonstration reactor	Fukushima	Mihama	Fukushima	Fukushima	Mihama	Mihama	
Burn up (MWD/T)		110~ 5,640 Av. 3,890	6,640~ 10,200 Av. 9,390	10,840~ 19,470 Av. 14,830	10,200~ 11,900 Av. 10,800	10,200~ 11,900 Av. 10,800	19,400 28,000 Av. 21,100	19,600~ 30,000 Av. 21,500	
Initial Enrichment(%)		2.6	2.09	2.277	2.09	2.09	2.277 and 3.04	2.277 and 3.04	
Assemblies		57	24	16	24	12	7	17	157
Amounts of fuel (tU)		3.3	4.7	6.4	4.7	2.3	2.8	6.8	31
Product	U (t)	2.9	5.6	4.6	5.6	4.9		5.9	30*
	(Pu) (kg)	5.4	18.3	38	24	33		49	168
MUF	U (%)	1.1	0.2	0.7	0.5	0.5			
	Pu (%)	−0.8	1.7	−1.1	0.2	0.3			

*Since part of this value is returned to process, the inventory of UO_3 storage amounts to about 28t

Table 3. Impurities in uranium product (Sample of GTP campaign).

Items		Results	Regulation
Impurities		0.72 [%]	2.25 [%]
Activity	Zr- 95	1×10^{-3} [μCi/g-U]	0.5 [μCi/g-U]
	Nb- 95	1×10^{-3} "	0.5 "
	Ru-103	1×10^{-3} "	0.5 "
	Ru-106	1×10^{-3} "	0.5 "
	Cs-137	1×10^{-3} "	0.5 "
	Ce-144	1×10^{-3} "	0.5 "
Plutonium		5 [ppb/U]	10 [ppb/U]

Table 4. Impurities in plutonium product (Sample of GTP campaign).

Items	Results	Regulation
Metal impurities*	1,510 ppm (Pu)	5,000 ppm (Pu)
Fission product	50 μCi/g-Pu (Zr, Nb, Ru, Cs and Ce was not detected) **	50 μCi/g-Pu
Americium	140 ppm (Pu)	5,000 ppm (Pu)
Organic concentration	0.2 vol %	0.5 vol %
Insoluble residual	Non detected	5,000 ppm (Pu)

* Including uranium and excluding americium

** Below 4×10^{-2} μCi/g-Pu

Table 5. Radioactivities release to the environment.

Items / Campaign	Period	Kr^{85} Ci	H^3 (Ci)		Release to sea		
			to sea	to air	The number of times	Amount (m^3)	Total β Ci (Except H^3)
JPDR	'77 Sep.~Dec.	5.4×10^3	5.7×10	4.7	28	5,100	1.7×10^{-2}
BWR	'78 Jan.~Mar.	1.7×10^4	6.9×10	2.0	37	6,600	3.5×10^{-2}
PWR	'78 Apr.~Jun.	3.5×10^4	6.6×10^2	1.3×10	48	7,800	6.9×10^{-3}
GT·BWR	'78 Jun.~Oct.	1.3×10^4	1.4×10	1.0×10	80	14,900	1.0×10^{-1}
PGT and GT·PWR	'79 '80 Nov.~Feb.	5.0×10^4	1.7×10^3	2.1×10	264	48,400	2.5×10^{-1}
Total		1.2×10^5	2.5×10^3	5.1×10	457	82,800	4.1×10^{-1}

Experience in the Replacement of the Failed Acid-Recovery Evaporator at the Tokai Reprocessing Plant

Shotaro HAYASHI, Osamu YAMAMURA
and Sadao ARAYA

Abstract

Through the replacement of the failed acid-recovery evaporator for about eight months, valuable know-hows in connection with maintenance in a hot cell were obtained.

A new evaporator was made of stainless steel (25Cr-20Ni-0.25Nb), and was fabricated in Japan. Many mock-up tests for welding were performed and evaluated before actual manufacture, and the best welding procedure was selected based on the results of such mock up tests.

The welding works of the evaporator and connected pipes in the cell were carried out successuflly in spite of operational space limitations. Also the personal exposure had been well controlled and the contamination on human body and out-cell area had been prevented completely.

1. Introduction

On 24th August 1978, a leakage of process solution in the acid-recovery evaporator into steam condensate was detected by a radiation monitor on the steam condensate line, and the plant operation was stopped immediately.

As the result of inspection of the evaporator, defects were found at five points on the welded parts between the heating tubes and the upper tube sheet of the reboiler.

Based on the inspection results, it was decided to replace the evaporator as a whole, and then actual replacement work was started in March 1979. The replacement work was proceeded according to the following procedures: enlarging the cell opening, constructing the scaffolding, cutting and removing connected pipes and the evaporator, installing the new evaporator, welding the evaporator and pipes, removing the scaffolding, test-running the evaporator and finally closing the cell. The replacement work was completed entirely by the end of October 1979, and the plant operation was resumed in the following November.

The outline of the replacement work of the failed acid-recovery evaporator was already reported[1], and dismantling and removal works of the evaporator was also described in detail[2]. The present paper describes the detail of fabrication and installation work of the new evaporator.

2. Acid-Recovery Evaporator

The spent fuel reprocessing plant in the Tokai Works, with a capacity of 0.7 t-U/day, was designed and constructed for reprocessing the spent fuels from light water reactors. The acid-recovery unit is the equipment for treating the medium activie liquid waste as well as for recovering used HNO_3. A process flow sheet of the acid-recovery unit is shown in Fig. 1. The acid-recovery evaporator is of a thermo-siphon type which consists of a reboiler and a separation column, and it is made of stainless steel (25Cr-20Ni-0.25Nb, and SUS-304L).

The acid-recovery evaporator is normally operated under the following conditions: feeding rate of 2.3 m^3/h, temperature of 110°C, and HNO_3 concentration of 8 N in the reboiler. The net operating period since the beginning of the hot test amounts to about 3000 hours.

The acid-recovery cell containing the acid-recovery evaporator is located at the west side of the maintenance area crossing north to south in the main plant. This cell is provided with concrete walls of about 1 m thick. The floor level of the cell is 5.35 m underground, the ceiling is 16 m high, and the floor area is 58 m^2. The cell is installed with fifteen pieces of equipment and connected pipes.

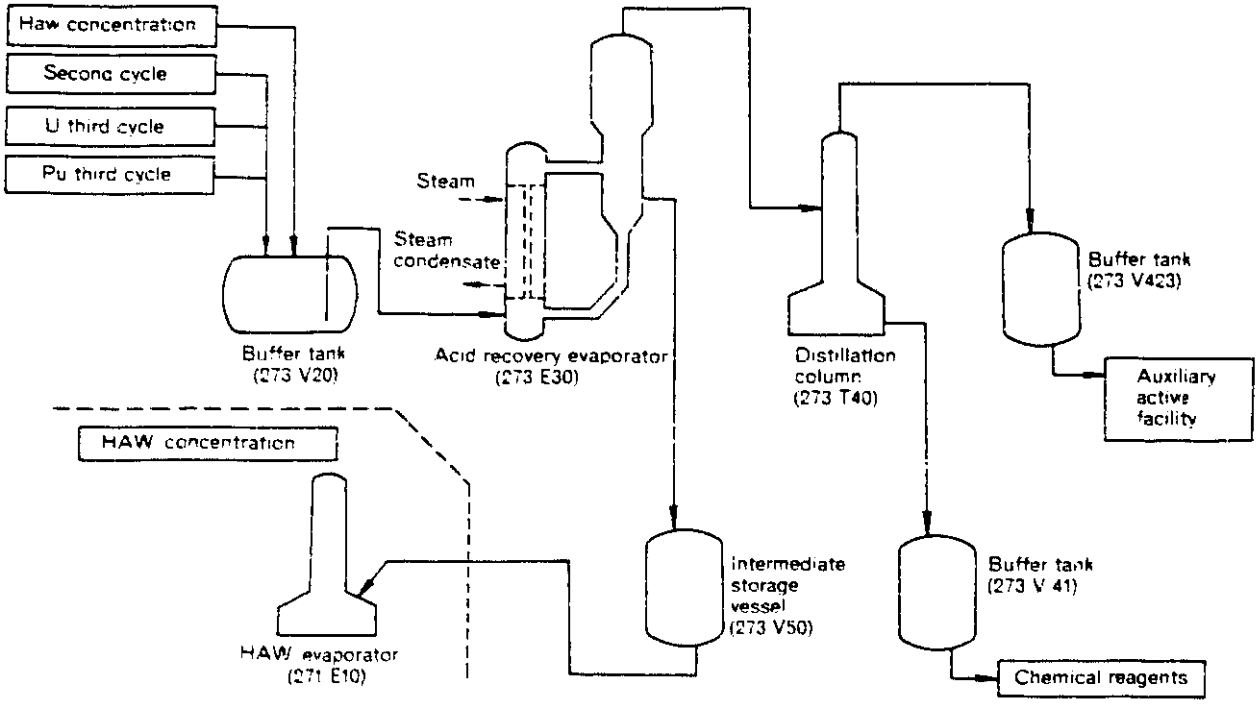

Fig. 1. Process flow sheet of acid recovery unit.

3. Fabrication of New Evaporator

3.1 Material

It was decided that the new evaporator was made of stainless steel similar to the old one and needed material was ordered to VDM Corporation in West Germany. This material called "CRONIFER 25-20Nb" is a kind of superior high chrome-nickel steel which is resistant to intergranular corrosion by adding niobium and minimizing the carbon content. The chemical composition of this steel is shown in Table 1.

Corrosion tests with HNO_3 on CRONIFER 25-20Nb, SUS-310S, SUS-316L, SUS-304L, and titanium were performed, and the results of corrosion tests are summarized in Fig.2 and Table 2. As these results show, it is apparent that CRONIFER 25-20Nb is superior to others in corrosion resistance.

3.2 Design

Though the new evaporator was designed on the basis of the old one, it has received some modifications such as deletion of the steam jet for liquid dilution, replacement of the perforated plates with the wire-mesh demisters, and supplement of the buffle plates in the reboiler, which were designed from the actual operating experiences.

3.3 Welding in the Factory

The new evaporator was fabricated in Japan in about three months as scheduled.

The TIG method which is a kind of arc welding was adopted for the welding. Prior to each welding, careful mock-up tests were performed to confirm welding procedures and to train the welders.

Special attention was paid to the welding of the tube sheet and heating tubes, since the defect in the old evaporator was found at these welded spots. As shown in Fig. 4, the joint of the old evaporator was simply fillet-welded, while in the new evaporator, a U-shape opening was prepared between the heating tube and tube sheet before welding. To obtain the good adhesion condition between the heating tube and tube sheet, the tube expansion was also performed around welding points with the special expander before and after welding. Each expansion rate of tubes was about 3%.

The cross section of the welded zone is shown in Fig. 5. The penetration situation of welded zone to materials is confirmed to be satisfactory.

Table 1. Chemical Composion of CRONIFER 25-20 Nb (%).

Item	C	Si	Mn	P	S	Ni	Cr	Nb
Specification	≤0.030	≤0.5	≤1.0	≤0.040	0.030	19~22	23~26	0.15~0.30
Measured value	0.014	0.28	0.79	0.024	0.004	20.55	23.40	0.20

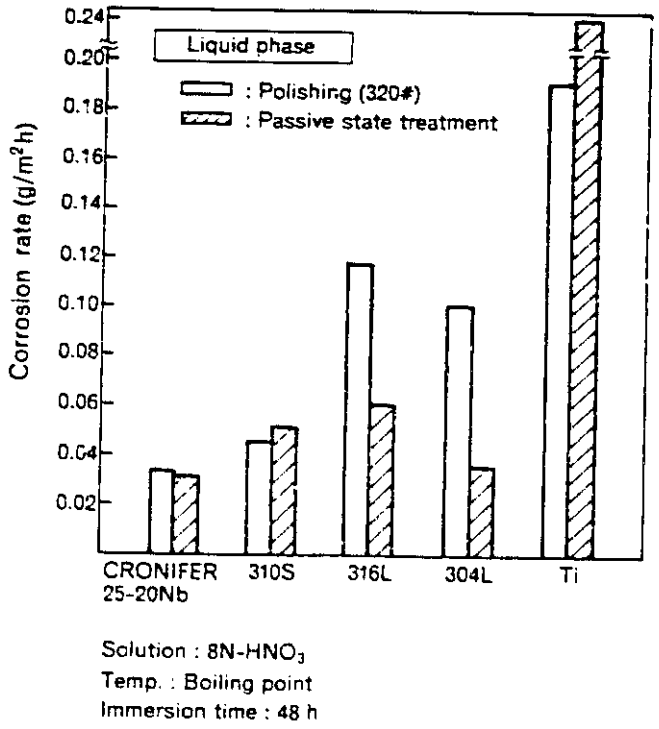

Fig. 2. Results of corrosion test with HNO_3.

Table 2. Intergranular corrosion of materials with HNO_3.

(Depth of corrosion : μm)

	Concentration of HNO_3					
	8N			11N		
Heat treatment	AS	W	W+T	AS	W	W+T
CRONIFER 25-20 Nb	0	0	0	0	10	10
SUS 310S	0	0	25	0	10	150
SUS 316L	0	0	0	30	25	35
SUS 304L	0	0	10	20	20	70
Ti	0	0	0	0	0	0

Heat treatment AS : As received
W : Welded
W+T : Heat treated (650°C, 1 h) after welding

Test conditions
Temp. : Boiling point
Immersion time : 48 h
Phase : Liquid

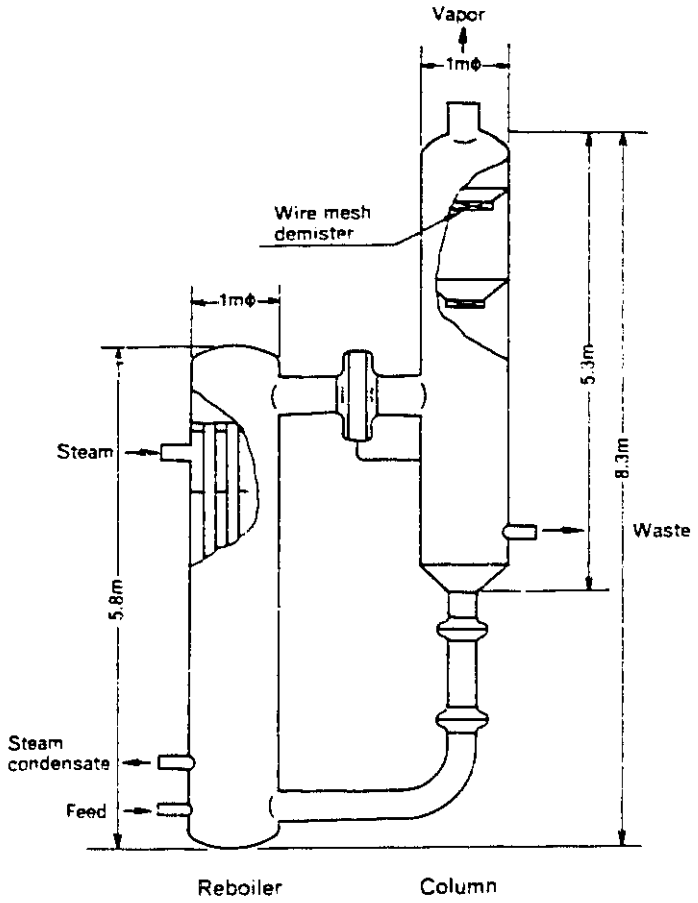

Fig. 3. New acid recovery evaporator.

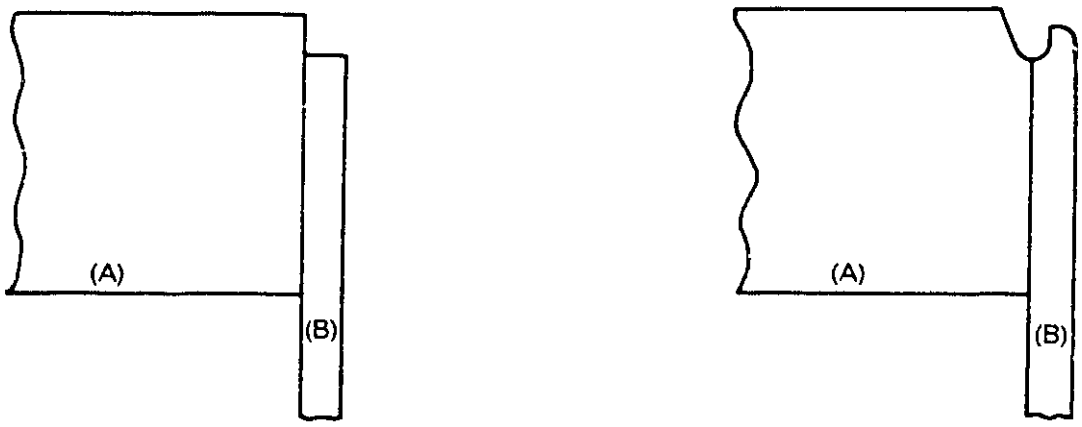

Old evaporator

New evaporator

(A) : Tube sheet (34mm in thickness)
(B) : Heating tube (42mm in outside-diameter)

Fig. 4. Shape of groove for welding of tube sheet and heating tubes.

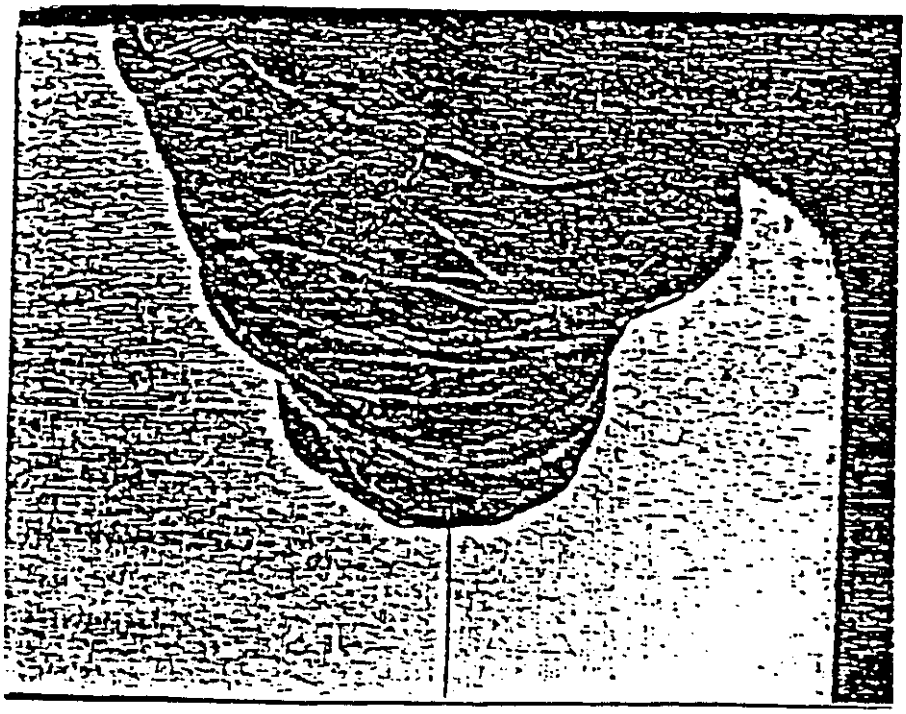

Fig. 5. Cross section of welded zone between heating tube and tube sheet.

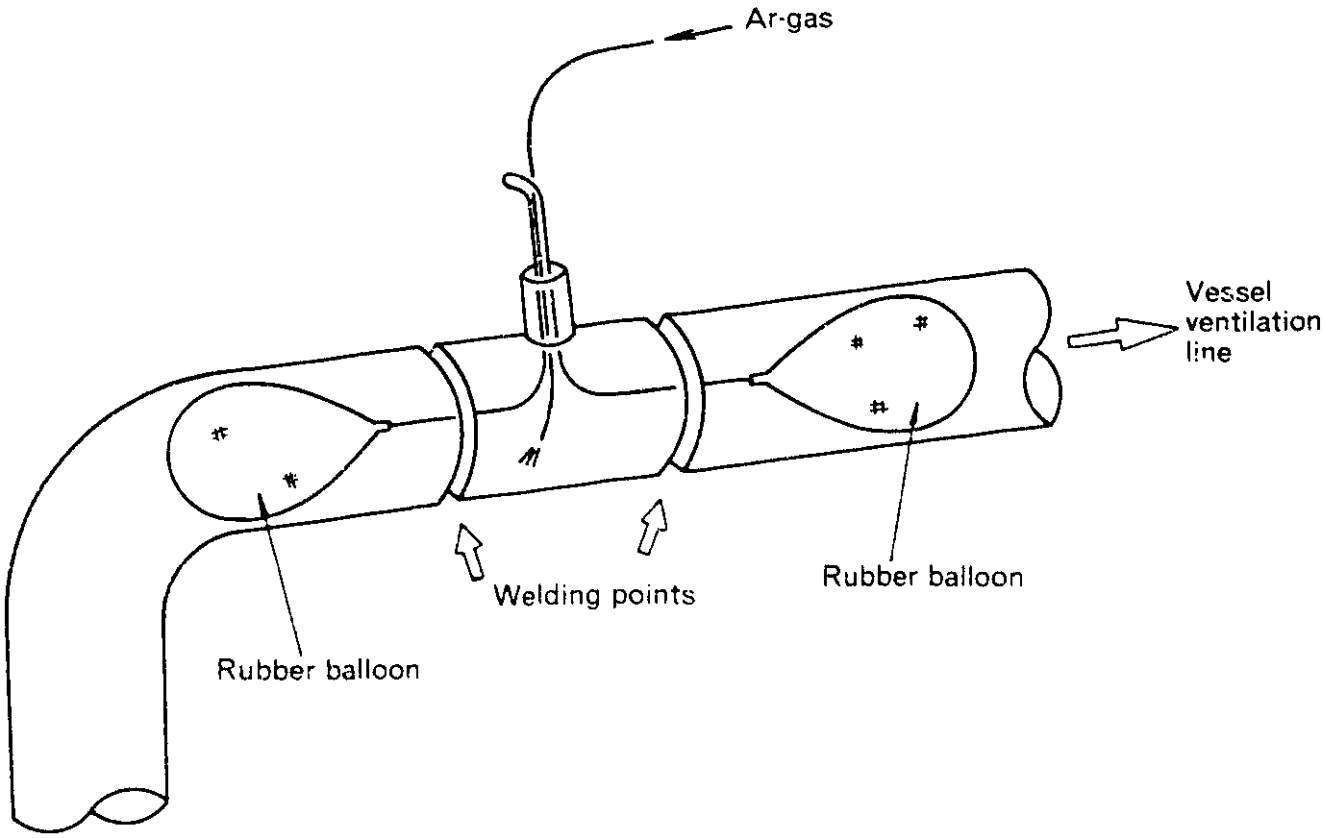

Fig. 6. Ar-gas sealing method for pipings connected with the vessel ventilation line in welding work.

4. Installation of New Evaporator

The new evaporator was composed of five components of a column, a reboiler, and three connection pipes. These components were carried into the acid-recovery cell and assembled after several adjustments such as direction, alignment, vertical centering, and level. The welding in the cell was begun with evaporator components, and then other connected pipes.

Several difficulties were supposed in welding in the cell; in addition to the operational space limitations, a welder must work wearing protective cloths and a full face mask, and several welders have to operate in rotation due to restriction of working time. Prior to the actual in-cell welding, the welders were trained in mock up tests with the protective cloths outside the plant.

The most serious problem in welding work is to shield the work piece with argon gas, and various attempts were made for shielding. Generally, a sealing method with a Hi-selon (polyvinyl alcohol film) near the welded part is used, but this method was not so effective for pipings connected to the vessel ventilation line because the welding was performed without stopping the operation of the ventilation line. Instead of this method, rubber balloons were used, and the nozzle for inserting the rubber balloons was plug-welded as illustrated in Fig. 6.

5. Radiation Control

The radiation monitoring in the cell has been carried out through the in-cell working of dismantling and removing the old evaporator and installing the new one. This monitoring included air dose rate, air contamination level, and surface contamination level. The air dose rate was significantly decreased to about 25 mR/h by removing the old evaporator. Also contamination levels after removal were about 10^{-13} Ci/cm^3 in the air and about 10^{-5} Ci/cm^2 on the surface.

The installation working in the cell was performed under such a condition. The value of personal exposure dose rate was limited to 300 mrem/week and 100 mrem/day. External exposure was measured with individual dosimeter which was checked on a daily basis, and the limited values above mentioned were well controlled by restricting the in-cell working time of any individual. The results of personal exposure dose during in-cell work are summarized in Table 3.

Internal exposure was prevented by the respirator covering whole face and was not detected for any individual through the entire in-cell working.

Use of protective cloths and green-houses were effective to prevent contaminations on human body and out-cell area.

Table 3. Personal exposure dose during in-cell work

	Number of person	Total exposure dose (man-rem)	Average exposure dose (m rem/person)	Maximum exposure dose for individual (m rem)
Cell opening	26	0.1	5	19
Construction of scaffolding	108	9.4	87	265
Dismantlement and removal of evaporator	149	17.2	116	363
Preparation for installation	132	13.8	105	200
Installation of new evaporator	171	17.8	116	334
Cell closing	82	0.8	10	51
Total	191	59 1	309	850

* Above values of exposure dose were obtained from a summation of alarm meter readings.

6. Conclusion

In October 1979, the replacement of the acid-recovery evaporator was completed as scheduled and hot operation of the plant was resumed in November. After that the reprocessing plant has been operated successfully and the guarantee test was completed in February 1980.

This replacement was the first large-scale maintenance work in a hot cell in Japan, and through the experience of this work plenty of valuable information was obtained in connection with maintenance of the spent fuel reprocessing plant.

Acknowledgement

The authors would like to acknowledge the continuing guidance and encouragement of Mr. H. Akutsu, Mr. G. Fukuda, and Mr. I. Tanaka. They also wish to thank Mr. T. Tachihara, Mr. K. Nakata, and their colleagues for their contributions to this work.

References

(1) Akutsu, H. : "Repair Works of Tokai Reprocessing Plant" Atoms in Japan, January P. 13 (1980)

(2) Hayashi, H. , Araya, S. and Tanaka, I. : "Experience in the Replacement of Failed Acid Recovery Evaporator at the Tokai Reprocessing Facility" Specialist Meeting on Decommissioning Requirements in the Design of Nuclear Facilities, OECD/NEA, March (1980).

Uranium Enrichment Development Division

Activity of Uranium Enrichment Development Division (Jan. 1979—Mar. 1980)

The first stage construction of the pilot plant was completed on schedule at Ningyo Toge Works and the production of enriched uranium started in September, 1979. The operation has no problem and the cascade is operated successfully as designed. The second stage construction is also satisfactorily progressing.

At the Tokai Works we have continued research and development works for the third stage of the pilot plant and a future demonstration plant. Various experiments and studies have been made to verify performance of a centrifuge, controllability of a cascade, reliability of plant components, and other capacities. We have also participated in a project on demonstration plant design which is planned mainly at the headoffice of PNC.

1. Development of Centrifuge

For the third stage of the pilot plant, experimental and theoretical studies were made on performance, reliability and productivity of the centrifuge. Research and development works have been made on materials and elements for a future plant and designs have also been developed for a future machine with a high performance and a low fabrication cost.

2. Development of Cascade Technology

Both dynamic and static characteristics were examined on the cascades which consist of the centrifuges for the first and the second stage of the pilot plant. The data obtained are useful for operating the pilot plant and designing a future demonstration plant.

3. Life Test of Centrifuge

The pilot plant operation was preceded by life testing of prototype machines, which were satisfactorily operated for several years. Another life testing started with machines for a demonstration plant.

4. Development of Plant Components

The technique of UF_6 transfer was established by making various tests with cold traps, chemical traps and pumps in the UF_6 Reliability Test Facility. Investigations were made on a more rational and economical system of UF_6 handling for a future plant.